Kinematic, Metamorphic, and Geochronologic Constraints on the Evolution of the Lhagoi Kangri Gneiss Dome, Southern Tibet: Insight into Mid-Crustal Processes During Himalayan Orogenesis

A Dissertation Presented for the
Doctor of Philosophy
Degree
The University of Tennessee, Knoxville

Timothy Francis Diedesch
December 2016

Copyright © 2016 by Timothy Diedesch

All rights reserved.

DEDICATION

This dissertation is dedicated to Barbara, Jon, Josh, and Jessica whom have continually supported me and helped me grow through all of my experiences.

ACKNOWLEDGMENTS

I would like to thank Micah Jessup and John Cottle for their guidance and support during this research project as well as for sharing their interest in the Himalaya with me. I thank the rest of my committee: Robert D. Hatcher, Jr., Lawrence Taylor, and Brian Edwards for dedicating their time and expertise to help strengthen my research and writing. I also thank our collaborator at the Chinese Academy of Geological Sciences in Beijing, Dr. Lingsen Zeng, without whom much of the work presented here would not have been possible. Erik Heider and Michael Smith are thanked for their direct contributions to this research project while undergraduates at The University of Tennessee, and I would also like to thank the following colleagues whom provided inspiration for some of this work or whom engaged in helpful discussion regarding the various research problems addressed herein: Jackie Langille, Kyle White, Remington Leger, Cameron Hughes, and Michael Lucas. A number of past and present members of the Planetary Geosciences Institute have been very helpful, but in particular, Allan Patchen's assistance with electron microprobe analyses was invaluable. Gareth Seward at the University of California, Santa Barbara conducted the EBSD analyses, without which the first chapter would be incomplete.

I would also like to acknowledge my gratitude to the funding agencies responsible for supporting my research. Primary funding for this project was provided by National Geographic (NG-CRE-8490-08) and the National Science Foundation grants (EAR-0911561 and EAR-0911416) awarded to Micah Jessup and John Cottle. Additional funding was through the College of Arts and Sciences Penley-Thomas Fellowship and the Department of Earth and Planetary Sciences George D. Swingle Fellowship awarded to Tim Diedesch. The DigitalGlobe Foundation generously provided high-resolution satellite imagery that greatly improved the geologic map of the Lhagoi Kangri dome.

ABSTRACT

The north Himalayan gneiss domes are a series of isolated structures in southern-central Tibet that expose middle crust and record an early history of deformation, metamorphism, and partial melting. The domes are windows into the processes and physical conditions that promoted growth and uplift of the Himalaya during the early stage of collision (Eocene to Miocene) between India and Asia. Mechanisms responsible for creating the north Himalayan gneiss domes are crucial to understanding the early tectonic evolution of large orogens, such as the Himalaya, particularly with respect to crustal rheology and how middle crust is exhumed in collisional settings. Models for the formation and exhumation of these domes have been previously proposed and are based on both field evidence and thermomechanical modeling of the India-Asia collision. Each model has a set of predictable kinematic, metamorphic, and magmatic characteristics. This project focuses on a previously unstudied north Himalayan gneiss dome, Lhagoi Kangri, in order to (1) identify patterns of strain and metamorphism in the Himalayan middle to lower crust, (2) test previously developed models for north Himalayan gneiss domes, and (3) provide further constraints on the degree of commonality between the domes. Lhagoi Kangri is located ~100 km northeast of Mt. Everest. It comprises a cover of deformed, upper greenschist and amphibolite facies metasedimentary rocks and a core of orthogneiss and leucogranite. Results of this study indicate that rocks near the core-cover contact experienced Barrovian metamorphism c. 45–40 Ma followed by a prolonged period (≥11 My) of high temperatures (≥550 °C) during which pervasive ductile deformation resulted in the development of a distributed shear zone coeval with nearly isothermal decompression, the magnitude of which corresponds to ≥12 km of exhumation. The prolonged high temperatures, nearly isothermal decompression, and distributed ductile deformation demonstrate that there was structural continuity between the Lhagoi Kangri dome and other north Himalayan gneiss domes. Furthermore, these observations suggest that the middle crust was sufficiently weak to promote lateral flow that, in the Lhagoi Kangri dome, was accompanied by vertical attenuation.

TABLE OF CONTENTS

INTRODUCTION 1
Purpose 1
Geologic Background 1
North Himalayan Gneiss Dome Models 4
Diapirism 6
Upper Crustal Extension 7
Thrust Ramping or Underthrusting 8
Methods Overview 8
Kinematic Analysis 9
Microstructures and Deformation Temperatures 10
Thermobarometry 13
In-situ U-Th-Pb Monazite Geochronology 14
TiO2 Activity Modeling and Titanium-in-quartz Geothermometry 16
References 18
CHAPTER I: TECTONIC EVOLUTION OF THE MIDDLE CRUST IN SOUTHERN TIBET FROM STRUCTURAL AND KINEMATIC STUDIES IN THE LHAGOI KANGRI GNEISS DOME 23
Abstract 24
Introduction 25
Previous Work 27
Tectonic Models 28
Geologic Background 28
Lhagoi Kangri Lithology 29
Structural Characteristics 36
D_1 Deformation 37
Mesoscale Observations 37
Microscale Observations 37
D_2 Deformation 41
Mesoscale Observations 41
Microscale Observations 41
D_2 Kinematic Indicators 43
D_2 Quartz, Feldspar, and Calcite Microstructures 50
Background and methods 50
LKD calcite microstructures 51
LKD quartz and feldspar microstructures 52
D_2 Quartz Crystallographic Preferred Orientations 56
Background and methods 56
Quartz CPO patterns 59
Porphyroblast Inclusion Trails 60
Discussion 63
Interpretation of D_2 Microstructures and Quartz CPO Patterns 63
Tectonic Evolution of the Lhagoi Kangri Dome 67
Comparison to Other NHGD 71
Tectonic Implications 72
Conclusions 76
References 77

Appendix 1.1 84
Appendix 1.2 85
Appendix 1.3 86
Appendix 1.4 87
CHAPTER II: BARROVIAN METAMORPHISM AND DUCTILE DEFORMATION ACCOMPANIED BY NEAR-ISOTHERMAL DECOMPRESSION IN THE LHAGOI KANGRI DOME, SOUTH CENTRAL TIBET 88
Abstract 89
Introduction 90
Geologic Setting 93
Lhagoi Kangri Dome 94
Summary of Petrographic Analyses 96
Unit Ts Schist 96
Unit Ps Schist 97
Unit Ps Paragneiss 101
Methods 104
Thermobarometry 104
P-T Pseudosections 105
In-situ Monazite Petrochronology 106
Mineral Compositions and Average P-T 108
Unit Ts Samples 108
Unit Ps Schist Samples 108
Unit Ps Paragneiss Samples 116
Pseudosections 117
In-Situ U-Th-Pb Monazite Geochronology and Chemistry 120
Discussion 125
Monazite Petrochronology 125
Prograde Metamorphism 128
Decompression 129
Tectonic Implications 133
Conclusions 134
References 136
Appendix 2.1 141
Appendix 2.2 144
Appendix 2.3 145
Appendix 2.4 148
Appendix 2.5 150
Appendix 2.6 152
Appendix 2.7 155
Appendix 2.8 169
CHAPTER III: INFLUENCE OF METAMORPHISM AND DYNAMIC RECRYSTALLIZATION ON TITANIUM-IN-QUARTZ IN PELITIC ROCKS FROM THE LHAGOI KANGRI DOME, SOUTHERN TIBET 170
Abstract 171
Introduction 172
Geologic Setting and Sample Description 173
Methods 178
Results 181

Quartz CL Imaging 181
Ti-in-quartz Analyses 183
LK11-16c 183
LK11-54 185
LK11-59 185
LK11-60 186
Titanium Activity Modeling 186
Implications for Ti-in-quartz Thermometry 192
Summary and Conclusions 196
References 198
CONCLUSION 200
VITA 201

LIST OF TABLES

Table 1.1. Representative kinematic and deformation temperature data 46
Table 2.1. Modal analyses and modeled bulk compositions for pseudosections 107
Table 2.2. Average mineral compositions of main solid-solution phases 109
Table 2.3. P-T estimates for Barrovian metamorphism 112
Table 3.1. Ti-in-quartz analyses and previous P-T constraints 184

LIST OF FIGURES

Figure 1. Simplified geologic map of the Himalaya 2
Figure 2. South to north cross section through the Himalaya 3
Figure 3. Landsat image of Everest area 4
Figure 4. Possible mechanisms responsible for forming the North Himalayan gneiss domes 5
Figure 5. Diagram of quartz slip systems 10
Figure 6. Sketches of quartz microstructures 11
Figure 7. Schematic diagram showing the relationship between deformation temperature and calcite twin morphology. 12
Figure 1.1. Simplified geologic map of southern Tibet 26
Figure 1.2. Geologic map of portions of the Lhagoi Kangri dome 30
Figure 1.3. Cross sections through the north and south sides of the Lhagoi Kangri dome 32
Figure 1.4. Stratigraphic section of Lhagoi Kangri bedrock 33
Figure 1.5. Field photographs 35
Figure 1.6. Simplified Lhagoi Kangri dome map showing variation of shear sense 38
Figure 1.7. Photos and photomicrographs of D_1 structures. 40
Figure 1.8. Photomicrographs of microscale D_2 structures 42
Figure 1.9. Mesoscale examples of D_2 kinematic indicators 44
Figure 1.10. Photomicrographs and thin section scans of microscale D_2 kinematic indicators 45
Figure 1.11. Photomicrographs of calcite twin microstructures 52
Figure 1.12. Representative quartz and feldspar microstructures 53
Figure 1.13. Quartz CPO data by structural position 57
Figure 1.14. Photomicrographs showing relationship between porphyroblast inclusion trails and matrix fabric 61
Figure 1.15. Variation in interpreted deformation temperatures and shear sense with depth 66
Figure 1.16. Deformation temperature field gradients 68
Figure 1.17. Block diagram summarizing the D_2 structures and kinematic indicators 70
Figure 2.1. Simplified geologic maps of south-central Tibet and the Lhagoi Kangri dome 91
Figure 2.2. Geologic cross section and outcrop photos 95
Figure 2.3. Photomicrographs of the unit Ts schist samples 97
Figure 2.4. Photomicrographs of unit Ps schist samples 99
Figure 2.5. Photomicrographs of the unit Ps paragneiss samples 102
Figure 2.6. Examples of garnet compositional profiles and Mn Kα X-ray images 114
Figure 2.7. P-T pseudosection model for sample LK11-60 118
Figure 2.8. Monazite X-ray images showing locations of LASS spot analyses and ages 121
Figure 2.9. U-Th/Pb Concordia plots for the LKD monazite geochronology samples 122
Figure 2.10. Plots of monazite age versus chondrite-normalized element abundances 127
Figure 2.11. Generalized P-T-t-D path for high grade rocks in the LKD 130
Figure 3.1. Geologic map of a portion of the Lhagoi Kangri dome 174
Figure 3.2. Backscattered electron (BSE) images and photomicrographs of LK11-16c 176
Figure 3.3. BSE images of different microstructural domains in sample LK11-59 177
Figure 3.4. BSE images of two fine matrix quartz domains from sample LK11-60 178
Figure 3.5. BSE image and photomicrograph of LK11-54 179
Figure 3.6. Example blue-filtered cathodoluminescence (CL) images 182
Figure 3.7. P-T pseudosections for Ps metapelites 188
Figure 3.8. Modeled $a\mathrm{TiO_2}$ for the LKD metapelites 190
Figure 3.9. Diagram showing effects of decreased $a\mathrm{TiO_2}$ on location of Ti-in-quartz isopleths 194

LIST OF ATTACHMENTS

Monazite laser ablation split-stream U-Th/Pb ages and geochemical analyses Appendix2.8.pdf

INTRODUCTION

Purpose

The primary goal of this project is to characterize the tectonic processes responsible for the formation and exhumation of the Lhagoi Kangri gneiss dome (LKD), and to place it in the context of the evolution of Himalayan crust following initial collision of India with Asia. In particular, this study will: (1) identify spatial and temporal patterns of deformation within and adjacent to the dome; (2) characterize the timing of metamorphism and its relationship to local deformation; (3) determine timing of emplacement and deformation mechanisms accommodated by leucogranites within the dome; and (4) integrate observations related to these processes in order to test various models of North Himalayan gneiss dome genesis. These gneiss domes are a fundamental record of early syncollisional tectonic processes and a window into continental crustal rheology. Therefore, through detailed kinematic analysis, thermobarometry, thermochronology, and geochronology on LK gneiss dome samples, this study will provide valuable constraints on mid-crustal processes of continent-continent collision.

Geologic Background

The Himalayan orogen is situated between the stable Indian craton to the south and the Indus-Tsangpo suture zone, which marks the boundary between the Eurasian and Indian Plates, to the north (Fig. 1; Gansser, 1980; Molnar and Tapponier, 1977). Collision between the two plates began ~55 Ma (e.g., Guillot et al., 2003) and continues through the present day at a rate of ~35 mm/yr (Bettinelli et al., 2006). Modern plate motion is accommodated by south-vergent thrusting in the foreland and by east- and west-dipping normal faults, as well as conjugate strike-slip faults, in the orogenic core and the interior of the Tibetan Plateau (e.g., Armijo et al., 1986; Kapp and Guynn, 2004; Taylor et al., 2003).

The northern Himalaya and southern margin of the Tibetan Plateau can be separated into three lithotectonic units that are bounded by major faults that strike parallel to the orogen (Fig. 2; e.g., Hodges, 2000; Yin and Harrison, 2000): (1) the Lesser Himalayan series (LHS); (2) the Greater Himalayan series (GHS); and (3) the Tethyan sedimentary sequence (TSS). The Lesser Himalayan series is the structurally

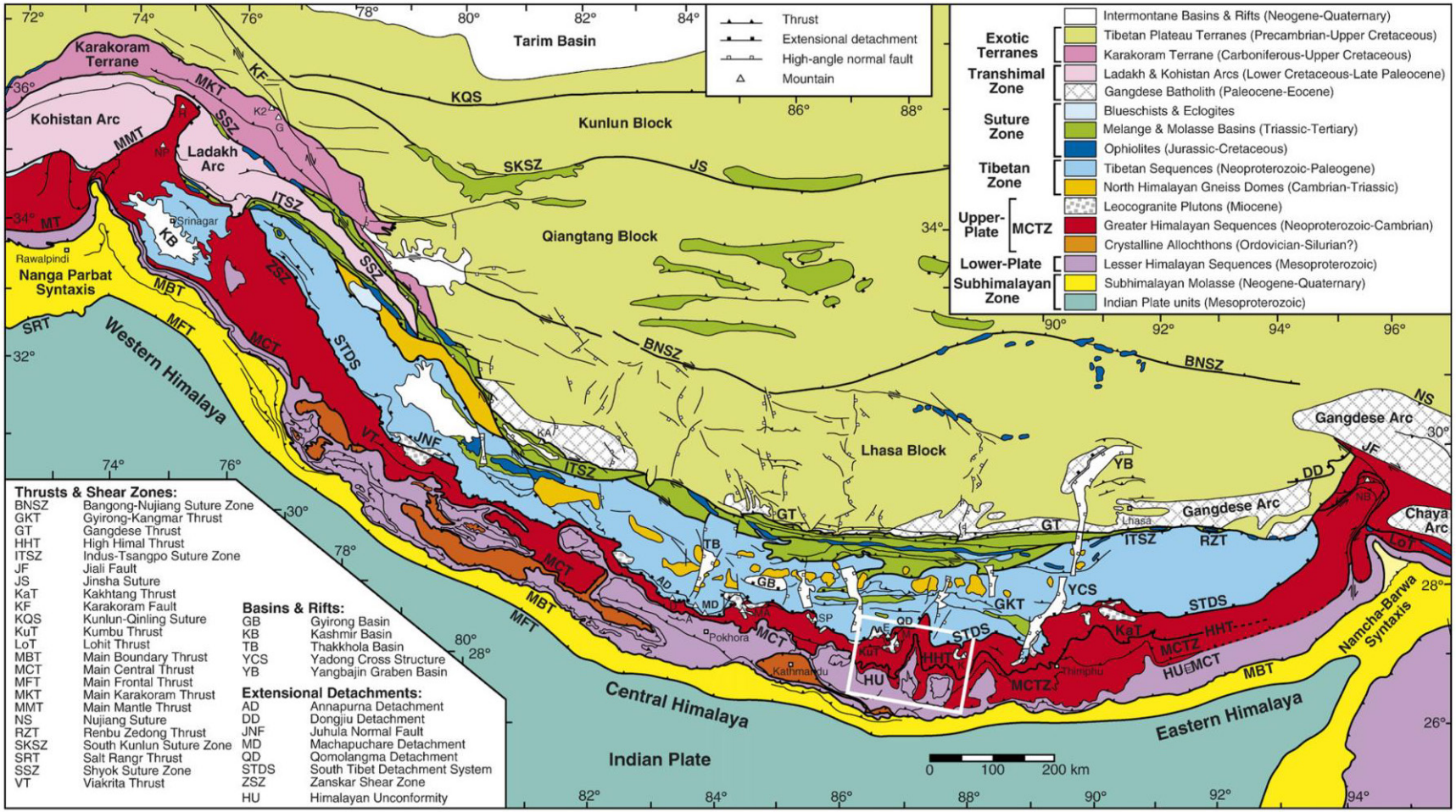


Figure 1. *Simplified geologic map of the Himalaya. Note distribution of North Himalayan gneiss domes (orange bodies in Tibetan Zone). White box is approximate location of Figure 3. ITSZ - Indus-Tsangpo suture zone. For other relevant abbreviations, see text. After Goscombe et al. (2006).*

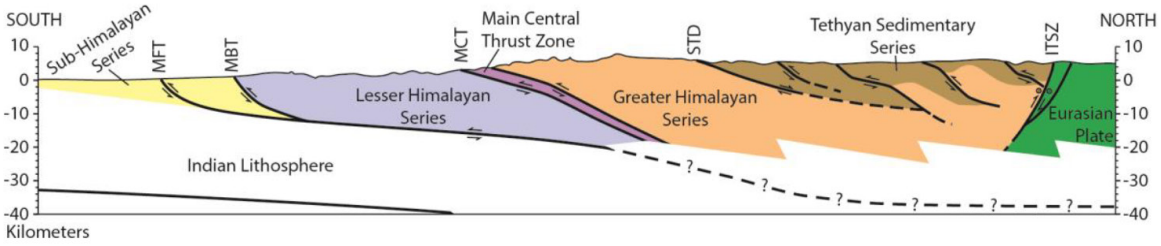


Figure 2. *South to north cross section through the Himalaya showing major lithotectonic units discussed in text. Modified after Hauck et al. (1998) and Lavé & Avouac (2001).*

lowest unit that comprises the Himalaya foothills, and is composed mainly of lower-greenschist to lower-amphibolite facies metasedimentary rocks. The base of the LHS is the Main Boundary thrust, which juxtaposes LHS on Quaternary foreland deposits of the actively deforming Sub-Himalayan Zone. The upper boundary of the LHS is the Main Central thrust zone (MCT), which faulted GHS over LHS. The GHS is composed of granites and upper-amphibolite facies metamorphic rocks that are interpreted to represent the core of the Himalaya. The GHS also comprises the footwall of the South Tibetan detachment system (STDS), a low-angle, top-down-to-the-north fault system that juxtaposes TSS on GHS. The TSS is a nearly continuous Cambrian to Eocene stratigraphic sequence that is generally unmetamorphosed except in localized zones where crustal thickening was sufficient to initiate regional metamorphism (e.g., Carosi et al., 1998; Searle et al., 1999).

The highest degree of TSS metamorphism is spatially associated with the North Himalayan gneiss domes (NHGD), a series of tens-of-km-scale domes cored by gneiss and leucogranites exposed between the STDS and the Indus-Tsangpo suture zone and forming a roughly east-west belt that spans western to east-central Himalaya (~078—089 °E; Fig. 1). Metamorphosed TSS forms the carapaces of these domes and is typically intruded by dikes and sills that may or may not be genetically related to magma bodies within the cores of the domes (cf., Lee et al., 2000; Aoya et al., 2006). Some domes are cored entirely by granite while others contain a combination of granite and orthogneiss, which has led to a multitude of different ideas about how they formed, and consequently, their role in the tectonic evolution of the Himalaya (Aoya et al., 2006). Particular emphasis has been placed on the contact between the domes and the overlying metamorphosed TSS that has led to the emergence of two conflicting viewpoints: (1) the contact is the margin of a pluton that ascended through the crust (e.g., Le

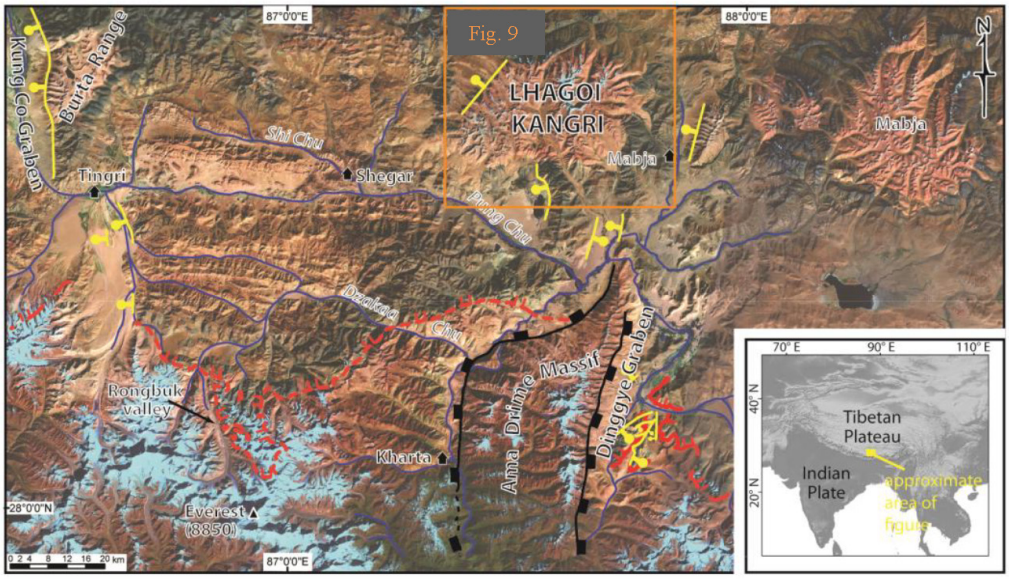


Figure 3. *Landsat image of Everest area highlighting location and characteristics of the Lhagoi Kangri and Mabja gneiss domes. From Jessup and Cottle (2010).*

Fort, 1986), and (2) the contact is a structural discontinuity, possibly a domed, northern projection of the STDS (e.g., Chen et al., 1990; Lee et al., 2004).

Lhagoi Kangri gneiss dome is a ~40 x 25 km elliptical structure with an east-west-oriented long axis. It is located ~100 km north of Mt. Everest and < 50 km west of the well-studied Mabja dome (Fig. 3; Lee et al., 2004). The entirety of previous geologic research conducted on the Lhagoi Kangri gneiss dome (LKD) consists of a series of zircon and monazite U-Pb ages (15.5 + 0.8 Ma) from a granite that intruded the western margin of LK (Schärer et al., 1986).

North Himlayan Gneiss Dome Models

Several models have been proposed for the development and exhumation of the North Himalayan gneiss domes based upon geological observations (e.g., Burg et al., 1984; Chen et al., 1990; Lee et al., 2000; Lee et al., 2004) and thermomechanical modeling of the India-Asia collision (Beaumont et al., 2004)(Fig. 4). These models fall into a spectrum defined by three end members: (1) diapirism driven by density or viscosity contrasts (e.g., Teyssier and Whitney, 2002; Beaumont et al., 2004), (2) footwall exhumation during syncollisional extension (e.g., Chen et al., 1990), and (3) ramping or

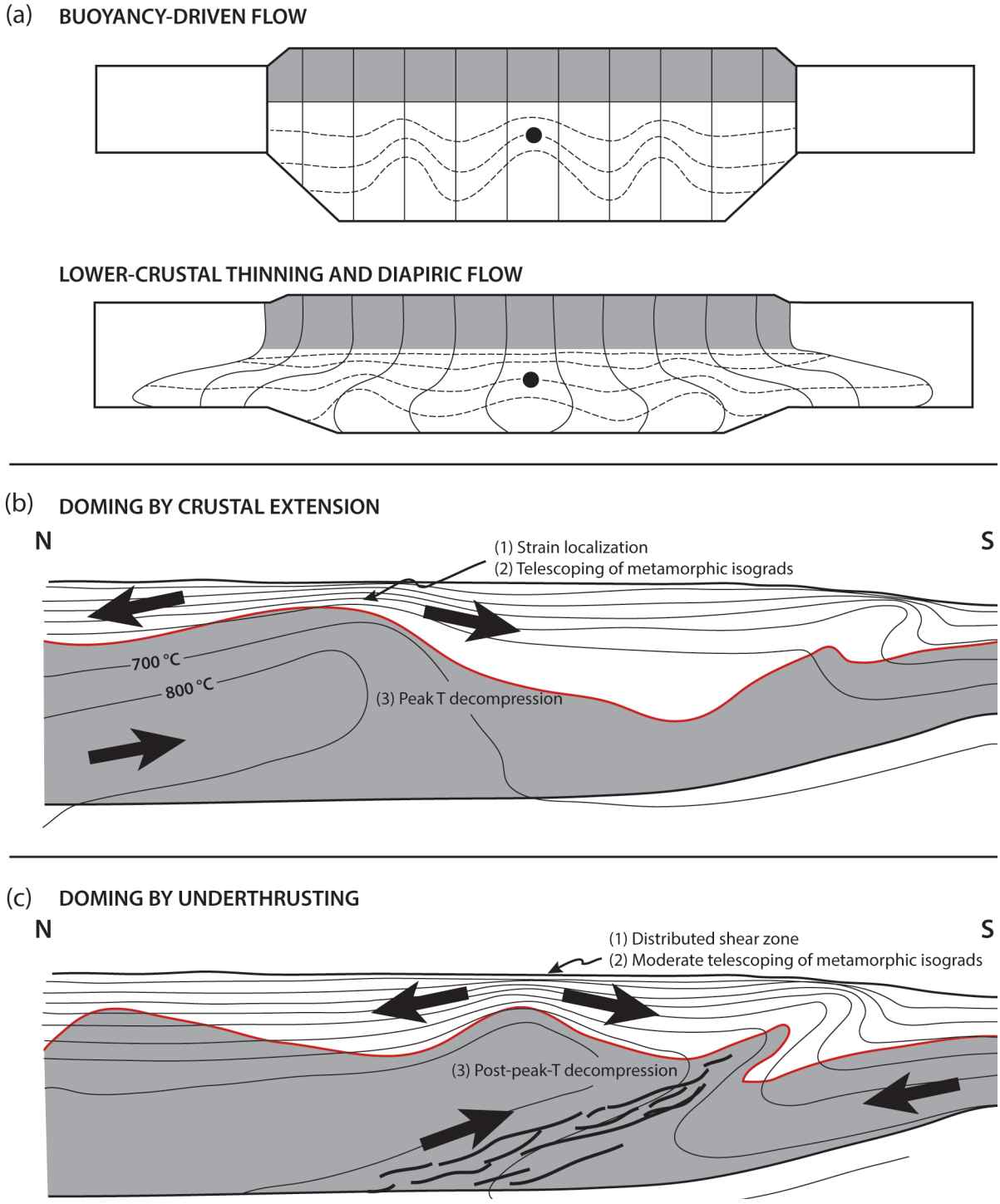


Figure 4. *Possible mechanisms responsible for forming and exhuming North Himalayan gneiss domes. (a) Diapirism or buoyancy-driven uplift of ductile lower crust. (b) Crustal extension with doming of ductile lower crust into space created by faulting, and (c) doming by underthrusting beneath a weak lower crustal channel. Modified from Teyssier and Whitney (2002) and an M. Jessup and J. Cottle NSF proposal.*

duplexing in a thrust fault system (e.g., Lee et al., 2000; Beaumont et al., 2004). Each model comprises a predictable set of kinematic, metamorphic, and magmatic processes, including temporal and spatial patterns between each process. Consequently, NHGD models are testable through field and lab analyses. Individual conditions are not uniquely diagnostic of one particular model, so metamorphic, structural, and magmatic data must all be integrated in order to sufficiently evaluate each formation mechanism. Both field observations (e.g., Grujic et al., 2002) and thermomechanical modeling (Beaumont et al., 2001; Beaumont et al., 2004) suggest that North Himalayan gneiss domes may occur in conjunction with, or as a result of, channelized flow of low viscosity mid-crustal material (e.g., Beaumont et al., 2004; Lee et al., 2004; Langille et al., 2010), in which case specific gneiss dome mechanisms vary somewhat from the ideal end members outlined above. The main field evidence supporting channel flow is metamorphic isograds that are right-way-up at the base of the GHS and inverted at the top, as well as variations in kinematic vorticity throughout the GHS (e.g., Grujic et al., 2002). The main objectives of this research are to evaluate the processes that formed the Lhagoi Kangri gneiss dome, and to determine how it relates to larger scale mid- to lower-crustal processes in the Himalaya (Chambers et al., 2009; Jessup et al., 2006; Langille et al., 2012; Larson et al., 2010; Vannay & Grasemann, 2001).

Diapirism

Models of gneiss dome emplacement that invoke diapirism (Fig. 4a), such as that of Teyssier and Whitney (2002), predict salient geometric and kinematic characteristics in addition to core-rock P-T-t paths and patterns of cover-rock metamorphism. Map- to outcrop-scale geometric features for an ideal diapiric gneiss dome include: (1) a pluton or migmatite body centered within the dome, (2) concentric foliation within the core that is concordant with the core-cover contact, (3) radiating mineral lineations that record shear during dome development, and (4) tangential mineral or intersection lineations within the dome that form from flexural flow folding induced during intrusion. Pure end-member diapirism produces a core-up sense of shear and an increase in strain intensity with proximity to the margin of the gneiss dome, which contrasts with the uniformly distributed strain expected of simple fold interference models (Teyssier and Whitney, 2002). Additionally, if deformation at the margins of the dome is related to diapirism then it should be coeval with magma emplacement. A component of channel flow superposed on the diapirism model will produce asymmetry in diapiric structural fabrics resulting in more

recumbent nappe-style geometry with the relative rates and durations of the two processes (diapirism and lateral flow) controlling the specific geometry of the resultant dome (Whitney et al., 2004). Since the North Himalayan gneiss domes occur in a relatively symmetric east-west-striking antiform, it may be hypothesized that, if channel flow was an important mechanism in southern Tibet, buoyant ascent outpaced or outlasted channel flow. Diapirism generates predictable metamorphic characteristics in core and cover rocks: most notably rapid, near-isothermal decompression at relatively high temperature (> 700°C; Teyssier and Whitney, 2002). Also, spatial and temporal trends of metamorphism within the gneiss dome should mimic those of magmatism such that metamorphic isograds are concentric about the intrusion. Diapirism acting alone is the most effective process for producing near-isothermal decompression, but other processes in combination can achieve similar results and are addressed in the other models below.

Upper Crustal Extension

Another effective means for producing North Himalaya-style gneiss domes is through synconvergent extension, which can be induced by bulk pure shear (gravitational collapse; Burchfiel & Royden, 1985; Rey et al., 2001) or channel flow (Beaumont et al., 2004). Gravitational collapse models for the Himalaya invoke the concept that large topographic variations induce lateral pressure gradients that can act independently of (Burchfiel and Royden, 1985), or in conjunction with (Kapp and Guynn, 2004), plate tectonic forces to extend the crust. Under channel flow models, upper crustal extension could be initiated by the above processes; however, under asymmetric channel flow, in which the upper crust is sufficiently weak that it is at least partially coupled to the lower crustal channel, upper crustal extension could be initiated in the hinterland to balance foreland transport in the hanging wall of the channel (Beaumont et al., 2004; Hodges, 2006). For the central Himalaya, channel flow-induced extension would generate normal faults that strike roughly east-west with top-north or top-south shear sense in contrast to the top-east or top-west normal faults documented throughout the Tibetan Plateau (e.g., Armijo, 1986; Taylor et al., 2003). Regardless of how upper crustal extension is initiated, it could serve to localize channel exhumation, and if lateral flow outpaces or outlasts extension, it is predicted that the channel would dome into spaces created by extension (Fig. 4b; Beaumont et al., 2004; Hodges, 2006). Geologic characteristics of this model include: (1) telescoping of metamorphic isograds and (2) decompression

at lower pressure and temperature than that of Barrovian metamorphism, although temperature during both phases may be similar. Since burial metamorphism takes place prior to extension, metamorphic isograds formed during burial should be telescoped as a result of vertical thinning during extension and decompression conditions recorded in the rocks should partially or entirely overprint the burial conditions.

Thrust Ramping or Underthrusting

Two variants of compression-related doming are postulated for the north Himalayan gneiss domes: (1) ramping of the hanging wall of a blind thrust (Lee et al., 2000, 2004), and (2) indentation and underthrusting of strong Indian craton (e.g., Beaumont et al., 2004, 2006; Fig. 4c). In either case, the primary distinction from other modes of dome formation and exhumation is that cooling should take place from bottom to top since hotter material in the antiformal stack would be juxtaposed on relatively cooler rocks along the thrust fault, which would result in a concentric pattern of cooling ages from older in the center of the dome to younger at the margins. Doming could conceivably continue through moderate and even low temperature cooling steps, thus the respective thermochronologic data would be domed as well (e.g., Lee et al., 2000). Furthermore, if doming was the product of late-stage ramping, the contact of the gneiss dome with overlying metasedimentary rocks would act as a passive marker through dome formation. If the contact was passively domed, it is expected that either: (1) the dome contact is a stratigraphic contact that records no strain; or (2) that any strain accommodated by the contact predates doming-related deformation. Lee et al. (2000, 2004) suggested that the margins of some NHGDs represent a structurally lower, ductile portion of the STDS, which, if passively domed, would still preserve consistent top-to-the-north shear sense at all positions along an individual dome boundary.

Methods Overview

As with most geologic problems, testing NHGD models for Lhagoi Kangri requires a combination of field observation, sample collection, and lab analysis. Two summers of field work (2010 and 2011) yielded a suite of samples appropriate for characterizing structural, metamorphic, and magmatic aspects of the LKD using a plethora of analytical methods. Kinematic and deformation

temperature analyses will serve to constrain both the conditions attendant to deformation during evolution of the dome as well as the spatial and temporal patterns of deformation throughout the study area. Petrography and thermobarometry will be employed to determine the metamorphic conditions of the cover rocks, from burial through exhumation and doming. U-Th-Pb geochronology of monazite in metasedimentary rocks will be used to resolve the time component of metamorphism and deformation, while U-Th-Pb geochronology of zircon in granite will be used to resolve the timing of deformation and magmatism. In order to quantify the rates and patterns of cooling within and around LK, moderate temperature cooling steps (550-300 °C) will be characterized using $^{40}Ar/^{39}Ar$ thermochronology on individual mineral phases. Combined, these analyses will serve to constrain the P-T-t-D path of rocks within and adjacent to Lhagoi Kangri and to quantify the pertinent variables that distinguish the various NHGD models.

Kinematic Analysis

Thin sections cut parallel to lineation and perpendicular to foliation (XZ plane) will be used to document shear-sense indicators recorded in rocks from various structural levels above and below the boundary of the gneiss dome. Microstructures such as tails or strain shadows on porphyroblasts or porphyroclasts, mica fish, shear bands, and grain-shape fabrics where present will be used to determine shear sense for individual samples.

Crystallographic orientation of quartz grains can also be used to quantify the kinematics of a sample. During plastic deformation, movement of dislocations through the crystal lattice serves to generate slip on crystal planes leading to realignment of the crystal axes, and with continuous deformation a pattern, or lattice-preferred orientation (LPO), may emerge amongst the population of grains in a given sample (e.g., Lister and Hobbs, 1980; Fig. 5). In thin sections oriented parallel to the XZ plane, electron backscatter diffraction (EBSD) can be used to document orientation of quartz crystallographic axes, and the resulting LPO patterns, plotted on a stereonet, yield information about the symmetry or asymmetry of deformation. Since XZ samples are oriented perpendicular to the flow plane, asymmetric LPOs can be used to interpret the shear-sense during the main fabric development (Law, 1990). EBSD analysis was conducted on a FEI Quanta 400 scanning electron microscope (SEM) equipped with a Nordlys 2 EBSD camera and housed at the University of California, Santa Barbara.

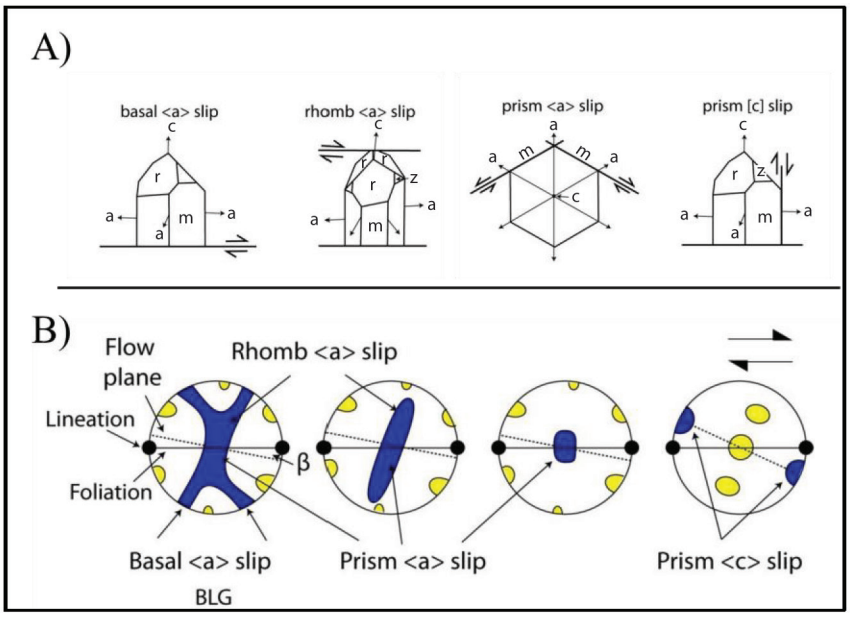


Figure 5. *Diagram of (a) quartz slip systems active during moderate to high temperature deformation, and (b) idealized stereographic projections of LPO patterns with c-axis orientations in blue and a-axis orientations in yellow. Modified from Schmid and Casey (1986) and Passchier and Truow (2005).*

Microstructures and Deformation Temperatures

Quartz, feldspar, and calcite textural and microstuctural analysis will provide the basis for estimating deformation temperatures throughout the metasedimentary cover rocks and the highest structural levels within the dome, and quartz LPO patterns can also be used to quantify deformation temperatures.

Quartz and feldspar exhibit specific textures in deformed rocks that are dependent upon the temperature of the rock during deformation. At a temperature range of 250–650 °C, quartz deforms internally by dislocation creep and this strain is accommodated by dynamic recrystallization. Three regimes are defined and quantified for quartz dynamic recrystallization fabrics and their associated temperatures: (1) bulging (BLG) recrystallization, which dominates at temperatures of 280–400 °C, subgrain-rotation (SGR) recrystallization, which takes place at 400–500 °C, and (3) grain-boundary migration (GBM) recrystallization, which dominates at 500–650 °C (Hirth and Tullis, 1992; Stipp et al., 2002; Fig. 6). Feldspar tends to deform by brittle fracture under the same conditions as quartz BLG, and at slightly higher temperatures will develop textures such similar to those acquired by quartz through dynamic recrystallization. Feldspar deformation mechanisms are only qualitative temperature

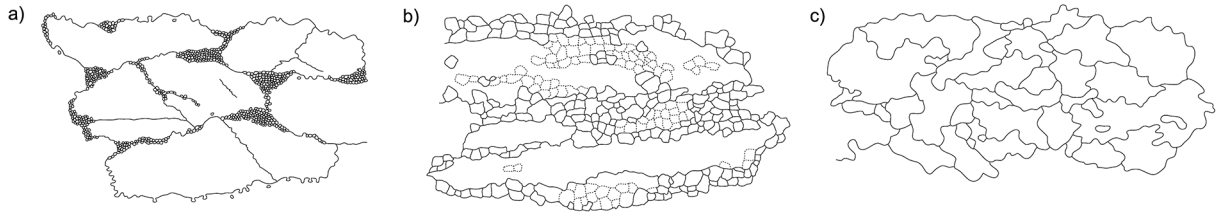


Figure 6. *Sketches of quartz microstructures associated with (a) bulging—BLG, (b) subgrain rotation—SGR, and (c) grain boundary migration—GBM dynamic recrystallization mechanisms. From Stipp et al (2002).*

indicators since the transitions between each mechanism are highly sensitive to fluid content (e.g., Tullis and Yund, 1991), but they provide necessary constraints when interpreted in conjunction with quartz microstructures.

At temperatures below ~400 °C, calcite accommodates strain by mechanical twinning, the morphology and pervasiveness of which provide insight into deformation temperature. Calcite mechanical e-twins manifest texturally as narrow bands that transect an individual grain, and the thickness of these bands increases with increasing deformation temperature (Ferrill et al., 2004; Fig. 7a). Calcite microstructures are dominated by thin twins (Type I) below 170 °C and thick twins (Type II) above 200 °C. Type I twins are < 1μm thick and typically <0.5 μm, whereas Type II twins range from 1 to 10 μm thick. At 200 °C Type II twins form both spontaneously and by Type I twin-boundary migration, whereas new type I twins do not form (Ferrill et al., 2004). Additionally, there is an inverse relationship between twin thickness and number of twin bands per unit length, so under Type II conditions twin intensity (# of twins/mm) does not exceed ~40/mm (Fig. 7b). At higher deformation temperatures (> 300 °C), calcite twins develop a curved morphology (Type III) and begin to dynamically recrystallize, forming irregular twins (Type IV; Ferrill et al., 2004). Since other strain-accommodation processes such as pressure solution and brittle fracture are also common in carbonates, calcite textural and microstructural characteristics can also constrain deformation history. For instance, Ferrill et al. (2004) outline two scenarios: one in which twinning at 200 °C is followed by heating, and one in which twinning is followed by cooling. In the former case type II twins and grain-boundary recrystallization would dominate the texture, whereas in the latter, type II twins and cross-cutting type I twins would define the overall texture.

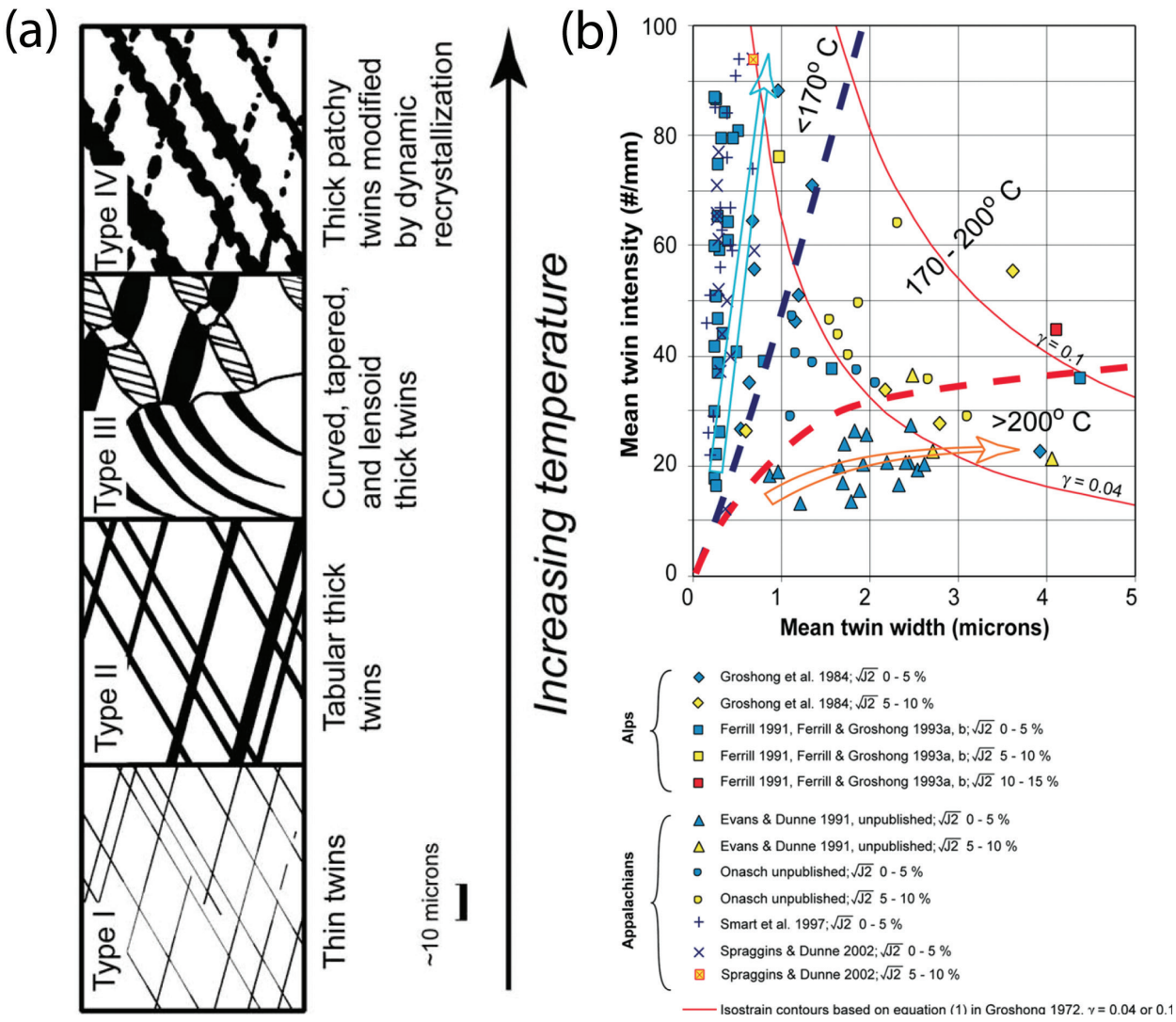


Figure 7. *(a) Schematic diagram showing the relationship between deformation temperature and calcite twin morphology. (b) Plot of twin intensity versus twin width showing range of variability of natural and lab samples. From Ferrill et al (2004).*

Thermobarometry

Thermobarometric analyses will be applied to samples with appropriate mineral assemblages to estimate pressure and temperature conditions during metamorphism. Phases such as garnet, plagioclase, biotite, muscovite, and aluminum silicates are first checked for textures indicative of equilibrium using a petrographic microscope. In addition to textural relationships, detailed petrographic analysis will also be used to document the relationships between particular metamorphic phases and structural fabric. For relevant phases, such as those listed above, chemical compositions will be determined using a Cameca SX-100 electron microprobe housed at the University of Tennessee. Major element zoning patterns in garnet are indicative of the P-T history of the sample. Particularly, decreases in Mn and Fe# (Fe/[Fe + Mg]) from core to rim are assumed to reflect growth during prograde metamorphism (e.g., Tracy et al., 1976; Yardley, 1977). Qualitative evaluations of garnet zoning in selected samples will be made by generating element maps for Mg, Mn, Ca, and Fe on the microprobe. Patterns in the element maps will also be used to interpret the types of secondary chemical processes that disrupt normal zoning patterns. Metapelites like those from Lhagoi Kangri are particularly susceptible to retrograde net-transfer reactions involving garnet, which can lead to significant overestimate of peak temperature and are generally recognized by a small increase in Mn from near-rim to rim (Kohn and Spear, 2000). In order to quantify chemical compositions, point analyses using the microprobe will be conducted for garnet, and other metamorphic phases, using results of element mapping to identify the best locations for conducting quantitative analysis.

To establish the most complete P-T paths for LKD samples, quantitative compositional data will be applied to three common thermobarometric analysis methods. Traditional thermodynamic calculations and calculations involving the software THERMOCALC (Powell and Holland, 1994) will be applied to equilibrium assemblages. Traditional thermodynamic calculations will involve combinations of exchange and net-transfer reactions that are expected to take place in metapelites such as: (1) Fe-Mg exchange between garnet and biotite (GARB), a good thermometer because volume change of reaction (dVr) is small; (2) anorthite = grossular + aluminum silicate + quartz (GASP), a net-transfer reaction, which makes a good barometer because net-transfer reactions have large dVr; and (3) almandine + rutile = ilmenite + aluminum silicate + quartz (GRAIL), another net-transfer reaction. The merit of the activity models for these reactions have been evaluated on the basis of: (1) consistency of variables such as P, T,

and X between the samples used to define the models and those for the LKD samples; and (2) internal consistency, in other words, consistency between activities and thermodynamic data used for different reactions. In particular, the GARB 5AV activity model of Holdaway (2000) is most appropriate for LK rocks, and as a consequence, the GASP recalibration of Holdaway (2001) is the most internally consistent with respect to GARB 5AV.

Since THERMOCALC is not equipped to calculate distribution coefficients for Fe-Mg exchange reactions, temperature errors are typically quite large, and GARB 5AV solutions are more accurate. However, THERMOCALC computes net-transfer devolitalization reactions and allows the user to input values for xH20, so one method for improving THERMOCALC P-T results is to vary the value of xH20 input into THERMOCALC's average P-T mode (Searle et al., 2003; Jessup et al., 2008). An acceptable result is reached when two criteria are met: (1) the THERMOCALC temperature result is consistent with the GARB 5AV solution and (2) the xH20 value used falls within a range that is reasonable for the geologic setting. Since THERMOCALC requires mineral activities as input, the companion software, AX, will be used to calculate activities. Finally, EMPA compositional data will be used to develop pseudosections, petrogenetic grids that pertain to individual rock compositions, which will be constructed for key samples and for those in which the equilibrium assumption is tenuous. Bulk rock compositions will be estimated using a combination of petrographic point-count analysis and EMPA. A reasonable approximation of bulk rock composition is reached by multiplying average mineral compositions, calculated from EMPA data, by their estimated modal percentage, which is calculated from point-count analyses. The pseudosections will be constructed with the assistance of the Perplex v. 6.6.6 software (Connolly, 2009).

In-situ U-Th-Pb Monazite Geochronology

^{238}U, ^{235}U, and ^{232}Th isotopes decay through a series of intermediate steps to daughter isotopes of Pb: ^{206}Pb, ^{207}Pb, and ^{208}Pb, respectively. The governing principle justifying the use of U-Th-Pb decay as a dating tool is that the half-lives of the intermediate isotopes are negligible with respect to the half-lives of the U and Th parent isotopes. Closure temperature (Tc), the temperature at which the parent and daughter isotopes cease to diffuse, varies for the U-Pb system depending on the mineral phase in which it is present (Dodson, 1973). The two phases that will be considered in this study are zircon and

monazite, for which closure temperatures generally exceed ~900 °C (e.g., Dodson, 1973; Cherniak et al., 2004). The following equations (Faure and Mensing, 2005) relate isotope ratios to age and result in three independent solutions:

$$t_1 = \frac{1}{\lambda_1} \ln \left(\frac{\left(^{206}\mathrm{Pb}/^{204}\mathrm{Pb}\right) - \left(^{206}\mathrm{Pb}/^{204}\mathrm{Pb}\right)_i}{^{238}\mathrm{U}/^{204}\mathrm{Pb}} + 1 \right) \quad (1)$$

$$t_2 = \frac{1}{\lambda_2} \ln \left(\frac{\left(^{207}\mathrm{Pb}/^{204}\mathrm{Pb}\right) - \left(^{207}\mathrm{Pb}/^{204}\mathrm{Pb}\right)_i}{^{235}\mathrm{U}/^{204}\mathrm{Pb}} + 1 \right) \quad (2)$$

$$t_3 = \frac{1}{\lambda_3} \ln \left(\frac{\left(^{208}\mathrm{Pb}/^{204}\mathrm{Pb}\right) - \left(^{208}\mathrm{Pb}/^{204}\mathrm{Pb}\right)_i}{^{232}\mathrm{Th}/^{204}\mathrm{Pb}} + 1 \right) \quad (3)$$

where t_n is time elapsed since closure and λ_n is the decay constant for the parent isotope in each. In both analysis techniques described below, isotope data are plotted on a graph of $^{207}Pb/^{235}U$ vs. $^{206}Pb/^{238}U$ and $^{208}Pb/^{232}Th$ vs. $^{206}Pb/^{238}U$ to determine if the age solutions are concordant. Discordance can arise from several sources, such as presence of original common lead or lead loss during reheating (e.g., Faure and Mensing, 2005).

U-Th-Pb analysis of growth domains in metamorphic monazite grains will be used to constrain the timing of metamorphism in Lhagoi Kangri. In-situ analysis is particularly useful in this instance because the textural context between monazite and other metamorphic phases is preserved, so the ages obtained from analyses can be linked to metamorphic reactions or growth of particular mineral phases. In ideal samples, the in-situ monazite ages relate to the time at which estimated P-T conditions were reached, so the in-situ technique will primarily be used on the metapelite samples selected for thermobarometry. The preservation of textural context means that in-situ monazite analysis can also be used to constrain ages of structural fabric development in appropriate samples.

In order to catalog the samples that are appropriate for in-situ monazite dating, a combination of petrographic analysis and electron microprobe analysis will be used to identify monazite grains. In samples where accessory phases are difficult to identify or differentiate, whole-thin section X-ray maps of Ce will be generated on the Cameca SX-100 at University of Tennessee. Ce maps highlight monazite particularly well and are overlain on Al or Mg X-ray maps that provide textural context for locating the monazite grains (Williams and Jercinovic, 2002). Once appropriate grains are identified in a sample,

additional X-ray maps of U, Th, Pb, and Y will be generated to characterize compositional zonation and the possibly highlight particular age domains. Samples will be analyzed using the laser-ablation split-stream (LASS) inductively coupled plasma mass spectrometry (ICP-MS) set-up at University of California, Santa Barbara. In a typical laser-ablation ICP-MS set-up, a laser is focused on a grain in order to ablate a small portion that is then routed into the mass spectrometer to identify specific elemental or isotopic species. The LASS system is designed to split the ablation aerosol into multiple quantities to allow simultaneous analysis on more than one mass spectrometer. For in-situ monazite geochronology, one mass spectrometer will used to measure U, Th, and Pb isotope ratios and another will be used to monitor the rare-earth element (REE) abundances at each spot analyzed (e.g., Kylander-Clark, 2013). REE patterns in metamorphic monazite are critical indicators of metamorphic reactions that take place between monazite and phases like garnet (e.g., Pyle and Spear, 1999), so the LASS capability of simultaneously monitoring REE and U-Th-Pb ratios throughout a monazite grain permit interpretation of the timing of specific metamorphic events such as peak-temperature or decompression.

TiO_2 Activity Modeling and Titanium-in-quartz Geothermometry

Experiments by Wark and Watson (2006) indicate that solubility of Ti in quartz is strongly temperature-dependent, and subsequent experimental calibrations of this solubility led to the development of the Ti-in-quartz (TitaniQ) thermobarometer (Thomas et al., 2010). TitaniQ has subsequently been used in a number of studies to constrain metamorphic temperatures (e.g., Ashley et al., 2013; Cherniak et al., 2007; Spear and Wark, 2009; Storm and Spear, 2009), deformation temperatures (e.g., Behr and Platt, 2011; Cross et al., 2015; Grujic et al., 2011; Kidder et al., 2013; Kohn and Northrup, 2009; Nachlas et al., 2014), and to constrain time scales of metamorphism via volume diffusion calculations (Cherniak et al., 2007; Spear et al, 2012). TitaniQ calculations require the assumption that $a\mathrm{TiO_2} = 1$ or that $a\mathrm{TiO_2}$ can be precisely calculated from phase equilibria involving Ti-bearing phases such as those of Ghent and Stout (1984).

In this study the Perple_X software described above was used to model $a\mathrm{TiO_2}$ for selected samples over a range in pressure and temperature. Titania activity was then used to calculate Ti-in-quartz concentration isopleths over the same range in pressure and temperature using the solubility equation:

$$\mathrm{RTln}X_{TiO_2}^{quartz} = -60952 + 1.520T - 1741P + \mathrm{RTln}a_{TiO_2} \quad (4)$$

developed by Thomas et al. (2010), where R is the ideal gas constant, T is temperature in Kelvins, and P is pressure in kbar. This is the most appropriate Ti-in-quartz solubility calibration to use on metapelitic rocks (e.g., Ashley et al., 2013). TitaniQ calculations are particularly useful in this type of study because, as outlined above, quartz is typically involved in both metamorphic and deformation processes, giving it the potential to tease out details of P-T-t-D paths that are not given by microstructural analyses and phase equlibria modeling.

References

Aoya, M., Wallis, S. R., Kawakami, T., Lee, J., Wang, Y., and Maeda, H., 2006, The Malashan gneiss dome in south Tibet: comparative study with the Kangmar dome with special reference to kinematics of deformation and origin of associated granites: Geological Society, London, Special Publications, v. 268, no. 1, p. 471-495.

Armijo, R., Tapponnier, P., Mercier, J. L., and Han, T.-L., 1986, Quaternary extension in southern Tibet: Field observations and tectonic implications: Journal of Geophysical Research: Solid Earth, v. 91, no. B14, p. 13803-13872.

Ashley, K. T., Webb, L. E., Spear, F. S., and Thomas, J. B., 2013, P-T-D histories from quartz: A case study of the application of the TitaniQ thermobarometer to progressive fabric development in metapelites: Geochemistry, Geophysics, Geosystems, v. 14, no. 9, p. 3821-3843.

Beaumont, C., Jamieson, R. A., Nguyen, M. H., and Lee, B., 2001, Himalayan tectonics explained by extrusion of a low-viscosity crustal channel coupled to focused surface denudation: Nature, v. 414, no. 6865, p. 738-742.

Beaumont, C., Jamieson, R. A., Nguyen, M. H., and Medvedev, S., 2004, Crustal channel flows: 1. Numerical models with applications to the tectonics of the Himalayan-Tibetan orogen: Journal of Geophysical Research: Solid Earth, v. 109, no. B6, p. B06406.

Beaumont, C., Nguyen, M. H., Jamieson, R. A., and Ellis, S., 2006, Crustal flow modes in large hot orogens: Geological Society, London, Special Publications, v. 268, no. 1, p. 91-145.

Behr, W. M., and Platt, J. P., 2011, A naturally constrained stress profile through the middle crust in an extensional terrane: Earth and Planetary Science Letters, v. 303, no. 3–4, p. 181-192.

Bettinelli, P., Avouac, J.-P., Flouzat, M., Jouanne, F., Bollinger, L., Willis, P., and Chitrakar, G., 2006, Plate Motion of India and Interseismic Strain in the Nepal Himalaya from GPS and DORIS Measurements: Journal of Geodesy, v. 80, no. 8-11, p. 567-589.

Burchfiel, B. C., and Royden, L. H., 1985, North-south extension within the convergent Himalayan region: Geology, v. 13, no. 10, p. 679-682.

Burg, J. P., Guiraud, M., Chen, G. M., and Li, G. C., 1984, Himalayan metamorphism and deformations in the North Himalayan Belt (southern Tibet, China): Earth and Planetary Science Letters, v. 69, no. 2, p. 391-400.

Carosi, R., Lombardo, B., Molli, G., Musumeci, G., and Pertusati, P. C., 1998, The south Tibetan detachment system in the Rongbuk valley, Everest region. Deformation features and geological implications: Journal of Asian Earth Sciences, v. 16, no. 2–3, p. 299-311.

Chambers, J., Caddick, M., Argles, T., Horstwood, M., Sherlock, S., Harris, N., Parrish, R., and Ahmad, T., 2009, Empirical constraints on extrusion mechanisms from the upper margin of an exhumed high-grade orogenic core, Sutlej valley, NW India: Tectonophysics, v. 477, no. 1–2, p. 77-92.

Chen, Z., Liu, Y., Hodges, K. V., Burchfiel, B. C., Royden, L. H., and Deng, C., 1990, The Kangmar Dome: A Metamorphic Core Complex in Southern Xizang (Tibet): Science, v. 250, no. 4987, p. 1552-1556.

Cheng, H., King, R. L., Nakamura, E., Vervoort, J. D., and Zhou, Z., 2008, Coupled Lu–Hf and Sm–Nd geochronology constrains garnet growth in ultra-high-pressure eclogites from the Dabie orogen: Journal of Metamorphic Geology, v. 26, no. 7, p. 741-758.

Cherniak, D. J., Watson, E. B., Grove, M., and Harrison, T. M., 2004, Pb diffusion in monazite: a combined RBS/SIMS study: Geochimica et Cosmochimica Acta, v. 68, no. 4, p. 829-840.

Cherniak, D. J., Watson, E. B., and Wark, D. A., 2007, Ti diffusion in quartz: Chemical Geology, v. 236, no. 1–2, p. 65-74.

Connolly, J. A. D., 2009, The geodynamic equation of state: What and how: Geochemistry, Geophysics,

Geosystems, v. 10, no. 10, p. Q10014.
Cross, A. J., Kidder, S., and Prior, D. J., 2015, Using microstructures and TitaniQ thermobarometry of quartz sheared around garnet porphyroclasts to evaluate microstructural evolution and constrain an Alpine Fault Zone geotherm: Journal of Structural Geology, v. 75, p. 17-31.
Dodson, M., 1973, Closure temperature in cooling geochronological and petrological systems: Contributions to Mineralogy and Petrology, v. 40, no. 3, p. 259-274.
Duchene, S., Blichert-Toft, J., Luais, B., Telouk, P., Lardeaux, J. M., and Albaréde, F., 1997, The Lu-HF Dating of Garnets and the Ages of the Alpine High-Pressure Metamorphism: Nature, v. 387, no. 6633, p. 586-589.
Faure, G., and Mensing, T.M., 2005, Isotopes: Principles and Applications, Third Edition: Hoboken, New Jersey, Wiley and Sons, Inc., 896 p.
Ferrill, D. A., Morris, A. P., Evans, M. A., Burkhard, M., Groshong Jr, R. H., and Onasch, C. M., 2004, Calcite twin morphology: a low-temperature deformation geothermometer: Journal of Structural Geology, v. 26, no. 8, p. 1521-1529.
Ganguly, J., and Tirone, M., 1999, Diffusion closure temperature and age of a mineral with arbitrary extent of diffusion: theoretical formulation and applications: Earth and Planetary Science Letters, v. 170, no. 1–2, p. 131-140.
Gansser, A., 1980, The significance of the Himalayan suture zone: Tectonophysics, v. 62, no. 1–2, p. 37-52.
Ghent, E. D., and Stout, M. Z., 1984, TiO2 activity in metamorphosed pelitic and basic rocks: principles and applications to metamorphism in southeastern Canadian Cordillera: Contributions to Mineralogy and Petrology, v. 86, no. 3, p. 248-255.
Goscombe, B., Gray, D., and Hand, M., 2006, Crustal architecture of the Himalayan metamorphic front in eastern Nepal: Gondwana Research, v. 10, no. 3–4, p. 232-255.
Grove, M., and Harrison, T.M., 1996, 40Ar* diffusion in Fe-rich biotite: American Mineralogist, v. 81, p. 940—951.
Grujic, D., Hollister, L. S., and Parrish, R. R., 2002, Himalayan metamorphic sequence as an orogenic channel: insight from Bhutan: Earth and Planetary Science Letters, v. 198, no. 1, p. 177-191.
Grujic, D., Stipp, M., and Wooden, J. L., 2011, Thermometry of quartz mylonites: Importance of dynamic recrystallization on Ti-in-quartz reequilibration: Geochemistry, Geophysics, Geosystems, v. 12, no. 6.
Guillot, S., Garzanti, E., Baratoux, D., Marquer, D., Mahéo, G., and de Sigoyer, J., 2003, Reconstructing the total shortening history of the NW Himalaya: Geochemistry, Geophysics, Geosystems, v. 4, no. 7, p. 1064.
Harrison, T.M., 1981, Diffusion of 40Ar in hornblende: Contributions to Mineralogy and Petrology, v. 78, no. 3, p. 324-331.
Hirth, G., and Tullis, J., 1992, Dislocation creep regimes in quartz aggregates: Journal of Structural Geology, v. 14, no. 2, p. 145-159.
Holdaway, M. J., 2000, Application of new experimental and garnet Margules data to the garnet-biotite geothermometer: American Mineralogist, v. 85, no. 7-8, p. 881-892.
Holdaway, M.J., 2001, Recalibration of the GASP geobarometer in light of recent garnet and plagioclase activity models and versions of the garnet-biotite geothermometer: American Mineralogist, v. 86, no. 10, p. 1117-1129.
Hodges, K. V., 2000, Tectonics of the Himalaya and southern Tibet from two perspectives: Geological Society of America Bulletin, v. 112, no. 3, p. 324-350.
Hodges, K.V., 2006, A synthesis of the Channel Flow-Extrusion hypothesis as developed for the Himalayan-Tibetan orogenic system in Law, R.D., Searle, M.P., and Godin, L., Channel Flow,

Ductile Extrusion, and Exhumation of Lower-Middle Crust in Continental Collision Zones: Bristol, United Kingdom, Geological Society Special Publication, 625 p.
Jessup, M.J., Law, R.D., Searle, M.P., and Hubbard, M.S., 2006, Structural evolution and vorticity of flow during extrusion and exhumation of the Greater Himalayan slab, Mt. Everest Massif, Tibet/Nepal: implications for orogeny-scale flow partitioning in Law, R.D., Searle, M.P., and Godin, L., eds., Channel Flow, Ductile Extrusion, and Exhumation of Lower-Middle Crust in Continental Collision Zones: Bristol, United Kingdom, Geological Society of London, Bristol, 625 p.
Kapp, P., and Guynn, J. H., 2004, Indian punch rifts Tibet: Geology, v. 32, no. 11, p. 993-996.
Kidder, S., Avouac, J. P., and Chan, Y. C., 2013, Application of titanium-in-quartz thermobarometry to greenschist facies veins and recrystallized quartzites in the Hsüehshan range, Taiwan: Solid Earth, v. 4, no. 1, p. 1-21.
Kohn, M. J., and Northrup, C. J., 2009, Taking mylonites' temperatures: Geology, v. 37, no. 1, p. 47-50.
Kohn, M. J., and Spear, F., 2000, Retrograde net transfer reaction insurance for pressure-temperature estimates: Geology, v. 28, no. 12, p. 1127-1130.
Kylander-Clark, A. R. C., Hacker, B. R., and Cottle, J. M., 2013, Laser-ablation split-stream ICP petrochronology: Chemical Geology, v. 345, no. 0, p. 99-112.
Langille, J., Lee, J., Hacker, B., and Seward, G., 2010, Middle crustal ductile deformation patterns in southern Tibet: insights from vorticity studies in Mabja Dome: Journal of Structural Geology, v. 32, p. 70-85.
Larson, K. P., Godin, L., Davis, W. J., and Davis, D. W., 2010, Out-of-sequence deformation and expansion of the Himalayan orogenic wedge: insight from the Changgo culmination, south central Tibet: Tectonics, v. 29, no. 4, p. TC4013.
Law, R. D., 1990, Crystallographic fabrics: a selective review of their applications to research in structural geology: Geological Society, London, Special Publications, v. 54, no. 1, p. 335-352.
Lee, J., Hacker, B., and Wang, Y., 2004, Evolution of North Himalayan gneiss domes: structural and metamorphic studies in Mabja Dome, southern Tibet: Journal of Structural Geology, v. 26, no. 12, p. 2297-2316.
Lee, J., Hacker, B. R., Dinklage, W. S., Wang, Y., Gans, P., Calvert, A., Wan, J., Chen, W., Blythe, A. E., and McClelland, W., 2000, Evolution of the Kangmar Dome, southern Tibet: Structural, petrologic, and thermochronologic constraints: Tectonics, v. 19, no. 5, p. 872-895.
Le Fort, P., 1986, Metamorphism and magmatism during the Himalayan collision, in Coward, M. P., and Ries, A. C., eds., Collision tectonics: Geological Society of London Special Publication 19, p. 159–172.
Lister, G. S., and Baldwin, S. L., 1996, Modelling the effect of arbitrary P-T-t histories on argon diffusion in minerals using the MacArgon program for the Apple Macintosh: Tectonophysics, v. 253, no. 1–2, p. 83-109.
Lister, G. S., and Hobbs, B. E., 1980, The simulation of fabric development during plastic deformation and its application to quartzite: the influence of deformation history: Journal of Structural Geology, v. 2, no. 3, p. 355-370.
Lovera, O. M., Richter, F. M., and Harrison, T. M., 1991, Diffusion domains determined by 39Ar released during step heating: Journal of Geophysical Research: Solid Earth, v. 96, no. B2, p. 2057-2069.
Molnar, P., and Tapponnier, P., 1977, The collision between India and Eurasia: Scientific American, v. 236, n. 4, p. 30—41.
Merrihue, C., and Turner, G., 1966, Potassium-argon dating by activation with fast neutrons: Journal of Geophysical Research, v. 71, no. 11, p. 2852-2857.
McDougall, I., and Harrison, T., 1999, Geochronology and thermochronology bt the 40Ar/39Ar method: New York, Oxford University Press, 269 p.

Mitsuishi, M., Wallis, S. R., Aoya, M., Lee, J., and Wang, Y., 2012, E–W extension at 19 Ma in the Kung Co area, S. Tibet: Evidence for contemporaneous E–W and N–S extension in the Himalayan orogen: Earth and Planetary Science Letters, v. 325–326, no. 0, p. 10-20.

Nachlas, W. O., Whitney, D. L., Teyssier, C., Bagley, B., and Mulch, A., 2014, Titanium concentration in quartz as a record of multiple deformation mechanisms in an extensional shear zone: Geochemistry, Geophysics, Geosystems, v. 15, no. 4, p. 1374-1397.

Passchier, C. W., and Trouw, R. J., 2005, Microtectonics: Berlin, Federal Republic of Germany, Springer, 366 p.

Patchett, P. J., Kouvo, O., Hedge, C. E., and Tatsumoto, M., 1981, Evolution of continental crust and mantle heterogeneity: Evidence from Hf isotopes: Contributions to Mineralogy and Petrology, v. 78, no. 3, p. 279-297.

Powell, R., and Holland, T., 1994, Optimal geothermometry and geobarometry: American Mineralogist, v. 79, p. 120-133.

Pyle, J. M. and Spear, F. S., 1999, Yttrium zoning in garnet: coupling of major and accessory phases during metamorphic reactions: Geological Materials Research, v. 1, p. 1-49.

Quigley, M., Liangjun, Y., Xiaohan, L., Wilson, C. J. L., Sandiford, M., and Phillips, D., 2006, 40Ar/39Ar thermochronology of the Kampa Dome, southern Tibet: Implications for tectonic evolution of the North Himalayan gneiss domes: Tectonophysics, v. 421, no. 3–4, p. 269-297.

Rey, P., Vanderhaeghe, O., and Teyssier, C., 2001, Gravitational collapse of the continental crust: definition, regimes and modes: Tectonophysics, v. 342, no. 3–4, p. 435-449.

Rudge, J. F., Reynolds, B. C., and Bourdon, B., 2009, The double spike toolbox: Chemical Geology, v. 265, no. 3–4, p. 420-431.

Schärer, U., Xu, R.-H., and Allègre, C. J., 1986, U(Th)Pb systematics and ages of Himalayan leucogranites, South Tibet: Earth and Planetary Science Letters, v. 77, no. 1, p. 35-48.

Scherer, E. E., Cameron, K. L., and Blichert-Toft, J., 2000, Lu–hf garnet geochronology: closure temperature relative to the Sm–Nd system and the effects of trace mineral inclusions: Geochimica et Cosmochimica Acta, v. 64, no. 19, p. 3413-3432.

Schmid, S. M., and Casey, M., 1986, Complete fabric analysis of some commonly observed quartz C-axis patterns, Mineral and Rock Deformation: Laboratory Studies, Volume 36: Washington, DC, AGU, p. 263-286.

Searle, M. P., Noble, S. R., Hurford, A. J., and Rex, D. C., 1999, Age of crustal melting, emplacement and exhumation history of the Shivling leucogranite, Garhwal Himalaya: Geological Magazine, v. 136, no. 05, p. 513-525.

Spear, F. S., Ashley, K. T., Webb, L. E., and Thomas, J. B., 2012, Ti diffusion in quartz inclusions: implications for metamorphic time scales: Contributions to Mineralogy and Petrology, v. 164, no. 6, p. 977-986.

Spear, F. S., and Wark, D. A., 2009, Cathodoluminescence imaging and titanium thermometry in metamorphic quartz: Journal of Metamorphic Geology, v. 27, no. 3, p. 187-205.

Stipp, M., Stünitz, H., Heilbronner, R., and Schmid, S. M., 2002, The eastern Tonale fault zone: a ‘natural laboratory’ for crystal plastic deformation of quartz over a temperature range from 250 to 700 °C: Journal of Structural Geology, v. 24, no. 12, p. 1861-1884.

Storm, L. C., and Spear, F. S., 2009, Application of the titanium-in-quartz thermometer to pelitic migmatites from the Adirondack Highlands, New York: Journal of Metamorphic Geology, v. 27, no. 7, p. 479-494.

Taylor, M., Yin, A., Ryerson, F. J., Kapp, P., and Ding, L., 2003, Conjugate strike-slip faulting along the Bangong-Nujiang suture zone accommodates coeval east-west extension and north-south shortening in the interior of the Tibetan Plateau: Tectonics, v. 22, no. 4, p. 1044.

Teyssier, C., and Whitney, D., 2002, Gneiss domes and orogeny: Geology, v. 30, p. 1139-1142.
Thomas, J. B., Bruce Watson, E., Spear, F. S., Shemella, P. T., Nayak, S. K., and Lanzirotti, A., 2010, TitaniQ under pressure: the effect of pressure and temperature on the solubility of Ti in quartz: Contributions to Mineralogy and Petrology, v. 160, no. 5, p. 743-759.
Tracy, R. J., Robinson, P., and Thompson, A. B., 1976, Garnet composition and zoning in the determination of temperature and pressure of metamorphism, central Massachusetts: American Mineralogist, v. 61, no. 7-8, p. 762-775.
Tullis, J., and Yund, R. A., 1991, Diffusion creep in feldspar aggregates: experimental evidence: Journal of Structural Geology, v. 13, no. 9, p. 987-1000.
Vannay, J.-C., and Grasemann, B., 2001, Himalayan inverted metamorphism and syn-convergence extension as a consequence of a general shear extrusion: Geological Magazine, v. 138, no. 03, p. 253-276.
Wark, D. A., and Watson, E. B., 2006, TitaniQ: a titanium-in-quartz geothermometer: Contributions to Mineralogy and Petrology, v. 152, no. 6, p. 743-754.
Williams, M. L., and Jercinovic, M. J., 2002, Microprobe monazite geochronology: putting absolute time into microstructural analysis: Journal of Structural Geology, v. 24, no. 6–7, p. 1013-1028.
Yardley, B. W. D., 1977, An empirical study of diffusion in garnet: American Mineralogist, v. 62, no. 7-8, p. 793-800.
Yin, A., and Harrison, T. M., 2000, Geologic Evolution of the Himalayan-Tibetan Orogen: Annual Review of Earth and Planetary Sciences, v. 28, no. 1, p. 211-280.

CHAPTER I
TECTONIC EVOLUTION OF THE MIDDLE CRUST IN SOUTHERN TIBET FROM STRUCTURAL AND KINEMATIC STUDIES IN THE LHAGOI KANGRI GNEISS DOME

A version of this chapter was originally submitted by Timothy Diedesch, Micah Jessup, John Cottle, and Lingsen Zeng:

Diedesch, T.F., Jessup, M.J., Cottle, J.M., Zeng, L., 2016, Tectonic evolution of the middle crust in southern Tibet from structural and kinematic studies in the Lhagoi Kangri gneiss dome: Lithosphere, doi: 10.1130/L506.1.

My major contributions to this paper include: (1) conducting the microstructural and kinematic analysis as well as the deformation temperature analyses from quartz microstructures, (2) writing the manuscript, (3) creating most of the illustrations, and (4) submitting and revising the manuscript.

Abstract

Field, structural, kinematic, and deformation temperature analyses were conducted on rocks from the Lhagoi Kangri gneiss dometo establish the geologic history of the dome, identify deformation phases in the dome, and to relate these phases to the tectonic evolution of the Himalayan middle crust. The Lhagoi Kangri dome, one of a series of gneiss-cored domes in southern Tibet, records stratigraphy and structural features similar to previously studied north Himalayan gneiss domes. Field mapping reveals a sequence of rocks that comprise a cover of unmetamorphosed to amphibolite-grade siliciclastic and minor carbonate rocks overlying a core predominantly composed of foliated and lineated orthogneiss intruded by relatively undeformed granite, which also intrudes the cover rocks both concordantly and discordantly. Field observations and microstructural analyses suggest that the contact between the core and cover rocks was originally a nonconformity, but we do not rule out the possibility of later slip along the surface, as has been reported for correlative structures in other domes. Lhagoi Kangri rocks were pervasively deformed during at least two major tectonic phases. The earliest deformation event (D_1) resulted in shortening and thickening of crust, the record of which is largely eliminated, particularly in lower structural levels, by transposition and recrystallization during the second phase (D_2). Ductile deformation during D_2 is characterized at higher structural levels by crenulation cleavage that tightens with depth, while at lower structural levels D_2 is manifested as a distributed shear zone that records evidence of both plane strain and coaxial flattening, possibly indicating overall heterogeneous general shear. The shear zone is ~3 km thick and contains rocks with mostly symmetrical top-to-north and top-to-south shear-sense indicators with a dominant top-to-north component at lower structural levels.

Microstructural analyses and quartz c-axis fabrics indicate a range of D_2 shear zone temperatures from 200 to 300 °C at the upper boundary to 630 °C at the lowest structural levels sampled with minimal evidence of lower temperature overprinting. The interpreted temperatures define a wide range in thermal field gradients (18–90 °C/km) that suggest that temperature indicators were locked in at relatively late stages of D_2. The structural framework and kinematic history of the Lhagoi Kangri dome are similar to previously studied north Himalayan gneiss domes as well as to transects through the South Tibetan detachment system, which supports previous interpretations of structural continuity between the north Himalayan gneiss domes and other middle crustal exposures in the Himalaya. The Lhagoi Kangri distributed shear zone, in particular, may represent a deeper ductile manifestation of the South Tibetan detachment system.

Introduction

The North Himalayan antiform delineates a series of structural domes, the north Himalayan gneiss domes (NHGD), that trends approximately parallel to the orogenic front (Fig. 1.1). Granite and orthogneiss within the cores of the NHGD are often interpreted to correlate with rocks of the Greater Himalayan sequence (GHS), the Himalayan tectonostratigraphic unit representing exhumed middle to lower crust (e.g., Nelson et al., 1996; Zhang et al., 2004; Lee et al., 2006; Lee and Whitehouse, 2007; King et al., 2011). Separating the GHS from the overlying Tethyan sedimentary sequence (TSS) is the South Tibetan detachment system (STDS), a series of north-dipping, low-angle normal faults and top-to-north sense shear zones that can be traced nearly continuously along strike of the orogen (e.g., Burg et al., 1984; Burchfiel et al., 1992; Kellett and Grujic, 2012). In many NHGD, the contact between the core and the TSS is a top-to-north-sense shear zone that is interpreted as an exhumed, downdip projection of the STDS (e.g., Chen et al., 1990; Lee et al., 2000, 2006; Quigley et al., 2006; Larson et al., 2010; King et al., 2011). This interpretation is also corroborated by geophysical evidence at the approximate longitude of the Kangmar dome (Fig. 1.1; Nelson et al., 1996). Given their unique position within the Himalaya-Tibet orogenic system and their correlation with the GHS, the NHGD have been the subject of research questions with direct implications to Himalayan tectonics, i.e., (1) if there is structural continuity between the GHS and the NHGD and how is this manifested in the domes, (2) how the NHGD were formed and

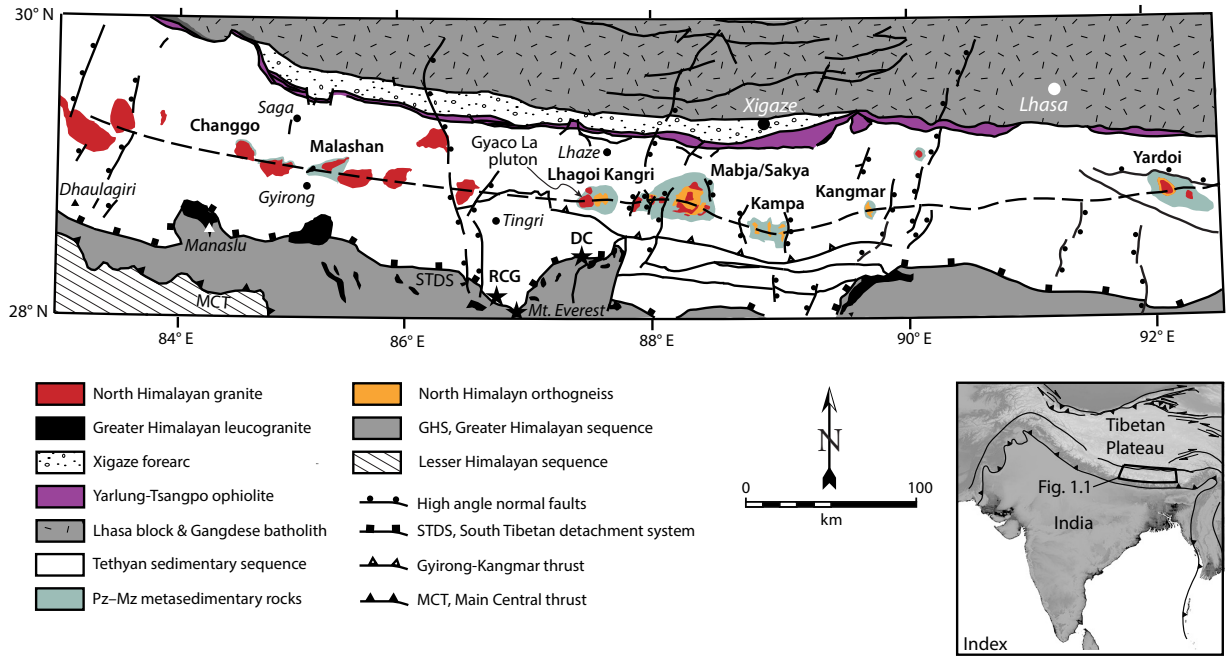


Figure 1.1. *Simplified geologic map of southern Tibet showing the major lithotectonic units, the trace of the north Himalayan antiform (bold dashed line), and the location of the Lhagoi Kangri dome in relation to previously studied domes mentioned in the text. Stars mark locations of transects through South Tibetan detachment system (see discussion in text). DC—Dzakaa Chu; RCG—Ra Chu and Gondasampa; MCT—Main Central thrust; Pz—Paleozoic; Mz—Mesozoic. Inset shows the location of the map with respect to India and Eurasia. Modified from Lee et al. (2004), King et al. (2011), and Larson et al. (2010).*

exhumed, and (3) the structural and stratigraphic relationships between core and carapace rocks in the gneiss domes. Our study represents the first comprehensive investigation of the sparsely documented Lhagoi Kangri dome (LKD). In this contribution, data from field and detailed structural analyses are used to establish a general geologic history for LKD rocks that in turn is used to revisit the above questions and to provide additional data to test previous models regarding the tectonic evolution of the Himalayan middle crust.

Previous Work

At least 15 domes have been identified along the North Himalayan antiform (e.g., Burg et al., 1984; Debon et al., 1986; Watts et al., 2005), and 6 of these domes have been studied in detail. Of the six previously studied domes, Changgo (Larson et al., 2010) Malashan (Aoya et al., 2005; Kawakami et al., 2007; Gao et al., 2013; Gao and Zeng, 2014), Yardoi (Aikman et al., 2008; Zeng et al., 2009, 2011, 2014), and Mabja-Sakya (Zhang et al., 2004; Lee et al., 2006; Lee and Whitehouse, 2007) contain granite bodies with Eocene to Miocene (35–10 Ma) U/Pb zircon ages, whereas Kangmar (Schärer et al., 1986; Lee et al., 2000) and Kampa (Quigley et al., 2008) contain only granitic gneiss with Neoproterozoic to Cambrian (560–500 Ma) U/Pb zircon ages. Granitic gneiss with Neoproterozoic to Cambrian age is also reported in Mabja-Sakya (Lee and Whitehouse, 2007) and Yardoi (e.g., Zeng et al., 2009). These data support two end-member origins for the gneissic cores: (1) Eocene–Miocene synorogenic plutons that intruded their host rock (e.g., Malashan and Changgo domes; Aoya et al., 2005; Larson et al., 2010), or (2) granites that crystallized in the Neoproterozoic–Cambrian and were subsequently metamorphosed and deformed during the Eocene–Miocene (e.g., Kangmar and Kampa; Lee et al., 2000; Quigley et al., 2008). The Mabja-Sakya dome is interpreted as a mixture of the two end members: Neoproterozoic–Cambrian orthogneiss that was migmatized and intruded by anatectic melts during the Oligocene–Miocene (e.g., King et al., 2011). In terms of the early tectonic framework of the Himalaya-Tibet system, these results indicate that the cores of the NHGD are the structurally highest levels of the GHS that underwent Cenozoic metamorphism and were deformed in a northern equivalent (e.g., Quigley et al., 2008) or a distributed mid-crustal portion of the STDS (Lee et al., 2000, 2004; Zhang et al., 2004; King et al., 2011).

Tectonic Models

Several mechanisms have been proposed for formation of the North Himalayan antiform and doming of NHGD rocks. Le Fort et al. (1987) attributed doming in the NHGD to buoyant rise of lower crustal melt, whereas Burg et al. (1984) suggested that the Kangmar dome was produced by formation of a thrust duplex. In contrast, Chen et al. (1990) preferred an interpretation where the Kangmar dome formed exclusively from extension, likening it to metamorphic core complexes in the North American Cordillera. Lee et al. (2006) interpreted Mabja-Sakya doming to be the result of out-of-sequence, south-vergent thrusting, and patterns in 40Ar/39Ar cooling ages from Kangmar dome are also suggested to arise from ramping on a blind thrust (Lee et al., 2000). Similarly, Larson et al. (2010) suggested that doming and exhumation of the Changgo culmination resulted from out-of-sequence thrusting and folding, while Yin et al. (1999) and King et al. (2011) concluded that doming of the NHGD could also have resulted from rise of melt-weakened GHS in response to regional horizontal compression. Thermomechanical modeling of the Himalayan orogeny produced NHGD-like features from a southward-flowing mid-crustal channel through either contemporaneous, localized upper crustal extension or by underthrusting triggered by impingement of a rigid body, such as the Indian lithosphere, into the channel (Beaumont et al., 2004). In these models the STDS represents the upper boundary of the channel. Recent studies along structural transects through the STDS south-southwest of LKD emphasize middle crustal strain patterns, particularly that the degree of apparent telescoping of thermal field gradients varies spatially, to support channel flow or wedge extrusion models (e.g., Cottle et al., 2011; Law et al., 2011). At the very least, the apparent STDS strain patterns are most compatible with Himalayan tectonic models in which the STDS and related structures accommodated appreciable amounts of displacement during Oligocene–Miocene time (e.g., Cottle et al., 2011; Law et al., 2011).

Geologic Background

The LKD is a ~20 × 40 km elliptical structure at present erosion level with an east-west–trending long axis located 100 km north-northeast of Mount Everest (Fig. 1.1; Tibet Bureau of Geology and Mineral Resources, 1993; Watts et al., 2005). Burg et al. (1984) originally identified the LKD during regional reconnaissance mapping. Schärer et al. (1986) published zircon (501 Ma) and monazite (15.5 ± 0.8 Ma) 206Pb/238U ages from a single sample of Lhagoi Kangri leucogranite, but they did not

provide the location where the sample was collected or its geologic context. Rolfo et al. (2004) presented preliminary data characterizing the lithology, structure, and metamorphic conditions recorded in LKD rocks that they interpreted to be similar to those of other NHGD. Watts et al. (2005) produced a geologic map of LKD using band ratios of thermal emission imagery from ASTER (Advanced Spaceborne Thermal Emission and Reflection Radiometer) that showed the presence of both gneiss and a two-mica granite body, the Gyaco La pluton (Debon et al., 1986), in the core of the dome. In addition, they identified a crescent-shaped body in map view as a muscovite-rich schist or quartzite layer that outlines the domal geometry.

Lhagoi Kangri Lithology

The rock types composing the LKD broadly correspond to the sequence defined for the adjacent Mabja-Sakya dome (Lee et al., 2004) and that of surrounding southern Tibet as originally mapped by the Tibet Bureau of Geology and Mineral Resources (1993). LKD age assignments follow the conventions of previous regional stratigraphic and field mapping studies (e.g., Tibet Bureau of Geology and Mineral Resources, 1993; Liu and Einsele, 1994). Despite the relative absence of vegetation, both exposure and accessibility throughout the LKD are poor due to its remoteness and the fact that it is actively eroding as evidenced by large colluvium and landslide deposits. As a result, the number of mapped units is intentionally parsimonious (Figs. 1.2–1.4).

The structurally lowest formation in LKD, unit og, is a dominantly felsic orthogneiss complex composed of intervals with variable mode, texture, and local ptygmatic segregations of leucosome (Fig. 1.4). The orthogneiss forms rounded subcrops at the highest elevations in LKD (Fig. 1.5a), and its exposure is typically limited to felsenmeer, except along cliff lines where it is sheltered by overlying metasedimentary rocks. Most orthogneiss documented in this study is coarse grained and contains the assemblage quartz + plagioclase + biotite with large (1–5 cm) K-feldspar augen. In particular instances the orthogneiss also contains sillimanite and/or cordierite. At lower structural levels, the orthogneiss unit contains amphibolite, dikes of undeformed pegmatite, and fine-grained leucogranite. Within ~200 m of the contact with the overlying schist and quartzite, the orthogneiss is fine grained and comprises garnet- or cordierite-bearing assemblages. Orthogneiss exposures typically exhibit a well-developed foliation defined by sheets of biotite ± white mica and a lineation of aligned quartz aggregates that is typically

Figure 1.2. *Geologic map of portions of the Lhagoi Kangri dome (LKD). Inset shows the area of the map overlain on the extent of the LKD from Figure 1.1. Cross-section lines A-A' and B-B' correspond to Figure 1.3. Thick gray lines are the extents of sample transects discussed in the text. White boxes denote locations of samples analyzed in this study.*

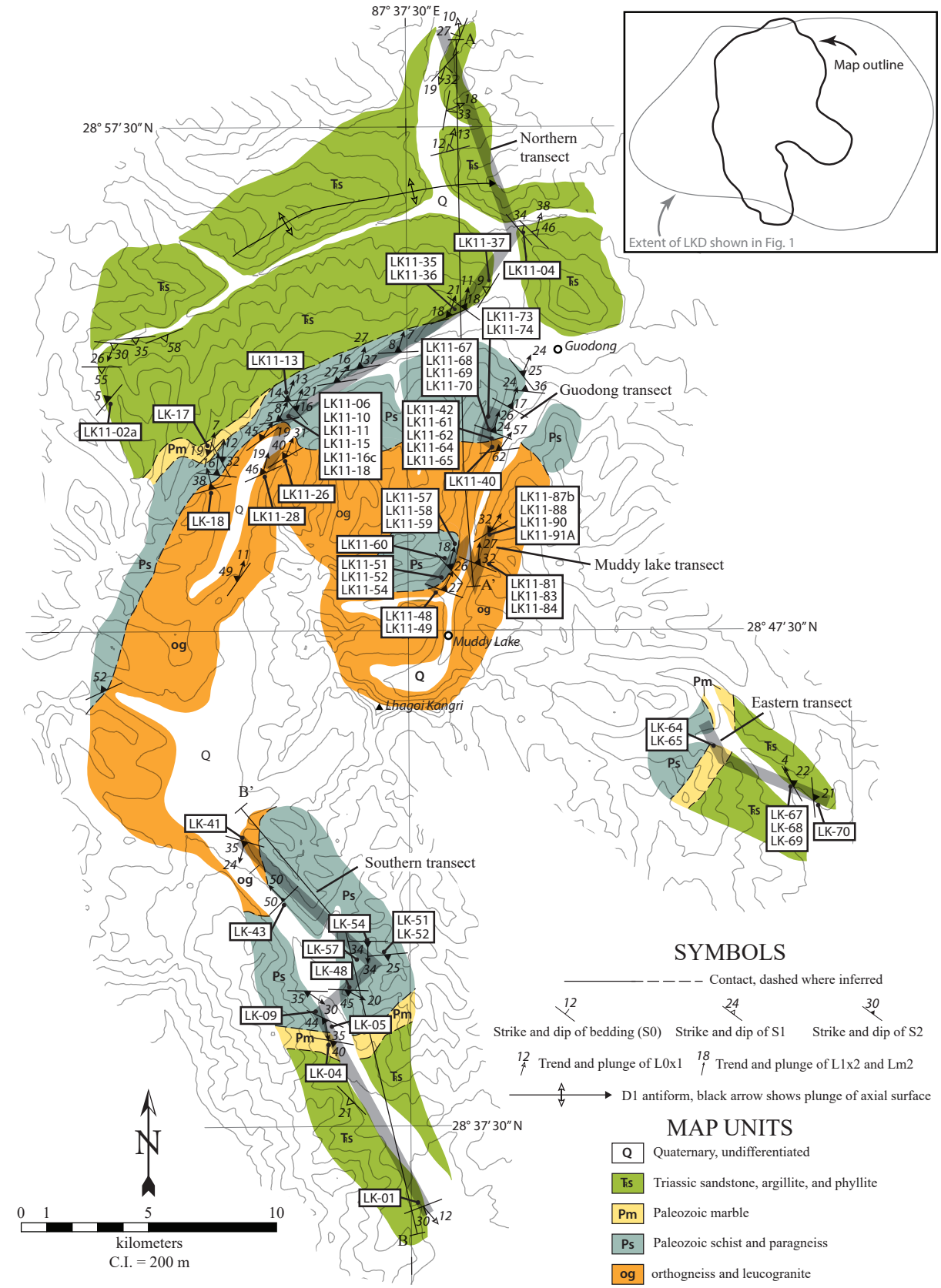


Figure 1.2. Continued.

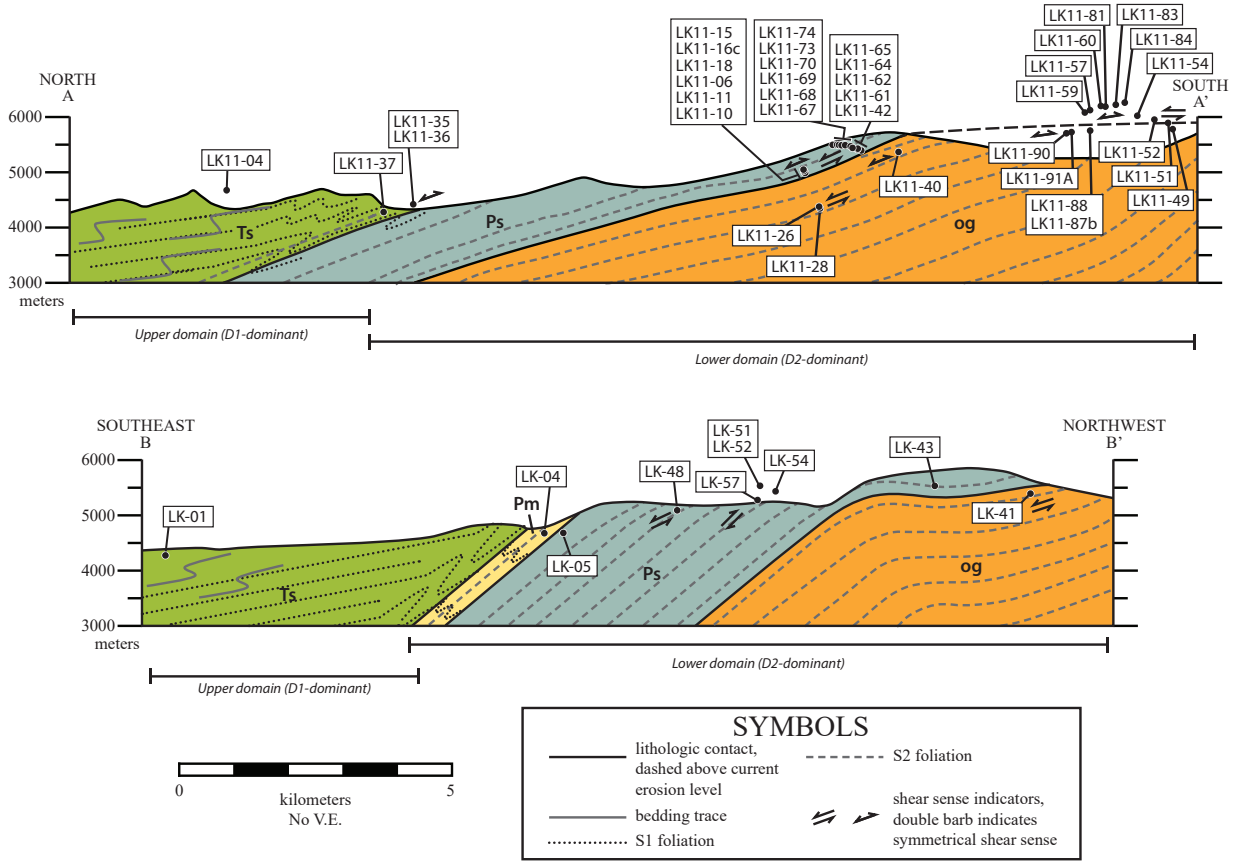


Figure 1.3. *Cross sections through the north (A-A') and south sides (B-B') of the Lhagoi Kangri dome. Unit labels are as in Figure 1.2. Samples shown above or below the topographic profile are projected from beyond the plane of the cross section. Where sample labels contain multiple sample numbers, the samples are listed according to relative structural position. For simplicity, most shear-sense arrows represent a bulk shear sense; more detailed shear-sense data can be found in Table 1.1 and Figure 1.6. V.E.—vertical exaggeration.*

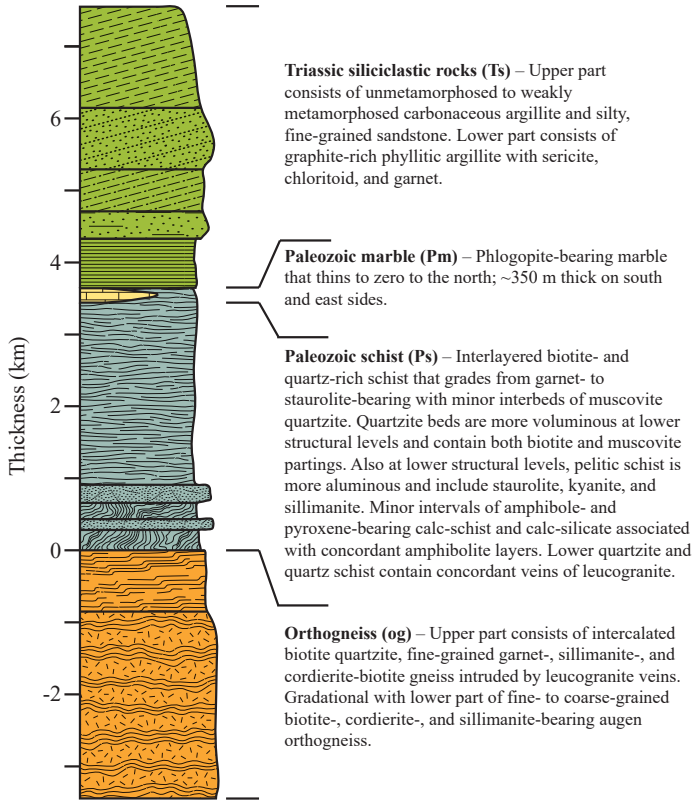


Figure 1.4. *Stratigraphic section of Lhagoi Kangri bedrock. Thicknesses estimated from cross sections and calculated with respect to the core-cover contact. Age assignments after Liu and Einsele (1994) and Lee et al. (2004). See text for details.*

weakly developed if present it all. The contact between unit og and the overlying Paleozoic schist and quartzite (Ps) has high structural relief (~1 km) along its trace. The nature of the contact is not clearly defined due to poor exposure. However, in the central portion of the dome where the most detailed sampling transects were carried out (Fig. 1.2), the orthogneiss is interlayered with quartzite, indicating an originally intrusive contact.

The lowest metasedimentary unit is a Paleozoic package (Ps) of micaceous and quartzose schist (Fig. 1.5b), quartzite, and paragneiss with minor calc-silicate (Fig. 1.5c). Throughout the Lhagoi Kangri, unit Ps forms distinct reddish-brown to yellow cliff bands, although it is also manifested as blockfields that are difficult to distinguish from those of the underlying orthogneiss. All unit Ps rock types exhibit well-developed foliation and poorly to strongly developed lineation. In schist and quartzite outcrops, the main foliation is defined by aligned micas and it contains a mineral lineation defined by elongate quartz and biotite as well as by elongate porphyroblasts like staurolite and kyanite. Foliation in the calc-silicate intervals manifests as green, beige, and purple layers (e.g., Fig. 1.5c) that reflect compositional domains. Where present, lineations in calc-silicate are defined by elongate quartz and biotite aggregates. Quartzite mineralogy in unit Ps appears to vary systematically with depth. Structurally lower quartzite horizons contain biotite as the only mica phase, whereas white mica joins biotite at higher structural levels. Rocks in the lower one-third of unit Ps are intruded by centimeter- to meters-thick leucogranite and pegmatite bodies with variable contact geometry: some are concordant with the main foliation and are isoclinally folded and/or boudinaged, while other bodies intrude obliquely to the dominant fabric and are largely undeformed (e.g., Figs. 1.5b, 1.5d). Within 100 m of the contact with the subjacent orthogneiss, unit Ps contains amphibolite layers that are concordant with the main foliation and with compositional contrasts in the metasedimentary host. Garnet-andalusite schist and epidote-clinopyroxene calc-silicate are also present near the contact with the orthogneiss and are locally spatially related to the amphibolite layers; however, particularly on the south side of the dome, calc-silicate layers also delineate a transition between Ps schist and overlying Paleozoic marble (Pm). The upper contact of Ps is relatively sharp where exposed, and along its trace it juxtaposes both Pm and the Triassic siliciclastic unit (Ts) over reddish-brown biotite-bearing quartzose schist.

Unit Pm is a discontinuous, highly weathered quartz- and phlogopite-bearing marble with a maximum thickness of ~350 m and thinning to zero on the north side of the dome (Figs. 1.2 and 1.3).

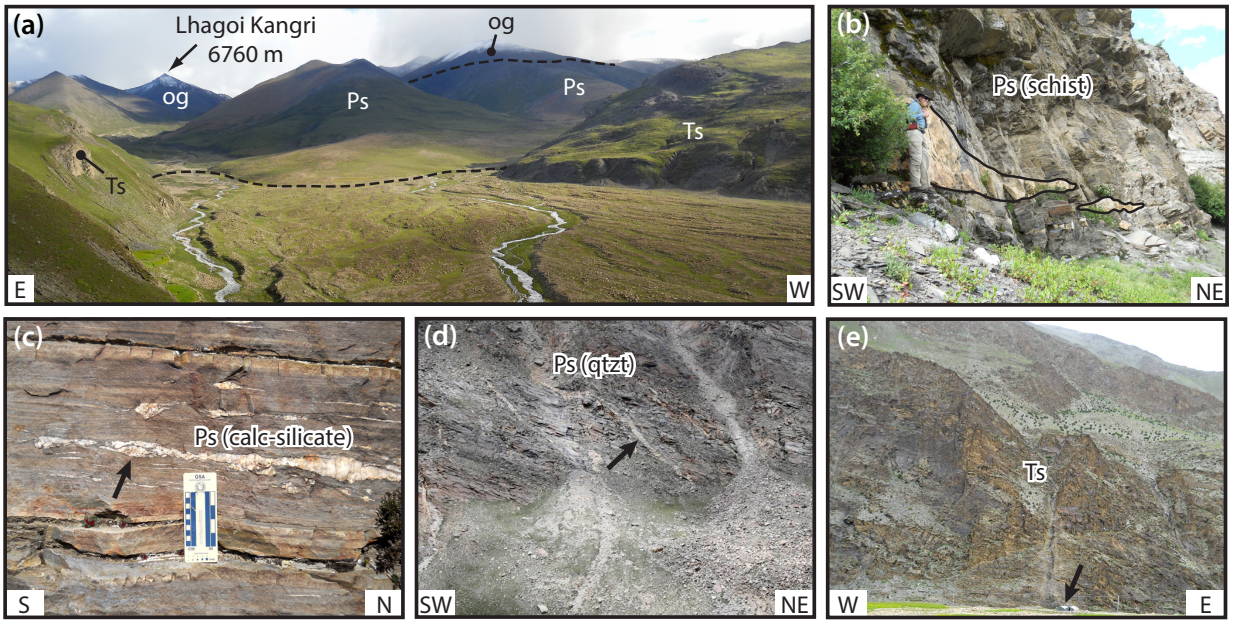


Figure 1.5. *(a) Panorama of the north flank of the Lhagoi Kangri dome viewed toward the south showing the relative position of stratigraphic units and their typical geomorphic expression. Ps–Paleozoic schist and quartzite unit; Ts—Triassic siliciclastic unit; og—orthogneiss and leucogranite. (b) Outcrop of Ps pelitic schist with some quartzite intervals (lighter layers) and a large granitic boudin highlighted in red. (c) Representative outcrop of calc-silicate interval from near the base of unit Ps. Note the sheared and boudinaged quartz + calcite stringers (black arrow). (d) Cliff outcrop of base of unit Ps predominantly consisting of quartzite with minor aluminous schist and intruded by discordantly whitish leucogranite veins (black arrow). (e) Typical large cliff band of Ts on the northern side of the dome. For scale, the tent at the base (black arrow) is ~2 m high.*

This observation is consistent with previous regional mapping that shows Permian–Carboniferous limestone deposits pinching out north of the Lhagoi Kangri (Liu and Einsele, 1994). Marble outcrops are scarce throughout the study area, but they form narrow yellow cliff bands where present. The marble contains a pervasive foliation defined by alternating yellow and white bands that represent relatively quartz-rich and quartz-poor intervals. Where present, lineations on primary foliation surfaces are defined by elongate quartz and biotite aggregates. The upper contact of unit Pm is not well exposed in most accessible areas of the LKD, but the marble is a distinct lithologic package in that it is the only calcite-rich rock type observed in the metasedimentary carapace, apart from vein fill in epidote-bearing intervals of unit Ps.

Within the study area, Triassic siliciclastic rocks (Ts) dominate the highest structural levels on all sides of the dome (Figs. 1.4 and 1.5a). Unit Ts stands out in contrast to the other metasedimentary rocks in that it typically forms spectacular ridgelines of ≥1 km of relief (e.g., Fig. 1.5e). The lower portion of Ts consists of pervasively foliated, dark gray chloritoid- and garnet-bearing graphitic phyllite, and the upper portion consists of gray interbedded carbonaceous argillite, siltstone, and fine-grained sandstone with minor quartz pebble conglomerate. On the north side of the dome, finer grained intervals in the lower portion are phyllitic and crenulated with small, randomly oriented laths (0.1–0.2 mm) of chloritoid that overprint the crenulations.

Structural Characteristics

Based on field observations and structural analysis, two ubiquitous deformation phases are recorded in LKD rocks. Structures that define the first phase (D_1) are not well documented in the field. Instead D_1 is implied by pervasive cleavage development at higher structural levels that is progressively overprinted by a second pervasive deformation event (D_2) over a few hundred meters structurally down section (Fig. 1.3). D_2 is characterized by a pervasive foliation and mineral stretching lineation at lower structural levels within the LKD (Figs. 1.3 and 1.6). In the lowermost schist, D_1-related fabrics are only weakly preserved, and D_1 fabric is indistinguishable in the core orthogneiss. In addition to pervasive D_1 and D_2 deformation, metasedimentary cover rocks preserve structures that are only observed locally (D_3?), such as open folds with gently northeast-inclined axial planes that refold mesoscale F_2 folds. Brittle deformation features are relatively rare in the LKD. Given the paucity of data relating to other

deformation phases, this study focuses primarily on D_2 deformation. The area investigated comprises four structural domains that are defined by variation in average dip direction of S_2 foliation (Figs. 1.6b–1.6e), and each domain encompasses one or two sampling transects (Fig. 1.2). The northern and southern domains are the most complete structural sections, from weakly metamorphosed unit Ts to the core orthogneiss. Consequently, the northern and southern transects are the only ones where unobscured D_1 fabrics are documented. The central domain comprises ~600 m of section above the core-cover contact plus ~100 m below it, while the eastern domain represents only ~500 m of the metasedimentary cover rocks, spanning the lowermost Triassic siliciclastic unit down to the uppermost Paleozoic schist.

D_1 Deformation

Mesoscale observations

Mesoscale D_1 is ambiguous throughout much of the study area because it is generally weakly developed at higher structural levels and progressively overprinted by D_2 at lower structural levels, factors that compound poor accessibility to parts of the dome due to high relief, inadequate infrastructure, and active erosion. Within the areas investigated, D_1 fabric is a discrete cleavage (S_1) at a low angle to compositional layering in unit Ts argillite. In the northern domain, S_1 cleavage is more apparent at low structural levels where it forms well-developed pencil cleavage with intersection lineations (L_{2x1}) that plunge gently north-northwest (Fig. 1.7a). In the southern domain D_1 fabric is not well defined except where it is crenulated by D_2 (Fig. 1.7b).

Microscale Observations

Samples at the highest structural levels in the northern and southern domains preserve a weakly developed microscale fabric that, similarly to the mesoscale counterpart, is subparallel to compositional heterogeneity (Fig. 1.7c). S_1 fabric is defined by sheets of chlorite, biotite, ilmenite, and quartz. Microscale fabrics are also most easily identified at lower structural levels where they are crenulated by S_2 foliations in phyllitic intervals (Fig. 1.7d).

Figure 1.6. *Simplified Lhagoi Kangri dome (LKD) map showing variation of shear sense (black arrows) around the dome. Black lines represent boundaries of structural domains discussed in text. Insets (b–e) show equal-area stereographic projections of structural data from each domain. Black dots are poles to* S_2 *foliation and red dots are* L_2 *stretching lineations. The number of measurements n for each domain are given as n = number of poles to* S_2*, number of* L_2 *lineations. Pm—Paleozoic marble; Ps—Paleozoic schist and quartzite unit; Ts—Triassic siliciclastic unit; og—orthogneiss and leucogranite; C.I.—contour interval.*

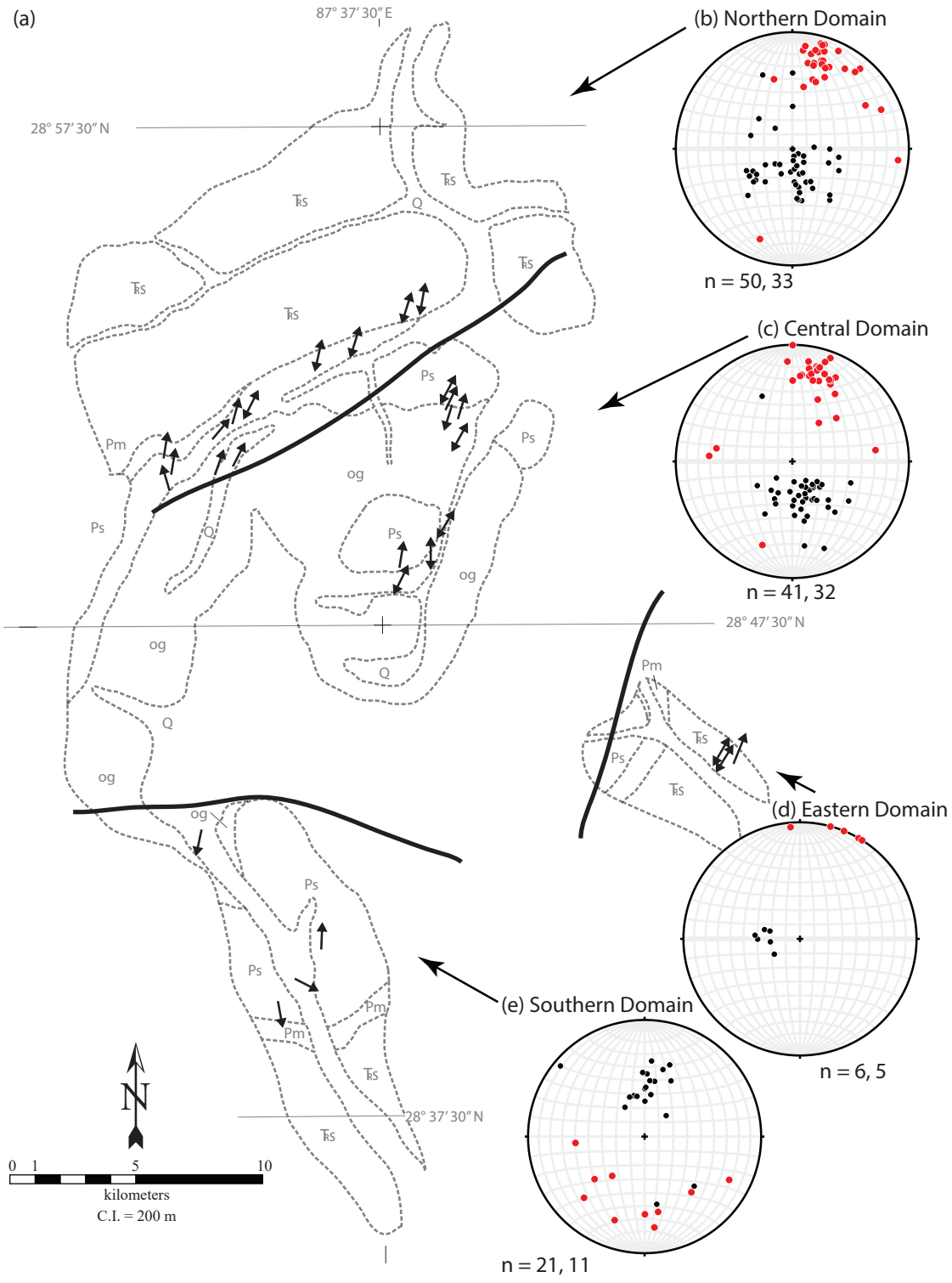


Figure 1.6. Continued.

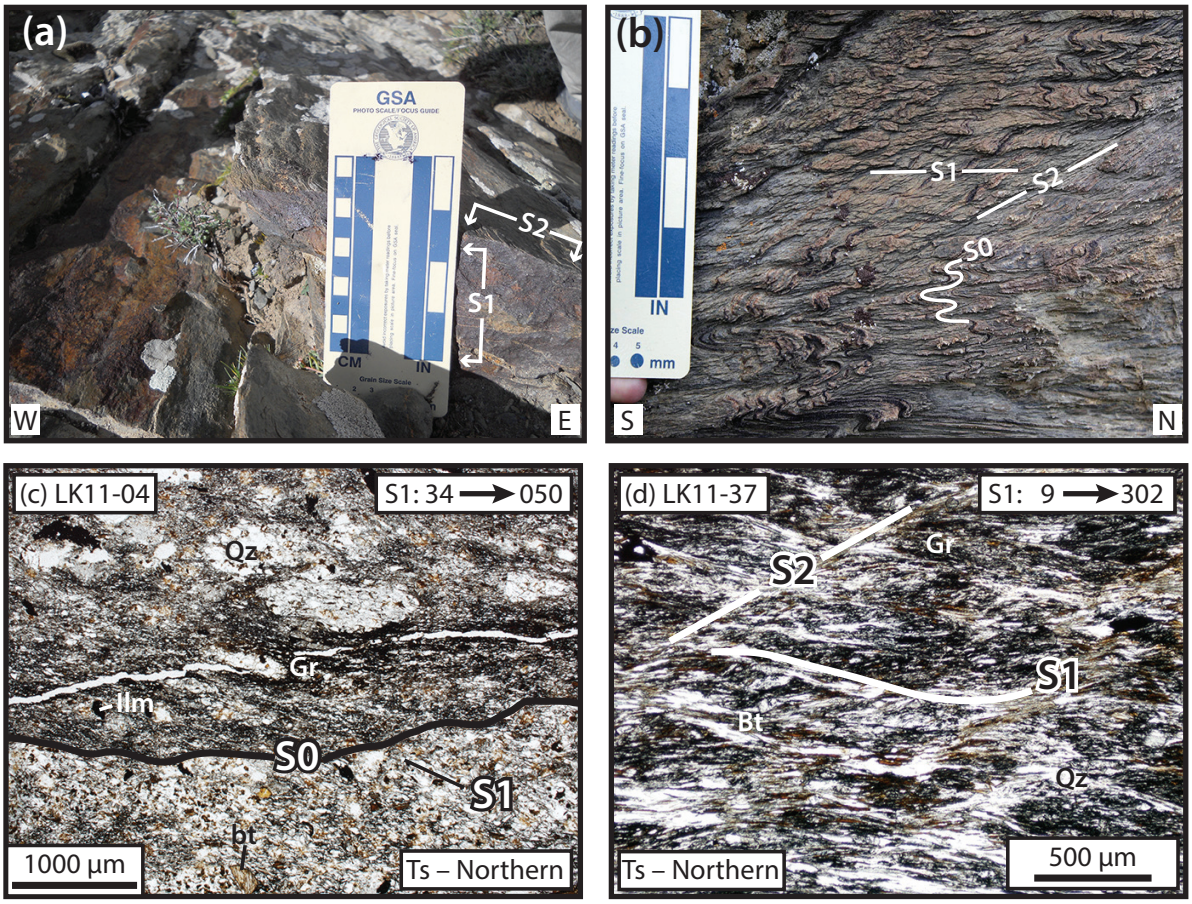


Figure 1.7. *(a) Pencil cleavage in unit Ts (Triassic siliciclastic) argillite in the northern domain formed by the intersection of S_1 and S_2. Viewing direction is approximately north and down the plunge of the L_{2x1} intersection lineations. (b) S_2 crenulation cleavage in pelitic schist on a vertical surface in the southern domain viewed toward the west. Moderately south dipping S_2 fabric is superposed on compositional layering (S_0) and S_1 axial planar cleavage. (c) Plane polarized light photomicrograph of a unit Ts sample from the northern domain. Original compositional layering (S0) is defined by grain size variations and is crosscut by moderately northeast dipping S_1 foliation that is slightly oblique to S0. Mineral abbreviations: gr—graphite; qz—quartz; ilm—ilmenite; bt—biotite. Mineral abbreviations are from Whitney and Evans (2010). (d) Plane polarized light photomicrograph of crenulation cleavage in a graphitic schist (Ts) from the northern domain. S_1 is defined by interlayering of graphite, biotite, and quartz, whereas S_2 is defined by biotite ± chlorite.*

D_2 Deformation

Mesoscale Observations

Regional D_2 deformation is characterized by a penetrative foliation and mineral stretching lineation throughout most of the structural section sampled during this study. S_2 progresses from crenulation cleavage at higher structural levels to a continuous, gently to moderately dipping schistosity that is concentric about the dome (Figs. 1.2, 1.3, and 1.6). In the northern domain S_2 also defines axial planes that dip gently to moderately northward. L_2 stretching lineations are defined by elongate porphyroblasts like chloritoid and staurolite in fine-grained metasedimentary rocks and by aligned quartz and biotite aggregates in coarse-grained metasedimentary intervals and in the core orthogneiss. In the northern and central domains, S_2 dips northward and L_2 lineations plunge approximately downdip (Figs. 1.6b, 1.6c). In the eastern domain S_2 dips gently east while L_2 mineral stretching lineations trend north-northeast, approximately parallel to the strike of S_2 (Fig. 1.6d). The southern domain contains S_2 foliation that generally dips southward instead of northward, and trends of L_2 lineations are scattered (Fig. 1.6e). At moderate structural levels in the southern domain, finer grained intervals record well-developed F_2 crenulations with average S_2 axial planar attitude of 077/45°SE (e.g., Fig. 1.7b) that is not as prominent in the northern domain.

Microscale Observations

Microstructural analyses of LKD samples indicate variation in D_2 fabric development with structural depth similar to the mesoscale variation. Starting in the Triassic schist and progressing downsection into units Ps and the orthogneiss, S_2 becomes increasingly pervasive, forming a continuous aligned-quartz and mica-chlorite cleavage in quartz-rich intervals and a domainal cleavage with submillimeter spacing defined by quartz microlithons and biotite ± white mica in pelitic intervals (Figs. 1.8a, 1.8b). Marble (unit Pm) from the northern domain also contains a pervasive S_2 foliation defined by biotite aggregates. In unit Ps, F_2 crenulations are commonly preserved within the S_2 mica domains even at lower structural levels where S_2 dominates the fabric (Appendix 1.2). Some pelitic schist (unit Ps) samples from the central domain contain elongate, kinked porphyroblasts such as kyanite and plagioclase with tails that merge with well-developed S_2 schistosity (e.g., Fig. 1.8c).

The core orthogneiss also exhibits a variety of D_2 textures, from fine grained and weakly

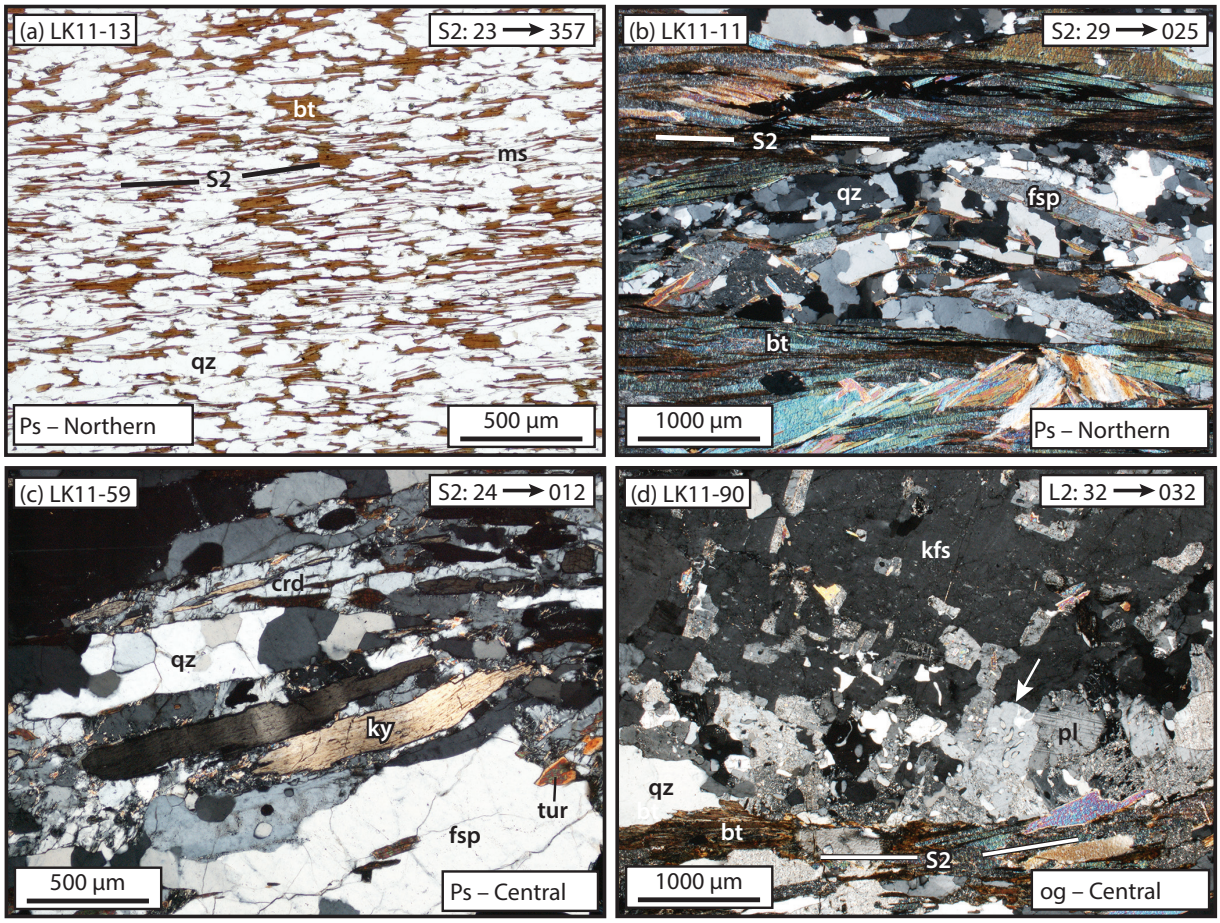


Figure 1.8. *Photomicrographs of microscale D_2 structures from the Lhagoi Kangri dome. Sample orientations are given in the upper-right corner as dip and dip direction of foliation (S_2) or plunge and trend of lineation (L_2) when lineation is present. Dip or plunge is to the right in all photomicrographs. Ps—Paleozoic schist and quartzite unit; og—orthogneiss and leucogranite. Mineral abbreviations: bt—biotite; crd—cordierite; fsp—feldspar; gr—graphite; kfs—K-feldspar; ky—kyanite; ms—muscovite; qz—quartz; ilm—ilmenite; tur—tourmaline. (a) Characteristic S_2 fabric in quartz schist shown in plane polarized light. (b) Spaced S_2 fabric in micaceous schist shown in cross polarized light. (c) Kinked kyanite in S_2 matrix in a biotite-sillimanite paragneiss from the central domain. (d) K-feldspar porphyroclast in orthogneiss from the central domain that contains myrmekite lobes (white arrow) on grain boundaries that are subparallel to S_2 (delineated at the bottom). Photomicrograph in cross polarized light. Additional examples of D_2 microstructures are in Appendix 1.2.*

foliated to coarse grained with well-developed gneissic banding (Appendix 1.2). S_2 foliation in coarser grained intervals is defined by elongate biotite (±white mica) that forms continuous 0.5–1.0-mm-thick bands, while the finer grained fabric is defined by thin (0.5 mm) discontinuous biotite layers and isolated individual biotite grains with a preferred orientation. The orthogneiss leucosome also contains alkali feldspar porphyroclasts. In samples from both the northern and central domains, some K-spar porphyroclasts have myrmekite lobes that are localized along grain boundaries parallel to the matrix foliation (Fig. 1.8d).

D_2 Kinematic Indicators

Mesoscale features throughout the LKD record shear sense associated with D_2 deformation. Centimeter-thick shear bands with decimeter-scale spacing that are subparallel to the regional S_2 foliation are preserved in unit Ps on the north side of the dome and record mixed top-to-south-southwest and top-to-north-northeast shear sense (e.g., Fig. 1.9a). Shear bands are also preserved in the core orthogneiss, although the example documented (Fig. 1.9b) was not collected in situ. Rocks in the northern and central domains also contain boudin trains comprising veins of quartz ± calcite. At the resolution of the study only three examples of boudinage were documented, but these examples derive from various structural levels within the metasedimentary cover sequence, and all are accompanied by pervasive S_2 schistosity (Figs. 1.5c, 1.9c, and 1.9d). Boudin attitudes were not measured, but in one instance where exposure and fracturing allowed observation on X/Z and approximate Y/Z planes, their geometry suggests that the boudins are three-dimensional chocolate tablets (Ghosh, 1988) that are subparallel to the local attitude of S_2 (265/20°NE).

Microscale kinematic indicators, such as strain shadows on porphyroblasts and C'-type shear bands, variably record symmetrical and asymmetrical shear sense in both the metasedimentary rocks and the orthogneiss. Near the core-cover contact, particularly in the central domain, samples record dominantly top-to-north-northeast shear (Table 1.1; Figs. 1.3 and 1.6). In the northern and eastern domains, garnet and chloritoid porphyroblasts in unit Ts graphitic schist contain both symmetric (Φ-type) and mixed top-to-north-northeast and top-to-south-southwest σ-type strain shadows in S_2 matrix schistosity (Fig. 1.10a; Appendix 1.2). Unit Ps in the northern and central domains contains garnet and staurolite porphyroblasts framed by σ-type strain shadows of quartz with chlorite and biotite that record

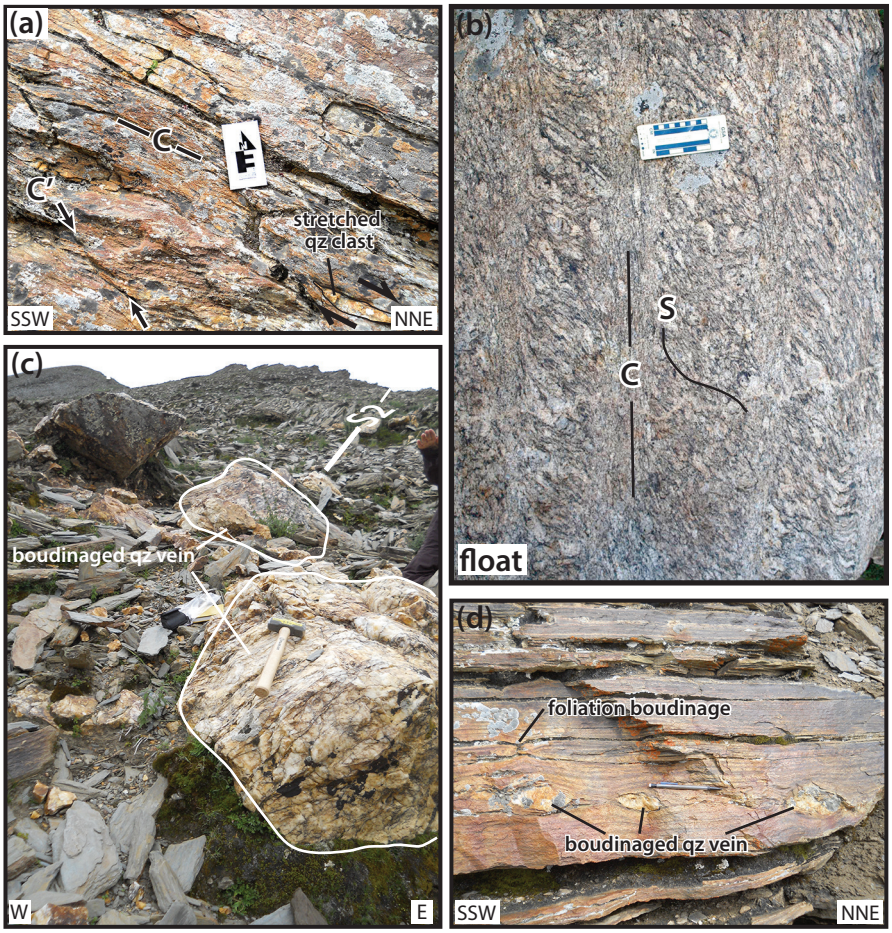


Figure 1.9. *Mesoscale examples of D_2 kinematic indicators. (a) C and C' shear bands in quartz schist from the central domain indicating top-to-north-northeast shear sense. Note asymmetry of stretched quartz (qz) clast in lower right that also records top-to-north-northeast shear sense. (b) Boulder of orthogneiss from the north side of the dome with well-developed centimeter-scale shear bands. (c) Example of boudinaged quartz (qtz) vein from unit Ts (Triassic siliciclastic unit) in the northern domain. (d) Boudinaged quartz vein and S_2 foliation in a quartz schist interval (Ps—Paleozoic schist and quartzite unit). Shear sense in C and D cannot be evaluated because the viewing plane is not equivalent to the XZ plane of strain.*

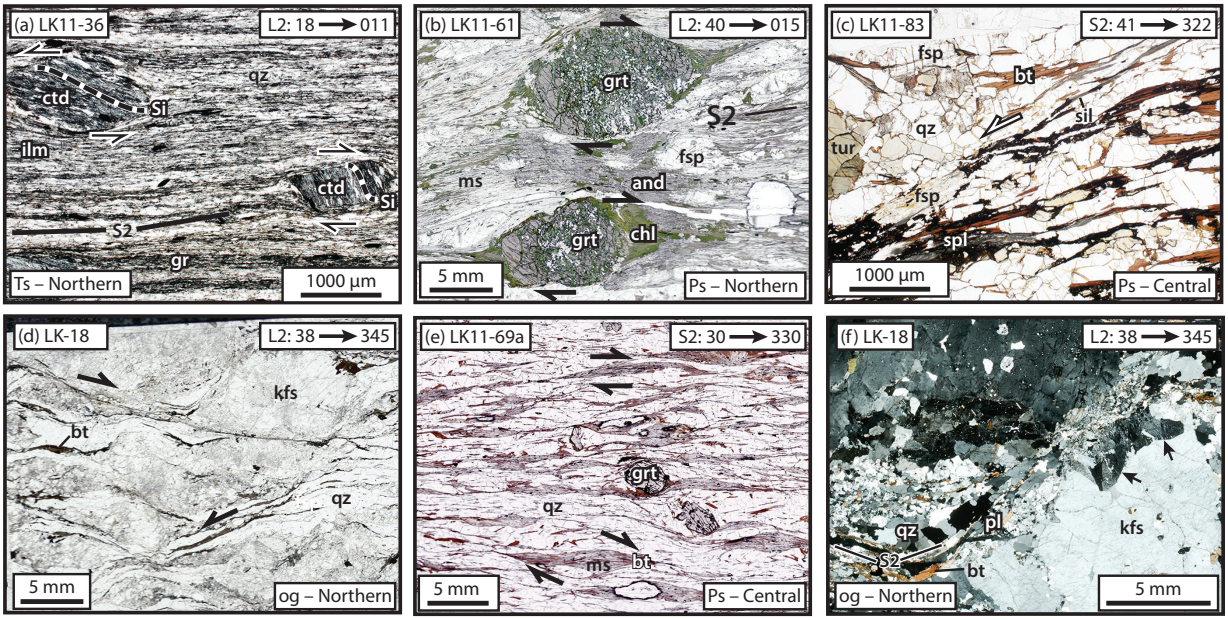


Figure 1.10. *Photomicrographs and thin section scans of microscale D_2 kinematic indicators from different structural levels within the Lhagoi Kangri dome (LKD). Additional examples are presented in Appendix 1.2. Sample orientations are given in upper right corner as dip and dip direction of foliation (S_2) or plunge and trend of lineation (L_2) when present. Dip or plunge is to the right in all photomicrographs. Ts—Triassic siliciclastic unit; Ps—Paleozoic schist and quartzite unit; og—orthogneiss and leucogranite. Mineral abbreviations: and—andalusite; bt—biotite; chl—chlorite; ctd—chloritoid; fsp—feldspar; gr—graphite; grt—garnet; ilm—ilmenite; kfs—K-feldspar; ms—muscovite; qz—quartz; tur—tourmaline. (a) Chloritoid porphyroblasts in graphitic schist (Ts) with asymmetric tails recording opposing top-to-north-northeast and top-to-south-southwest shear sense. Sigmoidal inclusion trails (Si) in the chloritoid porphyroblasts also indicate opposing shear sense. (b) Thin section scan showing two garnet porphyroblasts from garnet-andalusite schist with unambiguous top-to-north shear sense indicated by asymmetric biotite + chlorite strain shadows. (c) C' shear band filled by fibrolite and indicating top-to-south shear sense in a unit Ps paragneiss. (d) Thin section scan of orthogneiss from the northern domain exhibiting conjugate top-to-northwest and top-to-southeast shear bands. (e) Thin section scan of unit Ps schist with muscovite fish that record top-to-north-northwest shear sense. The same sample also contains muscovite fish that record top-to-south-southeast shear sense (Appendix 1.2). (f) Photomicrograph of the left edge of a large K-feldspar porphyroclast from the orthogneiss that exhibits asymmetric myrmekite (black arrows). Matrix fabric (S_2), defined by biotite and recrystallized quartz, wraps around the porphyroclast, forming asymmetric tails (example at bottom left) that indicate top-to-north-northwest shear sense. This is consistent with shear sense derived from the myrmekite asymmetry if it is assumed to have grown synkinematically.*

Table 1.1. Representative kinematic and deformation temperature data.

Sample	Latitude (°N)	Longitude (°E)	Lithology	Distance to Ps-og contact (m)*	Deformation style†	Shear sense (°)	Shear sense indicators	Microstructure§,**	[c] fabric O.A.#	Deformation temperature (°C)
Northern domain										
Northern transect										
LK11-36	28.897	87.643	Ts, Schist	1340	D_1/D_2; cc	Mixed	Strain shadows	-	-	-
LK11-35	28.897	87.642	Ts, Schist	1300	D_1/D_2; cc	Mixed	Strain shadows	-	-	-
LK11-15	28.863	87.581	Ps, Quartzite	40	D_2; sb	Top-205	C' shear bands, mica fish	Qz GBM I	-	>550
LK11-16c	28.863	87.581	Ps, Schist	40	D_1/D_2; sb,cc	Top-090	Strains shadows, C' shear bands	Qz GBM I	-	>550
LK11-18	28.864	87.580	Ps, Schist	35	D_2; sb	Top-060	C' and C shear bands	Qz GBM I	-	>550
LK11-06	28.865	87.582	Ps, Schist	30	D_2; sb	Top-200	C' and C shear bands	Qz GBM I	-	>550
LK11-10	28.864	87.582	Ps, Schist	25	D_2; sb	Top-210	C' and C shear bands	Qz GBM I, fsp SGR	-	>550
LK11-26	28.850	87.576	og, Gneiss	-600	D_2: sb	Top-031	C' shear bands	Qz GBM II, qz chessboard, fsp SGR	-	~630 ± 30
LK11-28	28.848	87.575	og, Gneiss	-650	D_2; sb	Top-015	C' shear bands, strain shadows	-	-	-
Miscellaneous										
LK-17	28.849	87.553	Pm, Marble	-	D_2; sb	Top-015	C' shear bands	Type II–III cal twins	-	200–300
LK-18	28.840	87.550	og, Gneiss	-	D_2; sb	Top-345	C' shear bands, asymmetric myrmekite	Qz GBM II	-	>550
Central domain										
Guodong transect										
LK11-74	28.861	87.657	Ps, Quartzite	600	-	Mixed	Oblique grain shape	Qz GBM I, SGR	57–60°	450–530
LK11-73	28.861	87.657	Ps, Schist	530	D_1/D_2; cc, sb	Top-015	S-C shear bands	Qz GBM I, brittle fsp	-	>550
LK11-70	28.861	87.657	Ps, Schist	490	D_2; sb	Top-310	C' shear bands	Qz GBM I	-	>550

Table 1.1. Continued

Sample	Latitude (°N)	Longitude (°E)	Lithology	Distance to Ps-og contact (m)*	Deformation style†	Shear sense (°)	Shear sense indicators	Microstructure§,**	[c] fabric O.A.#	Deformation temperature (°C)
LK11-69	28.860	87.658	Ps, Schist	450	D_2; sb	Mixed	SC and C' shear bands, mica fish	Qz GBM I	-	>550
LK11-68	28.860	87.658	Ps, Schist	430	D_2; sb	Top-005	C' shear bands, asymmetric strain shadows	Qz GBM I	-	>550
LK11-67	28.859	87.658	Ps, Quartzite	400	D_1/D_2; sb, si	Top-356	S-C shear bands	-	-	-
LK11-65	28.859	87.658	Ps, Schist	350	D_2	Top-015	Strain shadows, weak C' shear bands	-	-	-
LK11-64	28.859	87.659	Ps, Schist	340	D_2; sb	Top-350	C' shear bands	Qz GBM I	-	>550
LK11-62	28.859	87.659	Ps, Schist	300	D_2; sb	Mixed	C' shear bands, strain shadows	-	-	-
LK11-61	28.859	87.659	Ps, Schist	300	D_2; sb	Top-015	C' shear bands, strain shadows, mica fish	-	-	-
LK11-42	28.859	87.659	Ps, Schist	270	D_1/D_2; sb, si	Top-015	C' shear bands, spiral inclusion trail	-	-	-
LK11-40	28.857	87.659	og, Gneiss	-340	D_2; sb	Mixed	Strain shadows, C' shear bands	Qz GBM II, qz chessboard	-	~630 ± 30
Muddy Lake transect										
LK11-84	28.816	87.652	Ps, Schist	440	D_2; sb	Mixed	C' and C shear bands	Qz GBM I	-	>550
LK11-83	28.815	87.651	Ps, Schist	380	D_2; sb	Mixed	C' and C shear bands	Qz GBM I	-	>550
LK11-81	28.814	87.651	Ps, Schist	325	D_2; sb	Top-005	S-C shear bands	Qz GBM I	-	>550
LK11-60	28.815	87.643	Ps, Schist	325	D_2; sb	Mixed	C' shear bands, asymmetric strain shadows	Qz GBM I	-	>550
LK11-59	28.814	87.643	Ps, Schist	275	D_2; sb	Top-012	C' shear bands, asymmetric strain shadows	Qz GBM I	-	>550
LK11-57	28.813	87.643	Ps, Quartzite	260	D_2	-	-	Qz GBM I	76–77°	550–660
LK11-54	28.811	87.642	Ps, Quartzite	155	-	-	-	Qz GBM II	74–75°	550–650
LK11-52	28.810	87.642	Ps, Quartzite	70	-	-	-	Qz GBM II, qz chessboard	-	~630 ± 30

Table 1.1. Continued

Sample	Latitude (°N)	Longitude (°E)	Lithology	Distance to Ps-og contact (m)*	Deformation style†	Shear sense (°)	Shear sense indicators	Microstructure§,**	[c] fabric O.A.#	Deformation temperature (°C)
LK11-51	28.808	87.641	og, Gneiss	0	-	-	-	Qz GBM II, qz chessboard	-	~630 ± 30
LK11-49	28.807	87.640	og, Gneiss	-50	D_2	Top-010	Weak oblique grain shape	-	-	-
LK11-87b	28.816	87.653	og, Gneiss	-85	D_2	-	-	Qz GBM I	68–70°	480–610
LK11-88	28.820	87.655	og, Gneiss	-85	D_2	-	-	Qz GBM II, fsp SGR	-	>550
LK11-91A	28.825	87.656	og, Gneiss	-90	D_2; sb	Mixed	C' and C shear bands	-	-	-
LK11-90	28.823	87.655	og, Gneiss	-100	D_2; sb	Mixed	C' and C shear shear bands, strain shadows	Qz GBM II, qz chessboard, fsp SGR	-	>550
Eastern domain										
Eastern transect										
LK-70	28.740	87.771	Ts, Schist	-	D_2?	Top-022	Strain shadows	-	-	-
LK-69	28.740	87.770	Ts, Schist	-	D_1/D_2; si	Mixed	Strain shadows, C' shear bands	-	-	-
LK-68	28.740	87.771	Ts, Schist	-	D_1/D_2; si	Mixed	Strain shadows	-	-	-
LK-67a	28.742	87.768	Ts, Schist	-	D_1/D_2; si, sb	Top-335	Strain shadows	-	-	-
LK-65	28.751	87.740	Pm, Marble	-	D_2	-	-	Type III–IV calcite twins	-	>250
Southern domain										
Southern transect										
LK-04	-	-	Pm, Marble	3000	D_2	-	-	Type I–II cal twins	-	>200
LK-05	28.660	87.593	Ps, Schist	2700	D_1/D_2; cc	-	-	Qz SGR	-	450–550
LK-48	28.672	87.603	Ps, Schist	1800	D_2	Top-180	Strain shadows, S-C fabric	Qz GBM I	-	>550
LK-52	28.682	87.613	Ps, Schist	1200	D_1/D_2; si, sb	Top-350	Strain shadows	Qz GBM II, qz chessboard	-	~630 ± 30

Table 1.1. Continued

Sample	Latitude (°N)	Longitude (°E)	Lithology	Distance to Ps-og contact (m)*	Deformation style†	Shear sense (°)	Shear sense indicators	Microstructure§,**	[c] fabric O.A.#	Deformation temperature (°C)
LK-51	28.682	87.617	Qz Vein in Ps	1200	-	-	-	Qz GBM II	-	>550
LK-54	28.686	87.609	Ps, Quartzite	1000	-	-	-	Qz GBM II, qz chessboard	72–73°	520–630
LK-41	28.720	87.561	og, Gneiss	-	D_2	Top-195		Qz chessboard, fsp SGR	-	~630 ± 30

Note: All samples discussed in the text and shown in Figure 2 and Figures 8-15 are listed in this table.

*Southern domain values are distance to lowest sample since the core-cover contact is not well constrained. Other values were calculated by projection into the cross section planes (Fig. 3).

†Structural fabrics documented in each sample and abbreviated as follows: cc, crenulation cleavage; sb, shear bands; si, sigmoidal inclusions.

§SGR, subgrain rotation; GBM I and GBM II, impurity-hindered and non-impurity-hindered grain boundary migration, respectively; fsp, feldspar; cal, calcite.

#O.A., c-axis fabric opening angle.

mixed top-to-north-northeast (Fig. 1.10b) and top-to-south-southwest (Appendix 1.2) shear sense. Garnet schist in the southern domain also contains porphyroblasts with asymmetric strain shadows on garnet with both top-to-south-southwest and top-to-north-northeast shear sense (Table 1.1), although data are too sparse to suggest an apparent relationship between shear sense and structural position, as noted for the central domain.

The lowermost schist and orthogneiss in the northern, central, and southern domains contains microscale C'-type shear bands, mica fish, and, in the orthogneiss, asymmetric myrmekite. The C'-type shear bands in these units record both top-to-north and top-to-south shear sense, but are predominantly top-to-north indicators (e.g., Figs. 1.10c, 1.10c; Appendix 1.2; Table 1.1). Mica fish in schist and paragneiss intervals also record mixed top-to-north and top-to-south shear sense where present (Fig. 1.10e; Appendix 1.2). Some K-feldspar porphyroclasts in the LKD orthogneiss exhibit myrmekite overgrowths and recrystallized tails similar to features that Simpson and Wintsch (1989) identified as deformation induced and suggested were viable kinematic indicators. In LKD samples, shear-sense inferred from myrmekite overgrowth is consistent with that from porphyroclast tails and matrix shear fabric (e.g., Fig. 1.10f), suggesting their viability for use as kinematic indicators in the LKD as well. Myrmekite could also have grown prior to D_2 deformation, but it is beyond the scope of this study to determine myrmekite growth mechanisms.

D_2 Quartz, Feldspar, and Calcite Microstructures

Background and methods. Quartz and feldspar microstructures (e.g., Tullis and Yund, 1987; Hirth and Tullis, 1992; Pryer, 1993; Stipp et al., 2002b) are documented for 28 samples, and calcite twin morphology (Ferrill et al., 2004) is documented for 4 samples (Table 1.1).

Quartz microstructures in LKD samples fall into two of three recrystallization types originally defined by Stipp et al. (2002b) for naturally deformed quartz in the Italian Alps: (1) subgrain rotation recrystallization (SGR) and (2) grain-boundary migration recrystallization (GBM), which can be further subdivided into GBM I and GBM II on the basis of impurity-hindered versus non-impurity-hindered grain-boundary migration. In that study temperatures associated with quartz recrystallization mechanisms were delimited by thermobarometry of synkinematic mineral assemblages. The temperatures determined are 400–500 °C for SGR, >500 °C for GBM, and 630 ± 30 °C for chessboard extinction, which is a

characteristic feature of GBM II. Quartz dynamic recrystallization microstructures are also controlled by other factors, such as strain rate and hydrolytic weakening (e.g., Kronenberg and Tullis, 1984; Post and Tullis, 1998; Stipp et al., 2006); Stipp et al. (2002a) demonstrated that recrystallization mechanisms in the Alps samples were also influenced by strain rate.

Feldspars exhibit dislocation creep mechanisms similar to that of quartz (e.g., Tullis and Yund, 1987, 1991), and plastic deformation usually occurs in naturally deformed samples at ~450 °C and higher (e.g., Pryer, 1993). However, deformation mechanisms in feldspar are also influenced by strain rate and hydrolytic weakening (e.g., Tullis and Yund, 1991). Feldspar grains can also fracture or boudinage at higher temperatures if they are included in a rheologically weaker matrix such as quartz and mica (e.g., Fitz Gerald and Stünitz, 1993; Stünitz and Fitz Gerald, 1993).

In coarse-grained limestone and marble, calcite twinning is an important deformation mechanism at low temperatures (400 °C), and Ferrill et al. (2004) determined that there is a positive correlation between calcite twin width and deformation temperature such that thin twins (Type I, <1 μm) are dominant at temperatures <170 °C while thick twins (Types II–IV, >1 μm) are dominant at temperatures >200 °C. The geometry of the twin boundaries varies with increasing temperature, from straight boundaries formed at lower temperature (Type II), curved at moderate temperature (Type III), to patchy (indicative of partial dynamic recrystallization) at higher temperatures (Type IV, >250 °C). Complete dynamic recrystallization typically occurs at temperatures 300 °C (e.g., Weber et al., 2001; Ferrill et al., 2004). However, in calcite veins or localized fault zones, incipient dynamic recrystallization can begin at temperatures lower than 250 °C in response to high strain rate (Ferrill et al., 2004). Calcite twinning is also influenced by total strain, and so interpretations of calcite twin morphology must be made cautiously and with consideration of alternatives.

LKD calcite microstructures. Representative samples of phlogopite-bearing marble were collected from all three domains, and exhibit a range in calcite microstructures from Type I through Type IV twins (Table 1.1; Fig. 1.11; Appendix 1.2). A sample from the southern domain (LK-04) exhibits Type I and II calcite twins (Fig. 1.11a), whereas a correlative sample from the eastern domain (LK-65) exhibits Type III and IV twins (Fig. 1.11b), indicating at least partial dynamic recrystallization. From the northern domain, sample LK-17 (Table 1.1; Appendix 1.2) contains Type I and II twins as well as thick twins with

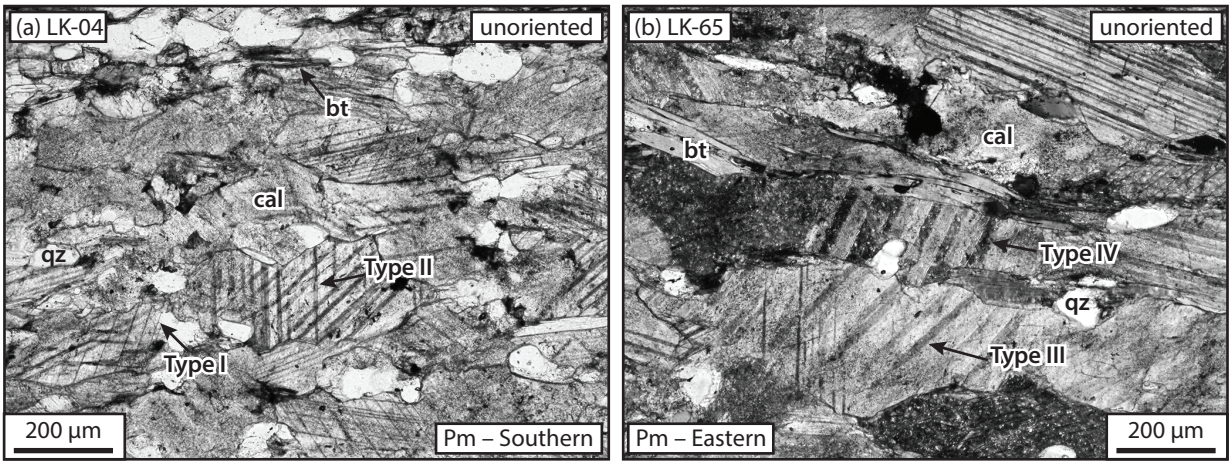


Figure 1.11. *(a) Plane polarized light photomicrograph of marble from southern domain that contains Types I and II calcite twins. Mineral abbreviations: bt—biotite; cal—calcite; qz—quartz. Pm—Paleozoic marble. (b) Calcite grains in marble from eastern domain that exhibit tapered (Type III) and patchy (Type IV) calcite twins, indicating partial dynamic recrystallization. Photomicrograph in cross polarized light with quarter-wave plate inserted.*

tapered boundaries (Type III). Patchy twin boundaries (Type IV) are not recorded in this sample, but clusters of small, unstrained grains surrounding large twinned grains indicate dynamic recrystallization in this sample as well (Appendix 1.2).

LKD quartz and feldspar microstructures. The Guodong and Muddy Lake transects from the central domain (Figs. 1.2 and 1.6; Table 1.1) are representative of the range in quartz and feldspar recovery mechanisms associated with D_2 deformation. The following observations are presented in order of highest to lowest structural level, summarized in Table 1.1, and shown in Figures 1.12a–1.12f. (For additional examples of quartz and feldspar microstructures, see Appendix 1.2)

Sample LK11-74 is a mica-bearing quartzite that marks the top of the Guodong transect, sampled ~600 m above the contact with the core orthogneiss. LK11-74 contains dynamically recrystallized quartz grains with amoeboidal grain boundaries characteristic of GBM I and subgrain formation indicating SGR (Fig. 1.12a). These quartz microstructures are dispersed throughout the sample rather than partitioned into particular domains (e.g., microscale shear zones), which suggests that both dynamic recrystallization mechanisms (SGR and GBM) operated coevally. Structurally lower quartzite and quartz schist samples from the transect exhibit dominant GBM I recrystallization (Table 1.1) with grain interiors that are free

Figure 1.12. *Representative quartz and feldspar microstructures from unit Ps (Paleozoic schist and quartzite) quartzite samples from the central domain. Photomicrographs are shown in cross polarized light unless otherwise noted. Additional examples are in Appendix 1.2. Mineral abbreviations: bt—biotite; fsp—feldspar; qz—quartz; wm—white mica. (a) Amoeboidal quartz grains with lobate boundaries and discrete subgrains (black arrows) that indicate a combination of grain-boundary migration recrystallization (GBM) and subgrain rotation recrystallization (SGR) mechanisms. (b) Large amoeboidal quartz grains from unit Ps schist that contain inclusions of biotite, indicating non-impurity-hindered grain-boundary migration (GBM II). (c) Quartzite (Ps) from the Muddy Lake transect that exhibits amoeboidal grains with lobate boundaries containing inclusions of biotite, although locally some are pinned by biotite, generally indicating GBM recrystallization. (d) Orthogneiss (og—orthogneiss and leucogranite) from the Muddy Lake transect that contains large, amoeboidal quartz grains with chessboard extinction indicating GBM II recrystallization. (e) Aluminous schist from the top of the Guodong transect that contains plagioclase grains with microcracks (white arrow) and quartz grains with amoeboidal grain boundaries that are locally impurity-hindered, indicating GBM I. (f) Feldspar grains in orthogneiss from the northern domain that exhibit subgrain formation (SGR; white arrow) and are interspersed with quartz that exhibit lobate grain boundaries and mica inclusions, indicating GBM II recrystallization.*

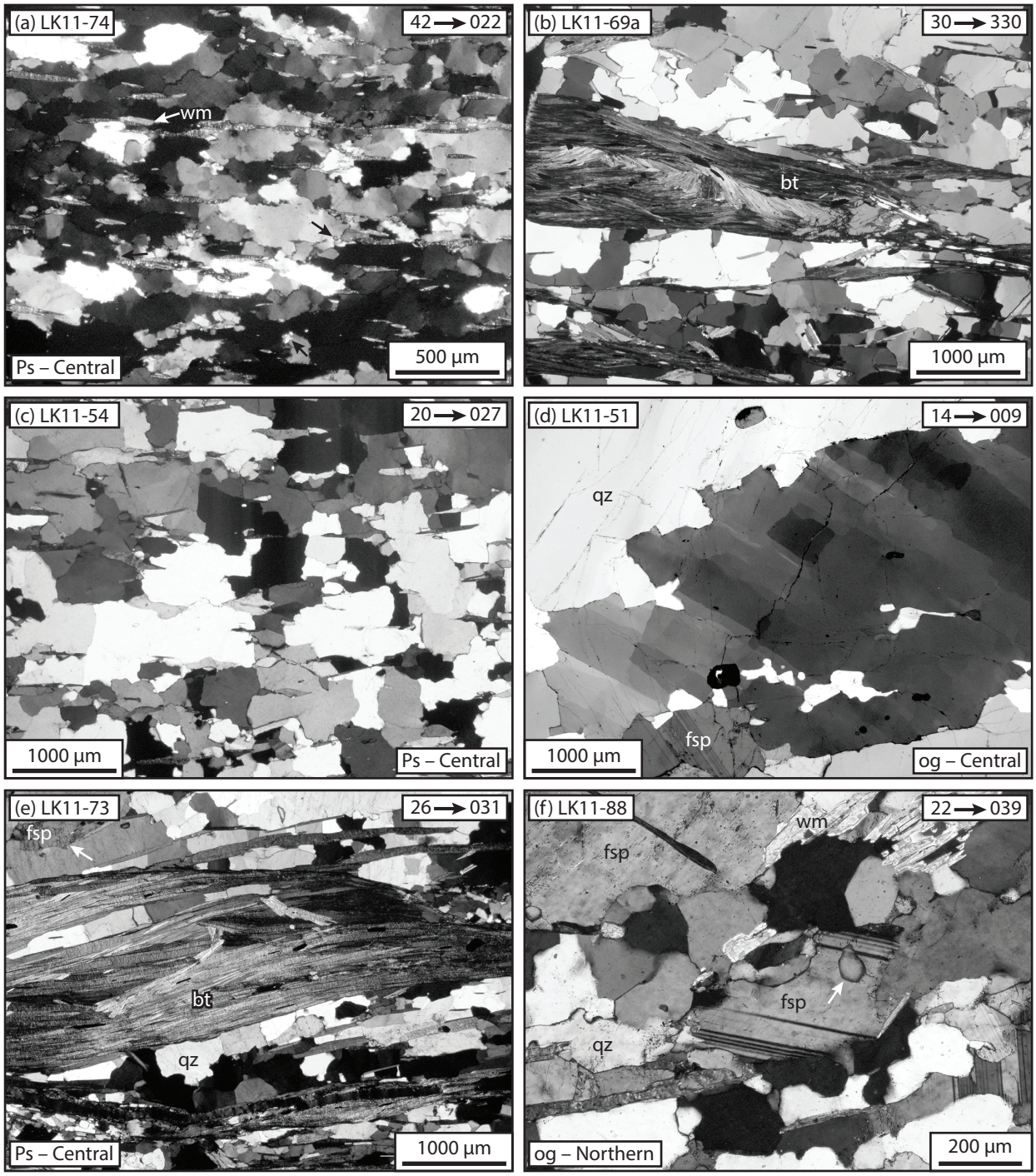


Figure 1.12. Continued.

of subgrains (e.g., Fig. 1.12b). Orthogneiss at the base of the transect also exhibits quartz grain-boundary migration microstructures and chessboard extinction (collectively, GBM II).

The adjacent Muddy Lake transect spans a range in structural levels similar to that of the Guodong transect and contains abundant quartzite that is compositionally similar to LK11-74 (i.e., impure quartzite with biotite ± white mica flakes). The Muddy Lake quartzite samples are characterized by quartz GBM microstructures at all structural levels along the transect (Table 1.1; e.g., Fig. 1.12c). At lower structural levels, starting ~150–250 m above the orthogneiss contact, there is an apparent shift in recrystallization mechanism from impurity-hindered (GBM I) to non-hindered grain-boundary migration (GBM II), and chessboard extinction is also more common at lower structural levels (Table 1.1; Fig. 1.12d; Appendix 1.2).

Feldspar microstructures indicate an apparent correlation with structural depth. At the upper part of the Guodong transect, feldspar grains exhibit brittle microcracks and undulose extinction while quartz grains in the same sample exhibit GBM I microstructures (LK11-73; Fig. 1.12e; Table 1.1). Deformation lamellae and undulose extinction are not evident in quartz grains, suggesting that (1) the quartz and feldspar microstructures developed under similar conditions, but the quartz was rheologically weaker (e.g., Stünitz and Fitz Gerald, 1993), or (2) the feldspar microstructures were inherited from some previous deformation. In contrast, many orthogneiss samples from the Guodong and Muddy Lake transects contain feldspar grains with bulging grain boundaries and subgrain structures (e.g., Fig. 1.12f; Table 1.1; Appendix 1.2). In these same orthogneiss samples, quartz grains generally record GBM II and chessboard extinction microstructures.

The southern transect encompasses a wider range in structural levels, and sampling resolution is much lower than in the Guodong and Muddy Lake transects, but the samples collected suggest a similar correlation between structural depth and quartz and feldspar microstructures. The structurally highest quartz schist sample (LK-05; Table 1.1) records quartz SGR microstructures, and at progressively lower structural levels there is an apparent shift first to GBM I (sample LK-48) and then to GBM II (sample LK-52) microstructures.

D_2 Quartz Crystallographic Preferred Orientation Patterns

Background and methods. Quartz crystallographic preferred orientation (CPO) patterns (Lister et al., 1978; Lister and Hobbs, 1980; Lister and Dornsiepen, 1982; Mainprice et al., 1986; Schmid and Casey, 1986; Law, 1990; Kruhl, 1998) were analyzed from 10 LKD samples (Table 1.1). The CPO patterns were collected by electron backscatter diffraction (EBSD) analysis using an FEI Quanta 400 scanning electron microscope equipped with a Nordlys 2 EBSD camera and housed at the University of California, Santa Barbara. Samples chosen for EBSD analysis mostly overlap those chosen for quartz and feldspar microstructural analysis, and all samples are derived from structural levels that generally encompass the regime of GBM I recrystallization (Table 1.1; Fig. 1.13). Thin sections were polished using 0.25 μm diamond grit followed by 3 h on a vibratory polisher coated with 0.05 μm colloidal silica gel. The samples contain large grain sizes and weakly developed, relatively homogeneous fabric. For these reasons, EBSD analyses for each sample were carried out over the entire area of a standard rectangular thin section (27 × 46 mm) using a 100 μm step size, with the exceptions of samples LK11-57 and LK11-87b, which were carried out over approximately half of the total thin section area at a step size of 100 μm. Analyses were set up to only index quartz and were processed using HKL CHANNEL 5 EBSD software. Data processing involved filling unindexed pixels in which five neighbor pixels share a common orientation. Individual grains are defined on the basis of a 15° critical misorientation angle. Because grain sizes in the LKD samples are generally larger than the step size, CPO plots presented in Figures 1.13b–1.13d were plotted using a one point-per-grain (PPG) approach in which individual grains are given equal weight, although for the LKD samples there is little or no difference in CPO fabric between raw and PPG data (e.g., Appendix 1.3).

Quartz CPO patterns, particularly [c]-axis orientations, reflect active crystallographic slip systems during deformation (e.g., Schmid and Casey, 1986) that are controlled predominantly by temperature, strain rate, strain path, and degree of hydrolytic weakening (Tullis et al., 1973; Lister, 1977; Lister and Hobbs, 1980; Lister and Dornsiepen, 1982; Tullis and Yund, 1989; Law, 1990). In practice there are several possible quartz crystallographic slip systems (e.g., Schmid and Casey, 1986), but only basal <a>, prism <a>, and prism [c] slip are relevant to the LKD samples. Basal and prism define the lattice planes of the crystal along which slip occurs, while <a> and [c] refer to crystallographic orientations that define the slip direction. In instances where orientations of [c] axes from a sample

Figure 1.13. *(a) Quartz [c] axis fabric opening angle versus deformation temperature simplified from the original plot developed by Kruhl (1998) with modifications by Law (2014), Law et al. (2004), and Morgan and Law (2004). Boxes represent natural data sets referenced in Kruhl (1998) and Law (2014) from which a best-fit line (thin black) was previously derived. Gray bar represents ±50 °C error prescribed by Kruhl (1998) to account for uncertainties in the influence of strain rate and hydrolytic weakening. Box marked LKD represents the range of opening angles from the Lhagoi Kangri dome. (b) Contoured lower hemisphere stereogram of quartz (qz) crystallographic preferred orientations (CPO) from the Southern transect. Ps—Paleozoic schist and quartzite unit; dom—dominant. (c) From the Guodong transect. (d) From the Muddy Lake transect (og—orthogneiss and leucogranite; bt—biotite). As shown in the diagram at the top of B, all plots are from samples oriented perpendicular to S_2, parallel to L_2, and all plots are oriented to show geographic north to the right. Data are shown as point-per-grain with n = number of grains. Contours are multiples of uniform density (m.u.d.) with warmer colors representing higher m.u.d. and cooler colors representing lower m.u.d. The contour interval for all plots is 1 m.u.d. Interpreted opening angles and dominant slip systems are documented where applicable. Plots with discernible opening angles have background values (m.u.d. << 1.0) removed. Unaltered plots are in Appendix 1.3.*

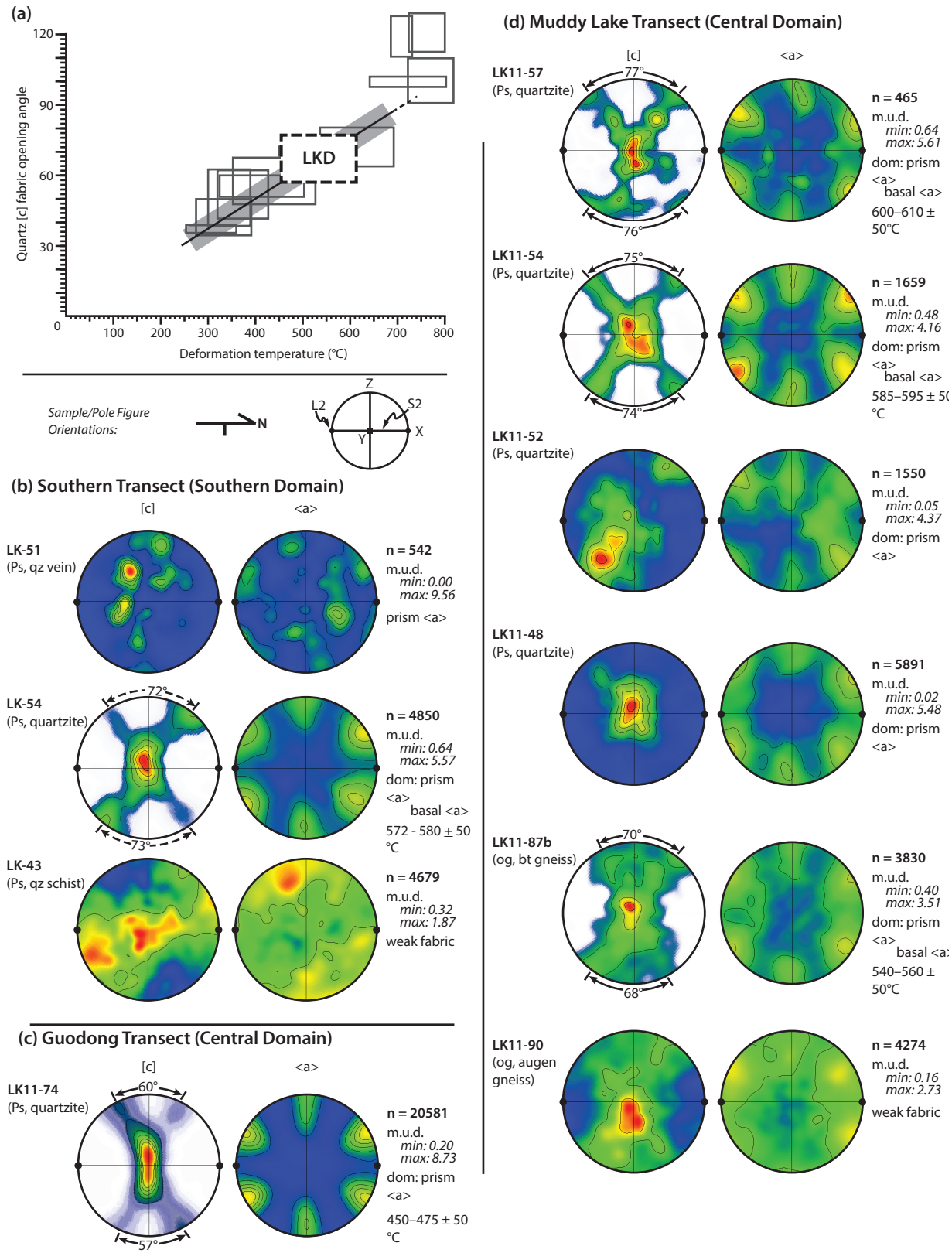


Figure 1.13. Continued.

viewed parallel to the XZ plane of strain (i.e., perpendicular to foliation, parallel to lineation) form a crossed-girdle pattern, the opening angle, defined as the angle between the two girdles (e.g., Appendix 1.3), has a positive correlation to temperature, although it can also be affected by strain rate, shear strain amount, and hydrolytic weakening (Tullis et al., 1973; Law, 1990; Kruhl, 1998; Law et al., 2011). Modeling (Lister, 1981) and experimentation (Gleason et al., 1993) suggest that changes in [c] fabric opening angle are related to a shift in dominant crystallographic slip system from basal <a> to prism [c] as a function of increasing temperature; however, it is important to emphasize that water and strain rate influence the activity of these systems.

Quartz CPO patterns. CPO patterns from the LKD are weakly to moderately developed in quartzite samples and weakly developed in two orthogneiss samples, one quartz schist sample, and one quartz vein sample (Fig. 1.13).

Three samples from the southern transect (Fig. 1.13b) bracket 500–700 m of structural thickness within unit Ps. The structurally shallowest sample, LK-51, is from a foliation-parallel quartz vein that exhibits a relatively strong [c] axis maximum. The next lowest sample (LK-54) from the southern transect is a quartzite derived from ~200 m structurally below LK-51. The c-axis pattern for sample LK-54 is defined by a strong Y-axis (central) maximum and a weakly developed crossed-girdle fabric that indicates dominant prism <a> slip and a component of basal <a> slip. The [c]-fabric opening angle is 72°–73° (Fig. 1.13b), and asymmetry in the peripheral arms of the crossed girdle, as well as asymmetry in the strength of <a> axis fabric, indicate a top-to-north shear sense. The structurally lowest EBSD sample from the southern transect (LK-43) is quartz schist from ~500 m below LK-54. The [c] axis plot for sample LK-43 resembles a CPO indicative of a combination of prism <a> and prism [c] slip (e.g., Lister and Dornsiepen, 1982; Bouchez et al., 1984; Morgan and Law, 2004), but the pattern is too weak to decipher.

One quartzite sample from the structurally highest level of the Guodong transect (LK11-74; Table 1.1; Fig. 1.13c) has a CPO with an elongate central [c] axis maximum, indicative of prism <a> slip, and weakly developed peripheral arms that resemble a Type I crossed-girdle pattern (e.g., Lister and Dornsiepen, 1982). The contour pattern is weak, but point data yield a fabric skeleton (Appendix 1.3) with an opening angle of 57°–60°.

Samples from the Muddy Lake transect characterize CPO variation with structural position over ~300 m of lowermost unit Ps and another ~100 m of the underlying orthogneiss (Fig. 1.13d; Table 1.1). Three of four quartzite samples from unit Ps (LK11-57, LK11-54, LK11-48) exhibit well-defined CPO patterns with a characteristic c-axis maximum near the center of the plot. The stereogram for the fourth quartzite sample (LK11-52) appears to be aligned obliquely to the XZ plane, but the amount of rotation required to produce an interpretable CPO pattern is inconsistent with the orientation of the thin section cut relative to fabric in the hand specimen. The two structurally highest samples (LK11-57 and LK11-54) exhibit well-developed Type I crossed girdles that comprise slightly weaker intermediate and peripheral maxima, and they indicate a component of basal <a> slip in addition to prism <a> slip implied by the strong central maxima. In sample LK11-54 the [c]-fabric peripheral arms and density of <a> axes record asymmetry that indicates top-to-north-northeast sense shear. Opening angles for samples LK11-57 and LK11-54 are 76°–77° and 74°–75°, respectively. Sample LK11-48, located proximal to the orthogneiss contact and ~70 m structurally below LK11-52, exhibits a CPO characterized by a well-developed central maximum but no peripheral arms, indicating dominant prism <a> slip. Samples LK11-87b and LK11-90 are biotite orthogneiss located 85 and 100 m, respectively, structurally below the contact with the overlying metasedimentary rocks (~85–100 m below sample LK11-48). Compared to the quartzite, the orthogneiss samples have relatively poorly defined CPO patterns. While they do exhibit faint Type I crossed-girdle fabrics, the most clearly defined aspect of the orthogneiss fabric is a Y axis maximum that indicates dominant prism <a> slip in sample LK11-87b.

Porphyroblast Inclusion Trails

Porphyroblast inclusion trail geometry was documented in order to constrain relative timing of deformation and metamorphism. Sigmoidal and spiral inclusion microstructures are commonly used to interpret early stages in the strain paths of deformed rocks (e.g., Passchier et al., 1992; Williams, 1994; Johnson, 1999; Williams and Jiang, 1999; Trouw et al., 2008). In LKD samples that contain them, porphyroblast inclusion trails exhibit variable geometry with respect to matrix S_2 fabric, constrain relative timing of porphyroblast growth and D_2 fabric development, and in some instances record D_2 kinematics.

Sigmoidal inclusion trails are preserved in chloritoid, garnet, and staurolite porphyroblasts

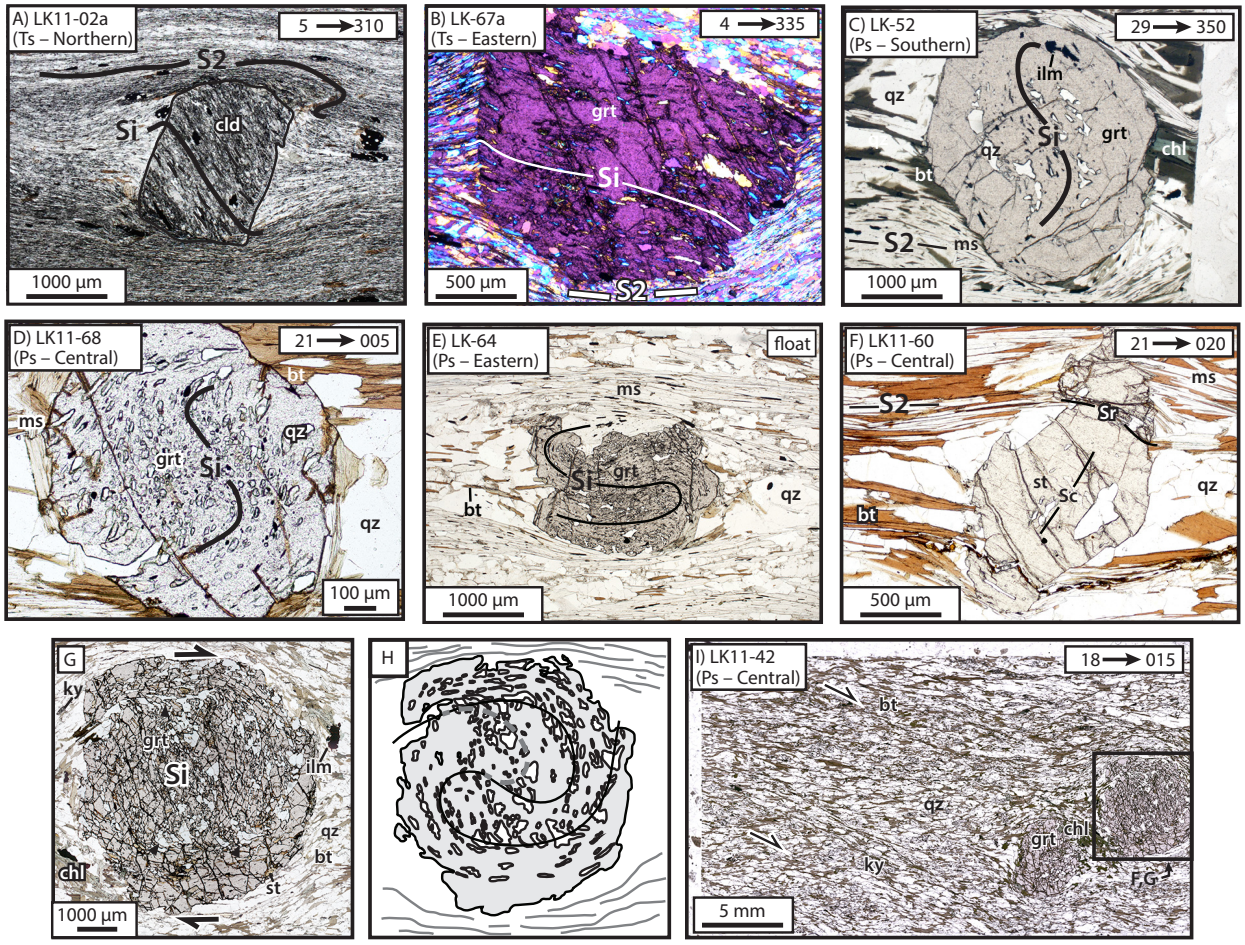


Figure 1.14. *Photomicrographs showing relationship between porphyroblast inclusion trails and matrix fabric throughout the Lhagoi Kangri dome (LKD). All images shown in plane polarized light unless otherwise noted. Ts—Triassic siliciclastic unit; Ps—Paleozoic schist and quartzite unit. Mineral abbreviations: bt—biotite; chl—chlorite; cld—chloritoid; grt—garnet; ilm—ilmenite; ms—muscovite; qz—quartz; st—staurolite. (a) Chloritoid porphyroblast in schist (Ts) from the northern domain with inclined inclusion trails that are continuous with the external foliation. Note the microfold outlined in upper right corner of the porphyroblast. Both features indicate top-to-310° shear sense. (b) Garnet porphyroblast in schist (Ts) from eastern domain with sigmoidal inclusion trail that is deflected at the porphyroblast-matrix interface but still continuous with matrix fabric. Photomicrograph in cross polarized light with quarter-wave plate inserted. (c) Unit Ps garnet with an inclusion trail that curves into parallelism with matrix fabric but is not continuous with the matrix fabric. (d, e) Additional examples of garnet from unit Ps that contain sigmoidal inclusion trails that, in contrast to C, are continuous with S_2 matrix foliation. (f) Staurolite porphyroblast in schist (Ps) from the central domain that has an inclined near-core (Sc) inclusion trail and a wavy near-rim (Sr) inclusion trail, the latter of which is continuous with matrix S_2. (g) Photomicrograph of snowball garnet from sample LK11-42 (unit Ps, central domain). Black triangles denote arc-shaped quartz aggregates discussed in text. (h) Sketch of G. Because inclusion trail is not well defined, two alternative interpretations are presented, as a thin black line and a gray dashed line. (i) Thin section scan of LK11-42 showing C'-type shear bands that indicate the same top-to-015° asymmetry as the spiral inclusion trails.*

from most pelitic rock samples with S_2 matrix fabric (units Ts and Ps). The curved trails are defined by elongated individual grains and aggregates of smaller grains that align to form the trails (Figs. 1.14a–1.14e). In a representative unit Ts chloritoid porphyroblast (Fig. 1.14a), inclusion trails are continuous with matrix S_2 fabric and the porphyroblasts are framed at top and bottom by microfolds. Garnet porphyroblasts in unit Ts contain inclusion trails that are commonly deflected at the grain boundary (e.g., Fig. 1.14b), but they are still continuous with matrix S_2 fabric. Similarly, garnet porphyroblasts in pelitic samples of unit Ps have sigmoidal inclusion trails that are typically continuous, or at least curve into parallelism, with S_2 matrix fabric (e.g., Figs. 1.14c–1.14e). Staurolite inclusion trails are rare and poorly defined where present. In a representative sample, staurolite porphyroblast inclusion trails are inclined to matrix fabric near the porphyroblast cores and are curved but continuous with matrix fabric near the rims (LK11-60; Fig. 1.14f). In contrast to the simpler inclined or sigmoidal trails recorded in most porphyroblasts, the structurally lowest metapelite sampled in the central domain (LK11-42; Table 1.1) contains snowball garnet characterized by spiral-shaped inclusion trails (Figs. 1.14g, 1.14h). The spiral shapes are defined not only by curvilinear trails, but also by arc-shaped clusters of inclusions (Fig. 1.14g).

In LKD samples, most porphyroblast inclusion trails are continuous with matrix foliation (e.g., Figs. 1.14a, 1.14b, 1.14d–1.14f), suggesting intertectonic (between D_1 and D_2) to syn-D_2 porphyroblast growth (e.g., Trouw et al., 2008; Johnson, 1999; Lee et al., 2000, 2004). In the samples where sigmoidal inclusion trails are not continuous with S_2 matrix foliation (e.g., LK-52; Fig. 1.14c), the trails still appear to curve into parallelism with matrix fabric and also indicate that their hosts are intertectonic to syn-D_2. In the case of LK11-02a (Fig. 1.14a), the microfolds adjacent to the porphyroblasts are best interpreted as deflection planes (Passchier et al., 1992) that indicate porphyroblast rotation during D_2 fabric development and, together with inclusion trail and strain shadow asymmetry, record top-to-310° shear sense. Likewise, the geometry of garnet-hosted inclusion trails in LK-67a and the continuity between inclusion trails and matrix foliation are indicative of early stages of synkinematic growth (e.g., Passchier et al., 1992; Trouw et al., 2008). These features imply top-to-335° shear sense, in agreement with asymmetric strain shadows on garnet from the same sample (Table 1.1). In other examples (Figs. 1.14c, 1.14d) distinction between syn-D_2 rotation and crenulation overgrowth is not possible. The snowball garnet hosted in LK11-42 is unequivocal evidence of synkinematic growth given that: (1) only two

pervasive deformation fabrics (D_1 and D_2) are recorded in the LKD rocks, and neither are likely to have rotated through >180° (e.g., Jiang and Williams, 2004); and (2) the shear sense implied by rotation (top-to-015°) of the porphyroblasts is consistent with shear sense recorded by C' shear bands in the matrix (Figs. 1.14g–1.14i; Table 1.1). These observations indicate that chloritoid, garnet, and staurolite grew post-D_1 to syn-D_2.

Discussion

Interpretation of D_2 Microstructures and Quartz CPO Patterns

Quartz and feldspar microstructures and quartz CPO fabrics show generally close agreement if interpreted as deformation temperature indicators and assuming average geologic strain rates (e.g., Kruhl, 1998; Stipp et al., 2002b) for D_2 deformation. As noted here, microstructures and CPO fabrics are influenced by a number of other variables, particularly strain rate and water content, that are not constrained for LKD rocks. This should be reemphasized for calcite microstructures as well, with the added caveat that total strain may also influence calcite twin width and intensity (Ferrill et al., 2004). As described in previous sections and summarized in Table 1.1, quartz microstructures exhibit a correlation with structural depth characterized by a progression from SGR, through transitional SGR-GBM to GBM I, and finally GBM II at the lowest structural levels. Quartz fabrics also exhibit a trend of increasing opening angle toward lower structural levels at least through the metasedimentary rocks if not the core orthogneiss (Figs. 1.12b–1.12d). Furthermore, the quartz fabric topology can be broadly described as transitioning from crossed girdles to single [c] axis maxima with increasing structural depth in the Muddy Lake transect (Fig. 1.12d), a fabric transition that has been ascribed to progressively increasing temperatures or shifts in recrystallization mechanism (e.g., Gleason et al., 1993; Stipp et al., 2002b). These patterns in microstructures and CPO fabrics could be primarily controlled by (1) increasing deformation temperatures, (2) decreasing strain rate, or (3) increasing water content. The third scenario is possible given that rocks at lower structural levels probably reached higher metamorphic grade that might be accompanied by greater degrees of dehydration (e.g., Harlov, 2012). Chessboard extinction microstructures and the activation of prism [c] slip, which is assumed to be responsible for chessboard extinction (e.g., Stipp et al., 2002b), are particularly sensitive to the presence of water (e.g., Bouchez et

al., 1984; Garbutt and Teyssier, 1991; Morgan and Law, 2004). In the lower structural levels of the LKD where chessboard extinction is common, quartz CPO fabrics do not exhibit prism [c] or transitional basal <a>–prism [c] patterns (i.e., Type II crossed girdles). This suggests that hydrolytic weakening is not the primary factor controlling microstructures and CPO fabrics in the LKD. Ultimately, none of these scenarios can be ruled out for the LKD, but independent temperature estimates can provide a test for the first scenario: deformation temperatures increasing with depth.

Rolfo et al. (2004) concluded that the LKD rocks from the base of the metasedimentary section reached granulite facies conditions, characterized by peak temperatures of 650–700 °C. They found that metamorphic mineral growth occurred concurrently with D_2 deformation, consistent with the observations that chloritoid, garnet, and staurolite in the metasedimentary rocks grew pre-D_2 to syn-D_2, suggesting overlap between deformation and metamorphic temperatures. Kinked kyanite grains (Fig. 1.8c) and fibrolite-bearing C' shear bands (Fig. 1.10c) provide additional petrologic evidence to suggest that there was some overlap between metamorphic and deformation temperatures in the LKD. Although precise metamorphic temperature calculations are beyond the scope of this study, we suggest that temperatures from the correlative metasedimentary rocks in the adjacent Mabja-Sakya dome are appropriate proxies. Calculated temperatures ranging from ~570 ± 50 °C in the garnet zone to ~700 ± 65 °C in the sillimanite zone (Lee et al., 2004) agree with the peak temperatures indicated by Rolfo et al. (2004) for the LKD. In addition, Langille et al. (2010) correlated quartz microstructures and [c] fabric opening angles to metamorphic temperatures in the Mabja-Sakya dome to delimit deformation temperatures between 450 °C and 700 °C. These considerations are a reasonable basis for interpreting temperatures from LKD microstructures and quartz opening angles. The proposed metamorphic temperatures require that higher temperature ranges for SGR (450–550 °C) and GBM (>550 °C), as suggested by Law (2014) for Himalayan samples, should be applied to the LKD samples (Table 1.1). These alternate temperature ranges derive from along the Main Central thrust (MCT; Fig. 1.1) at the base of the GHS, but are consistent with temperatures of combined SGR + GBM (490–530 °C) and exclusive GBM (>530 °C) interpreted for samples along the STDS in the Mount Everest region (Fig. 1.1; Law et al., 2011), assuming geologic strain rates of 10^{-12}–10^{-15} s^{-1}. Because the distribution of samples with chessboard extinction is consistent with the interpreted progression in quartz microstructures toward lower structural levels, as well as with assumed metamorphic temperatures, it is also considered a valid

indicator of deformation temperatures of ~630 ± 30 °C as interpreted by Stipp et al. (2002b). Previous studies reported temperatures as low as 550 °C (e.g., Garbutt and Teyssier, 1991) and as high as 750 °C (Morgan and Law, 2004) for prism [c] slip, depending on water activity. Although water activity is not constrained for LKD samples, the presence of chessboard extinction microstructures at only the lowest structural levels suggests that it was active at or near the peak temperatures (650–700 °C) estimated by Rolfo et al. (2004), that are compatible with the value estimated by Stipp et al. (2002b). Calcite twin microstructures are harder to reconcile with deformation temperatures, but note that the structural position of the samples that contain them is consistent with the pattern noted in quartz microstructures and CPOs.

Interpreted D_2 deformation temperatures are summarized with respect to structural position in Figure 1.15. The southern domain (Fig. 1.15a) covers a much larger structural thickness (~3 km) than the northern and central domains (Fig. 1.15b), but the latter are sampled at a much higher resolution. Two samples (LK11-04 and LK11-36) that did not yield interpretable D_2 microstructure are included to define an approximate upper boundary for D_2 deformation in the northern and central domains. The lower structural limit of D_2 is the structurally deepest sample collected, so it should not be considered the true lower boundary of D_2 deformation. However, the structural intervals over which deformation temperatures are interpreted in this study yield comparable thermal gradient estimates, suggesting that they are representative of the entire D_2 field gradient. The interpreted temperature indicators are active over a range, some of which have no defined upper limit (i.e., quartz GBM and chessboard extinction), so average LKD thermal field gradients cannot be calculated, and instead reasonable minimum and maximum values are defined below and shown in Figure 1.16. In the southern domain, a minimum thermal field gradient of 100 °C/km, over a present-day structural thickness of ~3 km, is bracketed by the upper limit of sample LK-04 (300 °C) and the lower limit for sample LK-41, which, from the lower limit of the chessboard extinction temperature (630 ± 30 °C), would be 600 °C. If sample LK-04 is rejected because calcite microstructures remain questionable temperature indicators for the LKD, the minimum field gradient is instead bracketed by the upper temperature limit for sample LK-05 (550 °C; Table 1.1), which yields a much lower field gradient of 18 °C/km. For the combined northern and central domains, a minimum field gradient is bracketed by the upper limit of sample LK11-74 (530 °C; Table 1.1) and the lower limit of sample LK11-26 (600 °C), which results in a minimum thermal field

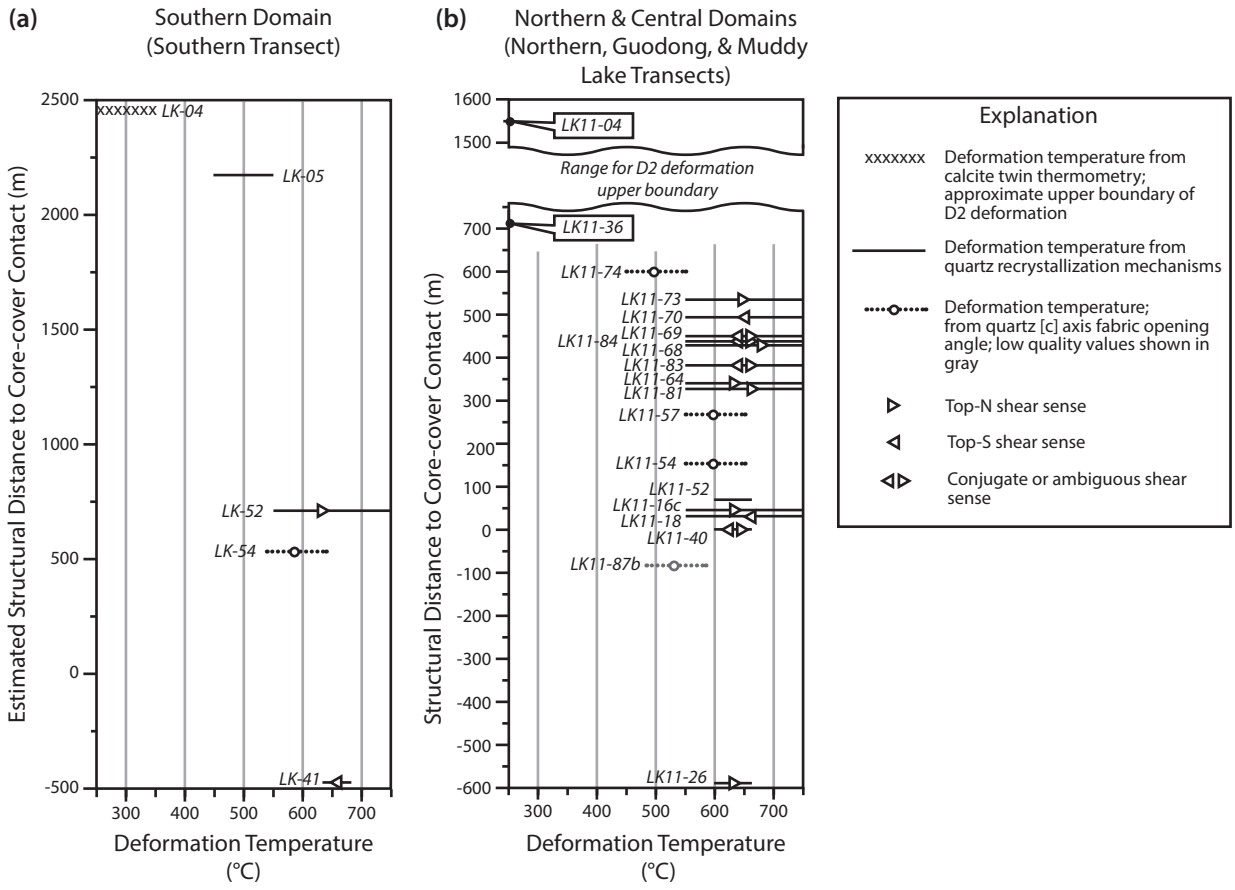


Figure 1.15. *Schematic diagram of variation in interpreted deformation temperatures and shear sense with depth. (a) In the southern domain. (b) In the northern and central domains combined. Samples listed in dialog bubbles are included to show constraints on the structural position of the upper D_2 boundary, and they do not have associated deformation temperatures.*

gradient of ~58 °C/km over 1.2 km of structural thickness. Calculation of maximum gradients is more problematic because many of the temperature indicators used do not have defined upper limits. However, a reasonable maximum D_2 thermal field gradient can be calculated along the southern transect. If sample LK-04 is rejected because the calcite twin temperatures are suspect, the lower temperature limit for the transect is set by the minimum deformation temperature for sample LK-05 (450 °C; Table 1.1). The upper temperature limit is set by the upper limit for sample LK-54 (630 °C; Fig. 1.15; Table 1.1) because a maximum temperature cannot be assigned to sample LK-41. These sample constraints yield a thermal field gradient of 90 °C/km over ~2 km. Collectively, the calculations that dismiss calcite microstructure thermometry indicate a range of 18–90 °C/km (Fig. 1.16a) for the D_2 thermal field gradient in the LKD.

Tectonic Evolution of the Lhagoi Kangri Dome

Structural, kinematic, and deformation temperature analyses in the LKD indicate that the rocks underwent a sequence of events that is generally consistent with the histories reported from six previously studied domes (Fig. 1.1; Lee et al., 2000, 2004; Aoya et al., 2006; Quigley et al., 2006; Larson et al., 2010; King et al., 2011; Gao et al., 2013).

In the LKD, D_1 is not well characterized in terms of geometry, kinematics, or major associated structures, so interpreting the origins of the mesoscale and microscale fabric in the highest structural levels investigated (S_1) is somewhat problematic. However, pervasive S_1 schistosity occurs in the upper interval of unit Ts, which is stratigraphically and structurally correlative to rocks in the adjacent Mabja-Sakya dome that record thickening by folding and thrusting following initial collision between India and Asia (Lee et al., 2004). Porphyroblast microstructures and preliminary petrology indicate that a phase of metamorphism in the LKD, defined by chloritoid and garnet growth in unit Ts and by garnet, staurolite, and kyanite growth in unit Ps, postdates D_1 deformation and could conceivably be a manifestation of regional Barrovian metamorphism (Burg et al., 1984) documented to occur near the end of crustal thickening in the Mabja-Sakya dome (e.g., Lee et al., 2004; Lee and Whitehouse, 2007; Smit et al., 2014). Timing of onset and the precise duration of LKD metamorphism are not established here, but microstructural evidence, particularly continuity between porphyroblast inclusion trails and matrix fabric, suggest that metamorphism and D_2 were at least partially coeval.

Mesoscale and microscale structures, a mix of symmetrical and asymmetrical (top-to-north-

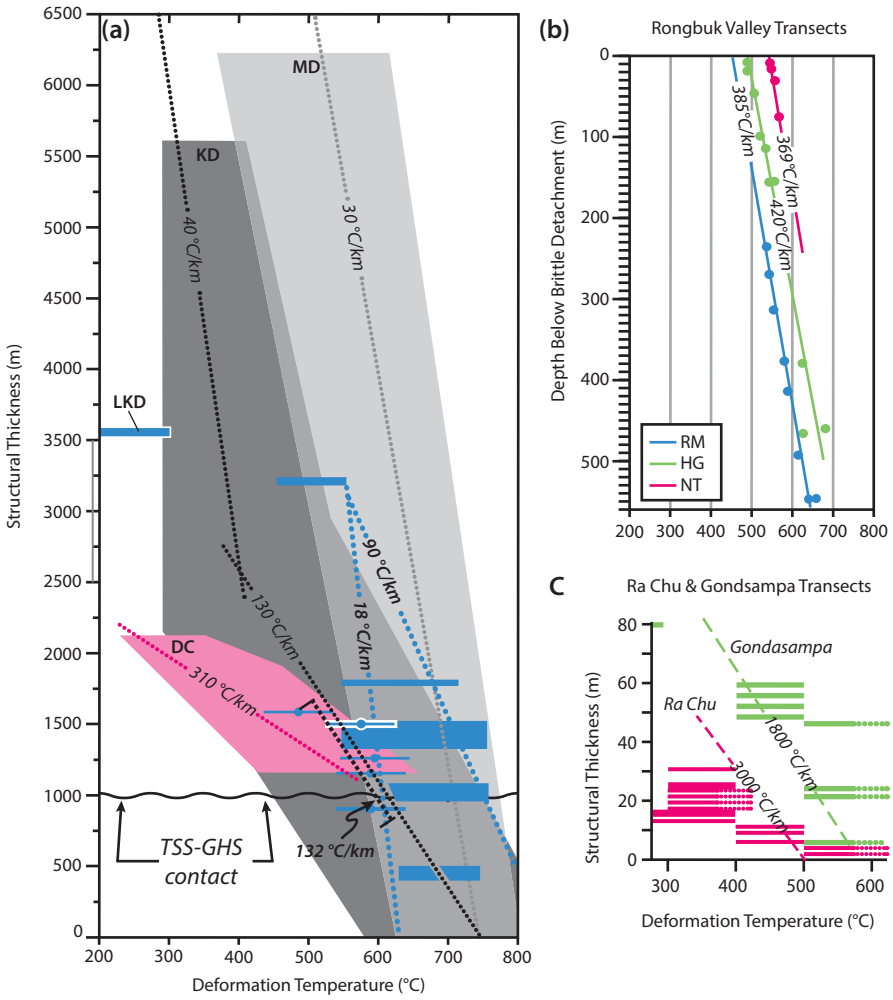


Figure 1.16. *(a) Deformation temperature versus depth profiles calculated from microstructure and quartz opening angle thermometry for the Lhagoi Kangri dome (LKD, blue bars and dots; this study), the Kangmar dome (KD, dark gray; after Wagner et al., 2010), the Mabja-Sakya dome (MD, light gray; after Langille et al., 2010), and the Dzakaa Chu transect (DC, pink; after Cottle et al., 2011). Dotted lines correspond to calculated deformation temperature gradients (color of line corresponds with data set color). Minimum and maximum gradients are shown for LKD as discussed in text. The black dashed line denotes a linear best fit to the LKD opening angles. Data for Kangmar, Mabja-Sakya, and Dzakaa Chu are simplified from the listed references, and a plot with original data can be viewed in Appendix 1.4. TSS—Tethyan sedimentary sequence; GHS—Greater Himalayan sequence. (b) Deformation temperatures and field gradients reported by Law et al. (2011) for three transects in the Rongbuk valley calculated from [c] axis fabric opening angle temperatures, shown without ±50 °C error bars to improve clarity. HG—Hermits Gorge; RM—Rongbuk Monastery; NT—Northern transect. Adapted from Law et al. (2011). (c) Deformation temperature transects along the South Tibetan detachment system at Ra Chu and Gondasampa (red and green, respectively; Jessup and Cottle, 2010).*

northeast) kinematic indicators, and penetrative rock fabrics suggesting plane strain all indicate that D_2 deformation defines a distributed ductile shear zone spanning a present-day thickness of 3 km. The present-day thickness includes at least 650 m of core orthogneiss up to the lowermost Triassic schist (Figs. 1.3 and 1.17). The original dip of the shear zone is likely modified by doming, but relatively consistent north-northeast–trending L_2 lineations in the northern, central, and eastern domains suggest that the average dip of S_2 in the northern domain (25° north-northeast) is a reasonable approximation. The top of the D_2-dominant interval is denoted by slaty S_1 cleavage in unit Ts that is progressively overprinted by S_2 crenulations down structural section. Within unit Ts but at even lower structural levels, crenulations are transposed and overprinted by penetrative S_2 schistosity and microscale S-C and C' shear bands (e.g., Figs. 1.8, 1.10, and 1.17). Pervasive L-S fabric, associated microscale C'-type shear bands, samples with symmetrical crossed-girdle quartz CPO patterns that generally indicate plane strain deformation (e.g., Lister and Hobbs, 1980; Law, 1990), and rare S_2 foliation-parallel chocolate tablet boudins that locally indicate flattening (e.g., Ghosh, 1988) may suggest that D_2 deformation involved a component of thinning across the shear zone. In particular, symmetrical top-to-north-northeast and top-to-south-southwest microscale shear sense indicators and generally symmetrical quartz CPO patterns could indicate a component of pure shear, as was previously suggested from similar observations in the Mabja-Sakya dome (Lee et al., 2004). However, in the case of the Mabja-Sakya dome, Langille et al. (2010) interpreted symmetrical shear-sense indicators to reflect either local bulk pure shear or heterogeneous strain partitioning in the presence of graphite (e.g., Selverstone, 2005), which is abundant in unit Ts in the LKD. It must then be considered that L-S fabrics are not exclusive to pure or general shear, and some LKD rocks also preserve asymmetric CPO patterns (e.g., LK-54 and LK11-54; Figs. 1.12b, 1.12d) and asymmetric boudinage (e.g., Fig. 1.5c) that suggest simple shear deformation. With careful consideration for the relative time when deformation temperatures were locked in, calculated D_2 thermal field gradients may be indicative of a bulk D_2 deformation history. At face value, the range in D_2 field gradient (18–90 °C/km) is compatible with expected continental geotherms (15–30 °C/km; e.g., England and Thompson, 1984), perhaps suggesting that there is no attenuation across the shear zone. In general, mesoscale and microscale observations, as well as interpreted deformation temperatures documented in this study, define D_2 deformation as a ductile, layer-parallel (S_2) shear zone penetrative through a current structural thickness of 3 km.

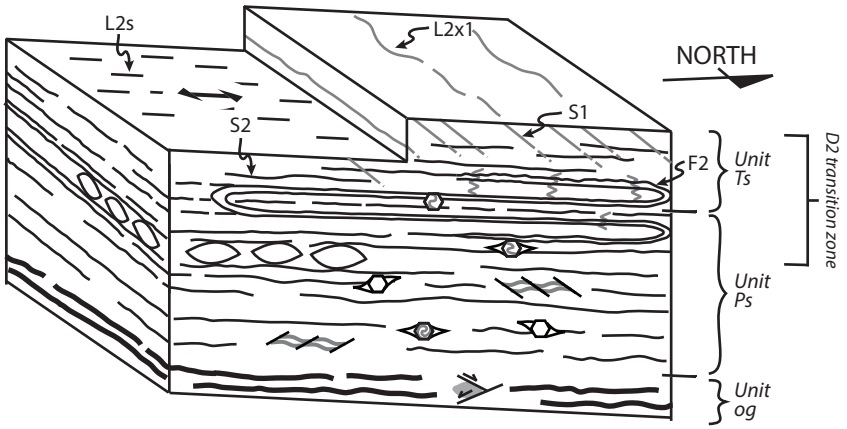


Figure 1.17. *Schematic block diagram summarizing the mesoscale and microscale structural characteristics and kinematic indicators that define the D_2 shear zone, including the interpreted D_1-D_2 transition zone. The implied viewing direction is to the west and features depicted are not to scale. Ts—Triassic siliciclastic unit; Ps—Paleozoic schist and quartzite unit; og—orthogneiss and leucogranite.*

Structures or rock fabrics that are unambiguously related to doming were not observed, but the concentric trajectory of S_2 schistosity about the dome acts as a proxy. The foliation pattern could be primary (syn-D_2) or secondary (post-D_2), and in determining possible mechanisms for doming, it must also be considered that L_2 stretching lineations have a relatively consistent north-northeast trend in the northern, central, and eastern domains. This is particularly relevant to diapirism models, wherein the host rock is expected to have concentric trajectory about the intrusion, similar to that in the LKD, but stretching lineations related to diapirism are predicted to have a radial or tangential trajectory about the dome (Dixon, 1975; Bateman, 1984). Furthermore, in pure diapirism models kinematic indicators should record orthogneiss-up (relative to the metasedimentary cover) shear sense, and LKD kinematic indicators record variable core-up and core-down shear sense, particularly in the northern and central domains (Figs. 1.3, 1.6, 1.9, 1.10, 1.14, and 1.15; Table 1.1). However, concurrent regional strain patterns or lateral crustal flow can produce concentric foliations and unidirectional stretching lineations (e.g., Brun and Pons, 1981; Whitney et al., 2004) like those documented in the LKD. With this in mind, if LKD doming occurred synchronously with D_2 deformation, the observed structural fabrics reported here would permit a model in which both D_2 deformation and diapirism contributed to dome formation. If doming postdated D_2, a diapirism contribution could be ruled out because post-D_2 diapirism would be expected to overprint D_2 fabric with radial and/or tangential lineations and a core-up shear sense, none of which were

documented in the LKD.

Contractional (Burg et al., 1984) and extensional (Chen et al., 1990) end-member models for doming are not as easily evaluated for LKD data, although at the resolution of the field study, significant regional structures that could be implicated in these end-member doming models were not observed. In the case of end-member extension models such as that proposed by Chen et al. (1990) for the Kangmar dome and a variant proposed by Quigley et al. (2006) for the Kampa dome, the contact between orthogneiss and metasedimentary cover is an extensional detachment fault. Exposure of the core-cover contact in the LKD was limited in the areas we investigated, but, in the few places that it is exposed, the contact appears to be intrusive, particularly in the central domain where unit Ps quartzite and og orthogneiss are interfingered. Models in which doming occurs by buckling (Larson et al., 2010) or uplift in response to plate flexure (King et al., 2011) also cannot be ruled out.

Comparison to Other NHGD

Deformation characterized by mesoscale and microscale structures that are similar to D_2 in the LKD is ubiquitous among previously studied NHGD, although the details vary between each. Interpretation of D_2 deformation in the LKD as a diffuse shear zone, as opposed to a localized fault or mylonite zone at the core-cover contact, is generally consistent with findings in Kangmar and Mabja-Sakya, where it is inferred that D_2 deformation is a northward distributed mid-crustal manifestation of structurally higher, localized deformation on the STDS (Lee et al., 2000, 2004; Zhang et al., 2004; King et al., 2011). Of particular note is the observation that L_2 stretching lineations on the northern flanks of both the LKD and Mabja-Sakya consistently trend north to north-northeast, indicating structural continuity, at least through D_2 time, between these domes. Results for the LKD, Mabja-Sakya, and Kangmar differ from studies in Changgo (Larson et al., 2010), Kampa (Quigley et al., 2006), and Malashan (Kawakami et al., 2007), where deformation is marked by relatively localized shearing adjacent to the core-cover contact, but is also inferred to be a manifestation of the STDS (Changgo and Kampa) or a related fault (Malashan). The STDS in the Mount Everest region dips generally north-northeast and projects beneath the LKD and Mabja-Sakya (e.g., Lee et al., 2004); this is compatible with geophysical evidence at the longitude of the Kangmar dome (Nelson et al., 1996). The structural evolution interpreted for LKD supports previous investigations in Kangmar (Lee et al.,

2000), Mabja-Sakya (Lee et al., 2004, 2006; King et al., 2011), and Changgo (Larson et al., 2010) that indicate structural continuity between the GHS and NHGD prior to exhumation. Our interpretations are particularly consistent with kinematic analyses from the Kangmar dome (Wagner et al., 2010) that indicate a shift from symmetric to asymmetric top-to-north shear sense at lower structural levels, although it is important to reiterate that kinematic indicators at discrete structural intervals within the respective D_2 shear zones may not be explicitly related to bulk D_2 strain (e.g., Langille et al., 2010).

Tectonic Implications

The following discussion is predicated upon the assumption that the D_2 deformation in the LKD correlates to D_2 events in the Mabja-Sakya and Kangmar domes, which in turn have been correlated with deformation along the STDS (e.g., Lee et al., 2000, 2004, 2006; Lee and Whitehouse, 2007). In order to place the LKD into the broader context of middle crustal evolution during the Himalayan orogeny, LKD thermal field gradients are compared to similar data sets from (1) the STDS in the Mount Everest region (Law et al., 2011), (2) the STDS north of Mount Everest (Ra Chu and Gondasampa transects; Jessup and Cottle, 2010), (3) the STDS northeast of Mount Everest (Dzakaa Chu transect; Cottle et al., 2007), (4) the Kangmar dome (Wagner et al., 2010), and (5) the Mabja-Sakya dome (Langille et al., 2010). Only temperatures interpreted from quartz and feldspar microstructures, or from quartz [c] axis fabric opening angles, are considered since these are the data sets used for the LKD. However, metamorphic temperatures are also available for the other listed locations, except Ra Chu and Gondasampa, and the spatial and temporal association between metamorphic field gradients and deformation temperature field gradients for these locations are also key to constraining their tectonic evolution (e.g., Law et al., 2011). Two fundamental structural styles are represented by the selected study areas. In the case of the LKD, Mabja-Sakya, Kangmar, and Dzakaa Chu, the shear zone is distributed and penetrative through a present-day thickness of 1 km (Fig. 1.16a). In contrast, Ra Chu, Gondasampa, and Rongbuk valley transects are characterized by a highly attenuated shear zone of GHS rocks structurally separated from overlying TSS by a discrete, layer-parallel, brittle-ductile detachment (Law et al., 2004, 2011; Jessup et al., 2006; Jessup and Cottle, 2010; Figs. 1.16b, 1.16c). Specific sources for stratigraphic position and structural thicknesses, as well as a brief explanation for how thermal gradients were derived from other sources, are given in Appendix 1.1.

The LKD deformation temperatures interpreted from microstructural analysis and quartz [c] axis opening angles suggest a thermal field gradient of 18–90 °C/km over a current structural thickness of ~3 km (Figs. 1.15–1.17). The Dzakaa Chu transect records a field gradient of 310 °C/km over 1 km structural thickness (Cottle et al., 2011), while Mabja-Sakya has an estimated thermal gradient of 30 °C/km over 6.5 km, and Kangmar records deformation temperatures that define a composite gradient of 40 °C/km in the upper ~3.5 km and 130 °C/km for the lower 2–2.5 km (Fig. 1.16a; cf. Law et al., 2011). It is interesting that a linear regression through the opening angle temperatures for the LKD (Fig. 1.16a) also suggests an average gradient of 132 °C/km at lower structural levels, although the R^2 value (0.4) is low. Law et al. (2011) calculated deformation temperature gradients of 369, 385, and 420 °C/km for three transects in the Rongbuk valley over structural thicknesses of 550 m (Fig. 1.16b). Ra Chu and Gondasampa deformation temperature data indicate thermal gradients of 1800 °C/km over <100 m (Fig. 1.16c), an order of magnitude larger than any thermal gradient estimated from the other study areas. Such high estimated field gradients are probably due to the relative scale of the two transects, but they could also reflect variation in structural style with close proximity to the brittle detachment surface (e.g., Law et al., 2011). Calcite temperatures are included for the upper part of the Ra Chu transect, but eliminating those data would actually increase the estimated thermal field gradient.

Interpretations from differences in thermal field gradients between different locations should be made cautiously given that (1) temperature-depth profiles may be linear at one scale but nonlinear at another (e.g., the significantly larger gradients associated with smaller transects in Ra Chu and Gondasampa or the apparent steepening of the Kangmar field gradient with depth), and (2), if the STDS cuts down section through the GHS, it is expected that thermal field gradients would decrease even without the influence of telescoping along the STDS (e.g., Beaumont et al., 2004; Law et al., 2011). The effect in (2) may be evident when comparing thermal field gradients from Rongbuk valley, Dzakaa Chu, the LKD, and Mabja-Sakya. Note that between these transects thermal field gradients progressively decrease from 369 °C/km in Rongbuk valley to 30 °C/km in Mabja-Sakya. An explanation for this spatial pattern must also account for when in the strain history the deformation temperatures were locked in, both within individual settings and between study areas, as well as from what structural level of the crustal deformation zone these transects derive (e.g., Langille et al., 2010; Law et al., 2011).

In the Rongbuk Valley, Ra Chu, and Gondasampa areas the deformation history is characterized

by a progression in deformation temperatures (high to low) through time, interpreted to reflect changes during exhumation, telescoping of hotter isotherms, and strain localization (e.g., Law et al., 2004, 2011; Jessup et al., 2006; Jessup and Cottle, 2010). Similarly, Cottle et al. (2011) suggested that the deformation temperature gradient in Dzakaa Chu is best explained by progressive telescoping of isotherms from hotter to cooler during exhumation, although it was not accompanied by strain localization. The studies from the Kangmar and Mabja-Sakya domes provide more reasonable end-member possibilities for when LKD temperatures were set (1) prior to or during early stages of D_2 (Kangmar dome; Wagner et al., 2010), or (2) after or during late stages of vertical thinning (the Mabja-Sakya dome; Lee et al., 2004). The low Mabja-Sakya dome thermal field gradient (30 °C/km) would be expected of late-stage D_2 deformation at a time when Lee et al. (2004) suggested that regional isotherms relaxed toward a normal geothermal gradient, whereas the Kangmar dome has deformation temperatures that overlap with peak metamorphic temperatures (Wagner et al., 2010) and a higher field gradient that is best explained by deformation temperatures locked in during relatively early D_2 deformation (Law et al., 2011). The LKD thermal field gradient (18–90 °C/km) is similar to that of the Mabja-Sakya dome and the upper part of the Kangmar dome, suggesting that the D_2 temperatures in the LKD also record late-stage deformation. This is compatible with similarities in lithology and structural fabric between the LKD and Mabja-Sakya. However, it was postulated that the LKD opening angle temperatures might reflect a higher thermal field gradient (132 °C/km) at lower structural levels. Although this higher calculated LKD gradient could be an artifact of few data points or the smaller structural thickness over which it applies, it is consistent with the composite thermal field gradient interpreted for the Kangmar dome, which would indicate that deformation temperatures from lower structural levels were locked in during early stages of D_2 and temperatures at higher structural levels were locked in during later stages of D_2. This idea is at least compatible with porphyroblast-matrix relationships suggesting that D_2 deformation occurred contemporaneously with metamorphism.

Regardless of whether the LKD field gradient is linear in the range of 18–90 °C/km or steepens to ~132 °C/km at lower structural levels, the absence of microstructural overprinting in the LKD samples has direct implications for the way in which D_2 isotherms, and thus deformation, evolved along the LKD shear zone. Similar to the interpretations made by Cottle et al. (2007) for the STDS at Dzakaa Chu, the lack of an S_2-parallel brittle detachment in the LKD suggests that D_2 deformation records early, higher

temperature stages of deformation and shear zone development that, in the Everest area, are partially overprinted by extreme telescoping along the brittle STDS (e.g., Law et al., 2004; Jessup et al., 2006). The relatively low gradients in deformation temperature across the LKD shear zone are consistent with this interpretation. If the thermal gradient steepens at lower structural levels in the LKD, some telescoping must have occurred in the shear zone. Even if a linear thermal field gradient is applied, some telescoping is implied by the minimum gradient in the northern and central domains (58 °C/km) and the maximum gradient from the southern domain (90 °C/km). Under this paradigm, the absence of low-temperature overprinting is most consistent with a model in which originally higher temperature portions of the shear zone were passively translated to higher structural levels, which could be accomplished without substantial fabric overprinting by upward migration of the upper shear zone boundary through time (e.g., Williams et al., 2006), as proposed for Rongbuk Valley and Dzakaa Chu (Cottle et al., 2011; Law et al., 2011). Another process that might be expected to result in an apparent progression from high-temperature to low-temperature microstructures within the shear zone is strain localization during exhumation, which is a characteristic of crustal-scale faults (Sibson, 1977) or, perhaps more appropriately for the Himalaya, extrusive channel flow (e.g., Grujic et al., 1996, 2002). However, these processes would be predicted to produce lower temperature fabrics that overprint higher temperature fabrics. One other possibility is simultaneous deformation across the entire shear zone. This scenario cannot be ruled out, but it is unlikely given that, if the shear zone had any original dip as assumed here, displacement would result in exhumation in which lower temperature overprint of higher temperature fabrics would be predicted. Therefore, the favored model for D_2 in the LKD is that of a zone of heterogeneous simple or general shear in which the upper boundary migrated to structurally lower levels through time.

Ultimately, the D_2 deformation temperature field gradient preserved in the LKD is a complex function of both spatial and temporal variations in middle crustal ductile deformation during early Himalayan orogenesis. The data presented for the LKD shear zone do not distinguish between gravitational collapse-driven middle crustal deformation (e.g., Burchfiel and Royden, 1985) versus channel flow–type middle crustal deformation (Beaumont et al., 2004), but they do indicate that the LKD shear zone is a prominent structure that accommodated penetrative middle crustal ductile deformation. These findings are consistent with previous studies discussed herein that suggest that STDS-related structures played a significant role in transport and exhumation of the GHS.

Conclusions

Field observations and preliminary structural and petrographic analyses in the LKD suggest that the region underwent a multistage history of deformation and metamorphism during the Himalayan orogeny, consistent with events documented in other NHGD and the GHS. The first stage (D_1), largely preserved only at higher structural levels in Triassic siliciclastic rocks, involved burial and local development of slaty cleavage. Heating of the rocks during burial triggered the onset of prograde metamorphism recorded in the lowermost unit Ts and Ps pelitic assemblages. This initial overthickening and heating sufficiently weakened the LKD rocks so that they deformed through a distributed zone of penetrative ductile shearing (D_2) that was confined to the lowermost Triassic rocks down through the core orthogneiss, a present-day structural thickness of ~3 km. A wide range of associated deformation temperatures with no evidence of lower temperature overprinting also suggests that D_2 strain was never localized. A possibly telescoped deformation temperature gradient (58–90 °C/km at high structural levels, 132 °C/km at low structural levels), as well as local indications of flattening and plane strain suggest that the D_2 shear zone was defined by heterogeneous general shear, although simple shear is not ruled out. These observations are compatible with previously documented regional strain patterns and associated tectonic models that indicate that the STDS and related middle crustal ductile shear zones accommodated displacement between the GHS and the TSS during southward migration of the GHS. The Lhagoi Kangri geologic history is similar to that of the adjacent Mabja-Sakya dome and Dzakaa Chu transect, but more LKD data are necessary to exhaustively test ideas regarding its tectonic development, specifically its metamorphic evolution, and to further define its place in the early tectonic framework of the Himalaya.

References

Aikman, A.B., Harrison, T.M., and Lin, D., 2008, Evidence for early (>44 Ma) Himalayan crustal thickening, Tethyan Himalaya, southeastern Tibet: Earth and Planetary Science Letters, v. 274, p. 14–23, doi:10.1016/j.epsl.2008.06.038.

Aoya, M., Wallis, S.R., Kawakami, T., Lee, J., Wang, Y., and Maeda, H., 2006, The Malashan gneiss dome in south Tibet: Comparative study with the Kangmar dome with special reference to kinematics of deformation and origin of associated granites, in Law, R.D., and Searle, M.P., eds., Channel flow, ductile extrusion and exhumation in continental collision zones: Geological Society of London Special Publication 268, p. 471–495, doi:10.1144/GSL.SP.2006.268.01.22.

Aoya, M., Wallis, S.R., Terada, K., Lee, J., Kawakami, T., Wang, Y., and Heizler, M., 2005, North-south extension in the Tibetan crust triggered by granite emplacement: Geology, v. 33, p. 853–856, doi:10.1130/G21806.1.

Beaumont, C., Jamieson, R.A., Nguyen, M.H., and Lee, B., 2001, Himalayan tectonics explained by extrusion of a low-viscosity crustal channel coupled to focused surface denudation: Nature, v. 414, no. 6865, p. 738–742, doi:10.1038/414738a.

Beaumont, C., Jamieson, R.A., Nguyen, M.H., and Medvedev, S., 2004, Crustal channel flows: 1. Numerical models with applications to the tectonics of the Himalayan-Tibetan orogen: Journal of Geophysical Research, v. 109, B06406, doi:10.1029/2003JB002809.

Bouchez, J.L., Mainprice, D.H., Trepied, L., and Doukhan, J.C., 1984, Secondary lineation in a high-T quartzite (Galicia, Spain): An explanation for an abnormal fabric: Journal of Structural Geology, v. 6, p. 159–165, doi:10.1016/0191-8141(84)90093-2.

Brun, J. P., and Pons, J., 1981, Strain patterns of pluton emplacement in a crust undergoing non-coaxial deformation, Sierra Morena, southern Spain: Journal of Structural Geology, v. 3, no. 3, p. 219–229, doi:10.1016/0191-8141(81)90018-3.

Burchfiel, B.C., and Royden, L.H., 1985, North-south extension within the convergent Himalayan region: Geology, v. 13, p. 679–682, doi:10.1130/0091-7613(1985)13<679:NEWTCH>2.0.CO;2.

Burchfiel, B.C., Zhiliang, C., Hodges, K.V., Yuping, L., Royden, L.H., Changrong, D., and Jiene, X., 1992, The South Tibetan detachment system, Himalayan orogen: Extension contemporaneous with and parallel to shortening in a collisional mountain belt, in Burchfiel, B.C., et al., eds., The South Tibetan detachment system, Himalayan orogen: Extension contemporaneous with and parallel to shortening in a collisional mountain belt: Geological Society of America Special Paper 269, p. 1–41, doi:10.1130/SPE269-p1.

Burg, J.P., Guiraud, M., Chen, G.M., and Li, G.C., 1984, Himalayan metamorphism and deformations in the North Himalayan Belt (southern Tibet, China): Earth and Planetary Science Letters, v. 69, p. 391–400, doi:10.1016/0012-821X(84)90197-3.

Chen, Z., Liu, Y., Hodges, K.V., Burchfiel, B.C., Royden, L.H., and Deng, C., 1990, The Kangmar Dome: A metamorphic core complex in southern Xizang (Tibet): Science, v. 250, no. 4987, p. 1552–1556, doi:10.1126/science.250.4987.1552.

Cottle, J.M., Jessup, M.J., Newell, D.L., Searle, M.P., Law, R.D., and Horstwood, M.S.A., 2007, Structural insights into the early stages of exhumation along an orogen-scale detachment: The South Tibetan Detachment System, Dzakaa Chu section, Eastern Himalaya: Journal of Structural Geology, v. 29, p. 1781–1797, doi:10.1016/j.jsg.2007.08.007.

Cottle, J.M., Waters, D.J., Riley, D., Beyssac, O., and Jessup, M.J., 2011, Metamorphic history of the South Tibetan Detachment System, Mt. Everest region, revealed by RSCM thermometry and phase equilibria modelling: Journal of Metamorphic Geology, v. 29, p. 561–582, doi:10.1111/j.1525-1314.2011.00930.x.

Debon, F., Le Fort, P., Sheppard, S.M.F., and Sonet, J., 1986, The four plutonic belts of the Transhimalaya-Himalaya: A chemical, mineralogical, isotopic, and chronological synthesis along a Tibet-Nepal section: Journal of Petrology, v. 27, p. 219–250, doi:10.1093/petrology/27.1.219.

Dixon, J.M., 1975, Finite strain and progressive deformation in models of diapiric structures: Tectonophysics, v. 28, p. 89–124, doi:10.1016/0040-1951(75)90060-8.

England, P.C., and Thompson, A.B., 1984, Pressure-temperature-time paths of regional metamorphism. 1. Heat transfer during the evolution of regions of thickened continental crust: Journal of Petrology, v. 25, p. 894–928, doi:10.1093/petrology/25.4.894.

Ferrill, D.A., Morris, A.P., Evans, M.A., Burkhard, M., Groshong, R.H., Jr., and Onasch, C.M., 2004, Calcite twin morphology: A low-temperature deformation geothermometer: Journal of Structural Geology, v. 26, p. 1521–1529, doi:10.1016/j.jsg.2003.11.028.

Fitz Gerald, J.D., and Stünitz, H., 1993, Deformation of granitoids at low metamorphic grade. I: Reactions and grain size reduction: Tectonophysics, v. 221, p. 269–297, doi:10.1016/0040-1951(93)90163-E.

Gao, L.-E., and Zeng, L., 2014, Fluxed melting of metapelite and the formation of Miocene high-CaO two-mica granites in the Malashan gneiss dome, southern Tibet: Geochimica et Cosmochimica Acta, v. 130, p. 136–155, doi:10.1016/j.gca.2014.01.003.

Gao, L., Zeng, L., Hou, K., Guo, C., Tang, S., Xie, K., Hu, G., and Wang, L., 2013, Episodic crustal anatexis and the formation of Paiku composite leucogranitic pluton in the Malashan Gneiss Dome, southern Tibet: Chinese Science Bulletin, v. 58, p. 3546–3563, doi:10.1007/s11434-013-5792-4.

Garbutt and Teyssier, 1991, Prism (c) slip in the quartzites of the Oakhurst mylonite belt, California: Journal of Structural Geology, v. 13, p. 1458–1471, doi:10.1016/0191-8141(91)90028-H,

Ghosh, S.K., 1988, Theory of chocolate tablet boudinage: Journal of Structural Geology, v. 10, p. 541–553, doi:10.1016/0191-8141(88)90022-3.

Gleason, G.C., Tullis, J., and Heidelbach, F., 1993, The role of dynamic recrystallization in the development of lattice preferred orientations in experimentally deformed quartz aggregates: Journal of Structural Geology, v. 15, p. 1145–1168, doi:10.1016/0191-8141(93)90161-3. Grujic, D., Casey, M., Davidson, C., Hollister, L.S., Kündig, R., Pavlis, T., and Schmid, S., 1996, Ductile extrusion of the Higher Himalayan Crystalline in Bhutan: Evidence from quartz microfabrics: Tectonophysics, v. 260, p. 21–43, doi:10.1016/0040-1951(96)00074-1.

Grujic, D., Hollister, L.S., and Parrish, R.R., 2002, Himalayan metamorphic sequence as an orogenic channel: Insight from Bhutan: Earth and Planetary Science Letters, v. 198, p. 177–191, doi:10.1016/S0012-821X(02)00482-X.

Harlov, D.E., 2012, The potential role of fluids during regional granulite-facies dehydration in the lower crust: Geoscience Frontiers, v. 3, p. 813–827, doi:10.1016/j.gsf.2012.03.007.

Hirth, G., and Tullis, J., 1992, Dislocation creep regimes in quartz aggregates: Journal of Structural Geology, v. 14, p. 145–159, doi:10.1016/0191-8141(92)90053-Y.

Jessup, M.J., and Cottle, J.M., 2010, Progression from south-directed extrusion to orogen-parallel extension in the southern margin of the Tibetan Plateau, Mount Everest region, Tibet: Journal of Geology, v. 118, p. 467–486, doi:10.1086/655011.

Jessup, M.J., Law, R.D., Searle, M.P., and Hubbard, M.S., 2006, Structural evolution and vor-

ticity of flow during extrusion and exhumation of the Greater Himalayan Slab, Mount Everest Massif, Tibet/Nepal: Implications for orogen-scale flow partitioning, in Law, R.D., and Searle, M.P., eds., Channel flow, ductile extrusion and exhumation in continental collision zones: Geological Society of London Special Publication 268, p. 379–413, doi:10.1144/GSL.SP.2006.268.01.18.

Jiang, D., and Williams, P.F., 2004, Reference frame, angular momentum, and porphyroblast rotation: Journal of Structural Geology, v. 26, p. 2211–2224, doi:10.1016/j.jsg.2004.06.012.

Johnson, S.E., 1999, Porphyroblast microstructures; a review of current and future trends: American Mineralogist, v. 84, p. 1711–1726, doi:10.2138/am-1999-11-1202.

Kawakami, T., Aoya, M., Wallis, S.R., Lee, J., Terada, K., Wang, Y., and Heizler, M., 2007, Contact metamorphism in the Malashan dome, North Himalayan gneiss domes, southern Tibet: An example of shallow extensional tectonics in the Tethys Himalaya: Journal of Metamorphic Geology, v. 25, p. 831–853, doi:10.1111/j.1525-1314.2007.00731.x.

Kellett, D.A., and Grujic, D., 2012, New insight into the South Tibetan detachment system: Not a single progressive deformation: Tectonics, v. 31, TC2007, doi:10.1029/2011TC002957.

King, J., Harris, N., Argles, T., Parrish, R., and Zhang, H., 2011, Contribution of crustal anatexis to the tectonic evolution of Indian crust beneath southern Tibet: Geological Society of America Bulletin, v. 123, p. 218–239, doi:10.1130/B30085.1.

Kronenberg, A.K., and Tullis, J., 1984, Flow strengths of quartz aggregates: Grain size and pressure effects due to hydrolytic weakening: Journal of Geophysical Research, v. 89, no. B6, p. 4281–4297, doi:10.1029/JB089iB06p04281.

Kruhl, J.H., 1998, Prism- and basal-plane parallel subgrain boundaries in quartz: A microstructural geothermometer: Reply: Journal of Metamorphic Geology, v. 16, p. 142–146.

Langille, J., Lee, J., Hacker, B., and Seward, G., 2010, Middle crustal ductile deformation patterns in southern Tibet: Insights from vorticity studies in Mabja Dome: Journal of Structural Geology, v. 32, p. 70–85, doi:10.1016/j.jsg.2009.08.009.

Larson, K.P., Godin, L., Davis, W.J., and Davis, D.W., 2010, Out-of-sequence deformation and expansion of the Himalayan orogenic wedge: Insight from the Changgo culmination, south central Tibet: Tectonics, v. 29, TC4013, doi:10.1029/2008TC002393.

Law, R.D., 1990, Crystallographic fabrics: A selective review of their applications to research in structural geology, in Knipe, R.J., and Rutter, E.H., eds., Deformation mechanisms, rheology and tectonics: Geological Society of London Special Publication 54, p. 335–352, doi:10.1144/GSL.SP.1990.054.01.30.

Law, R.D., 2014, Deformation thermometry based on quartz c-axis fabrics and recrystallization microstructures: A review: Journal of Structural Geology, v. 66, p. 129–161, doi:10.1016/j.jsg.2014.05.023.

Law, R.D., Searle, M.P., and Simpson, R.L., 2004, Strain, deformation temperatures and vorticity of flow at the top of the Greater Himalayan Slab, Everest Massif, Tibet: Journal of the Geological Society [London], v. 161, p. 305–320, doi:10.1144/0016-764903-047.

Law, R.D., Jessup, M.J., Searle, M.P., Francsis, M.K., Waters, D.J., and Cottle, J.M., 2011, Telescoping of isotherms beneath the South Tibetan Detachment System, Mount Everest Massif: Journal of Structural Geology, v. 33, p. 1569–1594, doi:10.1016/j.jsg.2011.09.004.

Le Fort, P., Cuney, M., Deniel, C., France-Lanord, C., Sheppard, S.M.F., Upreti, B.N., and Vidal,

P., 1987, Crustal generation of the Himalayan leucogranites: Tectonophysics, v. 134, p. 39–57, doi:10.1016/0040-1951(87)90248-4.
Lee, J., and Whitehouse, M.J., 2007, Onset of mid-crustal extensional flow in southern Tibet: Evidence from U/Pb zircon ages: Geology, v. 35, p. 45–48, doi:10.1130/G22842A.1.
Lee, J., Hacker, B., and Wang, Y., 2004, Evolution of North Himalayan gneiss domes: Structural and metamorphic studies in Mabja Dome, southern Tibet: Journal of Structural Geology, v. 26, p. 2297–2316, doi:10.1016/j.jsg.2004.02.013.
Lee, J., Hacker, B.R., Dinklage, W.S., Wang, Y., Gans, P., Calvert, A., Wan, J., Chen, W., Blythe, A.E., and McClelland, W., 2000, Evolution of the Kangmar Dome, southern Tibet: Structural, petrologic, and thermochronologic constraints: Tectonics, v. 19, p. 872–895, doi:10.1029/1999TC001147.
Lee, J., McClelland, W., Wang, Y., Blythe, A., and McWilliams, M., 2006, Oligocene–Miocene middle crustal flow in southern Tibet: Geochronology of Mabja Dome, in Law, R.D., and Searle, M.P., eds., Channel flow, ductile extrusion and exhumation in continental collision zones: Geological Society of London Special Publication 268, p. 445–469, doi:10.1144/GSL.SP.2006.268.01.21.
Lister, G.S., 1977, Discussion: Crossed-girdle c-axis fabrics in quartzites plastically deformed by plane strain and progressive simple shear: Tectonophysics, v. 39, p. 51–54, doi:10.1016/0040-1951(77)90087-7. Lister, G.S., 1981, The effect of the basal-prism mechanism switch on fabric development during plastic deformation of quartzite: Journal of Structural Geology, v. 3, p. 67–75, doi:10.1016/0191-8141(81)90057-2.
Lister, G.S., and Dornsiepen, U.F., 1982, Fabric transitions in the Saxony granulite terrain: Journal of Structural Geology, v. 4, p. 81–92, doi:10.1016/0191-8141(82)90009-8.
Lister, G.S., and Hobbs, B.E., 1980, The simulation of fabric development during plastic deformation and its application to quartzite: the influence of deformation history: Journal of Structural Geology, v. 2, p. 355–370, doi:10.1016/0191-8141(80)90023-1.
Lister, G.S., Paterson, M.S., and Hobbs, B.E., 1978, The simulation of fabric development in plastic deformation and its application to quartzite: The model: Tectonophysics, v. 45, p. 107–158, doi:10.1016/0040-1951(78)90004-5.
Liu, G., and Einsele, G., 1994, Sedimentary history of the Tethyan basin in the Tibetan Himalayas: Geologische Rundschau, v. 83, p. 32–61, doi:10.1007/BF00211893.
Mainprice, D., Bouchez, J.-L., Blumenfeld, P., and Tubià, J.M., 1986, Dominant c slip in naturally deformed quartz: Implications for dramatic plastic softening at high temperature: Geology, v. 14, p. 819–822, doi:10.1130/0091-7613(1986)14<819:DCSIND>2.0.CO;2.
Morgan, S.S., and Law, R.D., 2004, Unusual transition in quartzite dislocation creep regimes and crystal slip systems in the aureole of the Eureka Valley–Joshua Flat–Beer Creek pluton, California: A case for anhydrous conditions created by decarbonation reactions: Tectonophysics, v. 384, p. 209–231, doi:10.1016/j.tecto.2004.03.016.
Nelson, K.D., et al., 1996, Partially molten middle crust beneath southern Tibet: Synthesis of Project INDEPTH results: Science, v. 274, no. 5293, p. 1684–1688, doi:10.1126/science.274.5293.1684.
Passchier, C.W., Trouw, R.A.J., Zwart, H.J., and Vissers, R.L.M., 1992, Porphyroblast rotation: eppur si muove?: Journal of Metamorphic Geology, v. 10, p. 283–294, doi:10.1111/j.1525-1314.1992.tb00083.x.

Post, A., and Tullis, J., 1998, The rate of water penetration in experimentally deformed quartzite: Implications for hydrolytic weakening: Tectonophysics, v. 295, p. 117–137, doi:10.1016/S0040-1951(98)00145-0.

Pryer, L.L., 1993, Microstructures in feldspars from a major crustal thrust zone: The Grenville Front, Ontario, Canada: Journal of Structural Geology, v. 15, p. 21–36, doi:10.1016/0191-8141(93)90076-M.

Quigley, M., Liangjun, Y., Xiaohan, L., Wilson, C.J.L., Sandiford, M., and Phillips, D., 2006, 40Ar/39Ar thermochronology of the Kampa Dome, southern Tibet: Implications for tectonic evolution of the North Himalayan gneiss domes: Tectonophysics, v. 421, p. 269–297, doi:10.1016/j.tecto.2006.05.002.

Quigley, M.C., Liangjun, Y., Gregory, C., Corvino, A., Sandiford, M., Wilson, C.J.L., and Xiaohan, L., 2008, U-Pb SHRIMP zircon geochronology and T-t-d history of the Kampa Dome, southern Tibet: Tectonophysics, v. 446, p. 97–113, doi:10.1016/j.tecto.2007.11.004.

Rolfo, F., Lombardo, B., Musumeci, G., Pertusati, P., and Peruzzo, L., 2004, Geology and metamorphism of the Lhako Kangri metamorphic dome, south Tibet: International Geological Congress, 32nd, Florence, Italy, v. 1, p. 585.

Schärer, U., Xu, R.-H., and Allègre, C.J., 1986, U(Th)Pb systematics and ages of Himalayan leucogranites, South Tibet: Earth and Planetary Science Letters, v. 77, p. 35–48, doi:10.1016/0012-821X(86)90130-5.

Schmid, S.M., and Casey, M., 1986, Complete fabric analysis of some commonly observed quartz C-axis patterns, in Hobbs, B.E., and Heard, H.C., eds., Mineral and rock deformation: Laboratory studies: The Paterson Volume: American Geophysical Union Geophysical Monograph 36, p. 263–286, doi:10.1029/GM036p0263.

Sibson, R.H., 1977, Fault rocks and fault mechanisms: Journal of the Geological Society [London], v. 133, p. 191–213, doi:10.1144/gsjgs.133.3.0191.

Simpson, C., and Wintsch, R.P., 1989, Evidence for deformation-induced K-feldspar replacement by myrmekite: Journal of Metamorphic Geology, v. 7, p. 261–275, doi:10.1111/j.1525-1314.1989.tb00588.x.

Smit, M.A., Hacker, B.R., and Lee, J., 2014, Tibetan garnet records early Eocene initiation of thickening in the Himalaya: Geology, v. 42, p. 591–594, doi:10.1130/G35524.1.

Stipp, M., Stünitz, H., Heilbronner, R., and Schmid, S.M., 2002a, Dynamic recrystallization of quartz: Correlation between natural and experimental conditions, in De Meer, S., et al., eds., Deformation mechanisms, rheology and tectonics: Current status and future perspectives: Geological Society of London Special Publication 200, p. 171–190, doi:10.1144/GSL.SP.2001.200.01.11.

Stipp, M., Stünitz, H., Heilbronner, R., and Schmid, S.M., 2002b, The eastern Tonale fault zone: A 'natural laboratory' for crystal plastic deformation of quartz over a temperature range from 250 to 700 °C: Journal of Structural Geology, v. 24, p. 1861–1884, doi:10.1016/S0191-8141(02)00035-4.

Stipp, M., Tullis, J., and Behrens, H., 2006, Effect of water on the dislocation creep microstructure and flow stress of quartz and implications for the recrystallized grain size piezometer: Journal of Geophysical Research, v. 111, B04201, doi:10.1029/2005JB003852.

Stünitz, H., and Fitz Gerald, J.D., 1993, Deformation of granitoids at low metamorphic

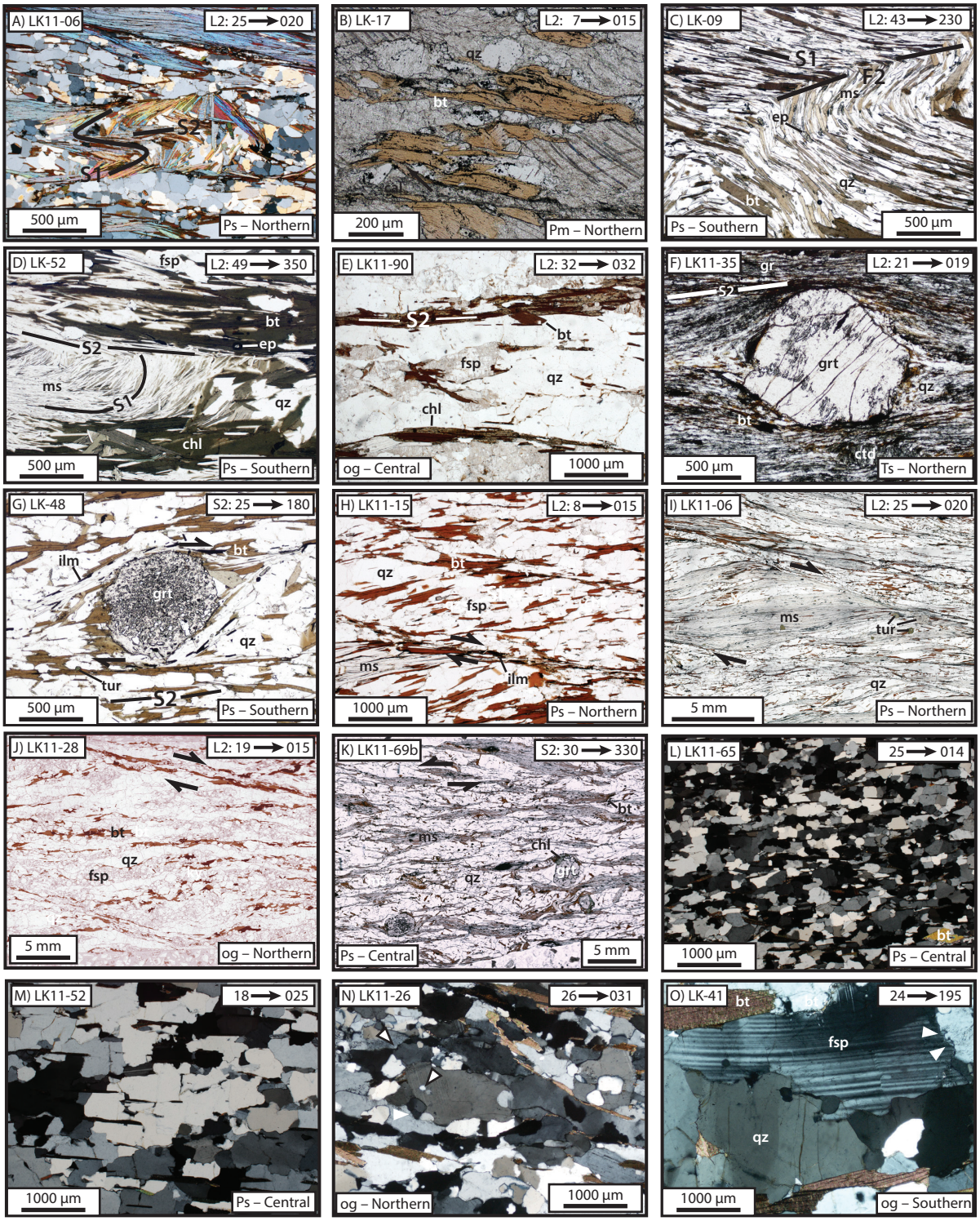
grade. II: Granular flow in albite-rich mylonites: Tectonophysics, v. 221, p. 299–324, doi:10.1016/0040-1951(93)90164-F.
Tibet Bureau of Geology and Mineral Resources, 1993, Regional geology of Xizang (Tibet) Autonomous Region: Beijing, Ministry of Geology and Mineral Resources Geological Memoir Series, scale 1:50,000.
Trouw, R.A.J., Tavares, F.M., and Robyr, M., 2008, Rotated garnets: A mechanism to explain the high frequency of inclusion trail curvature angles around 90° and 180°: Journal of Structural Geology, v. 30, p. 1024–1033, doi:10.1016/j.jsg.2008.04.011.
Tullis, J., and Yund, R.A., 1987, Transition from cataclastic flow to dislocation creep of feldspar: Mechanisms and microstructures: Geology, v. 15, p. 606–609, doi:10.1130/0091-7613(1987)15<606:TFCFTD>2.0.CO;2.
Tullis, J., and Yund, R.A., 1989, Hydrolytic weakening of quartz aggregates: The effects of water and pressure on recovery: Geophysical Research Letters, v. 16, p. 1343–1346, doi:10.1029/GL016i011p01343.
Tullis, J., and Yund, R.A., 1991, Diffusion creep in feldspar aggregates: Experimental evidence: Journal of Structural Geology, v. 13, p. 987–1000, doi:10.1016/0191-8141(91)90051-J.
Tullis, J., Christie, J.M., and Griggs, D.T., 1973, Microstructures and preferred orientations of experimentally deformed quartzites: Geological Society of America Bulletin, v. 84, p. 297–314, doi:10.1130/0016-7606(1973)84<297:MAPOOE>2.0.CO;2.
Wagner, T., Lee, J., Hacker, B.R., and Seward, G., 2010, Kinematics and vorticity in Kangmar Dome, southern Tibet: Testing midcrustal channel flow models for the Himalaya: Tectonics, v. 29, TC6011, doi:10.1029/2010TC002746.
Watts, D.R., Harris, N.B.W., and Group, T.N.G.S.W., 2005, Mapping granite and gneiss in domes along the North Himalayan antiform with ASTER SWIR band ratios: Geological Society of America Bulletin, v. 117, p. 879–886, doi:10.1130/B25592.1.
Weber, J.C., Ferrill, D.A., and Roden-Tice, M.K., 2001, Calcite and quartz microstructural geothermometry of low-grade metasedimentary rocks, Northern Range, Trinidad: Journal of Structural Geology, v. 23, p. 93–112, doi:10.1016/S0191-8141(00)00066-3.
Whitney, D.L., and Evans, B.W., 2010, Abbreviations for names of rock-forming minerals: American Mineralogist, v. 95, p. 185–187, doi:10.2138/am.2010.3371.
Whitney, D.L., Teyssier, C., and Vanderhaeghe, O., 2004, Gneiss domes and crustal flow, in Whitney, D.L., et al., eds., Gneiss domes in orogeny: Geological Society of America Special Paper 380, p. 15–33, doi:10.1130/0-8137-2380-9.15.
Williams, M.L., 1994, Sigmoidal inclusion trails, punctuated fabric development, and interactions between metamorphism and deformation: Journal of Metamorphic Geology, v. 12, p. 1–21, doi:10.1111/j.1525-1314.1994.tb00001.x.
Williams, P.F., and Jiang, D., 1999, Rotating garnets: Journal of Metamorphic Geology, v. 17, p. 367–378, doi:10.1046/j.1525-1314.1999.00203.x.
Williams, P.F., Jiang, D., and Lin, S., 2006, Interpretation of deformation fabrics of infrastructure zone rocks in the context of channel flow and other tectonic models, in Law, R.D., and Searle, M.P., eds., Channel flow, ductile extrusion and exhumation in continental collision zones: Geological Society of London Special Publication 268, p. 221–235, doi:10.1144/GSL.SP.2006.268.01.10.
Zeng, L., Liu, J., Gao, L., Xie, K., and Wen, L., 2009, Early Oligocene anatexis in the Yardoi

gneiss dome, southern Tibet and geological implications: Chinese Science Bulletin, v. 54, no. 1, p. 104–112, doi:10.1007/s11434-008-0362-x.
Zeng, L., Gao, L.-E., Xie, K., and Liu-Zeng, J., 2011, Mid-Eocene high Sr/Y granites in the Northern Himalayan Gneiss Domes: Melting thickened lower continental crust: Earth and Planetary Science Letters, v. 303, p. 251–266, doi:10.1016/j.epsl.2011.01.005.
Zeng, L., Gao, L.-E., Tang, S., Hou, K., Guo, C., and Hu, G., 2014, Eocene magmatism in the Tethyan Himalaya, southern Tibet, in Mukherjee, S., et al., eds., Tectonics of the Himalaya: Geological Society of London Special Publication 412, p. 287–316, doi:10.1144/SP412.8.
Zhang, H., Harris, N., Parrish, R., Kelley, S., Zhang, L., Rogers, N., Argles, T., and King, J., 2004, Causes and consequences of protracted melting of the mid-crust exposed in the North Himalayan antiform: Earth and Planetary Science Letters, v. 228, p. 195–212, doi:10.1016/j.epsl.2004.09.031.

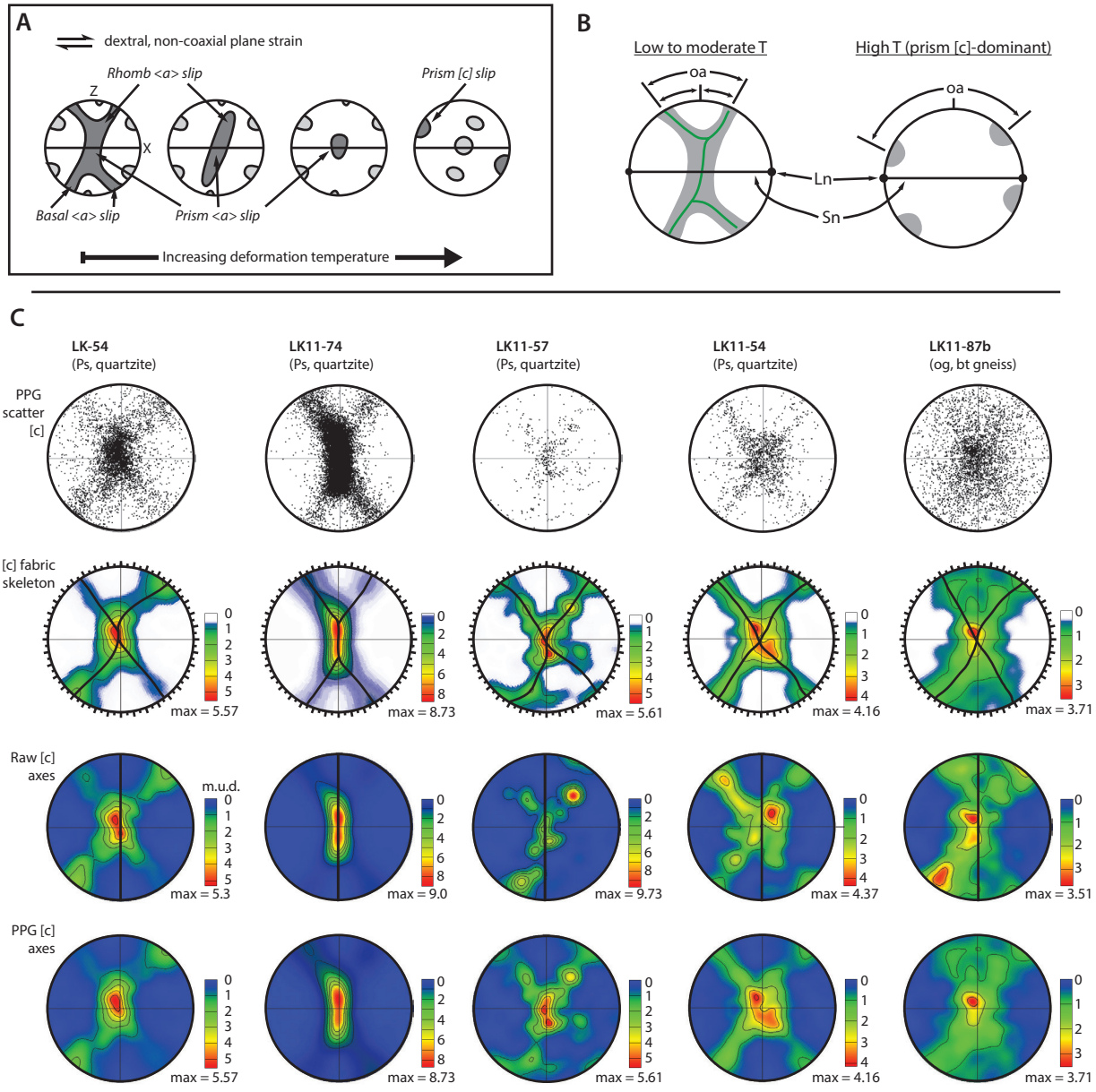
Appendix 1.1.
Derivation of Thermal Gradients from Previous Studies

Thermal gradients were calculated in previous investigations in the Rongbuk valley (Law et al., 2011, Fig. 10 therein) and Dzakaa Chu transect (Cottle et al., 2011, Fig. 8 therein). Thermal gradients for Ra Chu and Gondasampa were calculated here from data presented by Jessup and Cottle (2010, Table 1 therein). Law et al. (2011) also calculated thermal gradients in the Kangmar and Mabja-Sakya domes. In the case of the Kangmar dome, Law et al. (2011) measured thermal gradients off of a schematic cross section that contained interpreted deformation temperature isotherms (Wagner et al., 2010, Fig. 5c therein), and in the case of the Mabja-Sakya dome, they derived thermal gradients from a schematic structural section given in terms of distance below an interpreted chloritoid-in isograd (Langille et al., 2010, Fig. 9 therein). In an attempt to produce a more consistent comparison between the LKD and the other two NHGD, thermal gradients were recalculated for the Kangmar and Mabja-Sakya domes using quantitative structural depth versus deformation temperature data (Appendix 1.4) also derived from Wagner et al. (2010, Table 1 and Fig. 8 therein) and Langille et al. (2010, Table 1 and Fig. 9 therein). The results, which are reported in Figure 1.16, are not much different from those reported by Law et al. (2011), with one distinction. For the Kangmar dome, Law et al. (2011) identified a three-part thermal gradient in which the overall trend is characterized by an increase in thermal gradient with deepening structural position. In contrast, the Kangmar thermal gradient measured in this study from visual best fit in Appendix 1.4 only delineates a two-part thermal gradient. However, the relative increase of thermal gradient with lower structural level is also exhibited in our recalculated two-part thermal gradient.

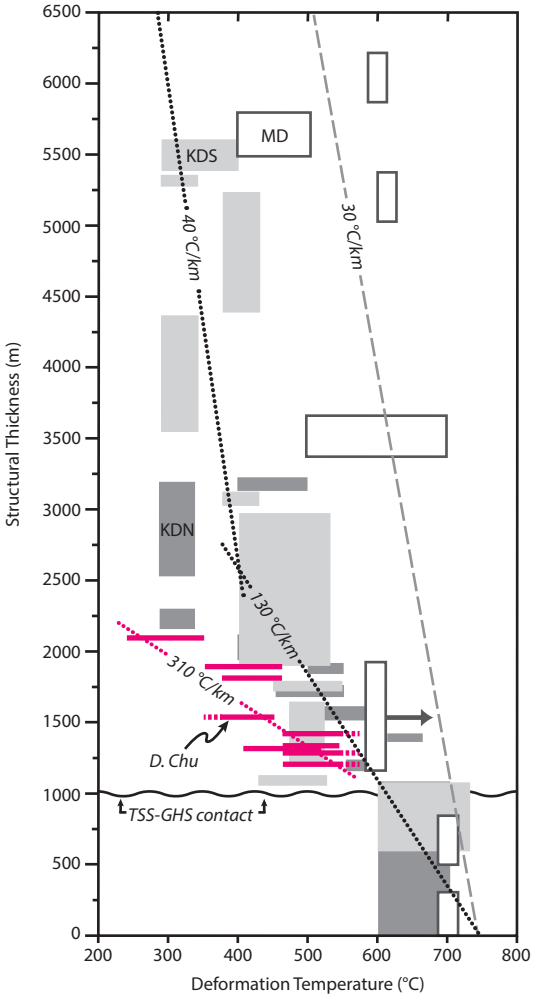
Appendix 1.2.
Additional examples of D2 microstructures and kinematic indicators.



Appendix 1.3.
Additional CPO Stereoplots Showing Derivation of Fabric Skeletons.



Appendix 1.4.
Deformation Temperature Data Used to Derive Thermal Field Gradients.



Explanation

MD — Mabja dome
Temperature indicators - quartz and feldspar microstructures plus mineral assemblages

KDS — Kangmar dome, south
Temperature indicators - matrix quartz, calcite, and feldspar microstructures, plus quartz opening angles and inferred active slip systems

KDN — Kangmar dome, north
Temperature indicators - matrix quartz, calcite, and feldspar microstructures, plus quartz opening angles and inferred active slip systems

Dzakaa Chu
Temperature indicators - matrix quartz, calcite, and feldspar microstructures, plus quartz opening angles and inferred active slip systems

CHAPTER II
BARROVIAN METAMORPHISM AND DUCTILE DEFORMATION ACCOMPANIED BY NEAR-ISOTHERMAL DECOMPRESSION IN THE LHAGOI KANGRI DOME, SOUTH CENTRAL TIBET

A version of this chapter will be submitted by Timothy Diedesch, Micah Jessup, John Cottle, and Lingsen Zeng:

Diedesch, T.F., Jessup, M.J., Cottle, J.M., Zeng, L., in prep, Barrovian metamorphism, ductile deformation, and near-isothermal decompression in the Lhagoi Kangri dome, south central Tibet: Journal of Metamorphic Geology.

My major contributions to this paper include: (1) conducting the electron microprobe and laser ablation split stream analyses, (2) constructing and calculating the pseudosection models, (3) writing the manuscript, and (4) creating the illustrations.

Abstract

The Lhagoi Kangri dome is one of a series of gneiss-cored domes that occur along the southern margin of the Tibetan Plateau. The dome exposes orthogneiss separated from overlying amphibolite facies to unmetamorphosed sedimentary rocks by a nonconformity and intruded by leucogranite dikes. At the lowest structural levels exposed a distributed, ≥ 2.5 km-thick shear zone is characterized by a mylonitic foliation and gently plunging lineation in the orthogneiss and high grade metasedimentary rocks. The penetrative L-S fabric overprints earlier ductile fabric development associated with burial and Barrovian metamorphism, and the shear zone contains both top-to-north and top-to-south shear sense indicators throughout, although top-to-north shear dominates at the lowest structural levels of the metasedimentary rocks. Thermobarometry, forward modeling of phase equilibria, and in-situ monazite petrochronology constrain the timing and conditions of metamorphism and ductile deformation associated with the shear zone. Garnet-zone rocks reached peak metamorphic conditions during Barrovian-style metamorphism of 550–570 °C and 6–7 kbar, while staurolite-kyanite zone rocks reached peak Barrovian conditions of 640–660 °C and 8–11 kbar. Garnet growth in the staurolite-kyanite zone rocks began at c. 45 Ma, and its subsequent breakdown to form Y + HREE enriched monazite 40–34 Ma brackets timing of peak metamorphism. Ductile deformation began contemporaneously with peak metamorphism as indicated by microstructural observations and 36–24 Ma, fabric-parallel monazite. The ductile deformation was also accompanied by near-isothermal decompression to form cordierite + biotite ± sillimanite assemblages and quartz-cordierite ssymplectite on garnet. The data presented here record early crustal thickening (c. 45 Ma) that began soon after collision of India with Asia and a nearly continuous record of Eocene (c. 40 Ma) to late Oligocene (c. 24 Ma) protracted high temperatures and

ductile deformation that is generally masked by monazite recrystallization during anatexis in other north Himalayan gneiss domes. These new data reinforce previous studies that indicate the middle crust of the Himalaya and southern Tibet remained at high temperatures for sufficiently long to induce weakening that could drive horizontal crustal flow.

Introduction

North Himalayan gneiss domes (NHGD) in southern Tibet (Fig. 2.1) delineate exposures of Himalayan middle crust deformed and exhumed in response to collision between India and Asia (e.g., Nelson et al., 1996; Harrison et al., 1997; Beaumont et al., 2004) beginning 55–50 Ma (e.g., Najman et al., 2010 ; Smit et al., 2014). The gneiss-cored domes are characterized by medium- to high-grade metasedimentary rocks that commonly define a Barrovian sequence concentric about the dome (Burg et al., 1984; Lee et al., 2000). Lu-Hf garnet ages date prograde metamorphism 54–49 Ma for the Mabja-Sakya and Kangmar domes (Smit et al., 2014). In previously studied NHGD, this early metamorphic record is ubiquitously modified by subsequent deformation, magmatism, and exhumation during the Oligocene–Miocene (e.g., Lee et al., 2000; Lee et al., 2004; Zhang et al., 2004; Aoya et al., 2005; Lee et al., 2006; Quigley et al., 2006; Kawakami et al., 2007; Lee and Whitehouse, 2007; Larson et al., 2010; Gao et al., 2013; Stearns et al., 2013). The youngest events recorded in the NHGD are broadly correlative, in timing and style, to extrusion of the Greater Himalayan Sequence (GHS), the lithotectonic unit representing the Himalayan high grade core, further south along the crest of the Himalaya (e.g., Lee and Whitehouse, 2007; Jessup et al., 2008; Chambers et al., 2009; Cottle et al., 2009). Models for formation and exhumation of the NHGD often invoke south-directed mid-crustal flow combined with north-directed underthrusting or focused upper crustal extension (e.g., Lee et al., 2000; Beaumont et al., 2004; Lee et al., 2004). Other models, or components of the south-directed extrusion models, are diapirism of lower crustal melt (Le Fort et al., 1987), thrust duplexing (Burg et al., 1984), and out-of-sequence thrusting (e.g., Lee et al., 2000; Larson et al., 2010). In addition to documenting metamorphism, deformation, and magmatism, constraints on the timing of these processes, particularly with respect to one another, is crucial for identifying the mechanisms that lead up to and drove middle crustal flow and exhumation. Although extensive work has already been done on piecing together P-T-t-D paths for GHS

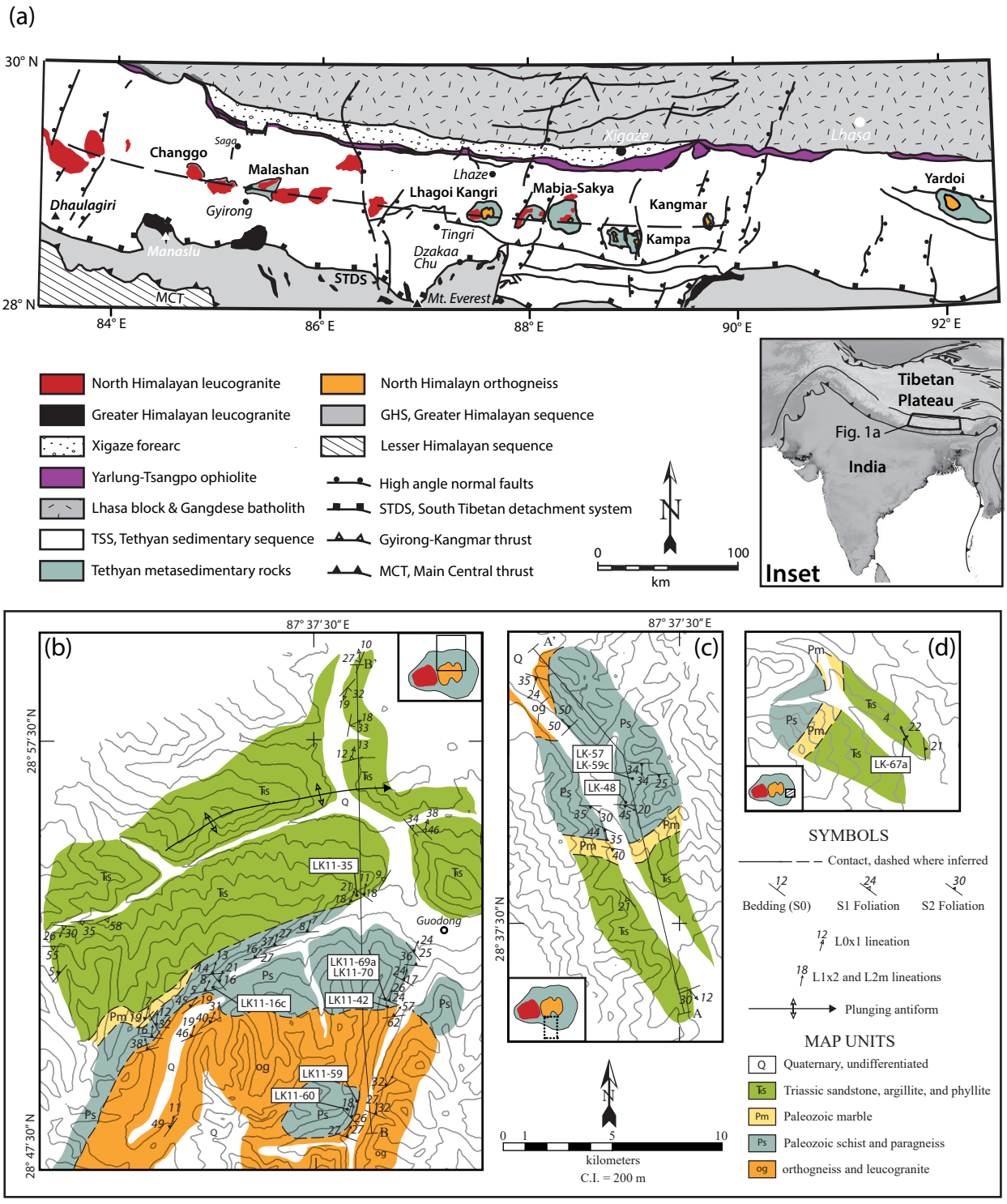


Figure 2.1. *(a) Simplified tectonic map of south-central Tibet showing the location of Lhagoi Kangri dome along with other previously studied gneiss domes. Modified from Lee et al. (2004) and Larson et al. (2010). (b–d) Geologic maps of portions of Lhagoi Kangri dome. The extent of Lhagoi Kangri dome covered by each map is shown by the diagonal-ruled boxes in the insets. White boxes on maps show locations of samples discussed in the text. Cross section lines BB' in (b) and AA' in (c) are shown in Figure 2.2a.*

exposures, fewer studies exist for the NHGD.

Of ≥ 15 NHGD identified (e.g., Watts et al., 2005), seven have been studied in detail: Changgo, Malashan, Lhagoi Kangri, Mabja-Sakya, Kampa, Kangmar, and Yardoi (Fig. 2.1). Most Oligocene–Miocene ages in the NHGD are derived from zircon in granites (e.g., Larson et al., 2010; Aoya et al., 2005; Lee et al., 2000, 2006) or migmatites (e.g., Zhang et al., 2004; King et al., 2007; Lee and Whitehouse, 2007; Gao et al., 2013), which are used to constrain age/duration of deformation and age/duration of anatexis, respectively. In Kangmar dome, Burg et al. (1984) first identified two main phases of ductile deformation (D_1 and D_2), as well as a prograde P-T path that terminated at some time between D_1 and D_2, which the authors suggested was recorded by biotite K/Ar ages of 40–20 Ma. Refined microstructural analysis by Lee et al. (2000) led to their interpretation that peak metamorphism occurred simultaneously with the onset of D_2 in Kangmar. For the Mabja-Sakya dome, Lee et al. (2004) reported similar observations of two major ductile deformation events punctuated by peak Barrovian metamorphism at the onset of D_2. Migmatite gneiss from the Mabja-Sakya dome yields a zircon U-Pb age of 35.0 ± 0.8 Ma that is interpreted as the peak of metamorphism and the onset of D_2 (Lee and Whitehouse, 2007) Granite ages of 14.2 ± 0.2 Ma and 14.5 ± 0.1 Ma (Lee et al., 2006) from Mabja-Sakya dome are interpreted to constrain the duration of D_2 deformation. Coupled U/Th-Pb values and Y + REE abundances of monazite in metapelitic rocks from Kangmar and Mabja-Sakya demonstrate that monazite crystallized nearly continuously from 29–14 Ma (Stearns et al., 2013). The authors interpreted compositional monazite domains to record Oligocene growth in the presence of garnet and Miocene growth during garnet breakdown, such that the age range reported effectively spans the end of Barrovian metamorphism (c. 20 Ma) and the onset of D_2 ductile deformation. Based on Lu-Hf garnet geochronology and garnet zoning patterns record prograde garnet growth in the Kangmar and Mabja-Sakya domes as early as 54.3 ± 0.6 Ma and younger, c. 48 Ma, garnet ages record recrystallization, possibly at the onset of D_2 deformation (Smit et al., 2014).

The present study reports new P-T estimates, pseudosection modeling results, and in-situ monazite petrochronology, that together constrain the evolution of NHGD-hosted Himalayan middle crustal rocks from the Lhagoi Kangri gneiss dome (LKD). Results from the LKD indicate that there are key differences to the adjacent Mabja-Sakya dome and exposures of the upper GHS, particularly in timing of mineral growth. Monazite petrochronology highlights differences compared to the Mabja-

Sakya dome, as well as to exposures of the upper GHS, in the interpreted timing of peak pressures, timing and duration of peak thermal conditions, and onset of D_2 deformation. In particular, the LKD has an older more protracted record of monazite (re)crystallization that, when considered alongside phase equilibria modeling and previous microstructural analyses, suggests that garnet recrystallization, at least in the LKD if not other NHGD, was episodic as a function of both prograde metamorphic reactions and ductile deformation under high temperatures for a protracted period lasting c. 40 Ma to at least c. 24 Ma . Collectively, these new results constrain a phase of the thermomechanical evolution of the middle crust that is not preserved in other study areas.

Geologic Setting

The Lhagoi Kangri dome exposes metamorphosed middle-crustal rocks over a 20 x 40-km elliptical area in southern Tibet (Fig. 2.1). It is located approximately midway between two major Himalayan tectonic boundaries: the Indus-Tsangpo suture zone to the north and the South Tibetan detachment system (STDS) to the south. The Indus-Tsangpo suture separates rocks of Laurasian affinity to the north from rocks of Indian and affinity to the south, and is generally regarded as the collision zone between India and Asia (Molnar and Tapponnier, 1977). The STDS, a low-angle, arc-parallel, normal fault system, juxtaposes unmetamorphosed rocks of the Tethyan sedimentary series (TSS) over the GHS (Fig. 2.1) (e.g., Burchfiel et al., 1992). Previous studies in southern Tibet indicate a correlation between rocks and structures in the NHGD and the GHS (e.g., Nelson et al., 1996; Lee et al., 2006; Lee and Whitehouse, 2007), and previous investigations identify major structures that are considered either down-dip projections of the STDS or correlative with the STDS (e.g., Lee et al., 2000; Lee et al., 2004; Quigley et al., 2006; Larson et al., 2010; Diedesch et al., 2016).

Among six previously studied north Himalayan gneiss domes, a generalized stratigraphic framework and structural chronology are shared between them (e.g., Burg et al., 1984). The cores of the Kangmar and Kampa domes consist of Neoproterozoic–Cambrian orthogneiss (Schärer et al., 1986; Lee et al., 2000; Quigley et al., 2008), whereas the cores of the Changgo and Malashan domes consist of Eocene–Miocene granite, and the Lhagoi Kangri, Mabja-Sakya, and Yardoi domes contain both orthogneiss and granite (e.g., Lee et al., 2004; Rolfo et al., 2004; Zeng et al., 2009). Domes with

orthogneiss cores are overlain by metasedimentary rocks that generally decrease in metamorphic grade up structural section, whereas domes cored by Eocene–Miocene granite intrude the metasedimentary rocks above them. The nature of the contact between core and mantling rocks varies from dome to dome with some domes containing a discrete, layer-parallel detachment (e.g., Chen et al., 1990; Quigley et al., 2006) while others preserve broad zones of distributed ductile deformation (e.g., Lee et al., 2004; Diedesch et al., 2016). Despite differences in structural style, however, all previously investigated domes record evidence for two distinct deformation events: (1) north-south contraction, D_1, and (2) younger ductile deformation characterized by sub-vertical thinning and sub-horizontal stretching, D_2 (e.g., Lee et al., 2000).

Lhagoi Kangri Dome

Lhagoi Kangri dome consists of Paleozoic orthogneiss separated from overlying Paleozoic metasedimentary rocks by an originally intrusive contact with high structural relief (Figs 2.1b–2.1d; Diedesch et al., 2016). Overlying the Paleozoic metasedimentary rocks is a Triassic siliciclastic unit (Ts) that progresses from garnet-bearing to weakly metamorphosed toward higher structural levels so that the whole package of rocks, from orthogneiss to Ts, decreases in metamorphic grade higher structural levels (Figs 2.1b–2.1d, 2.2a). Previous field investigations in Lhagoi Kangri identified two main deformation events that are equivalent to the D_1 and D_2 events described above for other domes (Rolfo et al., 2004; Diedesch et al., 2016). D_1-related structures are limited to discrete cleavage (S_1) that is subparallel to original compositional layering (Diedesch et al., 2016, Fig. 2.2b), but Rolfo et al. (2004) also identified F_1 folds with northwest-striking axial surfaces. D_1 structures are progressively overprinted down structural section by increasingly pervasive D_2 transposition. The progressive transposition is defined by a transition in S_2 fabric from crenulation cleavage at shallow structural levels (Fig. 2.2b) to mylonitic foliation at deeper structural levels (Figs 2.2c and 2.2d). The base of the transition zone down to the contact between orthogneiss and schist defines ~2.5 km of structural thickness, and the D_2 shear fabric continues to at least 600 m below the core-cover contact for a total of ≥ 3 km of distributed D_2 shear. On the north, east, and south sides of the dome, S_2 dips radially outward from the center indicating that doming took place syn- to post-D_2, while associated mineral stretching lineations (L_2) trend consistently NNE-SSW on all three sides. Both Rolfo et al. (2004) and Diedesch et al. (2016) reported mixed top-SSW and -NNE shear sense

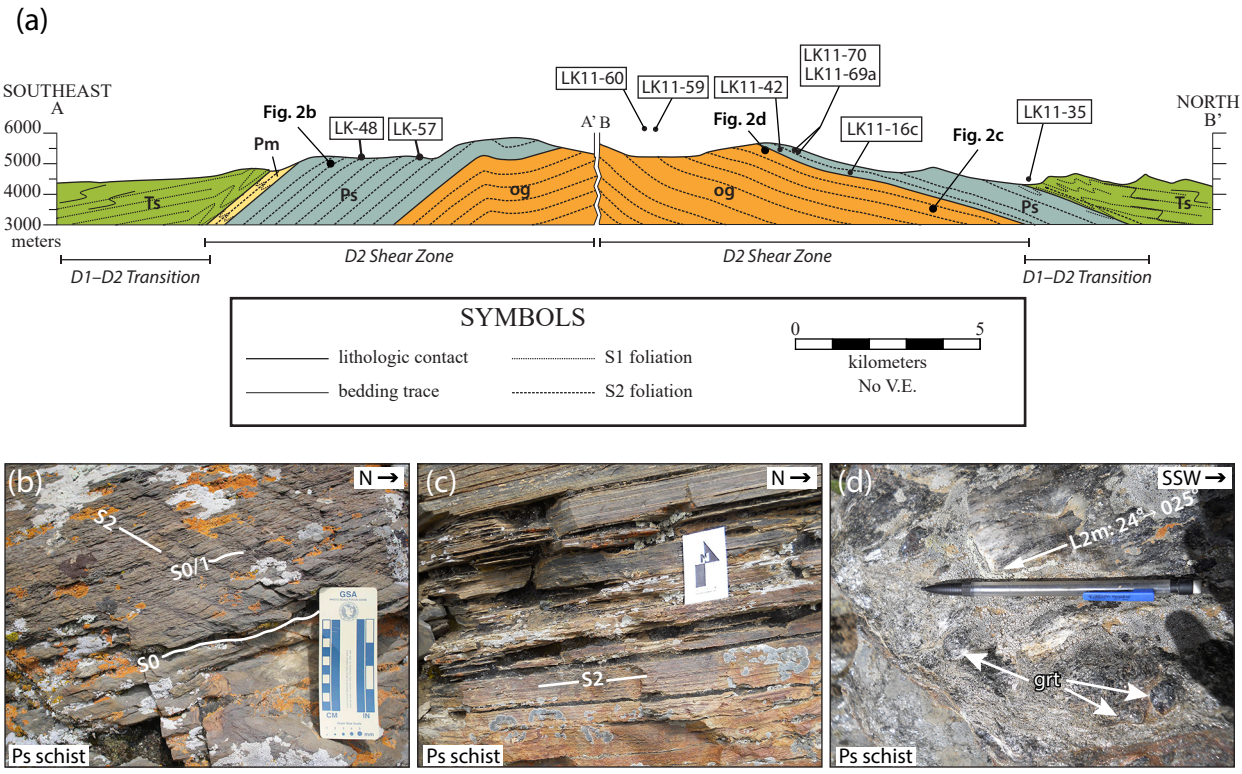


Figure 2.2. *(a) Composite south to north cross section through Lhagoi Kangri dome showing structural fabrics and transitions described in text. Boxed labels denote locations of samples discussed in the text with the exception of sample LK-59c, which derives from the east side of the dome and does not project into the view of the cross section. (b–d) Outcrop photos showing the progressive transposition of fabric with decreasing structural position that defines the D_2 distributed shear zone in the LKD.*

associated with D_2 indicating a component of coaxial shortening across the shear zone.

Metamorphic grade generally increases with structural depth in the LKD. Rolfo et al. (2004) documented progressive prograde index minerals: muscovite, chloritoid, biotite, and garnet. New field and microscale observations suggest this list should include staurolite, kyanite, and possibly sillimanite. The LKD core contains kyanite-bearing orthogneiss with cordierite overgrowths as well as garnet + orthopyroxene coronas on ilmenite interpreted to record early granulite facies metamorphism (peak T at 650–700 °C and P of 7–8 kbar) overprinted by decompression to cordierite-stable conditions (Rolfo et al., 2004).

Summary of Petrographic Analyses

Eleven pelitic schist and gneiss samples with garnet-bearing mineral assemblages were targeted for thermobarometric analysis, and a subset of these were chosen for pseudosection modeling and in-situ monazite geochronology. Of the eleven samples selected for this study, two graphitic schist samples were chosen from the structurally highest unit (Ts, samples LK11-35 and LK-67a; Fig. 2.3), while the rest of the samples derive from the underlying unit Ps and comprise six aluminous schist samples (LK-48, LK-57, LK-59c, LK11-70, LK11-69a, and LK11-60; Fig. 2.4) and three pelitic gneiss samples (LK11-59, LK11-42, and LK11-16c; Fig. 2.5). All of the samples are from D_2-dominant structural levels, and most samples that are oriented perpendicular to S_2 foliation and parallel to L_2 lineation exhibit kinematic indicators such as porphyroblast strain shadows, white mica (± biotite) fish, or C'-type shear bands. Below is a summary of petrographic observations arranged by rock unit from high to low structural level. Petrographic descriptions are given in more detail for all samples in Appendix 2.1.

Unit Ts Schist

Unit Ts samples are graphitic schists that contain garnet ± chloritoid porphyroblasts. Samples contain a mylonitic S_2 foliation (variable attitude around the dome perimeter; Figs 2.1b–2.1d) and a weak L_2 lineation that trends approximately north to north-northeast on three sides of the dome; Figs 2.1b–2.1d, 2.3a, 2.3b). L_2 lineations in unit Ts are defined by aligned chlorite + white mica and elongate quartz aggregates, while S_2 fabric is defined by intercalated fine- and coarse-grained domains that are dominated, respectively, by graphite and quartz. Ilmenite is also common in unit Ts samples and is

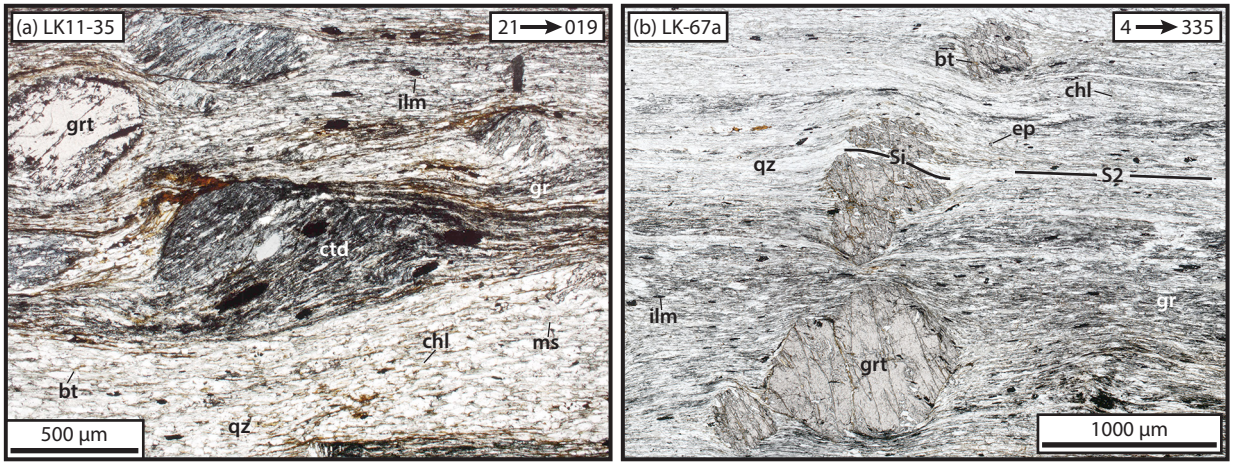


Figure 2.3. *Representative photomicrographs of the unit Ts schist samples analyzed in this study. (a) Graphitic garnet-chloritoid schist from the northern side of the dome (Fig. 2.1b). Note the inclusion trails in porphyroblasts are continuous with the external fabric. (b) Graphitic garnet schist from the eastern portion of the dome (Fig. 2.1d). Note that inclusion trails (Si) in garnet porphyroblasts are continuous with the matrix fabric. Mineral abbreviations after Whitney and Evans (2010).*

typically aligned parallel to the main foliation. Garnet and chloritoid porphyroblasts are more common in the graphitic intervals, whereas the strain shadows surrounding the porphyroblasts consist predominantly of coarser quartz + biotite ± ilmenite. Despite the textural differences, strain shadows and strain caps mantling unit Ts porphyroblasts are compositionally indistinct from the matrix. Garnet porphyroblasts are subhedral to euhedral . Where present, inclusions in garnet commonly form sigmoidal trails continuous with matrix S_2 fabric and consist of quartz ± biotite ± chlorite ± ilmenite (Fig. 2.3b; Diedesch et al., 2016). Chloritoid porphyroblasts are typically anhedral to subhedral and poikiloblastic. Like garnet, the most common inclusion phases in chloritoid are quartz and ilmenite with minor chlorite and biotite. Accessory clinozoisite occurs in the matrix, and less commonly as inclusions in garnet porphyroblasts. Porphyroblasts exhibit both top-to-north to -north-northeast and top-to-south to -south-southwest shear sense indicators, representative of the overall symmetrical shear sense previously reported at this structural level in the dome (Diedesch et al., 2016).

Unit Ps Schist

Unit Ps schist is characterized by matrix assemblages of biotite + white mica + quartz ± chlorite ± plagioclase and garnet ± biotite ± staurolite ± kyanite ± plagioclase ± fibrolite ± cordierite

porphyroblasts (Fig. 2.4). Matrix fabric in unit Ps is variable throughout the structural thickness, but S_2 predominantly consists of aligned white mica and biotite laths interspersed with quartz and plagioclase (e.g., Figs 2.4b–2.4e). Most unit Ps samples contain small, discontinuous C'-type shear bands or white mica fish. These features, along with porphyroblast strain shadows, collectively define symmetric top-to-south to top-to-south-southwest and top-to-north to top-to-north-northeast shear sense over most of the structural thickness of the unit, although shear sense is dominantly top-to-north-northeast at the lowest structural levels (Figs 2.4a, 2.4d–e; Diedesch et al., 2016).

In garnet-zone samples (e.g., LK-48; Fig. 2.4a), S_2 matrix consists of ilmenite, tourmaline, and apatite as minor phases, and in a few samples epidote grains are included in biotite or white mica laths. Allanite is also a common accessory phase. Garnet porphyroblasts are relatively small (≤ 400 μm), subhedral to anhedral, poikiloblastic, and commonly mantled by chlorite + white mica ± biotite. Where present, strain shadows on garnet porphyroblasts contain a similar assemblage of chlorite + white mica + quartz ± biotite. Garnet contain randomly oriented or sigmoidal inclusion trails that are defined by quartz + ilmenite + apatite ± biotite ± epidote. In many cases the inclusion trails are continuous with the matrix foliation.

Staurolite-zone samples (Figs 2.4b, 2.4c) contain the matrix assemblage quartz + plagioclase + white mica + biotite + ilmenite ± chlorite ± epidote. Generally, both garnet and staurolite porphyroblasts have inclusion-rich cores and inclusion-poor mantles. Some garnet porphyroblasts contain thin rims of chlorite, and most exhibit strain shadows of variable composition, with quartz + biotite ± chlorite being the most common assemblage. Inclusions in garnet are most commonly quartz, plagioclase, apatite, and ilmenite ± tourmaline ± epidote. Garnet porphyroblasts from the staurolite zone are typically larger (500–1000 μm; Figs 2.4b and 2.4c) than those in the garnet zone, while staurolite porphyroblasts range in size from ≤ 300 μm (Fig. 2.4b) to 500–1000 μm (Fig. 2.4c).

Kyanite-zone schist (Figs 2.4d and 2.4e) samples are characterized by the assemblage garnet + kyanite + quartz + white mica + plagioclase + biotite + ilmenite ± staurolite ± chlorite ± tourmaline. In kyanite-zone samples, staurolite is present in the matrix as well as within garnet, and in most cases exhibits inclusion-rich cores and inclusion-poor mantles. Kyanite porphyroblasts are typically subhedral–euhedral, and exhibit variable orientations with respect to the host foliation. In most cases the matrix fabric is not deflected around kyanite porphyroblasts. Garnet porphyroblasts from kyanite-zone schist are

Figure 2.4. *Photomicrographs of unit Ps schist samples. (a) Garnet-biotite schist from the southern portion of the dome. Note the shear sense indicated by C' shear bands. (b, c) Garnet-staurolite schist from the southern portion of the dome. Both samples are unoriented. (d) Garnet-kyanite schist from the central portion of the dome. Note the inclusion trail (Si) in at least one garnet porphyroblast in the sample. A large plagioclase porphyroblast that contains kyanite and staurolite inclusions is outlined in black in the lower portion of the image. (e) Garnet-biotite schist from the central portion of the dome. Black arrows show top-left shear sense indicated by white mica fish. (f) Garnet-cordierite-biotite schist from the central portion of the dome. Garnet porphyroblasts are partially replaced by cordierite + biotite + ilmenite + plagioclase + quartz. The cordierite porphyroblast in the upper left contains inclusions of biotite, quartz, and fibrolite. The dark outlined grain along the bottom edge of the cordierite porphyroblast is an optically distinct cordierite grain.*

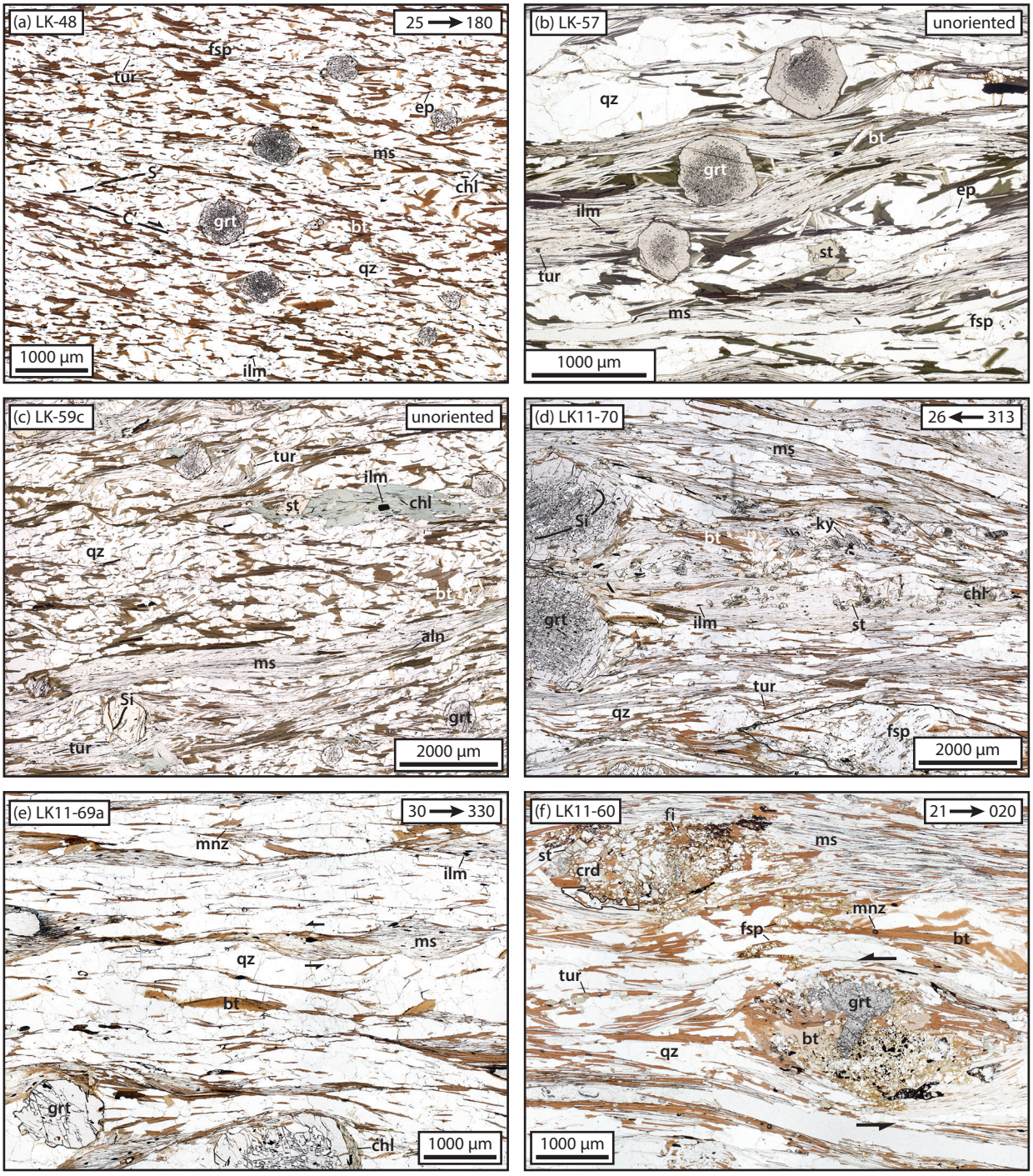


Figure 2.4. Continued.

typically large (>> 1 mm), euhedral, and contain sigmoidal or spiral inclusion trails defined by aligned quartz + apatite + ilmenite + tourmaline ± kyanite ± staurolite ± monazite ± allanite (e.g., Fig. 2.4d).

Sillimanite-zone schists are characterized by fibrolite intergrown with biotite, muscovite, or plagioclase (e.g., Fig. 2.4f). Garnet porphyroblasts in sillimanite-bearing samples are poikiloblastic and show textural evidence of resorption and replacement by quartz + cordierite + biotite ± sillimanite. Inclusions in garnet consist of randomly oriented quartz, staurolite and muscovite. Matrix phases consist of quartz with S_2-parallel plagioclase + white mica + biotite + ilmenite ± kyanite ± monazite. Cordierite porphyroblasts are anhedral, and host randomly oriented biotite with symplectic quartz intergrowths and radiating clusters of fibrolite, white mica, tourmaline, and staurolite.

Unit Ps Paragneiss

Paragneiss occurs at the deepest structural levels within unit Ps, and mineral assemblages and rock fabrics in representative samples are similar to those of the overlying schist. Matrix fabric in the paragneiss consists of spaced S_2 foliation defined by aligned biotite + white mica + ilmenite ± kyanite ± staurolite intercalated with flattened plagioclase and quartz (Fig. 2.5). The foliation is commonly broken up by discrete C' shear bands emphasized by concentrations of white mica or fibrolite that define overall symmetric top-to-north to top-to-north-northeast and top-to-south to top-to-south-southwest shear sense. Garnet porphyroblasts are typically large (>2 mm) and poikiloblastic. Inclusion patterns in garnet range from spiral or sigmoidal (Figs 2.5a and 2.5b) to random (Fig. 2.5c), with inclusions consisting of quartz + plagioclase + ilmenite + apatite ± white mica ± biotite ± staurolite ± kyanite ± epidote. Kyanite and staurolite porphyroblasts are anhedral to subhedral, and are typically aligned with, and concentrated along, S_2 surfaces (e.g., Figs 2.5a and 2.5b). Staurolite exhibits textural evidence for replacement by kyanite and biotite. In some samples, kyanite and garnet porphyroblasts are enclosed by cordierite mantles. In addition to the presence of fibrolite along C' shear bands, it also forms masses that replace S_2-parallel micas or plagioclase in the matrix as well as radiating fringes on garnet, typically along with biotite + quartz ± cordierite.

Figure 2.5. *Photomicrographs of the unit Ps paragneiss samples. (a) Garnet-kyanite paragneiss from the central portion of the dome (Fig. 1b). Note the linear inclusion trail in the garnet at the bottom right of the image. Cordierite forms nearly continuous haloes around most of the kyanite grains shown. (b) Garnet-staurolite-kyanite paragneiss from the central portion of the dome. The corner of a large garnet porphyroblast is outlined in black in the lower left. Yellowish inclusions in the garnet are staurolite grains. (c) Garnet-biotite paragneiss from the northern portion of the dome (Fig. 1b). Bold black arrows show sense of shear indicated by the tails of the garnet. Note the pronounced reaction rim along the bottom edge of the garnet grain. Dashed lines with arrows in the matrix delineate discrete C' shear bands with the same sense of shear as derived from the strain shadows. Mineral abbreviations in all photomicrographs after Whitney and Evans (2010).*

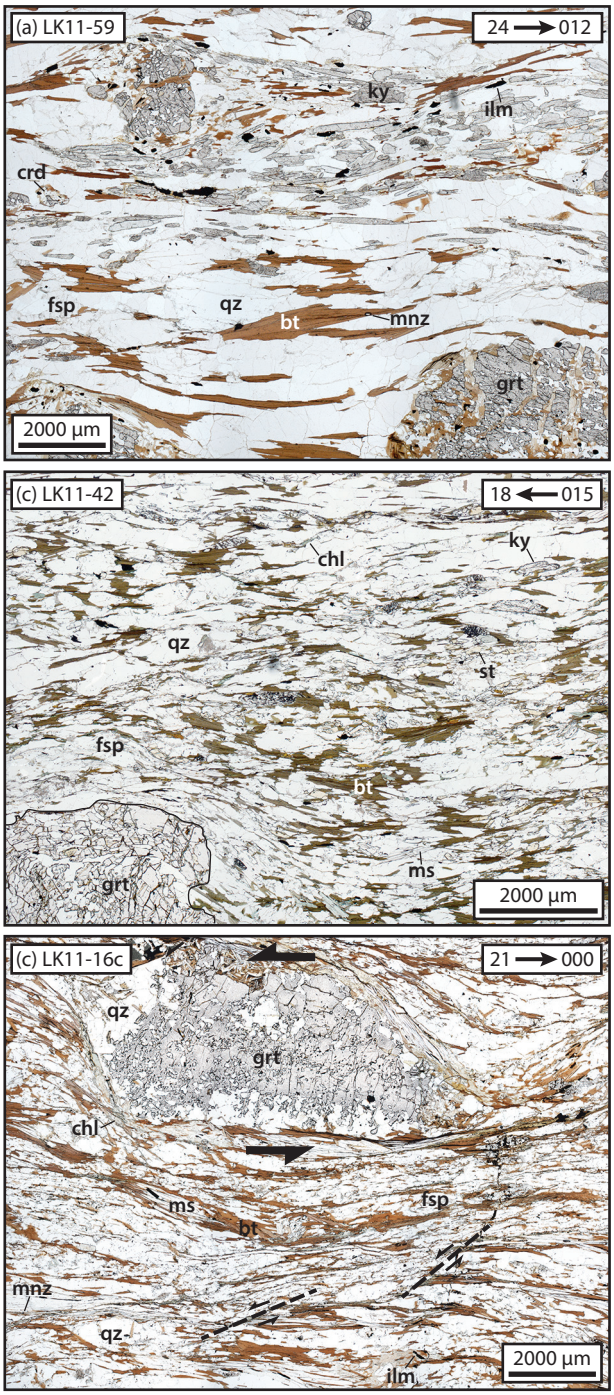


Figure 2.5. Continued.

Methods

Thermobarometry

Mineral compositions and zoning patterns were measured using a Cameca SX-100 electron probe microanalyzer (EPMA) at the University of Tennessee, Knoxville. Al, Mg, Ca, and Mn Kα X-ray images were collected using four wavelength-dispersive spectrometers, and the generated X-ray images were used along with backscattered electron (BSE) images to provide semi-quantitative constraints on compositional zoning in minerals and to identify the best targets for quantitative point analyses. X-ray images for garnet were generated using beam currents of 30–40 nA, a 15-keV accelerating potential, a 100-ms dwell time, and step-sizes of 3–6 μm depending on the sizes of the garnet and its inclusions. EPMA quantitative point analyses were conducted on all solid solution phases. Analysis conditions for the most common phases encountered are as follows. All measurements were obtained with an accelerating potential of 15 keV. Count times for all elements analyzed were 20 s for peak and 10 s for background except Y and Cr, which were analyzed using peak count times of 30 s and background count times of 10 s. Garnet analyses were carried out using a 30-nA beam current and a 1-μm spot size. Mica and chlorite analyses were carried out using a 20-nA beam current and spot sizes of 1–5 μm, and feldspar was analyzed with a 10-nA beam current and 5–10 μm spot sizes. Standard PAP corrections were applied to all analyses, and precision and accuracy were measured using synthetic and natural standards at the beginning and end of each analytical session.

For estimating pressure and temperature (P-T), compositions of phases obtained on the EPMA were processed using the software THERMOCALC v. 3.37 in average P-T mode (Holland and Powell, 1998). Calculations were made using the internally consistent thermodynamic dataset (tc-ds62) of Holland and Powell (2011). Phase activities for input in THERMOCALC were calculated using the updated companion program AX_2. THERMOCALC is designed for calculating phase equilibria and is not equipped for calculating distribution coefficients, as for Fe-Mg exchange between biotite and garnet, a common geothermometry tool, which can lead to unnecessarily large temperature errors. Therefore, we adopted a method of correction developed by Searle et al. (2003) and Jessup et al. (2006) in which THERMOCALC P-T estimates are matched as closely as possible to temperatures from garnet-biotite (GARB) geothermometry by varying the X_{H2O} input in the THERMOCALC interface. A result is only accepted when the temperatures of the two methods are consistent (within error) and if the X_{H2O} value is

reasonable for the geologic setting. Holdaway's (2000) GARB 5AV solution model was chosen for this purpose since it is most appropriate for rocks of similar composition and for P-T conditions expected of the LKD. With the exception of garnet, the mineral compositions used for thermobarometric analysis were either averaged, in the case where little chemical variability was measured, or selected through criteria suggested by Kohn and Spear (2000) in the case where retrograde exchange and net-transfer reactions significantly affect mineral chemistry. Specifically, biotite compositions involved in retrograde reactions with garnet tend to evolve higher Fe# (Fe/Fe + Mg), but the effect is often localized near garnet in which case biotite far from garnet are probably more representative of peak metamorphic conditions (e.g., Robinson, 1991; Spear and Florence, 1992; Kohn and Spear, 2000).

P-T Pseudosections

In addition to thermobarometric calculations, phase diagram sections were calculated in P-T space for four samples (LK11-69a, LK11-60, LK11-59, LK11-16c) using an estimated bulk composition for each sample. In the four samples, zoning in all phases is minimal, which permits the use of average phase compositions in conjunction with modal abundances in order to estimate an approximate bulk composition (e.g., Langille et al., 2012). Alternatively, the relative homogeneity of garnet in these samples precludes the possibility of estimating effective bulk compositions that account for fractionation during garnet growth, which could otherwise be used to model early prograde portions of a sample P-T path.

P-T pseudosections were calculated using the software package Perple_X 6.6.8 (Connolly, 2009; software revised in 2012), which applies a gridded minimization approach in lieu of direct calculation of phase boundaries, using an updated version (hp04ver.dat) of the Holland and Powell (1998) thermodynamic data file. Samples were modeled using the 10-component system MnNCKFMASTH, an expansion of the NCKFMASH that is generally considered representative of metapelite systems (e.g., White et al., 2001). MnO is an important addition to the system because the presence of even a small amount can influence first appearance of garnet (e.g., Spear and Cheney, 1989), while TiO_2 is often a significant component in both Ti-bearing oxides and major silicates such as micas, and indeed some LKD samples contain high-Ti biotite. In three of the four pseudosections, H_2O was treated as a saturated phase, whereas in the fourth (LK11-59) it was treated as a thermodynamic component in order to model

melt stability. The calculated bulk compositions for each sample are shown in Table 2.1. Solid solution models used for phase-diagram calculations are: garnet (White et al., 2000); Ti-biotite (White et al., 2007); ternary feldspar (Fuhrman and Lindsley, 1988); staurolite, white mica, ideal cordierite; chlorite (Holland and Powell, 1998); and an ideal solution model for ilmenite. The CORK equation of state for H_2O (Holland and Powell, 1998) was used in all phase-diagram calculations. One significant exception to this list was the use of Coggon and Holland's (2002) updated white mica solution model for sample LK11-69a since the original solution model of Holland and Powell (1998) is not designed for Na-rich white mica, which is abundant in the sample (Table 2.2).

In-situ Monazite Petrochronology

Monazite was mapped in thin section by EPMA . Details of analytical setup and conditions, as well as how grains were selected, can be found in Appendix 2.2.

In-situ LASS analyses of metamorphic monazite were carried out at the University of California, Santa Barbara, using a Photon Machines 193 nm ArF excimer laser with a HelEx ablation cell coupled to a Nu Instruments Nu Plasma high-resolution multi-collector ICPMS to measure U, Th, and Pb isotopes and an Agilent 7700S quadrupole ICPMS to simultaneously measure trace elements (using methods modified from Kylander-Clark et al., 2013; McKinney et al., 2015). The laser spot diameter was 9.7 μm and laser fluence ~1 Jm^2. During individual analyses, the laser was fired twice to provide a fresh surface for analysis after which the sample was ablated using a 3 Hz pulse for duration of 30 s. Between every seven to nine unknown analyses, monazite reference materials were analyzed to correct for instrumental drift, mass bias, and Pb/U and Pb/Th down-hole fractionation. The primary reference monazite was 44069 (424.9 Ma; Alenikoff, 2006) and secondary reference monazite Baineria (Kylander-Clark et al., 2013) and FC1 (55.6 Ma; Horstwood et al., 2003).

Data reduction for U-Th/Pb values and trace element abundances was carried out using Iolite v. 2.1.2 (Paton et al., 2010). All uncertainties are reported as 2σ at 95% confidence interval and include contributions from the reproducibility of the secondary reference materials. Concordia diagrams were generated for $^{208}Pb/^{232}Th$ vs. $^{206}Pb/^{238}U$ values using Isoplot v. 3.23 (Ludwig, 2000). Pb/Th values are used to calculate dates from monazite to avoid the effects of excess ^{206}Pb (e.g., Schärer et al., 1984), and because monazite generally contain high Th concentrations conducive to Th isotope measurements.

Table 2.1. Modal analyses and modeled bulk compositions for pseudosections.

		Modal Analaysis		Bulk Chemistry	
Sample	Mineral	Count	Mode	Oxide	Wt %
LK11-16c	Quartz	553	39.5	SiO_2	66.6
	Biotite	378	27.0	TiO_2	0.69
	Muscovite	220	15.7	Al_2O_3	15.0
	Plagioclase	194	13.9	MgO	3.00
	Garnet	27	1.93	CaO	0.68
	K-feldspar	18	1.28	MnO	0.12
	Chlorite	5	0.36	FeO	5.70
	Ilmenite	4	0.29	Na_2O	1.55
	Tourmaline	2	0.14	K_2O	4.02
	Sum	1401	100	H_2O	1.70
				Sum	99.02
LK11-59	Quartz	587	42.7	SiO_2	68.4
	Plagioclase	252	18.3	TiO_2	0.63
	Biotite	226	16.4	Al_2O_3	16.4
	Kyanite	119	8.64	MgO	2.51
	Garnet	92	6.69	CaO	0.92
	Cordierite	91	6.61	MnO	0.06
	Ilmenite	3	0.65	FeO	6.43
	Sum	1370	100	Na_2O	1.73
				K_2O	1.35
				H_2O	0.81
				Sum	99.22
LK11-60	Quartz	571	41.7	SiO_2	66.7
	Biotite	324	23.7	TiO_2	1.04
	Muscovite	266	19.4	Al_2O_3	15.5
	Plagioclase	128	9.35	MgO	2.49
	Cordierite	61	4.46	CaO	0.47
	Ilmenite	10	0.73	MnO	0.08
	Staurolite	6	0.44	FeO	5.96
	Garnet	3	0.22	Na_2O	1.08
	Sum	1369	100	K_2O	3.92
				H_2O	1.96
				Sum	99.17
LK11-69a	Quartz	830	60.5	SiO_2	76.1
	Muscovite	290	21.2	TiO_2	0.76
	Biotite	164	12.0	Al_2O_3	11.7
	Garnet	35	2.55	MgO	1.62
	Paragonite	27	1.97	CaO	0.04
	Ilmenite	15	1.09	MnO	0.05
	Chlorite	10	0.73	FeO	4.07
	Sum	1371	100	Na_2O	1.60
				K_2O	0.70
				H_2O	2.58
				Sum	99.21

Mineral Compositions and Average P-T

Unit Ts Samples

Compositional X-ray maps of Mn in garnet from unit Ts samples generally record a decrease in Mn abundance from core to rim with a slight increase near the grain boundary (Fig. 2.6a; Appendix 2.4). Such compositional trends are indicative of prograde growth, with the rim recording late-stage, retrograde net-transfer reactions, and quantitative point analysis transects through representative garnet indicate similar trends with a decrease in Fe# from core to rim, followed by a slight increase near grain boundaries (e.g., Robinson, 1991; Spear, 1991; Kohn and Spear, 2000).

Solid-solution matrix phases in unit Ts samples (chlorite, muscovite, and plagioclase; Table 2.2) do not show any substantial variation, and chloritoid porphyroblasts exhibit little or no zoning; therefore, the compositions of these phases were averaged for thermobarometric calculations (Table 2.3). THERMOCALC average PT mode yields estimates of 555 ± 60 °C and 479 ± 75 °C, respectively, at 7.3 ± 1.4 kbar and 7.3 ± 2.0 kbar. The relatively large errors in pressure and temperature are attributed to a lack of reasonable estimates on XH_2O, particularly because the GARB 5AV thermometry correction cannot be applied in the absence of biotite in the two representative samples.

Unit Ps Schist Samples

Compositional X-ray maps of Mn and quantitative point-analysis transects of garnet from the unit Ps schist samples yield two different types of garnet zoning. The three structurally highest samples (LK-48, LK-57, LK-59c) exhibit garnet zoning patterns consistent with prograde growth similar to those of the unit Ts samples, which are characterized by a decrease in Mn from core to rim and a slight increase at the very edge of the grain, indicative of retrograde net transfer reactions (Fig 2.6c; Appendix 2.4). In contrast the three structurally deeper samples (LK11-70, LK11-69a, and LK11-60) exhibit zoning patterns with relatively flat elemental profiles indicative of high temperature (≥ 600 °C) diffusion processes (Figs 2.6d, Appendix 2.4) (e.g., Spear, 1991). In the diffusion-modified garnet, characteristic of the structurally lower three samples, Mn and Fe# rim spikes are preserved, and therefore the lowest Mn composition are used for P-T estimates. The microstructural setting of matrix phases is an important consideration when choosing compositions for thermobarometric calculations. Brief descriptions of matrix-phase compositions used for THERMOCALC estimates are provided in the following and

Table 2.2. Average mineral compositions of main solid-solution phases.

	LK11-35	LK-67a	LK-48	LK-57	LK-59c	LK11-70	LK11-69a	LK11-60	LK11-59	LK11-42	LK11-16c
Zone[a]	Grt + Cld	Grt + Cld	Grt	St	St	St	Ky	Ky	Ky	Sil	Sil
Garnet[b] - Basis of 12 O											
SiO_2	37.0	37.1	37.4	37.3	37.4	37.4	37.2	36.9	37.4	37.5	37.4
TiO_2	0.05	0.07	0.04	0.02	0.03	0.00	0.03	0.03	0.00	0.01	0.03
Al_2O_3	21.2	21.2	20.9	21.1	21.3	21.2	21.1	21.0	21.5	21.3	21.2
FeO	35.0	33.9	32.7	32.9	32.1	34.9	35.6	33.8	34.1	30.6	30.7
MnO	0.59	1.48	1.35	2.03	1.36	0.44	0.98	3.87	0.41	2.81	3.25
MgO	1.43	1.13	2.66	2.84	2.99	4.08	3.72	2.36	4.83	3.37	3.13
CaO	4.43	6.23	5.35	4.35	5.11	2.35	1.28	2.37	2.26	4.41	4.35
Na_2O	0.02	0.00	0.02	0.00	0.03	0.00	0.05	0.00	0.02	0.02	0.02
K_2O	n.d.	n.d.	n.d.	n.d.	n.d.	n.d.	n.d.	n.d.	n.d.	n.d.	n.d.
Sum	99.6	101.1	100.1	100.5	100.4	100.4	100.0	100.4	100.5	100.0	100.0
Si	2.995	2.974	2.964	2.984	2.982	2.984	2.988	2.980	2.968	2.992	2.991
Ti	0.003	0.004	0.002	0.001	0.002	0.000	0.002	0.002	0.000	0.001	0.002
Al	2.022	1.999	1.954	1.987	2.003	1.993	2.000	2.000	2.007	2.005	1.996
Fe	2.373	2.274	2.277	2.199	2.144	2.327	2.397	2.282	2.262	2.040	2.054
Mn	0.041	0.100	0.091	0.138	0.092	0.030	0.067	0.265	0.028	0.190	0.220
Mg	0.173	0.135	0.314	0.339	0.356	0.485	0.446	0.284	0.571	0.401	0.373
Ca	0.385	0.535	0.454	0.373	0.437	0.201	0.110	0.205	0.192	0.377	0.373
Na	0.000	0.000	0.000	0.000	0.000	0.000	0.000	0.000	0.000	0.000	0.000
K	n.d.	n.d.	n.d.	n.d.	n.d.	n.d.	n.d.	n.d.	n.d.	n.d.	n.d.
Sum	7.991	8.022	8.057	8.021	8.015	8.020	8.010	8.018	8.028	8.005	8.009
X_{Alm}	0.799	0.747	0.726	0.721	0.708	0.765	0.794	0.752	0.741	0.678	0.680
X_{Sps}	0.014	0.033	0.029	0.045	0.030	0.010	0.022	0.087	0.009	0.063	0.073
X_{Prp}	0.058	0.044	0.100	0.111	0.117	0.159	0.148	0.094	0.187	0.133	0.124
X_{Grs}	0.130	0.176	0.145	0.122	0.144	0.066	0.037	0.068	0.063	0.125	0.123
Fe#	0.932	0.944	0.879	0.867	0.858	0.828	0.843	0.889	0.798	0.836	0.846
Biotite - Basis of 22 O											
n	–	–	8	7	22	14	12	26	44	19	26
SiO_2	–	–	35.6 (2)	35.1 (4)	36.1 (3)	36.1 (4)	36.3 (2)	35.2 (3)	35.6 (5)	36.0 (3)	35.9 (5)
TiO_2	–	–	1.61 (10)	0.85 (30)	1.61 (20)	1.46 (20)	1.48 (5)	2.38 (20)	2.06 (30)	1.64 (50)	1.70 (16)
Al_2O_3	–	–	18.8 (1)	19.4 (2)	19.0 (4)	18.8 (4)	19.2 (2)	19.5 (3)	18.6 (4)	18.6 (3)	19.4 (4)
FeO	–	–	19.0 (2)	21.0 (4)	18.6 (5)	17.8 (10)	17.8 (2)	20.3 (3)	19.4 (9)	17.8 (7)	17.4 (5)
MnO	–	–	0.09 (2)	0.09 (1)	0.10 (2)	0.08 (2)	0.03 (2)	0.15 (2)	0.04 (2)	0.08 (1)	0.11 (2)
MgO	–	–	10.0 (2)	9.39 (3)	10.4 (2)	11.3 (3)	10.9 (1)	8.63 (14)	10.4 (5)	11.4 (4)	10.7 (6)
CaO	–	–	0.02 (2)	0.01 (1)	0.02 (2)	0.02 (1)	0.03 (2)	0.00	0.00	0.00	0.00
Na_2O	–	–	0.17 (2)	0.33 (2)	0.34 (6)	0.30 (1)	0.57 (4)	0.29 (3)	0.26 (4)	0.27 (4)	0.28 (6)
K_2O	–	–	9.05 (1)	8.90 (3)	9.16 (10)	8.74 (6)	8.39 (15)	8.83 (12)	7.89 (60)	9.16 (25)	8.87 (30)
Sum	–	–	94.4	95.2	95.3	94.6	94.7	95.3	94.2	95.0	94.4
Si	–	–	5.398	5.342	5.396	5.405	5.407	5.328	5.386	5.386	5.384
Ti	–	–	0.184	0.097	0.181	0.164	0.166	0.271	0.234	0.184	0.192
Al	–	–	3.364	3.484	3.347	3.323	3.380	3.474	3.307	3.284	3.428
Fe	–	–	2.407	2.677	2.326	2.229	2.213	2.562	2.453	2.227	2.184
Mn	–	–	0.012	0.012	0.013	0.010	0.004	0.019	0.005	0.010	0.014
Mg	–	–	2.265	2.132	2.319	2.511	2.426	1.945	2.337	2.546	2.391

Table 2.2. Continued

	LK11-35	LK-67a	LK-48	LK-57	LK-59c	LK11-70	LK11-69a	LK11-60	LK11-59	LK11-42	LK11-16c
Ca	–	–	0.003	0.002	0.003	0.003	0.005	0.000	0.000	0.002	0.002
Na	–	–	0.050	0.097	0.099	0.087	0.165	0.085	0.076	0.078	0.081
K	–	–	1.750	1.727	1.748	1.669	1.595	1.703	1.521	1.748	1.696
Sum	–	–	15.4	15.6	15.4	15.4	15.4	15.4	15.3	15.5	15.4
Fe#	–	–	0.515	0.557	0.501	0.470	0.477	0.568	0.512	0.467	0.477
White Mica - Basis of 22 O											
n	26	30	13	8	27	25	35	26	–	14	24
SiO_2	46.1 (5)	46.9 (7)	45.7 (3)	45.8 (3)	45.8 (3)	46.2 (8)	46.1 (9)	46.2 (3)	–	46.1 (5)	46.0 (4)
TiO_2	0.19 (6)	0.25 (11)	0.54 (7)	0.46 (17)	0.40 (6)	0.47 (11)	0.38 (12)	0.75 (7)	–	0.38 (14)	0.35 (20)
Al_2O_3	35.9 (5)	35.6 (10)	34.9 (3)	35.2 (7)	35.0 (5)	35.9 (9)	37.1 (14)	35.2 (4)	–	34.7 (6)	36.9 (8)
FeO	1.44 (4)	1.48 (50)	1.71 (9)	2.46 (23)	2.08 (14)	1.47 (12)	1.42 (600	1.21 (37)	–	2.30 (12)	1.08 (31)
MnO	0.00	0.00	0.00	0.00	0.00	0.00	0.00	0.00	–	0.00	0.00
MgO	0.54 (12)	0.85 (23)	0.72 (5)	0.57 (16)	0.65 (11)	0.70 (26)	0.60 (93)	0.72 (10)	–	0.70 (11)	0.65 (21)
CaO	0.02 (1)	0.02 (2)	0.01 (1)	0.01 (1)	0.00	0.01 (1)	0.03 (2)	0.00	–	0.01 (1)	0.00
Na_2O	0.99 (9)	0.93 (21)	0.38 (6)	0.30 (6)	1.07 (9)	0.80 (14)	2.60 (21)	0.99 (13)	–	1.14 (16)	1.45 (20)
K_2O	9.42 (22)	9.09 (42)	9.98 (11)	8.59 (12)	9.80 (18)	8.78 (32)	7.03 (46)	9.30	–	9.10 (54)	8.59 (30)
Sum	94.6	95.2	93.9	93.4	94.9	94.3	95.4	94.3	–	94.4	95.1
Si	6.147	6.200	6.163	6.175	6.139	6.146	6.048	6.167	–	6.187	6.072
Ti	0.020	0.025	0.055	0.047	0.040	0.047	0.037	0.075	–	0.038	0.045
Al	5.644	5.554	5.544	5.590	5.533	5.641	5.754	5.543	–	5.483	5.741
Fe	0.161	0.164	0.193	0.277	0.233	0.164	0.156	0.135	–	0.258	0.119
Mn	0.000	0.001	0.000	0.001	0.001	0.000	0.000	0.000	–	0.000	0.000
Mg	0.107	0.167	0.145	0.115	0.130	0.139	0.117	0.143	–	0.140	0.128
Ca	0.003	0.003	0.001	0.001	0.000	0.001	0.004	0.000	–	0.000	0.000
Na	0.256	0.238	0.099	0.078	0.278	0.207	0.661	0.257	–	0.297	0.371
K	1.602	1.532	1.718	1.477	1.675	1.491	1.176	1.585	–	1.558	1.446
Sum	13.940	13.884	13.919	13.762	14.030	13.836	13.956	13.906	–	13.961	13.922
X_{Ms} [c]	0.746	0.709	0.793	0.741	0.736	0.729	0.568	0.721	–	0.687	0.704
X_{Pg}	0.161	0.174	0.091	0.146	0.146	0.176	0.367	0.164	–	0.180	0.227
X_{FeCel}	0.030	0.057	0.042	0.011	0.029	0.038	0.019	0.055	–	0.033	0.033
X_{MgCel}	0.057	0.055	0.066	0.092	0.080	0.051	0.038	0.051	–	0.092	0.028
Plagioclase - Basis of 8 O											
n	16	6	25	11	39	39	–	35	-	29	27
SiO_2	60.7 (13)	61.5 (10)	57.6 (5)	59.1 (12)	58.1 (6)	58.7 (11)	–	62.1 (5)	63.1 (7)	60.2 (3)	63.6 (3)
TiO_2	n.d.	n.d.	n.d.	n.d.	n.d.	n.d.	–	n.d.	n.d.	n.d.	n.d.
Al_2O_3	24.6 (10)	24.3 (6)	26.6 (3)	25.8 (8)	26.4 (4)	25.6 (5)	–	23.8 (2)	22.9 (4)	25.2 (2)	22.7 (2)
FeO	0.32 (16)	0.10 (3)	0.12 (8)	0.04 (1)	0.13 (12)	0.05 (5)	–	0.06 (6)	0.03 (3)	0.08 (6)	0.07 (7)
MnO	n.d.	n.d.	n.d.	n.d.	n.d.	n.d.	–	n.d.	n.d.	n.d.	n.d.
MgO	n.d.	n.d.	n.d.	n.d.	n.d.	n.d.	–	n.d.	n.d.	n.d.	n.d.
CaO	6.21 (100)	5.71 (74)	8.77 (34)	7.61 (93)	8.29 (46)	7.47 (46)	–	5.03 (27)	4.25 (43)	6.67 (21)	3.87 (14)
Na_2O	8.06 (64)	8.41 (44)	6.52 (18)	7.23 (49)	6.83 (24)	7.15 (31)	–	8.61 (19)	9.14 (24)	7.77 (16)	9.24 (10)
K_2O	0.07 (1)	0.10 (2)	0.08 (1)	0.08 (1)	0.08 (1)	0.08 (1)	–	0.17 (4)	0.11 (4)	0.08 (2)	0.12 (3)
Sum	100.1	100.1	99.8	100.0	99.8	99.0	–	99.8	99.5	100.0	99.6
Si	2.649	2.727	2.587	2.640	2.604	2.643	–	2.757	2.801	2.679	2.819
Ti	n.d.	n.d.	n.d.	n.d.	n.d.	n.d.	–	n.d.	n.d.	n.d.	n.d.

Table 2.2. Continued

	LK11-35	LK-67a	LK-48	LK-57	LK-59c	LK11-70	LK11-69a	LK11-60	LK11-59	LK11-42	LK11-16c
Al	1.349	1.269	1.409	1.359	1.393	1.358	–	1.247	1.197	1.323	1.184
Fe	0.010	0.004	0.005	0.001	0.005	0.002	–	0.002	0.003	0.003	0.003
Mn	n.d.	n.d.	n.d.	n.d.	n.d.	n.d.	–	n.d.	n.d.	n.d.	n.d.
Mg	n.d.	n.d.	n.d.	n.d.	n.d.	n.d.	–	n.d.	n.d.	n.d.	n.d.
Ca	0.351	0.271	0.422	0.364	0.398	0.361	–	0.239	0.202	0.318	0.184
Na	0.637	0.723	0.567	0.626	0.593	0.625	–	0.741	0.787	0.671	0.794
K	0.004	0.006	0.005	0.005	0.005	0.005	–	0.010	0.006	0.005	0.007
Sum	4.999	5.002	4.994	4.995	4.998	4.993	–	4.995	4.997	4.998	4.990
X_{An}	0.355	0.273	0.426	0.368	0.401	0.366	–	0.244	0.204	0.322	0.188
Staurolite - Basis of 24 O											
n	–	–	–	20	16	15	–	32	–	8	–
SiO_2	–	–	–	27.6 (1)	27.8 (1)	28.0 (2)	–	27.5 (3)	–	28.0 (2)	–
TiO_2	–	–	–	0.56 (4)	0.55 (2)	0.65 (6)	–	0.66 (7)	–	0.59 (8)	–
Al_2O_3	–	–	–	52.8 (3)	53.2 (2)	52.8 (3)	–	53.5 (7)	–	53.0 (2)	–
FeO	–	–	–	14.6 (1)	13.7 (1)	13.7 (4)	–	13.0 (2)	–	13.3 (1)	–
MnO	–	–	–	0.20 (2)	0.29 (2)	0.18 (6)	–	0.40 (3)	–	0.28 (2)	–
MgO	–	–	–	1.67 (8)	1.87 (7)	2.14 (22)	–	1.4 (1)	–	2.08 (9)	–
CaO	–	–	–	0.00	0.00	0.01 (1)	–	0.00	–	0.00	–
Na_2O	–	–	–	0.01 (1)	0.02 (1)	0.00	–	0.03 (1)	–	0.02 (1)	–
K_2O	–	–	–	0.00	0.00	0.00	–	0.00	–	0.00	–
Sum	–	–	–	97.4	97.4	97.5	–	96.6	–	95.2	–
Si	–	–	–	4.036	4.049	4.071	–	4.023	–	4.143	–
Ti	–	–	–	0.062	0.060	0.071	–	0.073	–	0.066	–
Al	–	–	–	9.091	9.118	9.041	–	9.240	–	9.262	–
Fe	–	–	–	1.779	1.660	1.667	–	1.592	–	1.649	–
Mn	–	–	–	0.025	0.036	0.022	–	0.050	–	0.035	–
Mg	–	–	–	0.364	0.405	0.464	–	0.303	–	0.002	–
Ca	–	–	–	0.000	0.000	0.002	–	0.000	–	0.003	–
Na	–	–	–	0.003	0.006	0.000	–	0.009	–	0.000	–
K	–	–	–	0.000	0.000	0.000	–	0.000	–	0.000	–
Sum	–	–	–	15.359	15.334	15.337	–	15.289	–	15.160	–

En-dashes indicate the phase was not present in the corresponding sample.

n.d.—not determined

n—number of analyses used to calculate average compositions

Mineral abbreviations are after Whitney and Evans (2010) unless otherwise noted below.

[a]Zone refers to the metamorphic zones as defined in the text. Cld—chloritoid, Grt—garnet, Ky—kyanite, Sil—sillimanite, St—staurolite.

[b]All reported garnet compositions are near-rim

[c]White mica mole fractions were calculated using the quaternary solution model of Keller et al (2005). FeCel—Fe-celadonite, MgCel—Mg-celadonite, Ms—muscovite, Pg—paragonite.

Table 2.3. P-T estimates for Barrovian metamorphism.

			GARB[a]	THERMOCALC Average P-T Mode						
Sample	Unit	Assemblage	T (°C)	T (°C)	P (kbar)	X_{H_2O}	Removed[b]	Cor.	Fit	n[c]
LK11-35	Ts	Grt + Cld + Chl + Wm + Pl + Qz	–	553 ± 11	6.5 ± 0.8	–	–	0.86	0.6	5
LK-67a	Ts	Grt + Chl + Wm + Pl + Qz	–	567 ± 14	6.1 ± 0.7	–	ames	0.539	1.04	4
LK-48	Ps	Grt + Bt + Wm + Pl + Qz	558	571 ± 29	6.8 ± 0.9	0.1	–	0.763	0.33	6
LK-57	Ps	Grt + St + Bt + Wm + Pl + Qz	664	651 ± 46	8.2 ± 1.1	1	pa	0.644	1.06	5
LK-59c	Ps	Grt + St + Bt + Wm + Pl + Qz	648	642 ± 25	8.0 ± 1.0	0.8	–	0.853	1.04	5
LK11-70	Ps	Grt + St + Ky + Bt + Wm + Pl + Qz	645	641 ± 19	6.9 ± 0.8	0.8	pa	0.001	0.51	6
LK11-69a	Ps	Grt +Bt + 2Wm + Qz (+ Pl)[d]	616	625 ± 110	6.2 ± 2.6	-	pa	0.487	0.96	4
LK11-60	Ps	Grt + St + Ky + Bt + Wm + Pl + Qz (+ Crd)	712	714 ± 27	8.8 ± 1.1	0.4	crd, fcrd, mncrd	0.787	0.96	8
LK11-59	Ps	Grt + Bt + Pl + Ky + Qz	680–697	–	–	–	–	–	–	–
LK11-42	Ps	Grt + St + Ky + Bt + Wm + Pl + Qz	654	650 ± 44	8.2 ± 1.7	0.4	fcel	0.843	1.69	6
LK11-16c	Ps	Grt + Bt + Wm + Pl + Qz	650	644 ± 21	9.9 ± 1.1	0.25	–	0.814	1.03	5

En-dashes indicate data that could not be calculated from interpreted assemblages and phase compositions.

[a]Garnet-biotite exchange thermometry; temperature calculated using model 5AV of Holdaway (2000)

[b]End-member abbreviations from Holland and Powell (1998)

[c]n - number of independent reactions for THERMOCALC P-T estimates

[d]Asemblage contains at least two distinct white mica phases. Plagioclase present in sample, but in too small of a quantity and too weathered for EPMA measurement

recorded in Table 2.2. See Appendix 2.3 for detailed descriptions of individual sample compositions.

Chlorite occurs at all metamorphic grades of the unit Ps schist, but it is typically confined to garnet strain shadows and porphyroblast rims in the garnet, staurolite, and kyanite zones. Garnet porphyroblasts from these zones generally exhibit clear near-rim retrograde zoning (Fig. 2.6), so associated chlorite is not considered for average P-T calculations in the representative samples. Biotite and white mica occur in all of the Ps schist samples with the exception of white mica in LK11-59 (Table 2.2). A systematic decrease in biotite Fe# from garnet-zone to staurolite-zone samples exists, but the highest average Fe# (0.56) is documented in a kyanite-zone sample (LK11-60). Although biotite compositions vary between different samples, the compositions within individual samples are relatively uniform and justify the use of average biotite compositions for P-T calculations. White mica compositions have no systematic variation with structural depth/metamorphic grade, although the compositions do vary from sample to sample. As with biotite, intra-sample elemental variation of white mica is minimal with the exception of LK11-69a, a kyanite-zone schist, which exhibits at least two distinct white mica compositions: one phengitic and one paragonitic. The average of all white mica compositions for LK11-69a is given in Table 2.2; individual white mica phases are discussed in Appendix 2.3. Plagioclase compositions for unit Ps schist have no systematic variation with structural level, but garnet- and staurolite-zone samples yield plagioclase measurements with generally higher anorthite mole fraction (X_{An} = 0.37–0.43) than those from the kyanite zone (X_{An} = 0.20–0.24). There is no intra-sample variation of X_{An} for any of the selected samples. Staurolite is unzoned and does not exhibit a systematic variation in chemistry with structural depth or metamorphic grade. In addition to these phases, the highest grade schist, LK11-60, also contains cordierite and fibrolite. However, these phases occur as replacements on the rims of garnet porphyroblasts and as coronae on biotite and kyanite, indicating that they are not in textural equilibrium, so they are not considered for P-T analysis.

Unit Ps schist samples all contain matrix phases of relatively uniform composition. Samples in the staurolite and kyanite zones contain garnet with diffusion-modified zoning profiles, which makes them suspect for calculating peak temperatures, particularly using GARB calculations. As summarized in Table 2.3, THERMOCALC average P-T calculations and GARB calculations show relatively good agreement for Ps schist samples. THERMOCALC results indicate P-T conditions of 6.8 ± 0.9 kbar and 571 ± 29 °C in the representative garnet zone sample (LK-48), which overlaps with a GARB temperature

Figure 2.6. *Examples of garnet compositional profiles and Mn Kα X-ray images for (a) garnet-chloritoid schist from unit Ts, (b) staurolite schist from unit Ps, (c) kyanite schist from unit Ps, and (d) staurolite-kyanite paragneiss from unit Ps. Black dashed lines highlighted with an arrow on the compositional profiles indicate the garnet composition chosen for average P-T calculations. Jagged white lines in the Mn Kα images represent the approximate location of the compositional transect. The dots along the transects represent locations of spot analyses, but they are not scaled to the diameter of the spot, which was ~1 μm for garnet. High inclusion density in nearly all porphyroblasts necessitated a non-linear transect.*

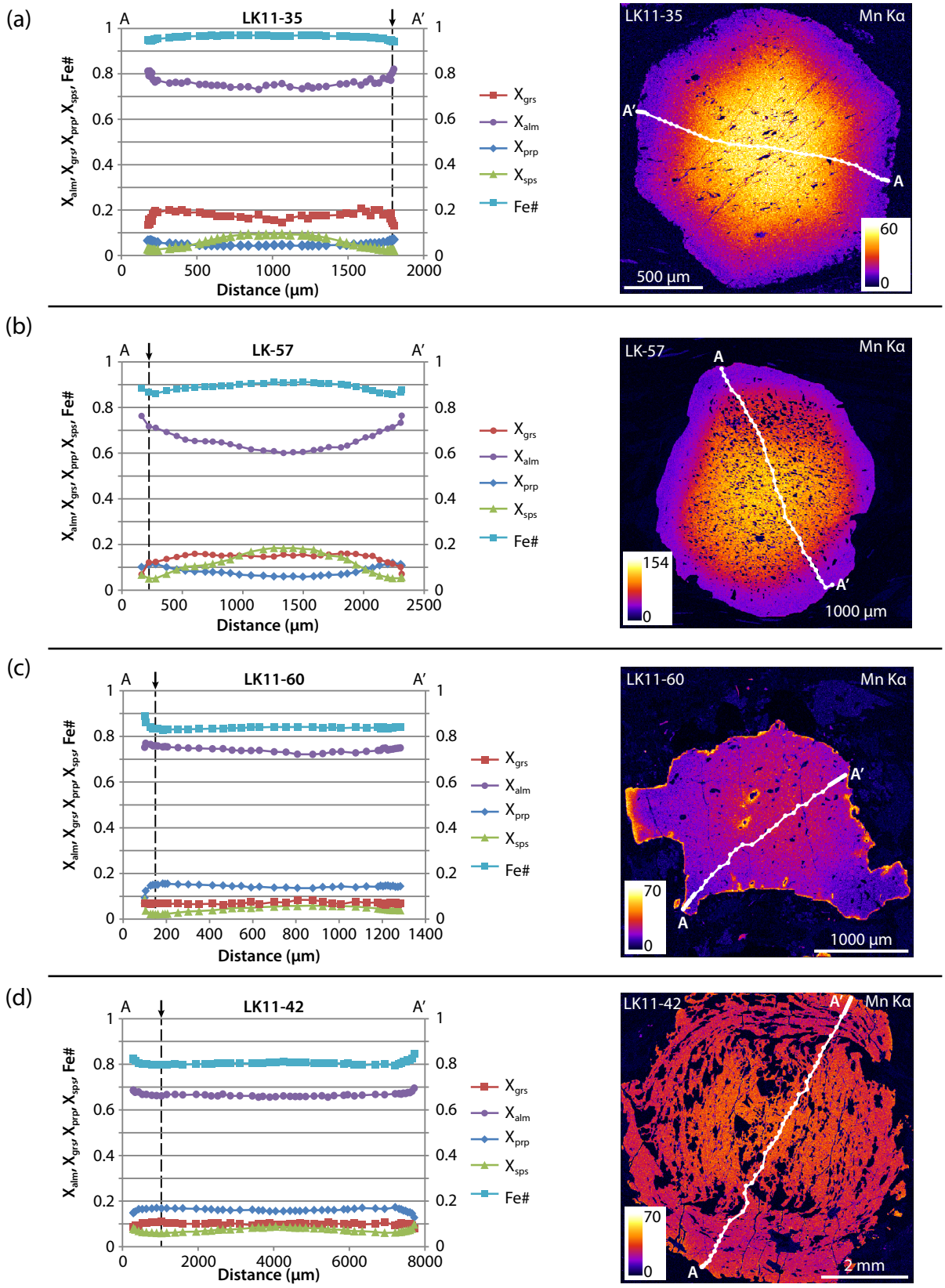


Figure 2.6. Continued.

of 558 °C. In the three staurolite-zone samples, GARB and mean THERMOCALC temperatures are all ~650 °C (Table 2.3), while average THERMOCALC pressure estimates range from 6.9 ± 0.8 kbar in LK11-70 to 8.2 ± 1.1 kbar in LK-57. The two kyanite-zone samples have drastically different calculated average P-T conditions: LK11-69a yielded a result of 625 ± 110 °C (GARB temperature of 616 °C) and 6.2 ± 2.6 kbar whereas LK11-60 yields a result of 714 ± 27 °C and 8.8 ± 1.1 kbar. As noted in Table 2.3 the source of large uncertainty in LK11-69a stems from the absence of plagioclase, yet the average temperature value is in good agreement with the GARB temperature despite the large THERMOCALC temperature uncertainty. The interpreted peak temperature and associated pressure of sample LK11-60 overlaps with that for anatexis of metapelites (e.g., Le Breton and Thompson, 1988; Patiño Douce and Johnston, 1991; Patiño Douce and Harris, 1998; Spear et al., 1999), but in high grade rocks it is possible for GARB temperatures calculated using large garnet grains to be much higher than the actual peak temperature attained (Spear and Florence, 1992). Since garnet from the sample exhibits diffusion-modified zoning and corona textures, assumptions of equilibrium compositions are dubious. The chosen garnet composition could represent significant post-growth dissolution and, if coupled with matrix biotite compositions as was done above, would produce an anomalously high GARB temperature (Kohn and Spear, 2000).

Unit Ps Paragneiss Samples

Garnet porphyroblasts in the gneissic samples (LK11-16c, LK11-42, LK11-59) yield relatively homogeneous elemental profiles as indicated by Mn X-ray maps and quantitative point-analysis transects (Fig. 2.6d; Appendix 2.4). Uniformly low Mn in garnet may be at least partially a function of low bulk Mn content as evidenced by relatively low abundances in other commonly Mn-bearing phases like ilmenite and biotite (e.g., Table 2.2), but Ca, Mg and Fe# are also relatively uniformly distributed in garnet from these samples. In addition to the ubiquitous evidence of high temperature diffusion in garnet, several porphyroblasts also exhibit a Fe# and Mn upswing at the rim, particularly where in contact with biotite or cordierite. Although diffusion-modified garnet compositions can lead to substantial underestimation of peak temperatures (e.g., Spear and Florence, 1992), P-T values are reported for these samples as the results provide proximate constraints for subsequent petrologic modeling. Since many porphyroblasts in the gneissic samples exhibit retrograde rims, the criteria of Kohn and Spear (2000), as

described above, are used for selecting garnet and biotite compositions that should best represent peak-temperature conditions.

Matrix-phase compositions other than white mica vary systematically in all three Ps paragneiss samples. White mica is not present in LK11-59 and in the other two samples (LK11-42 and LK11-16c) white mica compositions are relatively uniform throughout and characterized by muscovite mole fraction of ~0.7 (Table 2.2). In contrast, both biotite and plagioclase exhibit compositional trends associated with microstructural setting in the paragneiss samples. Generally, biotite compositions are characterized by higher Fe# (average ~0.50) adjacent to garnet porphyroblasts—in strain shadows, along reaction rims, and as inclusions—than biotite grains in the matrix (average ≤0.48). Plagioclase generally exhibits higher X_{An} contents as inclusions in garnet (X_{An} = 0.2–0.35), with the exception of LK11-59 which has plagioclase inclusions with X_{An} = 0.16–0.19, than in the matrix (X_{An} = 0.16–0.22). However, the compositions in these two microstructural settings overlap in the X_{An} = 0.20–0.25.

Because biotite exhibits slight compositional variation within the paragneiss samples, the average of the matrix compositions was selected for GARB calculations, because it is likely the best proxy for near-peak conditions (e.g., Kohn and Spear, 2000). LK11-59 contains only garnet, plagioclase, and biotite as solid-solution phases; therefore, a sufficient number of independent reactions could not be established to calculate average P-T. GARB temperatures are 680–697 °C for pressures of 6–10 kbar. The other two samples yield consistent GARB and average THERMOCALC temperatures of ~650 °C (Table 2.3), but LK11-42 yields an average pressure of 8.2 ± 1.7 kbar while LK11-16c yields an average pressure of 9.9 ± 1.1 kbar.

Pseudosections

Here we present a representative pseudosection model for sample LK11-60, selected because its compositional and microstructural characteristics permit the most complete P-T path interpretation. Three additional samples (LK11-16c, LK11-59, LK11-69a) were modeled and their results are presented in Appendices 2.5 and 2.6. All four samples were also selected because they contain monazite that brackets the timing of metamorphism and fabric development in the LKD.

The P-T pseudosection generated for sample LK11-60 (Fig. 2.7a) is dominated by large tetravariant and pentavariant phase fields with a smaller proportion of trivariant fields. A small divariant field shown in Figures 2.7a (field marked 7) and 2.7b denotes what should be considered a “near-peak”

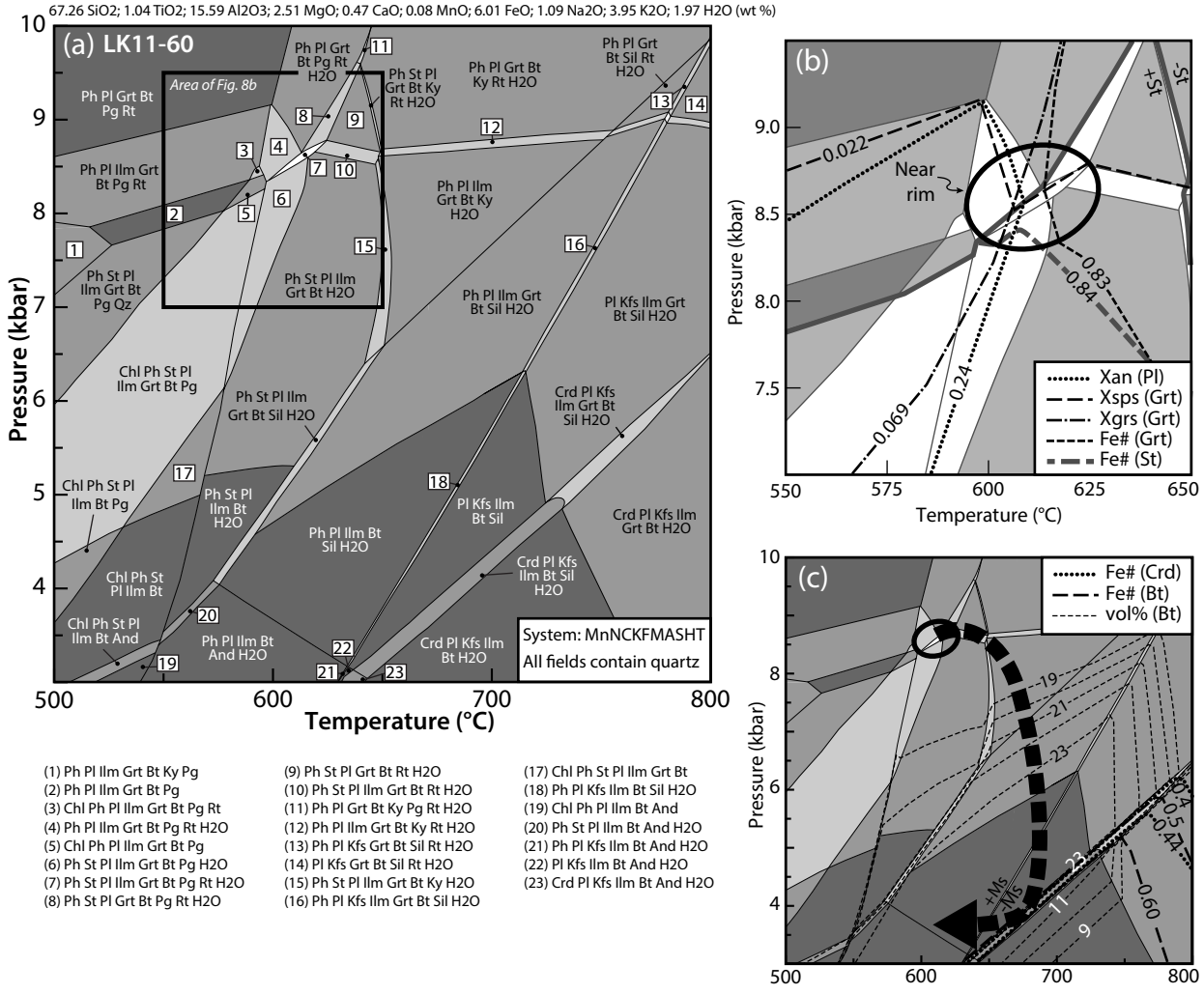


Figure 2.7. *(a) P-T pseudosection model for sample LK11-60. The darker the shade of the field, the higher the variance—white is divariant. Mineral abbreviations after Whitney and Evans (2010). (b) Blown up region around the divariant field labeled '7' in (a) showing compositional isopleths of near-rim garnet, staurolite, and plagioclase that bracket near peak conditions (black ellipse). (c) Simplified version of the P-T pseudosection in (a) showing modal proportions of biotite in conjunction with compositional isopleths of biotite and cordierite that constrain a near isothermal decompression path from the near-peak compositions. Path is projected initially to higher temperatures to more closely match the petrographically documented peak assemblage.*

assemblage (Ph + St + Pl + Ilm + Grt + Bt + Pg + Rt) that encompasses temperatures of 590–620 °C and pressures of 8.4–8.8 kbar. These conditions are considered a minimum for several reasons. Petrographic analysis suggests that kyanite is part of the stable assemblage, and the pseudosection topology shows that kyanite stability requires higher temperature than that of the divariant field, regardless of whether pressure is increased or decreased. Since the petrographically interpreted equilibrium assemblage includes staurolite and kyanite, measured staurolite compositions suggest slightly lower pressure for the "true" peak assemblage (Fig. 2.7b). Although garnet porphyroblasts in the sample exhibit zoning profiles that suggest they experienced substantial post-growth diffusion modification, isopleths representing garnet near-rim composition plot within the same divariant field (Fig. 2.7b). In contrast, the same garnet composition yields THERMOCALC average and GARB temperatures that are nearly 100 °C higher, but these temperatures are dubious since the coupled biotite compositions do not likely represent peak garnet growth conditions and it is worth further considering evolution of phase compositions and modes suggested in the forward model.

A plagioclase compositional isopleth that falls in the range of compositions for matrix feldspar grains ($An_{20–25}$) crosses the divariant field in Figure 2.7b with a steep positive slope. Owing to slow diffusion rates of Ca in metapelitic rocks (e.g., Chernoff and Carlson, 1997), plagioclase and grossular component in garnet can be inferred to preserve near-peak compositions where other chemical constituents experienced significant diffusion modification; however, textural evidence (Appendix 2.1) indicates that some plagioclase (a) post-dates kyanite growth, and (b) nucleated or recrystallized in equilibrium with cordierite. These textural observations are corroborated by the forward model, which predicts plagioclase compositions of $An_{20–25}$ at conditions of cordierite stability along the interpreted P-T path in Figure 2.7c (X_{An} is omitted to facilitate readability). In addition to plagioclase compositions, the near-isothermal decompression path depicted also predicts biotite growth at the expense of garnet and with increasing biotite Fe#. Measured biotite compositions from sample LK11-60 (average Fe# = 0.510) are consistent with this model since they are only predicted to exist under conditions where cordierite is stable. Since biotite compositions are relatively homogeneous throughout the sample, it is likely that biotite and cordierite (± plagioclase) represent approximate equilibrium at 650–730 °C and 3–5 kbar (Fig. 2.7a). White mica compositions (not shown) do not appear to correlate to the near-peak or decompression steps along the inferred P-T path, indicating that the sample system experienced departure

from equilibrium as implied by other textural and compositional evidence. Given that potassium feldspar is stable in LK11-60 at the decompression conditions given above but absent in the sample, it is possible that white mica completely replaced potassium feldspar during rehydration along a near-isobaric cooling path (Fig. 2.7c). However, there is no clear textural evidence in the sample to indicate relative timing of white mica growth.

Pseudosections for two of the other three samples (LK11-69a, LK11-59, LK11-16c; Appendices 2.5 and 2.6) yield similar results and additional P-T path constraints for the LKD rocks. As with the calculated P-T estimates, pseudosection models (Appendix 2.6) calculated for LK11-69a are suspect. Modeled composition isopleths for garnet and white mica exhibit steep pressure/temperature slopes that intersect over a broad range of pressures (6–11 kbar), although they do indicate similar temperatures (600–625 °C) to those calculated using THERMOCALC and GARB thermometry. However, no additional information can be gleaned regarding the P-T path experienced by this sample. In contrast, pseudosections for LK11-59 and LK11-16c (Appendix 2.6) do yield meaningful results when considered along with the measured phase compositions and mineral textural relationships (see Appendix 2.4 for detailed descriptions). Modeled garnet, plagioclase, cordierite, and biotite compositional isopleths for LK11-59 (Appendix 2.6) define a steeply sloped decompression path similar to that of LK11-60, which is not surprising considering the close proximity of these two samples and their similar chemistry. Additionally, composition isopleths representative of plagioclase inclusions and garnet hosts possibly constrain a portion of the prograde P-T path for LK11-59 from ~570 °C and ~8 kbar to the near-peak of 610–660 °C and 9.6–11 kbar (Appendix 2.6), which is lower than the GARB temperature (680–697 °C). The model for LK11-16c (Appendix 2.6), taken in conjunction with representative garnet host and plagioclase inclusion compositions, yields similar prograde P-T path constraints from ~570 °C and ~8 kbar to an estimated near-peak of 590–630 °C and 8.4–9.9 kbar (Appendix 2.6).

In-Situ U-Th-Pb Monazite Geochronology and Chemistry

Results from LASS analyses of four samples (LK11-69a, LK11-60, LK11-59, LK11-16c) are detailed below and summarized in Figures 2.8 and 2.9, as well as in Appendix 2.8. Sample LK11-69a contains 30–100 μm matrix monazite grains that generally contain high Y rims and either high Y or patchy Y cores (Fig. 2.8a; Appendix 2.7). Zoning of Th in all matrix grains is characterized by patchy

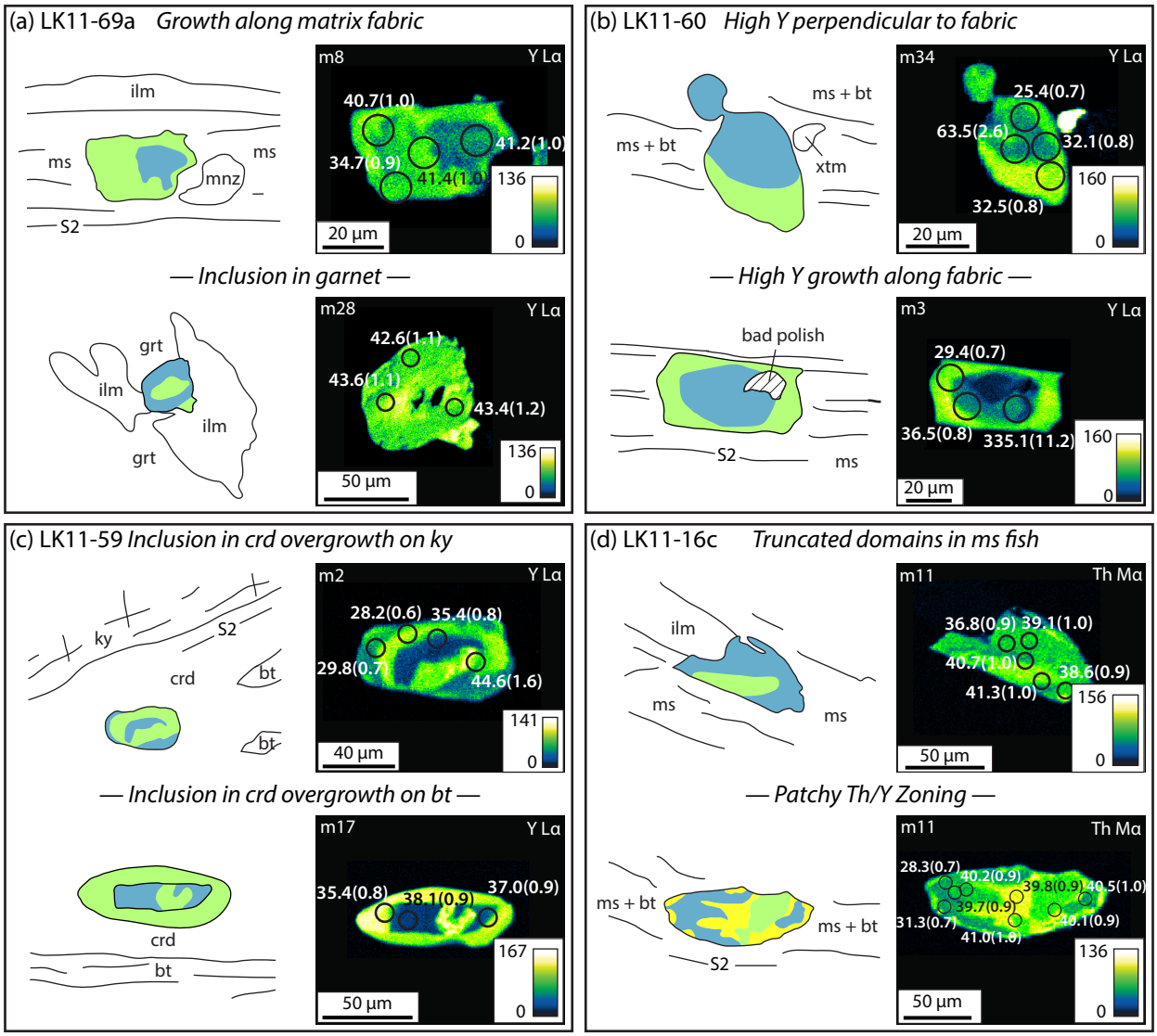


Figure 2.8. *Monazite X-ray images showing locations of LASS spot analyses and ages. (a) LK11-69a, (b) LK11-60, (c) LK11-59, and (d) LK11-16c. Sketches highlight the relationship between monazite zoning and surrounding matrix textures. X-ray images of grains are superimposed by circles that represent laser ablation split stream (LASS) analyses (~ 10 µm diameter, to scale). Numbers are the ages in Ma of each spot with 2σ uncertainty shown in parentheses.*

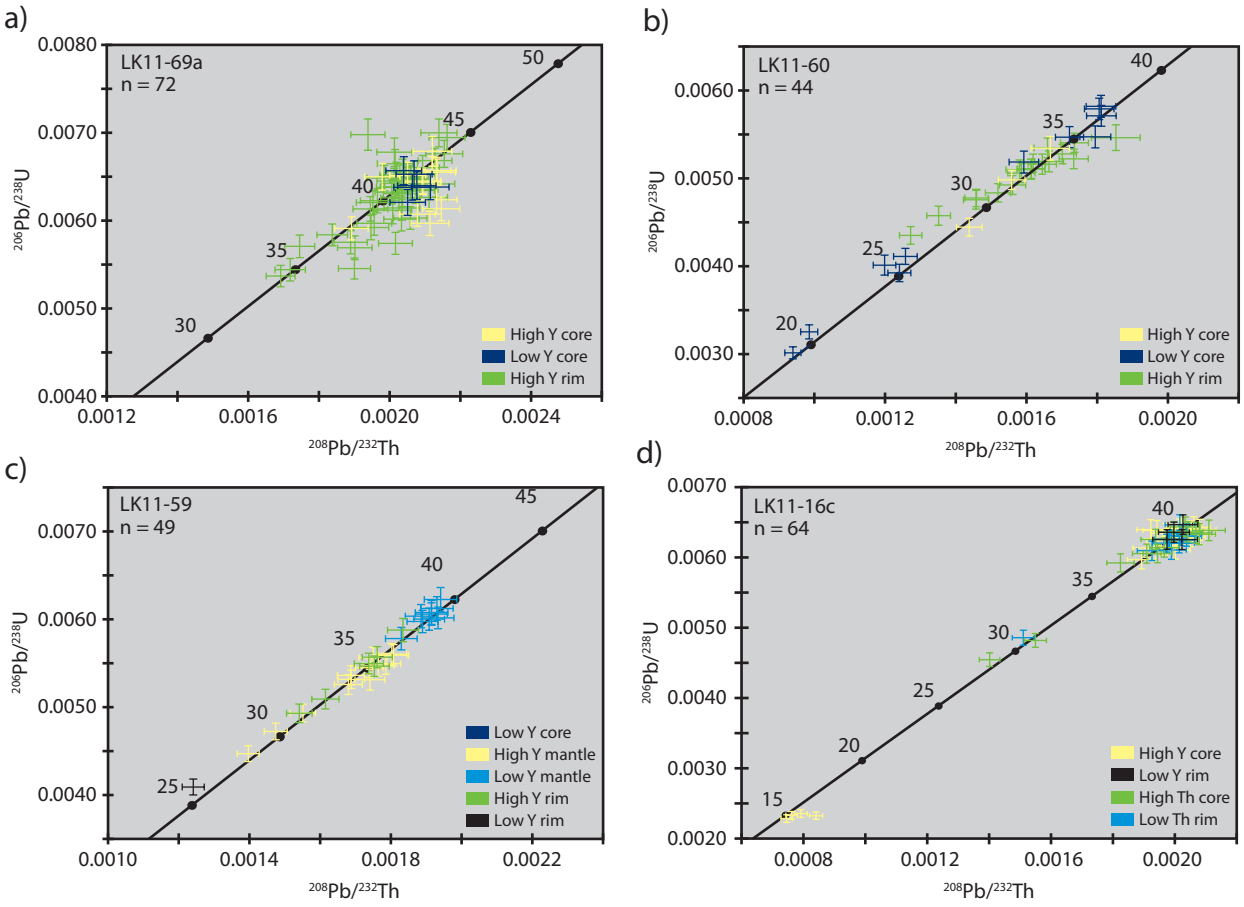


Figure 2.9. *U-Th/Pb Concordia plots for the LKD monazite geochronology samples.*

core composition and a low Th rim. Garnet-hosted monazite inclusions are preserved in LK11-69a, but only four were documented in a representative thin section, there are no consistent Y and Th zoning patterns between them, and only three (S5a: m10, m27, and m28) were suitable for petrochronology. Matrix grains are hosted in a variety of microstructural settings, but they most commonly occur as inclusions within white mica fish (Appendix 2.7). In some cases, rim growths on matrix grains are limited to faces oriented perpendicular to the matrix fabric (Fig. 2.8a; Appendix 2.7) while others completely encompass the cores of the grains. In 15 of 16 grains cores yield ages (n = 22) between 43.1 ± 1.1 Ma and 41.1 ± 1.0 Ma and high Y rims (n = 44) yield overlapping ages between 41.1 ± 1.0 Ma and 38.2 ± 1.0 Ma as well as three younger ages down to 34.2 ± 0.8 Ma (Figs 2.8a and 2.9a; Appendices 2.7 and 2.8). Two grains included in garnet (Appendices 2.7 and 2.8: m27, m28), yield core and mantle ages between 43.6 ± 1.1 Ma and 41.9 ± 1.1 Ma, and near-rim ages between 42.7 ± 1.1 Ma and 41.7 ± 1.1 Ma.

Matrix monazite are abundant in sample LK11-60, but monazite are not present as inclusions in porphyroblasts (Fig. 2.8b; Appendix 2.7). Many of the matrix grains in the thin section are too small (10–40 μm) to analyze distinct compositional domains, so only 12 grains were selected. Crystals contain low Y cores and high Y rims (Fig. 2.9b; Appendix 2.8). Th zonation is either inverse of Y zonation (high Th cores, low Th rims), or cores have patchy Th zoning and rims are uniformly low Th. In five of the 12 grains analyzed, cores are occupied by small (≤ 15 μm) apatite inclusions. All but one of the selected grains are hosted by matrix biotite or, less commonly, by matrix white mica. One exception (Appendix 2.7—m20) occurs in quartz, with compositional zoning is similar to that of the mica-hosted monazite grains. As with sample LK11-69a, high Y, low Th monazite rims either completely encompass cores of grains, or otherwise are limited to faces perpendicular to matrix foliation (Fig. 2.8b; Appendix 2.7). Most monazite in LK11-60 contain low Y (high Th) cores and high Y (low Th) rims, but when individual ages are considered, two populations of monazite emerge: those with distinctly old core ages (Pre-Himalayan) and those with relatively young core/mantle ages (Fig. 2.9b; Appendix 2.8). Young core ages vary from 36.5 ± 0.8 Ma to 29.0 ± 0.7 Ma (n = 23; Appendix 2.8). In contrast, rim ages are consistent regardless of whether they surround old cores, young cores, or young mantles, spanning from 35.0 ± 0.8 Ma to 25.7 ± 0.6 Ma. One small monazite grain (m26; Appendices 2.7 and 2.8) yields two core ages of 19.9 ± 0.5 Ma and 19.0 ± 0.5 Ma, but its high Y-rim was too thin to analyze.

In sample LK11-59 both matrix and garnet-hosted monazite are sparse, and garnet-hosted grains

are too small for accurate analyses. The matrix population is characterized by few, relatively large (50–120 μm) grains that are typically hosted by biotite or cordierite, and in some instances they occur along kyanite or ilmenite grain boundaries (Fig. 2.8c, Appendix 2.7). Of 13 grains suitable for analysis, at least three populations are loosely defined on the basis of zoning patterns. The first population has complex zoning that manifests as patchy high and low Y throughout the entire grain. The second population is defined by high Y cores, low Y mantles, and high Y rims, and the third population is defined by low Y cores, high Y mantles, and low Y rims. Although the variety and complexity of zoning patterns in monazite from sample LK11-59 could be ascribed to localized reactions or hydrothermal alteration (e.g., Montel, 1993; Williams et al., 1999; Cherniak and Pyle, 2008), the ages shown in Figures 2.8c and 2.9c, as well as Appendix 2.7, demonstrate a systematic relationship to Y content and intra-grain location that suggests the three styles of zoning are variations of one zoning pattern. High Y cores generally yield ages much older (Appendix 2.8) than observed in any other compositional domains; however, one high Y core (m2; Appendices 2.7 and 2.8) yields an age of 44.6 ± 1.6 Ma. Ages from low Y cores (n = 11) and low Y mantles (n = 12) are between 40.5 ± 1.0 Ma and 35.4 ± 0.8 Ma while ages from high Y mantles and high Y rims are between 36.5 ± 0.9 Ma and 28.2 ± 0.6 Ma (Fig. 2.9c). Only one grain had a low Y rim thick enough for analysis, and yielded one age of 25.1 ± 0.6 Ma (Appendix 2.7—m1).

Sample LK11-16c hosts large (≥ 100 μm) matrix monazite in four different microstructural settings (Fig. 2.8d; Appendices 2.7 and 2.8). No monazite are included in garnet or kyanite porphyroblasts, but some garnet porphyroblasts host allanite inclusions. In a representative thin section, matrix monazite are found: (1) within white mica and biotite fish (Appendix 2.7—m1, m14), (2) within a sharply defined microscale shear band (Appendix 2.7—m13), (3) within the hinge zone of a microscale fold (Appendix 2.7—m18, m19), and (4) included in quartz in the strain shadow of a large garnet porphyroblast (not analyzed for this study). Irrespective of microstructural setting, monazite analyzed have patchy Y and Th zoning, but a general compositional trend is characterized by higher Y and Th cores and lower Y and Th rims (Fig. 2.8d; Appendix 2.7). Boundaries between monazite compositional domains in LK11-16c are more sharply defined by Th than Y. Of grains in which core and rim domains are well defined, some appear to record growth along the host fabric (e.g., Appendix 2.7—m6), while others appear to be slightly oblique to, and truncated by, the external fabric (e.g., Appendix 2.7—m11). As with chemical zoning patterns, age distributions in individual grains are generally independent of

microstructural setting (e.g., Fig. 2.8d). Core ages are between 42.6 ± 1.1 Ma and 38.2 ± 0.9 Ma, and rims record ages from 41.31 ± 1.0 Ma to 30.5 ± 0.7 Ma (Fig. 2.9d). One monazite (m18) analyzed has the same Y and Th zoning, but core ages range from 17.0 ± 0.4 Ma to 15.1 ± 0.4 Ma while the low Y rim was not large or sharp enough to reliably analyze.

Discussion

Monazite Petrochronology

Y and Th compositions of metamorphic monazite are governed predominantly by reactions with or presence of other metamorphic phases such as garnet, allanite, apatite and xenotime (e.g., Pyle and Spear, 1999; Foster et al., 2000; Foster et al., 2004; Kohn et al., 2005; Spear, 2010), but processes such as coupled dissolution-precipitation (e.g., Seydoux-Guillaume et al., 2002; Kohn et al., 2005; Cherniak and Pyle, 2008; Williams et al., 2011) also influence monazite compositions and zoning patterns. Possible metamorphic reactions that involve monazite in rocks with metapelitic bulk composition include: (1) allanite growth at the expense of monazite at low temperature (250–450 °C; Janots et al., 2007); (2) monazite growth at the expense of allanite at low temperature (< 400 °C; Spear and Pyle, 2002), (3) monazite growth from the breakdown of garnet, plagioclase, and white mica at the staurolite isograd (Kohn and Malloy, 2004); (4) monazite growth at the expense of allanite at high temperatures (560–580 °C; Janots et al., 2009); and (5) crystallization of monazite from liquid produced by vapor-absent melting (740 °C; Pyle and Spear, 2003). Interactions between monazite, garnet, allanite, and xenotime at medium to high grade metamorphic conditions have predictable effects on the Y and Th compositions of monazite and the resultant zoning patterns. Of typical metapelitic phases, only allanite and monazite contain appreciable amounts of Th, but monazite more strongly fractionates Th leading to progressively lower Th contents with progressive monazite growth (Kohn and Malloy, 2004; Kohn et al., 2005). Zoning of Y in metamorphic monazite is typically influenced by garnet and xenotime, but can also be governed by allanite (e.g., Pyle and Spear, 2003; Spear and Pyle, 2010). Prior to garnet growth along a prograde P-T path, monazite Y zoning would generally be expected to be high to low. Garnet can sequester Y during prograde growth, so monazite that crystallizes during or after garnet growth is expected to have low Y compositions (e.g., Pyle and Spear, 1999; Pyle et al., 2001). Monazite that crystallizes during or after

garnet breakdown is expected to evolve high Y compositions, which often leads to development of high Y rims on low Y cores. Systematics of heavy rare earth elements (HREE) in monazite with respect to garnet growth and dissolution are also expected to be similar to that of Y (e.g., Zhu and O'Nions, 1999; Pyle et al., 2001; Stearns et al., 2013). In this way, pairing of mineral chemistry and geochronology provides a powerful tool for dating specific metamorphic events or reactions, and when considered alongside microstructural observations, offers insight into the potential interactions between deformation and metamorphism (e.g., Rutter and Brodie, 1995; Williams, 1994; Jamieson et al., 2002).

Monazite from Lhagoi Kangri dome metapelites generally record relatively continuous growth/recrystallization from c. 45 Ma to c. 25 Ma (e.g., Fig. 2.9). However, overlapping ages between samples, and in some cases between grains within an individual sample likely represent more than one distinct metamorphic process especially when changes in monazite chemistry are taken into consideration (Fig. 2.10). The four samples chosen for monazite petrochronology can be loosely grouped based on patterns of age versus geochemistry into two categories that do not correlate with lithology or structural position. Samples LK11-69a (Ps schist) and LK11-16c (Ps paragneiss) generally yield a concentration of older ages (44–38 Ma) paired with a broad range in Y and HREE abundance and relatively few ages below c. 34 Ma (n = 0 for sample LK11-69a and n = 8 for LK11-16c). The Y and HREE data for LK11-16c that correspond to ages younger than c. 34 Ma do not show any kind of systematic trend with age. The other two samples (LK11-60, Ps schist; LK11-59, Ps paragneiss) yield a relatively broad distribution of ages (45 to ≤ 25 Ma) that correspond to trends in Y and HREE abundance. These trends, described in more detail below, include: (1) a possible decrease in Y + HREE between c. 45 Ma and c. 40 Ma in LK11-59; (2) an increase from 40–35 Ma in LK11-59, and a similar increase in LK11-60 from 36–33 Ma; and (3) a decrease from 35–28 Ma in LK11-59, and a similar decrease in LK11-60 from 33–25Ma.

In samples LK11-69a and LK11-16c, Y abundances (Fig. 2.10a) are too scattered to indicate a trend, but HREE systematically decrease within a 44–34 Ma window in which most grains fall (Fig. 2.10b). In sample LK11-69a, where monazite included in garnet exhibits decreasing Y from core to rim and ages 44–42 Ma (Fig. 2.8a; Appendix 2.7), it is suggested that the HREE trends (Fig. 2.10b) record onset of garnet growth at c. 44 Ma, which continued until c. 34 Ma at which time high Y rims on matrix grains crystallized along matrix S_2 fabric. Since there is no significant difference in age between matrix and inclusion monazite, the span from 44–34 Ma records relatively continuous monazite growth/

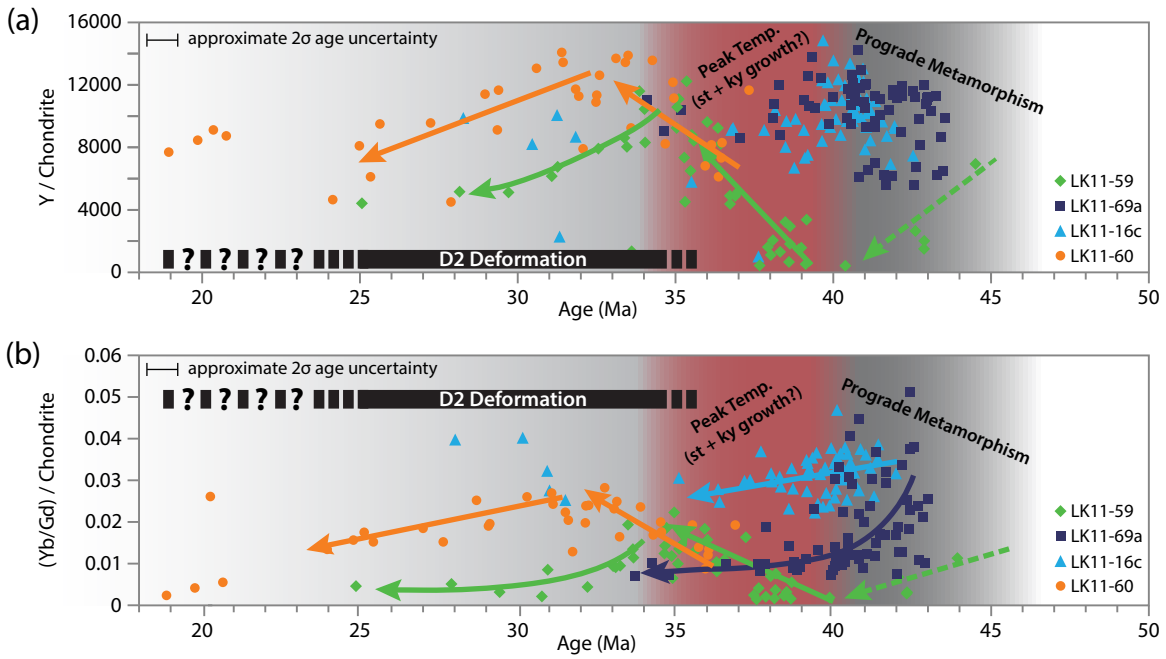


Figure 2.10. *Plots of monazite age versus chondrite-normalized element abundances. (a) Y and (b) HREE for the four samples chosen for monazite petrochronology. Note the two different types of trends (denoted by arrows) in the data, which are discussed in detail in the text. Shaded, labeled regions and D2 deformation bar correspond to age constraints discussed in text.*

recrystallization. In LK11-69a, several matrix monazite grains host allanite, xenotime, and apatite inclusions, so although monazite ages older than c. 44 Ma are not recorded, prograde metamorphism likely began prior to that with growth and subsequent breakdown of allanite + apatite ± xenotime to form high Y/high HREE monazite cores hosted in the garnet. Similarly, monazite analyses in LK11-16c define a negative HREE slope through time beginning by ≥42 Ma, which continues to at least c. 36 Ma at which point representative ages are sparse.

Monazite from samples LK11-60 and LK11-59 yield a longer and much more complex petrologic history than the other two samples. Sample LK11-59, in particular, records nearly continuous monazite growth 40–28 Ma and possibly as far back as c. 45 Ma though data are intermittent between 45 and 40 Ma. If the sparse 40–45 Ma ages are considered representative, then chemical evolution of monazite in this sample is characterized by two phases of Y + HREE depletion 45–40 Ma and 35–28 Ma, respectively, punctuated by an intervening period of Y + HREE enrichment with growth 40–35 Ma. Sample LK11-60 records a similar pattern of Y + HREE enrichment to depletion (36–33 Ma and 33–25 Ma, respectively) that is offset from the LK11-59 trend by 2–3 My (Figs 2.10a and 2.10b). One grain hosted in a cordierite overgrowth in LK11-60 indicates monazite growth took place as late as 19.0 ± 0.5 Ma. S_2 fabric development in the sample began c. 35 Ma and continued until at least 24.2 ± 0.6 Ma as constrained by ages obtained from high Y rims that grew along the matrix fabric. These ages overlap with the second phase of Y + HREE depletion in sample LK11-60, although the upper age limit interpreted for S_2 growth (35.0 ± 0.8 Ma) places it 2–3 My before Y + HREE depletion. Similarly, in LK11-59 synkinematic high-Y monazite rims constrain onset of S_2 fabric development to c. 36 Ma, predating observed Y + HREE depletion by 1–2 My, while the youngest rim ages indicate that fabric development continued until at least c. 31 Ma.

Prograde metamorphism

Thermobarometry and P-T pseudosection models from this study indicate that LKD rocks experienced peak metamorphic conditions during Barrovian metamorphism of 480–570 °C and 6–7 kbar through the garnet zone up to 640–660 °C and 8–11 kbar in the staurolite-kyanite zone (Table 2.3; Fig. 2.7; Appendix 2.6). Monazite crystallization attributed to metamorphic reactions involving allanite, apatite, or xenotime began by at least c. 45 Ma, constraining a minimum age for onset of prograde

metamorphism in the LKD. Garnet-hosted monazite inclusions with high to low Y zoning and nearly continuous ages of 44–34 Ma in samples LK11-69a and LK11-16c provide circumstantial evidence that prograde garnet growth began approximately contemporaneously with monazite growth and continued until c. 34 Ma. Rocks in the LKD that contain staurolite ± kyanite as both inclusions in garnet and as matrix porphyroblasts (e.g., LK11-70, LK11-60) suggest that their timing of growth overlaps with that of garnet (Fig. 2.11). The monazite ages that bracket prograde metamorphism in the LKD are ≥ 5 My older than monazite ages in the adjacent the Mabja-Sakya dome (Stearns et al., 2013) but ~10 My younger than Lu-Hf garnet ages from the Mabja-Sakya dome samples (Smit et al., 2014). From zircon ages of granitoids along the eastern Indus-Tsangpo suture zone (e.g., Fig. 2.1), Aikman et al. (2008) defined onset of crustal thickening in the Tethyan Himalaya at >44 Ma. Monazite geochronology investigations in the northwest India Himalaya yield 34–28 Ma (Chambers et al., 2009) and 40–31 Ma (Langille et al., 2012) ages for prograde metamorphism that are also slightly younger than those reported here, although these ages overlap when considering the duration of metamorphism interpreted for the Lhagoi Kangri dome. Timing of crustal thickening in the Tethyan Himalaya bracketed by these studies is correlative to ages reported for metamorphism and monazite growth of GHS rocks in central (48–30 Ma; Larson and Cottle, 2015) and western (43–33 Ma; Carosi et al., 2010) Nepal as well as in the Everest region ~100 km SSW of Lhagoi Kangri dome (39–16 Ma; Cottle et al., 2009).

Decompression

Mineral assemblages, microstructures, P-T path models, and monazite petrochronology reported in this study all indicate that higher grade rocks underwent exhumation characterized by substantial decompression (≥ 3.5 kbar) at nearly constant temperature (Figs 2.7–2.11; Appendix 2.6). Cordierite ± sillimanite ± biotite form overgrowths on garnet and kyanite porphyroblasts that grew during prograde metamorphism at 45–34 Ma. Monazite chemistry in two high grade rocks (LK11-60 and LK11-59) indicates growth during possible garnet breakdown at 40–34 Ma, while monazite textures in these samples indicate a c. 35 Ma minimum age for D_2 matrix fabric development. Pseudosections for these two samples predict maximum burial (assuming a lithostatic gradient of 3.3 km kbar $^{-1}$) to ~30 km (9 kbar) and ~36 km (11 kbar), respectively, during prograde staurolite and/or kyanite growth, which could also be responsible for inferred near-peak garnet breakdown. Monazite dissolution and precipitation, as

Figure 2.11. *Generalized P-T-t-D path for high grade rocks in the LKD. Polygons bordered by thick, gray lines represent THERMOCALC P-T estimates from st-, ky-, and sil-grade samples. Black-bordered polygons delineate stability fields and intersections of compositional isopleths interpreted from phase equilibria models of the sample numbers with which they are labeled. The high P, high T polygons are interpreted from: LK11-60—Stability field of interpreted equilibrium assemblage (Figs 2.7a, 2.7b); LK11-59—XAn-in-plagioclase and XSps-, Fe#-in-garnet isopleths (Appendix 2.7); LK11-16c—XAn-in-plagioclase and XSps-, Fe#-in-garnet isopleths (Appendix 2.7). The low P, high T polygons are interpreted from: LK11-60—stability field of Crd + Sil + Kfs (Fig. 2.7a) and Fe#-in-cordierite isopleths (Fig. 2.7c); LK11-59—stability field of Bt + Crd + Sil (Appendix 2.7) and Fe#-in-biotite and Fe#-in-cordierite isopleths (Appendix 2.7). As discussed in the text, the pseudosection for LK11-69a (Appendix 2.7) did not yield P-T path constraints. Two aluminosilicate triple points are shown: one derived from Holdaway and Mukhopadhyay (1993; gray dotted lines) and the other extrapolated from the pseudosection model of sample LK11-60 (Fig. 2.7). The st-in and ky-in isograds are also derived from Figure 2.7. Shading and labels along P-T trajectory correspond to features emphasized in Figure 2.10.*

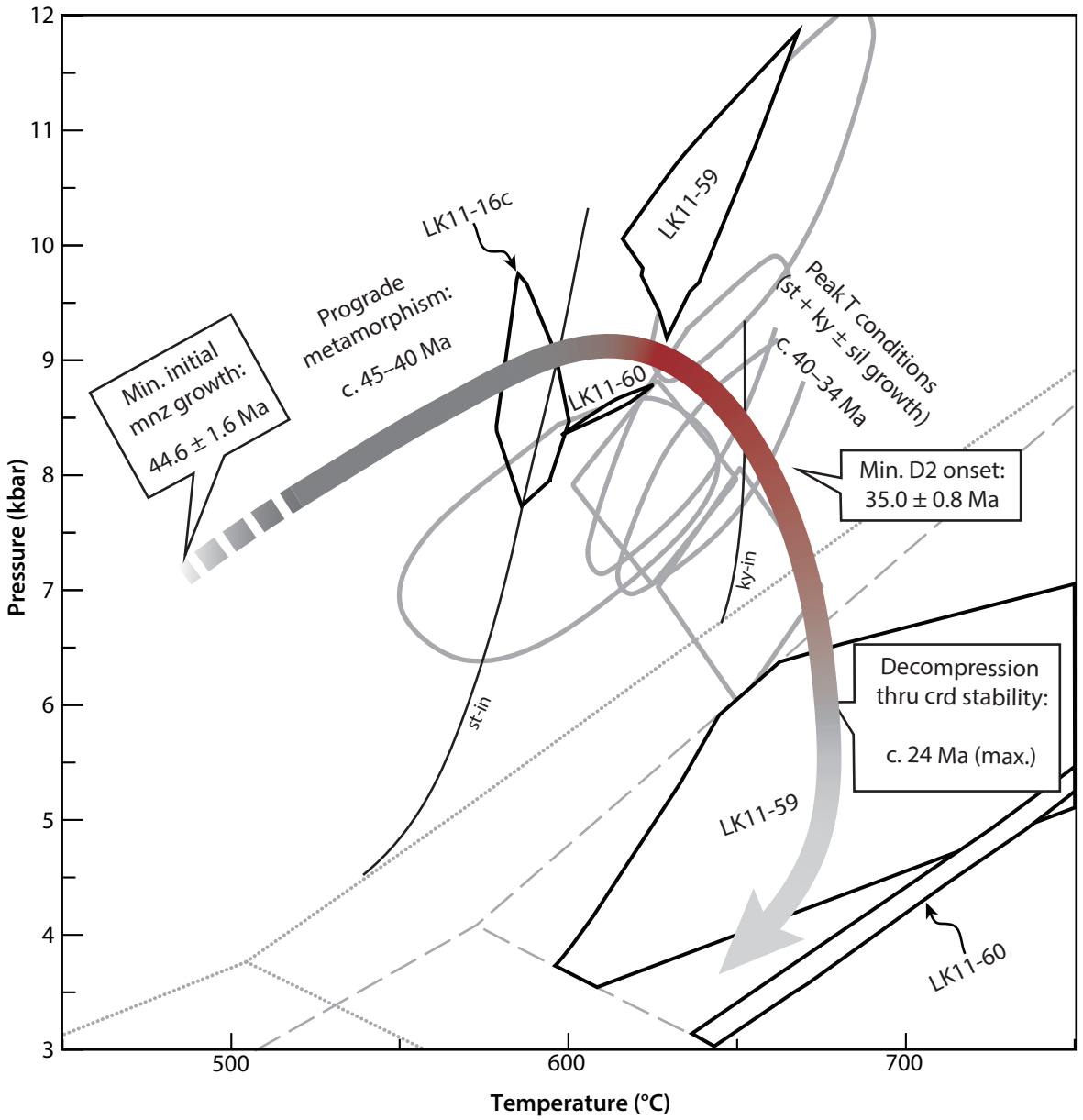


Figure 2.11. Continued.

might be expected from partial melting (e.g., Kohn et al., 2005), could be responsible for textural and chemical trends reported for the LKD monazite. Nearly continuous monazite growth/recrystallization reported in sample LK11-59 (40–28 Ma) suggests that if partial melt reactions occurred at deeper structural levels their effects were probably local (i.e., grain-scale) and of shorter duration than reported for GHS rocks in Langtang (1–4 My; Kohn et al., 2005) and Everest (3–4 My; Cottle et al., 2009) regions as well as for NHGD rocks in Mabja-Sakya (~5 My; King et al., 2010) and Leo Pargil (1–2 My; Lederer et al., 2013). While local anatexis cannot be ruled out as a source for monazite (re)precipitation, other potentially substantial Y + HREE reservoirs (garnet, allanite, and xenotime) have been identified in LKD samples and would likely have been available during monazite enrichment. Of these alternatives, it is suggested that garnet had the most significant impact on monazite systematics in the LKD. Breakdown of garnet followed by renewed growth at 35–32 Ma can account for the following observations: (1) garnet textures in high grade samples, (2) inferred metamorphic reactions from pseudosection modeling, (3) associated monazite chemical trends, and (4) 36–35 Ma constraint on initiation of S_2 fabric development.

Garnet compositions in high-grade LKD rocks are characterized by relatively homogeneous chemical composition with some representative porphyroblasts exhibiting slight chemical variation at the rims (e.g., Fig. 2.6c–2.6d; Appendix 2.4). These are interpreted to result from diffusion modification at relatively high temperature and by retrograde exchange ± net-transfer reactions, respectively. Since these diffusion profiles provide little or no details regarding garnet evolution between near-peak growth and the formation of retrograde rims, it is suggested that monazite chemical trends and modeled phase equilibria are more reliable representations of the petrogenesis of high-grade LKD rocks. First, some garnet in sample LK11-59 (e.g., bottom right corner of Fig. 2.5a) exhibit linear inclusion trails that are subparallel to the matrix fabric, suggesting that at least *some* garnet crystallization took place contemporaneous with D_2 fabric development. Although this observation alone does not indicate whether garnet growth occurred continuously or in pulses, continuous monazite chemical trends from LK11-59 (Figs 2.10a and 2.10b) suggest that crystallization between c. 40 Ma and ≤ 25 Ma took place during depletion and subsequent renewal of a Y + HREE reservoir. Furthermore, cordierite-bearing assemblages exhibit textural relationships that indicate garnet consumption during post-garnet growth decompression. Although monazite chemical data from LK11-16c are sparse at ≤38 Ma, garnet microstructures in the sample (Fig. 2.5c) indicate that dissolution occurred along grain boundaries parallel to S_2 fabric while sigma-type tails

indicate garnet recrystallization during the same time frame.

Precise constraints cannot be placed on the pressure of formation for cordierite assemblages since they define large, high variance fields in the modeled phase diagrams (e.g., Fig. 2.7), but a maximum of ~6 kbar (~ 19.8 km) is indicated by compositions of coexisting biotite and cordierite as well as by the presence of sillimanite in porphyroblast overgrowths. Using peak burial depth estimated for LK11-59 (~36 km; Appendices 2.5 and 2.6) as a starting point yields a minimum 16.2 km of exhumation along a near isothermal decompression path during D_2 deformation. As bracketed by ages associated with along-fabric monazite overgrowths, exhumation began c. 35 Ma and continued to at least c. 24 Ma, yielding an exhumation rate of 1.5 km My^{-1}. This value should only be considered a rough estimate since data presented only provide minimum constraints on amount and duration of exhumation, the two of which have opposing influences on calculated exhumation rates.

Tectonic Implications

The interpreted P-T-t-D history for the LKD rocks detailed in previous sections is summarized in Figure 2.11. While aspects of LKD tectonic evolution are unique to the Lhagoi Kangri region, the LKD rocks are a record of middle crustal processes that occurred in the Tethys Himalaya after onset of crustal thickening at 55–50 Ma and support previous geological investigations (e.g., Lee and Whitehouse, 2007) that suggest the NHGD and GHS coevolved, at least through the Eohimalayan phase of orogenesis (e.g., Hodges, 2000). In the adjacent Mabja-Sakya dome, Lee and Whitehouse (2007) constrained timing of peak metamorphism, which coincides with onset of ductile thinning, to 35 ± 0.8 Ma. Ductile vertical thinning in the LKD and Mabja-Sakya began nearly synchronously, but there are slight differences with respect to timing of peak metamorphism between the LKD and Mabja-Sakya. In the Mabja-Sakya dome, peak metamorphic conditions were interpreted to have been locked in successively from moderate (garnet-in) to high (kyanite- to sillimanite-in) grade during D_2 vertical thinning, which resulted in P-T estimates characterized by similar pressures but increasing temperatures at deeper structural levels (Lee et al., 2004). In contrast, the LKD data record a range in pressure of 6–11 kbar, although if these pressures were assumed to have formed under a lithostatic gradient of 3.3 km $kbar^{-1}$, then the LKD structural section was originally much thicker (~16.5 km) than its current ~2.5-km thickness (e.g., Fig. 2.2; c.f. Diedesch el al., 2016), which still indicates syn-metamorphic vertical thinning since interpreted P-T

paths (e.g., Figs 2.7c, 2.11) and monazite data (Fig. 2.10) for the LKD indicate that peak temperatures were attained after peak pressure and that ductile deformation began at the earliest c. 4 My later than the onset of peak temperatures. Partial melting accompanied peak metamorphism and ductile thinning c. 35 Ma in the Mabja-Sakya dome, whereas cordierite + biotite overgrowths and symplectic textures in high grade LKD rocks are indicative of sub-solidus, near-isothermal decompression within a similar time frame. Differences in local process between the LKD and Mabja-Sakya can be attributed to variations in rock compositions and differences in crustal depth (it is possible that the LKD records anatexis at lower structural levels than accessed during this study), and sustained high temperature during D_2 deformation is clearly a common theme as evidenced by syntectonic monazite ages of 35–24 Ma in the LKD and zircon ages of 35 ± 0.8 Ma and 16.2 ± 0.4 Ma (Lee and Whitehouse, 2007) in the Mabja-Sakya dome. Although a correlation between peak metamorphism in the GHS and the Mabja-Sakya dome has been previously reported by Cottle et al. (2009), it is worth restating here that GHS rocks south of Lhagoi Kangri as well as to the south-southwest, near Mt. Everest, locked in peak temperature conditions nearly synchronously with the Mabja-Sakya dome. Monazite petrochronology reported in this study indicates that the Lhagoi Kangri dome can also be added to this group. Further, these new data are the most detailed record of the early high temperature phase of middle crustal deformation and metamorphism in the Himalaya reported for any of the NHGD. The ages and temperatures reported for the LKD provide valuable constraints on the timing of initial crustal thickening and early thermomechanical evolution of the Himalaya, and they support previous studies that indicate these early Himalayan processes were distributed throughout what is now southern Tibet and the Himalaya.

Conclusions

Rocks from Lhagoi Kangri dome record an early phase of Barrovian metamorphism that is characterized by approximately concentric garnet, staurolite-kyanite, and sillimanite isograds that generally increase grade toward deeper structural levels. Garnet zone rocks record peak conditions of 550–570 °C at 6–7 kbar while staurolite-kyanite zone rocks record peak conditions of 640–660 °C at 8–11 kbar. Prograde garnet growth indicated by monazite-inclusion ages began by at least c. 45 Ma and continued until c. 40 Ma, which was followed by garnet breakdown between 40–35 Ma.

In high grade rocks, renewed garnet growth or recrystallization began c. 35 Ma and accompanied near isothermal decompression during ductile D_2 exhumation as indicated by formation of cordierite + biotite ± sillimanite-bearing overgrowths on prograde garnet and kyanite porphyroblasts, which continued until at least c. 24 Ma as recorded by syntectonic monazite growth. The timing of Barrovian metamorphism in the LKD is similar to that reported for the Mabja-Sakya and Kangmar domes (e.g., Lee and Whitehouse, 2007; Stearns et al., 2013; Smit et al., 2014) as well as for the Greater Himalayan sequence (e.g., Hodges et al., 1994; Cottle et al., 2009; Carosi et al., 2010; Smit et al., 2014), reinforcing previous authors' assertions that indicate a common evolution for rocks of the NHGD and GHS. More specifically, this study shows that prograde metamorphism, peak metamorphism, and ductile exhumation are contemporaneous between the LKD and the GHS in the Everest region, suggesting a continuity to the structure of the south Tibetan middle crust until at least Miocene time. The duration of high temperature metamorphism and deformation in the LKD (c. 40 to ≤ 24 Ma) is compatible with thermomechanical models (e.g., Beaumont et al., 2004) of lateral mid-crustal flow in the Himalaya that require protracted high temperatures to induce weakening.

References

Aikman, A. B., Harrison, T. M., and Lin, D., 2008, Evidence for Early (>44 Ma) Himalayan Crustal Thickening, Tethyan Himalaya, southeastern Tibet: Earth and Planetary Science Letters, v. 274, no. 1-2, p. 14-23.

Aleinikoff, J. N., Schenck, W. S., Plank, M. O., Srogi, L. A., Fanning, C. M., Kamo, S. L., and Bosbyshell, H., 2006, Deciphering igneous and metamorphic events in high-grade rocks of the Wilmington complex, Delaware: Morphology, cathodoluminescence and backscattered electron zoning, and SHRIMP U-Pb geochronology of zircon and monazite: Geological Society of America Bulletin, v. 118, no. 1-2, p. 39-64.

Aoya, M., Wallis, S. R., Terada, K., Lee, J., Kawakami, T., Wang, Y., and Heizler, M., 2005, North-south extension in the Tibetan crust triggered by granite emplacement: Geology, v. 33, no. 11, p. 853-856.

Beaumont, C., Jamieson, R. A., Nguyen, M. H., and Medvedev, S., 2004, Crustal channel flows: 1. Numerical models with applications to the tectonics of the Himalayan-Tibetan orogen: Journal of Geophysical Research: Solid Earth, v. 109, no. B6, p. B06406.

Burchfiel, B. C., Zhiliang, C., Hodges, K. V., Yuping, L., Royden, L. H., Changrong, D., and Jiene, X., 1992, The South Tibetan Detachment System, Himalayan Orogen: Extension Contemporaneous With and Parallel to Shortening in a Collisional Mountain Belt: Geological Society of America Special Papers, v. 269, p. 1-41.

Burg, J. P., Guiraud, M., Chen, G. M., and Li, G. C., 1984, Himalayan metamorphism and deformations in the North Himalayan Belt (southern Tibet, China): Earth and Planetary Science Letters, v. 69, no. 2, p. 391-400.

Carosi, R., Montomoli, C., Rubatto, D., and Visonà, D., 2010, Late Oligocene high-temperature shear zones in the core of the Higher Himalayan Crystallines (Lower Dolpo, western Nepal): Tectonics, v. 29, no. 4, p. n/a-n/a.

Catlos, E. J., Harrison, T. M., Kohn, M. J., Grove, M., Ryerson, F. J., Manning, C. E., and Upreti, B. N., 2001, Geochronologic and thermobarometric constraints on the evolution of the Main Central Thrust, central Nepal Himalaya: Journal of Geophysical Research: Solid Earth, v. 106, no. B8, p. 16177-16204.

Catlos, E. J., Harrison, T. M., Manning, C. E., Grove, M., Rai, S. M., Hubbard, M. S., and Upreti, B. N., 2002, Records of the evolution of the Himalayan orogen from in situ Th–Pb ion microprobe dating of monazite: Eastern Nepal and western Garhwal: Journal of Asian Earth Sciences, v. 20, no. 5, p. 459-479.

Chambers, J., Caddick, M., Argles, T., Horstwood, M., Sherlock, S., Harris, N., Parrish, R., and Ahmad, T., 2009, Empirical constraints on extrusion mechanisms from the upper margin of an exhumed high-grade orogenic core, Sutlej valley, NW India: Tectonophysics, v. 477, no. 1–2, p. 77-92.

Chen, Z., Liu, Y., Hodges, K. V., Burchfiel, B. C., Royden, L. H., and Deng, C., 1990, The Kangmar dome: a metamorphic core complex in southern Xizang (Tibet): Science, v. 250, no. 4987, p. 1552-1556.

Cherniak, D. J., and Pyle, J. M., 2008, Th diffusion in monazite: Chemical Geology, v. 256, no. 1–2, p. 52-61.

Chernoff, C. B., and Carlson, W. D., 1997, Disequilibrium for Ca during growth of pelitic garnet: Journal of Metamorphic Geology, v. 15, no. 4, p. 421-438.

Coggon, R., and Holland, T. J. B., 2002, Mixing properties of phengitic micas and revised garnet-phengite thermobarometers: Journal of Metamorphic Geology, v. 20, no. 7, p. 683-696.

Connolly, J. A. D., 2009, The geodynamic equation of state: What and how: Geochemistry, Geophysics,

Geosystems, v. 10, no. 10, p. Q10014.
Cottle, J. M., Horstwood, M. S. A., and Parrish, R. R., 2009, A new approach to single shot laser ablation analysis and its application to in situ Pb/U geochronology: Journal of Analytical Atomic Spectrometry, v. 24, no. 10, p. 1355-1363.
Dempster, T. J., 1985, Garnet zoning and metamorphism of the Barrovian type area, Scotland: Contributions to Mineralogy and Petrology, v. 89, no. 1, p. 30-38.
Diedesch, T., Jessup, M.J., Cottle, J.M., Zeng, L., 2016, Geologic evolution of Lhagoi Kangri dome, southern Tibet: Lithosphere, doi: 10.1130/L506.1.
Foster, G., Kinny, P., Vance, D., Prince, C., and Harris, N., 2000, The significance of monazite U–Th–Pb age data in metamorphic assemblages; a combined study of monazite and garnet chronometry: Earth and Planetary Science Letters, v. 181, no. 3, p. 327-340.
Foster, G., Parrish, R. R., Horstwood, M. S. A., Chenery, S., Pyle, J., and Gibson, H. D., 2004, The generation of prograde P–T–t points and paths; a textural, compositional, and chronological study of metamorphic monazite: Earth and Planetary Science Letters, v. 228, no. 1–2, p. 125-142.
Fuhrman, M. L., and Lindsley, D. H., 1988, Ternary-feldspar modeling and thermometry: American Mineralogist, v. 73, no. 3-4, p. 201-215.
Grujic, D., Hollister, L. S., and Parrish, R. R., 2002, Himalayan metamorphic sequence as an orogenic channel: insight from Bhutan: Earth and Planetary Science Letters, v. 198, no. 1, p. 177-191.
Guidotti, C.V., Yates, M.G., Dyar, M.D., Taylor, M.E., 1994, Petrogenetic implications of the Fe3+ content of muscovite in pelitic schists: American Mineralogist, v. 79, p. 793–795.
Harrison, T.M., Lovera, O. M., and Grove, M., 1997, New insights into the origin of two contrasting Himalayan granite belts: Geology, v. 25, no. 10, p. 899-902.
Holdaway, M. J., 2000, Application of new experimental and garnet Margules data to the garnet-biotite geothermometer: American Mineralogist, v. 85, no. 7-8, p. 881-892.
Holdaway, M. J., and Mukhopadhyay, B., 1993, A reevaluation of the stability relations of andalusite; thermochemical data and phase diagram for the aluminum silicates: American Mineralogist, v. 78, no. 3-4, p. 298-315.
Horstwood, M. S. A., Foster, G. L., Parrish, R. R., Noble, S. R., and Nowell, G. M., 2003, Common-Pb corrected in situ U-Pb accessory mineral geochronology by LA-MC-ICP-MS: Journal of Analytical Atomic Spectrometry, v. 18, no. 8, p. 837-846.
Jamieson, R. A., Beaumont, C., Nguyen, M. H., and Lee, B., 2002, Interaction of metamorphism, deformation and exhumation in large convergent orogens: Journal of Metamorphic Geology, v. 20, no. 1, p. 9-24.
Janots, E., Brunet, F., Goffé, B., Poinssot, C., Burchard, M., and Cemič, L., 2007, Thermochemistry of monazite-(La) and dissakisite-(La): implications for monazite and allanite stability in metapelites: Contributions to Mineralogy and Petrology, v. 154, no. 1, p. 1-14.
Janots, E., Engi, M., Rubatto, D., Berger, A., Gregory, C., and Rahn, M., 2009, Metamorphic rates in collisional orogeny from in situ allanite and monazite dating: Geology, v. 37, no. 1, p. 11-14.
Jessup, M. J., Cottle, J. M., Searle, M. P., Law, R. D., Newell, D. L., Tracy, R. J., and Waters, D. J., 2008, P–T–t–D paths of Everest Series schist, Nepal: Journal of Metamorphic Geology, v. 26, no. 7, p. 717-739.
King, J., Harris, N., Argles, T., Parrish, R., Charlier, B., Sherlock, S., and Zhang, H. F., 2007, First field evidence of southward ductile flow of Asian crust beneath southern Tibet: Geology, v. 35, no. 8, p. 727-730.
King, J., Harris, N., Argles, T., Parrish, R., and Zhang, H., 2010, Contribution of crustal anatexis to the tectonic evolution of Indian crust beneath southern Tibet: Geological Society of America Bulletin, v. 123, no. 1-2, p. 218-239.

Kohn, M. J., and Malloy, M. A., 2004, Formation of monazite via prograde metamorphic reactions among common silicates: implications for age determinations: Geochimica et Cosmochimica Acta, v. 68, no. 1, p. 101-113.
Kohn, M. J., Wieland, M. S., Parkinson, C. D., and Upreti, B. N., 2005, Five generations of monazite in Langtang gneisses: implications for chronology of the Himalayan metamorphic core: Journal of Metamorphic Geology, v. 23, no. 5, p. 399-406.
Kylander-Clark, A. R. C., Hacker, B. R., and Cottle, J. M., 2013, Laser-ablation split-stream ICP petrochronology: Chemical Geology, v. 345, no. 0, p. 99-112.
Larson, K. P., and Cottle, J. M., 2015, Initiation of crustal shortening in the Himalaya: Terra Nova, v. 27, no. 3, p. 169-174.
Larson, K. P., Godin, L., Davis, W. J., and Davis, D. W., 2010, Out-of-sequence deformation and expansion of the Himalayan orogenic wedge: insight from the Changgo culmination, south central Tibet: Tectonics, v. 29, no. 4, p. TC4013.
Le Breton, N., and Thompson, A. B., 1988, Fluid-absent (dehydration) melting of biotite in metapelites in the early stages of crustal anatexis: Contributions to Mineralogy and Petrology, v. 99, no. 2, p. 226-237.
Le Fort, P., Cuney, M., Deniel, C., France-Lanord, C., Sheppard, S. M. F., Upreti, B. N., and Vidal, P., 1987, Crustal generation of the Himalayan leucogranites: Tectonophysics, v. 134, no. 1–3, p. 39-57.
Lee, J., Hacker, B., and Wang, Y., 2004, Evolution of North Himalayan gneiss domes: structural and metamorphic studies in Mabja Dome, southern Tibet: Journal of Structural Geology, v. 26, no. 12, p. 2297-2316.
Lee, J., McClelland, W., Wang, Y., Blythe, A., and McWilliams, M., 2006, Oligocene-Miocene middle crustal flow in southern Tibet: geochronology of Mabja Dome: Geological Society, London, Special Publications, v. 268, no. 1, p. 445-469.
Lee, J., and Whitehouse, M. J., 2007, Onset of mid-crustal extensional flow in southern Tibet: Evidence from U/Pb zircon ages: Geology, v. 35, no. 1, p. 45-48.
Ludwig, K. R., 2000, User's manual for Isoplot/Ex rev. 3.23, vol. 1a. Berkeley Geochronology Center, Special Publication, 56.
Molnar, P., and Tapponnier, P., 1977, Relation of the tectonics of eastern China to the India-Eurasia collision: Application of slip-line field theory to large-scale continental tectonics: Geology, v. 5, no. 4, p. 212-216.
Montel, J.-M., 1993, Geochemistry of Accessory Minerals A model for monazite/melt equilibrium and application to the generation of granitic magmas: Chemical Geology, v. 110, no. 1, p. 127-146.
Najman, Y., Appel, E., Boudagher-Fadel, M., Bown, P., Carter, A., Garzanti, E., Godin, L., Han, J., Liebke, U., Oliver, G., Parrish, R., and Vezzoli, G., 2010, Timing of India-Asia collision: Geological, biostratigraphic, and palaeomagnetic constraints: Journal of Geophysical Research: Solid Earth, v. 115, no. B12, p. n/a-n/a.
Nelson, K. D., et al., 1996, Partially Molten Middle Crust Beneath Southern Tibet: Synthesis of Project INDEPTH Results: Science, v. 274, no. 5293, p. 1684-1688.
Patiño Douce, A. E., and Harris, N., 1998, Experimental Constraints on Himalayan Anatexis: Journal of Petrology, v. 39, no. 4, p. 689-710.
Patiño Douce, A. E., and Johnston, A. D., 1991, Phase equilibria and melt productivity in the pelitic system: implications for the origin of peraluminous granitoids and aluminous granulites: Contributions to Mineralogy and Petrology, v. 107, no. 2, p. 202-218.
Paton, C., Woodhead, J. D., Hellstrom, J. C., Hergt, J. M., Greig, A., and Maas, R., 2010, Improved laser ablation U-Pb zircon geochronology through robust downhole fractionation correction:

Geochemistry, Geophysics, Geosystems, v. 11, no. 3, p. n/a-n/a.
Pyle, J. M., Spear, F. S., Rudnick, R. L., and McDonough, W. F., 2001, Monazite–Xenotime–Garnet Equilibrium in Metapelites and a New Monazite–Garnet Thermometer: Journal of Petrology, v. 42, no. 11, p. 2083-2107.
Pyle, J.M., and Spear, F.S., 1999, Yttrium zoning in garnet: coupling of major and accessory phases during metamorphic reactions: Geological Materials Research, v. 1, n. 6, p. 1–49.
Pyle, J.M., and Spear F.S., 2003, Four generations of accessory-phase growth in low-pressure migmatites from SW New Hampshire: American Mineralogist, v. 88, p. 338.
Quigley, M., Liangjun, Y., Xiaohan, L., Wilson, C. J. L., Sandiford, M., and Phillips, D., 2006, 40Ar/39Ar thermochronology of the Kampa Dome, southern Tibet: Implications for tectonic evolution of the North Himalayan gneiss domes: Tectonophysics, v. 421, no. 3–4, p. 269-297.
Rice, A.H.N., Mitchell, J.I., 1991, Porphyroblast textural sector zoning and matrix displacement: Mineralogical Magazine, v. 55, p. 379–396.
Rolfo, F., Lombardo, B., Musumeci, G., Pertusati, P., and Peruzzo, L., Geology and Metamorphism of the Lhako Kangri Metamorphic Dome, South Tibet, in Proceedings 32nd International Geological Congress, Florence, 2004, International Union of Geological Sciences.
Rutter, E. H., and Brodie, K. H., 1995, Mechanistic interactions between deformation and metamorphism: Geological Journal, v. 30, no. 3-4, p. 227-240.
Searle, M. P., Simpson, R. L., Law, R. D., Parrish, R. R., and Waters, D. J., 2003, The structural geometry, metamorphic and magmatic evolution of the Everest massif, High Himalaya of Nepal–South Tibet: Journal of the Geological Society, v. 160, no. 3, p. 345-366.
Seydoux-Guillaume, A.-M., Paquette, J.-L., Wiedenbeck, M., Montel, J.-M., and Heinrich, W., 2002, Experimental resetting of the U–Th–Pb systems in monazite: Chemical Geology, v. 191, no. 1–3, p. 165-181.
Smit, M. A., Hacker, B. R., and Lee, J., 2014, Tibetan garnet records early Eocene initiation of thickening in the Himalaya: Geology, v. 42, n. 7.
Spear, F., and Cheney, J., 1989, A petrogenetic grid for pelitic schists in the system SiO2-Al2O3-FeO-MgO-K2O-H2O: Contributions to Mineralogy and Petrology, v. 101, no. 2, p. 149-164.
Spear, F. S., 2010, Monazite–allanite phase relations in metapelites: Chemical Geology, v. 279, no. 1–2, p. 55-62.
Spear, F. S., and Florence, F. P., 1992, The Archaean Limpo Granulite Belt: Tectonics and Deep Crustal Processes Thermobarometry in granulites: pitfalls and new approaches: Precambrian Research, v. 55, no. 1, p. 209-241.
Spear, F. S., and Pyle, J. M., 2002, Apatite, Monazite, and Xenotime in Metamorphic Rocks: Reviews in Mineralogy and Geochemistry, v. 48, n. 1, p. 293-335.
———, 2010, Theoretical modeling of monazite growth in a low-Ca metapelite: Chemical Geology, v. 273, no. 1–2, p. 111-119.
Spear, S. F., Kohn, J. M., and Cheney, T. J., 1999, P-T paths from anatectic pelites: Contributions to Mineralogy and Petrology, v. 134, no. 1, p. 17-32.
Stearns, M. A., Hacker, B. R., Ratschbacher, L., Lee, J., Cottle, J. M., and Kylander-Clark, A., 2013, Synchronous Oligocene–Miocene metamorphism of the Pamir and the north Himalaya driven by plate-scale dynamics: Geology, v. 41, no. 10, p. 1071-1074.
Watts, D. R., Harris, N. B. W., and Group, T. N. G. S. W., 2005, Mapping granite and gneiss in domes along the North Himalayan antiform with ASTER SWIR band ratios: Geological Society of America Bulletin, v. 117, no. 7-8, p. 879-886.
White, Powell, Holland, and Worley, 2000, The effect of TiO2 and Fe2O3 on metapelitic assemblages at greenschist and amphibolite facies conditions: mineral equilibria calculations in the system

K2O–FeO–MgO–Al2O3–SiO2–H2O–TiO2–Fe2O3: Journal of Metamorphic Geology, v. 18, no. 5, p. 497-511.
White, R. W., Powell, R., and Holland, T. J. B., 2001, Calculation of partial melting equilibria in the system Na2O–CaO–K2O–FeO–MgO–Al2O3–SiO2–H2O (NCKFMASH): Journal of Metamorphic Geology, v. 19, no. 2, p. 139-153.
———, 2007, Progress relating to calculation of partial melting equilibria for metapelites: Journal of Metamorphic Geology, v. 25, no. 5, p. 511-527.
Whitney, D. L., and Evans, B. W., 2010, Abbreviations for names of rock-forming minerals: American Mineralogist, v. 95, no. 1, p. 185-187.
Williams, M. L., 1994, Sigmoidal inclusion trails, punctuated fabric development, and interactions between metamorphism and deformation: Journal of Metamorphic Geology, v. 12, no. 1, p. 1-21.
Williams, M. L., Jercinovic, M. J., Harlov, D. E., Budzyń, B., and Hetherington, C. J., 2011, Resetting monazite ages during fluid-related alteration: Chemical Geology, v. 283, no. 3–4, p. 218-225.
Williams, M. L., Jercinovic, M. J., and Terry, M. P., 1999, Age mapping and dating of monazite on the electron microprobe: Deconvoluting multistage tectonic histories: Geology, v. 27, no. 11, p. 1023-1026.
Zhang, H., Harris, N., Parrish, R., Kelley, S., Zhang, L., Rogers, N., Argles, T., and King, J., 2004, Causes and consequences of protracted melting of the mid-crust exposed in the North Himalayan antiform: Earth and Planetary Science Letters, v. 228, no. 1–2, p. 195-212.
Zhu, X. K., and O'Nions, R. K., 1999, Zonation of monazite in metamorphic rocks and its implications for high temperature thermochronology: a case study from the Lewisian terrain: Earth and Planetary Science Letters, v. 171, no. 2, p. 209-220.the North Himalayan antiform with ASTER SWIR band ratios: Geological Society of America Bulletin, v. 117, no. 7-8, p. 879-886.
White, Powell, Holland, and Worley, 2000, The effect of TiO2 and Fe2O3 on metapelitic assemblages at greenschist and amphibolite facies conditions: mineral equilibria calculations in the system K2O–FeO–MgO–Al2O3–SiO2–H2O–TiO2–Fe2O3: Journal of Metamorphic Geology, v. 18, no. 5, p. 497-511.
White, R. W., Powell, R., and Holland, T. J. B., 2001, Calculation of partial melting equilibria in the system Na2O–CaO–K2O–FeO–MgO–Al2O3–SiO2–H2O (NCKFMASH): Journal of Metamorphic Geology, v. 19, no. 2, p. 139-153.
———, 2007, Progress relating to calculation of partial melting equilibria for metapelites: Journal of Metamorphic Geology, v. 25, no. 5, p. 511-527.
Whitney, D. L., and Evans, B. W., 2010, Abbreviations for names of rock-forming minerals: American Mineralogist, v. 95, no. 1, p. 185-187.
Williams, M. L., 1994, Sigmoidal inclusion trails, punctuated fabric development, and interactions between metamorphism and deformation: Journal of Metamorphic Geology, v. 12, no. 1, p. 1-21.
Williams, M. L., Jercinovic, M. J., Harlov, D. E., Budzyń, B., and Hetherington, C. J., 2011, Resetting monazite ages during fluid-related alteration: Chemical Geology, v. 283, no. 3–4, p. 218-225.
Williams, M. L., Jercinovic, M. J., and Terry, M. P., 1999, Age mapping and dating of monazite on the electron microprobe: Deconvoluting multistage tectonic histories: Geology, v. 27, no. 11, p. 1023-1026.
Zhang, H., Harris, N., Parrish, R., Kelley, S., Zhang, L., Rogers, N., Argles, T., and King, J., 2004, Causes and consequences of protracted melting of the mid-crust exposed in the North Himalayan antiform: Earth and Planetary Science Letters, v. 228, no. 1–2, p. 195-212.
Zhu, X. K., and O'Nions, R. K., 1999, Zonation of monazite in metamorphic rocks and its implications for high temperature thermochronology: a case study from the Lewisian terrain: Earth and Planetary Science Letters, v. 171, no. 2, p. 209-220.

Appendix 2.1.
Petrographic Descriptions

Unit Ts Schist.

LK11-35 (Fig. 2.3a) is a graphitic schist from the north side of the dome with garnet and chloritoid porphyroblasts. The sample contains a mylonitic S2 foliation (255°, 18° NE) and a weak L2 lineation (21° → 019°), the latter of which is defined by aligned chlorite + white mica and elongate quartz aggregates. Garnet porphyroblasts are subhedral to euhedral, generally idioblastic, and relatively inclusion poor. Where present, garnet inclusions form a textural sector zoning pattern (Rice and Mitchell, 1991), or, more commonly a sigmoidal trail that is continuous with matrix fabric. Inclusion phases in garnet are primarily quartz and minor ilmenite, while some garnet include minor chlorite and biotite although some inclusion trails are subparallel to the external fabric. In contrast, chloritoid grains are anhedral to subhedral and poikiloblastic, although they are also idioblastic with respect to garnet. The matrix of sample LK11-35 is defined by intercalated fine- and coarse-grained domains that are dominated, respectively, by graphite and quartz. Chlorite, white mica, and ilmenite are present throughout both domains and aligned parallel to the main foliation. Both garnet and chloritoid porphyroblasts are more common in the finer grained, graphitic intervals, while strain shadows surrounding the porphyroblasts consist predominantly of coarser aggregates of quartz + biotite ± ilmenite.

LK-67a (Fig. 2.3b), collected from the east side of the dome, is a graphitic schist that is mineralogically similar to LK11-35. The sample also contains a similar mylonitic S2 foliation (330 °, 21° NE) and L2 mineral lineation (4° → 335°) to that of LK11-35. Garnet porphyroblasts in LK-67a are generally subhedral and are idioblastic to hypidioblastic with respect to the matrix minerals. The porphyroblasts exhibit varying degrees of textural sector zoning, and inclusion patterns are random to S-shaped trails that bisect the grain boundary at a small angle to the external fabric (Diedesch et al., *in review*). Inclusions are predominantly quartz with minor amounts of biotite, chlorite, and ilmenite. Both coarse and fine grained domains contain equigranular quartz aggregates and laths of chlorite, as well as minor biotite, white mica, and ilmenite; however, fine grained intervals are compositionally distinct in that they also contain graphite. Accessory epidote (clinozoisite) is also present throughout the matrix and (rarely) as inclusions in garnet porphyroblasts. Garnet porphyroblasts are also mantled by strain caps and shadows, and mineral phases in the strain shadows are not compositionally distinct from the rest of the matrix. In both of the unit Ts samples, garnet and chloritoid porphyroblasts exhibit both symmetric and mixed top-NNE and top-SSW shear sense representative of the ambiguous shear sense associated with D2 deformation at this structural level in the dome (Diedesch et al., *in review*).

Unit Ps Schist.

LK-48 (Fig. 2.4a) is a garnet schist from the south side of the dome with a matrix foliation (S2; 090°, 34° S) defined, in order of decreasing abundance, by quartz + biotite + white mica + plagioclase (Fig. 2.4a). The matrix also contains small, discontinuous C'-type shear bands and white mica fish that collectively define a mixed top-S and top-N shear sense. Ilmenite, tourmaline, and apatite are minor matrix phases, and in a few instances epidote grains are included in matrix biotite and white mica laths. Allanite is also common as an accessory phase in the matrix, and is particularly evident where included in biotite and surrounded by pleochroic haloes. Garnet porphyroblasts are relatively small (≤ 400 μm), subhedral to anhedral, poikiloblastic, and frequently mantled by chlorite and white mica ± biotite, and with the addition of quartz, also defines the mineral assemblage in asymmetric strain shadows on the porphyroblasts. In contrast to the matrix kinematic indicators, asymmetric strain shadows on garnet consistently record top-S shear sense (Fig. 2.4a; Diedesch et al., *in review*). S-shaped inclusion trails in the garnet porphyroblasts are defined by quartz + ilmenite + apatite ± biotite ± epidote, and in many cases the trails intersect the grain boundaries at a subparallel trajectory to that of the matrix foliation

LK-57 (Fig. 2.4b) is an aluminous garnet-staurolite schist that contains spaced cleavage (unoriented) defined by mica domains of dominantly white mica, with lesser amounts of biotite, and intercalated with domains of amoeboidal quartz and plagioclase grains (Fig. 2.4b). Minor and accessory matrix phases in LK-57 include ilmenite, tourmaline, epidote, and zircon. Garnet porphyroblasts throughout the sample are subhedral to euhedral

and idioblastic with respect to the matrix. Cores of the porphyroblasts are inclusion-rich whereas the mantles are inclusion-poor. Some garnet porphyroblasts contain a thin mantle of chlorite, and most exhibit strain shadows of variable composition, with quartz + biotite ± chlorite being the most common assemblage. Inclusions in the garnet are quartz, plagioclase, apatite, and ilmenite ± tourmaline ± epidote. Staurolite porphyroblasts are substantially smaller than garnet porphyroblasts, subhedral, and variably idioblastic to hypidioblastic with respect to biotite and quartz (Fig. 2.4b). Inclusions in staurolite are sparse and consist of quartz ± tourmaline.

LK-59c (Fig. 2.4c) is a float sample collected from the south side of LKD that is of similar composition and contains a similar mineral assemblage to that of LK-57. The matrix fabric (S2?) consists of quartz (Q) and mica (M) domains. Q domains consist of equigranular patches of quartz with lesser plagioclase and thin, isolated laths of biotite. M domains are wide and composed mostly of white mica with a small proportion of biotite. Additional matrix phases are ilmenite and chlorite. In contrast to sample LK-57, staurolite porphyroblasts in LK-59c are roughly equal in size to garnet porphyroblasts and are subhedral to euhedral and idioblastic. Staurolite porphyroblasts are relatively inclusion free with a few examples of included quartz, whereas garnet porphyroblasts contain sigmoidal trails of quartz + apatite + epidote + ilmenite.

LK11-70 (Fig. 2.4d) is aluminous garnet-staurolite-kyanite schist sampled from the central portion of the dome 490 m structurally above the contact with the underlying orthogneiss. The matrix S2 foliation (223°, 26° NW) is defined by biotite and white mica layers with interspersed elongate aggregates of quartz ± plagioclase. Matrix phases also include tourmaline, ilmenite, rutile, and allanite, the latter of which occurs predominantly as inclusions in biotite laths. Minor amounts of chlorite replacing biotite occur throughout the matrix as well. Small staurolite and kyanite porphyroblasts are abundant throughout the sample and also occur as inclusions in much larger garnet porphyroblasts. Staurolite in the matrix, as well as staurolite inclusions in a large plagioclase porphyroblast, exhibit inclusion-rich cores and inclusion-poor mantles. In several instances staurolite is hypidioblastic with respect to kyanite and surrounded by biotite + muscovite + quartz, a texture suggestive of the Barrovian kyanite-in reaction: St + Qz + Ms = Ky + Bt + H_2O (e.g. Dempster, 1985). Kyanite porphyroblasts are idioblastic and exhibit variable orientations with respect to the foliation. Large plagioclase porphyroblasts are also present in sample LK11-70, and these contain cores with inclusion trails of staurolite + biotite + quartz + tourmaline aligned obliquely to matrix S2 fabric. Plagioclase mantles exhibit inclusion trails of biotite + staurolite + quartz + white mica that are parallel and continuous with S2 matrix. Garnet porphyroblasts in LK11-70 contain sigmoidal inclusion trails or millipede structures that are defined by aligned quartz, apatite, ilmenite, kyanite, staurolite, tourmaline, and minor allanite.

LK11-69a (Fig. 2.4e), a sample collected from the central domain ~40 m structurally below LK11-70, is a garnet-bearing pelitic schist with a matrix S2 foliation (240°, 30° NW) defined by quartz domains interspersed with white mica fish and fine layers of interfingered biotite and white mica that exhibit minor replacement by chlorite. Tails of mica fish consist of a larger proportion of biotite than the cores. The sample is particularly distinct in that it lacks a feldspar phase, but other matrix minerals include ilmenite, rutile, monazite, and zircon. Garnet porphyroblasts are subhedral, idioblastic, and contain large inclusions of quartz and ilmenite with smaller, less abundant chlorite that define a vaguely sigmoidal trail. Strain shadows framing the porphyroblasts consist of thin rims of chlorite in addition to quartz + biotite ± white mica.

LK11-60 (Fig. 2.4f) is a garnet-cordierite schist that was collected from another transect through the central part of the dome and derives from ~325 m structurally above the contact with the underlying orthogneiss. The matrix foliation (S2; 326°, 30° NE) is defined by aligned biotite and white mica that occurs in two compositional domains, quartz-poor and quartz-rich. Other matrix phases include plagioclase, ilmenite, and tourmaline with minor amounts of monazite as inclusions in biotite laths. Garnet porphyroblasts in the sample are poikiloblastic and show textural evidence of resorption and replacement by quartz + cordierite + biotite ± prismatic sillimanite. Inclusions in garnet consist of randomly oriented grains of quartz, staurolite and white mica. Cordierite porphyroblasts host randomly oriented, often anhedral, biotite with symplectic quartz intergrowths along with radiating clusters of fibrolite, white mica, staurolite, and rutile. At least one cordierite porphyroblast contains a linear trail of tourmaline inclusions as well. A petrographically distinct phase of cordierite forms rims on the cordierite porphyroblasts and also rims kyanite and biotite throughout the sample. Staurolite porphyroblasts distributed throughout the sample are

subhedral and idioblastic with respect to matrix white mica, biotite, and quartz, while inclusion trails composed of quartz in the mantles of the porphyroblasts are continuous with the matrix foliation.

Unit Ps Paragneiss.

LK11-59 (Fig. 2.5a) is a garnet- and kyanite-bearing pelitic gneiss collected from the central domain ~50 m below sample LK11-60 and ~275 m structurally above the core-cover contact. The sample contains poikiloblastic, subhedral garnet porphyroblasts set in an S2 matrix foliation (260°, 24° NW) defined by biotite interspersed with quartz, plagioclase, and kyanite that are aligned along S2. Garnet porphyroblasts are mantled by cordierite + quartz symplectites, which in some instances define a strain shadow assemblage with plagioclase and biotite. Garnet inclusions are predominantly randomly oriented quartz as well as apatite, epidote, and kyanite. Laths of kyanite that partly define the S2 matrix fabric are completely encircled by cordierite mantles that are intergrown with fine fibrolite fringes.

LK11-42 (Fig. 2.5b) is a garnet-, staurolite-, kyanite-, fibrolite-bearing pelitic gneiss that was collected along a transect in the central domain and derives from ~ 270 m structurally above the core-cover contact. Note the similarity in interpreted structural position between LK11-59 and LK11-42, although they were sampled from different locations within the dome. The sample contains large garnet porphyroblasts in a foliated (S2; 301°, 23°NE) and lineated (L2; 18° → 015°) matrix defined by aligned biotite and white mica, which also define C'-type shear bands. Thin quartz + plagioclase domains are intercalated with the micas in the matrix, and clots of chlorite occur in minor amounts, typically adjacent to garnet porphyroblasts. Kyanite and staurolite grains make up 2-3% of the matrix and are characterized by random orientation and subhedral to anhedral form. Staurolite in particular exhibits textures indicative of replacement by biotite and/or kyanite. Other matrix phases include ilmenite and epidote/allanite, both in relatively low abundance. It is worth noting, however, that monazite occurs in places as overgrowths on allanite grains. Garnet porphyroblasts are relatively scarce throughout, but where present form large (≥ 2 mm) subhedral to anhedral, poikiloblastic grains. Diedesch et al. (*in review*) described spiral-shaped inclusion trails in the garnet, which are defined predominantly by aggregates of quartz, as well as by plagioclase, staurolite, kyanite, apatite, and ilmenite. Strain shadows on the garnet porphyroblasts are defined by quartz + plagioclase + biotite ± staurolite, with biotite showing partial replacement by chlorite.

LK11-16c (Fig. 2.5c) is a garnet-bearing pelitic gneiss collected from the north side of the dome ~40 m structurally above the core-cover contact. The main fabric in the rock is defined by large white mica fish with interlayered quartz that are bounded by shear bands defined by smaller quartz and plagioclase aggregates. The sample was collected from the hinge of a cm-scale fold whose axis is subparallel to an L2 mineral stretching lineation (21° → 000°). Mica fish are mantled, particularly on surfaces parallel to the main fabric, by biotite. Matrix biotite also wraps around garnet porphyroblasts and in some places defines microscale folds with fold axes perpendicular to L2 (and thus perpendicular to the cm-scale fold from which the sample was derived). Biotite grains are also interspersed in small quantities within the white mica fish. Throughout LK11-16c, matrix feldspar grains are surrounded by quartz and exhibit a patchy texture that records intergrowth of plagioclase and potassium feldspar. Kyanite, tourmaline, epidote, ilmenite, rutile and monazite are also present in low abundances throughout the matrix. Garnet porphyroblasts are large (≥ 2 mm), subhedral to anhedral, and their grain boundaries are commonly truncated along the matrix fabric. One thin section cut in the plane parallel to L2 and perpendicular to S2 contains a garnet porphyroblast with asymmetric tails that, like the matrix mica fish, define a top-S sense of shear (Diedesch et al., *in review*). The garnet tails are also associated with biotite, quartz, and minor cordierite. On faces truncated by the main S2 schistosity, garnet porphyroblasts exhibit a reaction rim of quartz + biotite that transitions into a matrix dominated by white mica with lesser biotite ± plagioclase. Inclusions in garnet porphyroblasts appear randomly oriented and consist of quartz, plagioclase, biotite, ilmenite, apatite, and epidote.

Appendix 2.2.
Methods for Locating and Imaging Monazite

For the four samples selected, full thin section Al Kα, Ce Lα, and Y Lα X-ray images were generated using a step-size of 30 μm, beam defocused to 30 μm, a 100-nA beam current, and a 30-ms dwell time. The Al X-ray images provide spatial context while the Ce and Y images, overlain on the Al map, pinpoint locations of accessory phases such as monazite, xenotime, zircon, and allanite. While the minimum grain sizes detectable should theoretically be a function of the step size chosen (30 μm in the case), in practice we have used this method to identify locations of grains that are 10–15 μm in size, which is in agreement with effective minimum grain size of ~10 μm reported by Langille et al (2012). Typically, ~20 grains are selected per sample for detailed analysis, but the relatively low abundance of monazite in LKD samples resulted in as few as 12 suitable grains in one sample (LK11-60). For appropriate grains, Y Lα, Ce Lα, Th Mα, and U Mα X-ray images were generated on the EPMA using beam scanning (to obtain effective pixel sizes < 1 μm), a beam current of 100 nA, and a dwell time of 100 ms. The X-ray images were used to identify zoning patterns and potential age or growth domains, to evaluate potential links between the domains and microstucturalstructural setting, and to select the best targets for in-situ laser ablation split-stream (LASS) analysis.

Appendix 2.3.
Sample Compositions and P-T Estimates for Unit Ps Samples

Sample LK-48. Chlorite in sample LK-48 occurs only in contact with garnet, and in light of the fact that garnet exhibits a retrograde rim, we exclude chlorite from the peak Barrovian assemblage (Table 3). With a few exceptions in plagioclase, matrix phases do not exhibit any measurable compositional variation (Table S1), so we use average compositions for these phases (Table 2), which yields a P-T estimate of 575 ± 29 °C and 7.3 ± 0.9 kbar at XH_2O = 0.1. A GARB temperature of 558 °C at 7.3 kbar provides a constraint for estimated XH_2O.

Sample LK-57. In sample LK-57, white mica and biotite do not exhibit significant compositional variation, but our analyses of these phases are biased toward grains that occur within ~200 µm of the garnet, so it is best to consider these compositions average for 'near garnet' rather than total matrix (Table 2). Plagioclase and staurolite grains in the sample exhibit little or no zoning and no apparent compositional variation with microstructural setting, so these analyses are also averaged. P-T estimates for this assemblage are 596 ± 37 °C and 7.5 ± 0.9 kbar. These estimates are based on correction for implied XH_2O (1.0) using a GARB temperature of 661 °C at 7.5 kbar.

Sample LK-59c. In contrast to LK-57, matrix phase analyses for sample LK-59c are not biased toward a particular microstructural setting and still yield very little compositional heterogeneity. Chlorite is predominantly associated with retrograde garnet rims and garnet strain shadows, and as such is not considered part of the peak assemblage used for average P-T, which are 642 ± 23 °C and 8.1 ± 0.9 kbar at XH_2O = 1, consistent with GARB temperature of 649 °C at 8 kbar.

Sample LK11-70. Given the microstructural complexity of sample LK11-70, it is perhaps somewhat surprising but matrix biotite, muscovite and plagioclase show no compositional heterogeneity. Likewise, staurolite exhibits no zoning or compositional variation with microstructural setting Therefore, the compositions of these phases are averaged and, in conjunction with garnet near-rim compositions (lowest Mn), yield calculated P-T conditions of 650 ± 19 °C and 7.0 ± 0.8 kbar, calculated at XH_2O = 0.8 estimated based on a GARB temperature of 646 °C.

Sample LK11-69a. Sample LK11-69a contains the assemblage garnet + biotite + white mica + quartz ± chlorite. Garnet porphyroblasts analyzed yield nearly flat chemical profiles with a minor increase in Mn and Fe# 80–100 µm from grain edges (Appendix 2.4). The sample contains two distinct white mica phases as revealed by back-scattered electron imaging and quantitative point analyses (e.g. Table 2). Textures indicate that relict grains of white mica with phengitic composition (Xcel = 0.04–0.05, Xms ≥ 0.60) are overgrown by matrix quartz and white mica fish with a dominant paragonitic component (Xpg = 0.80–0.90). Since textural evidence suggests these minerals grew at different times and there is a solvus between these two phases, it does not make sense to average the compositions for use in thermobarometric analyses and such an average value yields unreasonable P-T conditions given the other phases present. However, the coexistence of two white mica phases and their microstructural relationship does provide semi-quantitative P-T information (e.g., Guidotti and Sassi, 1976; Coggon and Holland, 2002; Keller et al., 2005). Table 3 shows a THERMOCALC average P-T calculation using the older, phengitic white mica composition. The only other major solid-solution phases in the assemblage are biotite and chlorite, both of which exhibit fairly uniform composition. Biotite concentrated at the tails of white mica fish (Fig. 2.4e; Appendix 2.1) have similar composition to average matrix biotite, which are characterized by Fe# of 0.470–0.510. Chlorite is only present in small quantities, but its textural association is that of an alteration product of biotite along garnet rims and in the cores of the white mica fish. The lack of feldspar (see note in Table 3) and aluminosilicate in this sample results in an incomplete set of reactions and large errors in P-T estimates (654 ± 88 °C and 6.8 ± 2.3 kbar). The GARB temperature (619 °C) is comparable to the average P-T estimate, but corrections for XH_2O in the latter are precluded by an incomplete set of reactions.

Sample LK11-60. Sample LK11-60 is the most microstructurally complex of the unit Ps schist samples, yet simple textural relationships and compositional trends define the most likely equilibrium assemblage. Textural observations that are relevant to the interpreted assemblage are: (1) idioblastic matrix staurolite, (2) cordierite rims on matrix biotite and kyanite, and (3) replacement of garnet by quartz + cordierite + biotite ± sillimanite. To expand on the third observation, neither fibrolite nor prismatic sillimanite coexist with the matrix phases and instead are found only in conjunction with cordierite porphyroblasts and garnet reaction rims. Collectively, these observations suggest that the cordierite- and staurolite-bearing assemblages are not in equilibrium with one another (e.g. Pattison et al., 1999). Additionally, compositional X-ray maps and quantitative transects of garnet porphyroblasts (e.g. Fig. 2.6c) reveal diffusion modified, prograde zoning patterns with a distinct reaction rim, suggesting that only the rim composition is in equilibrium with the mantling cordierite + biotite + quartz ± sillimanite assemblage. If it is assumed that low Mn garnet near-rim compositions are representative of peak prograde growth, then the most likely equilibrium assemblage is biotite + muscovite + staurolite + kyanite. Such an interpretation is consistent with the observation that late-stage cordierite forms rims on other matrix phases, and quantitative biotite compositional analyses also provide evidence that perhaps a garnet-bearing equilibrium assemblage defines peak T conditions in the sample. Matrix biotite contains higher Ti concentrations than the biotite associated with cordierite reaction rims and cordierite porphyroblasts. Given that there is a general positive correlation between temperature and Ti content in biotite (e.g., Henry et al., 2005), these analyses suggest higher prevailing temperatures in the matrix than in the cordierite-bearing overgrowths. Therefore, average compositions of matrix biotite, feldspar, staurolite, and muscovite, in conjunction with near-rim garnet composition, are interpreted to best reflect prograde conditions. Thermobarometric calculations using these compositions yields P-T estimates of 625 ± 19 °C and 7.9 ± 0.7 kbar at $XH_2O = 1.0$, which is significantly lower than the GARB temperature of 712 °C. The interpreted peak temperature of sample LK11-60 overlaps with that for anatexis of metapelites (e.g. LeBreton and Thompson, 1988; Patiño Douce and Johnston, 1991; Patiño Douce and Harris, 1998; Spear et al., 1999), but in high grade rocks it is possible for GARB temperatures calculated using large garnet grains to be much higher than the actual peak temperature attained (Spear and Florence, 1992). Since garnet from the sample exhibits diffusion-modified zoning and coronal textures, assumptions of equilibrium compositions are dubious anyway. In particular, the chosen garnet composition could represent significant post-growth dissolution and, when coupled with matrix biotite compositions, would produce an anomalously high GARB temperature (Kohn and Spear, 2000).

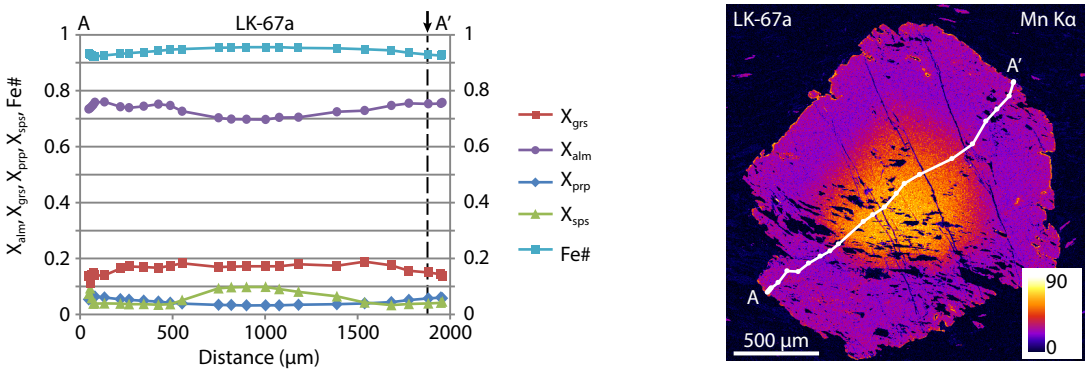
Sample LK11-59. Garnet porphyroblasts exhibit very little compositional variation in cross section (Fe# ± 0.03, Mn ± 0.004) except within ~100 μm of the edge where Fe# increases abruptly in conjunction with abrupt decrease in Mg content, while Mn content increases relatively steadily over the 100 μm width (Appendix 2.4). Biotite compositions in sample LK11-59 are dependent upon microstructural setting, although Fe# values overlap between each setting. Biotite grains that share grain boundaries with garnet (proximal matrix, strain shadow assemblages, and inclusions) generally record higher Fe# (0.523–0.586) than matrix grains that are remote with respect to garnet (0.461–0.518). Similarly, plagioclase and cordierite exhibit compositional variations between different microstructural settings. Matrix plagioclase exhibits slight zonation characterized by anorthite contents of 0.17–0.22 that generally increase from core to rim in individual crystals. Plagioclase associated with cordierite-quartz symplectite exhibit a similar anorthite-content variation, although the grains analyzed do not exhibitlack intracrystalline zonation noted in matrix grains. Plagioclase inclusions in garnet are too small to analyze, but grains that share their boundaries with garnet porphyroblasts exhibit compositions that tend toward the lower end ($An_{0.16–0.19}$) of the range reported for matrix grains. Cordierite Fe# values define two populations that coincide with distinct microstructural settings. Matrix grains, including those that rim relict kyanite, have Fe# ≤ ~0.35, whereas those that occur as porphyroblasts or reaction rims on garnet exhibit Fe# ≥ ~0.40. Ultimately, the mineral assemblage in this sample does not contain a sufficient number of phases for average thermobarometric calculations, but the microstructural and compositional complexities suggest that it would not yield a petrologically meaningful result anyway. However, using an average matrix biotite composition, which is likely the best proxy for near-peak conditions (e.g., Kohn and Spear, 2000), GARB calculations yield a first-order temperature constraint of 680–697 °C for pressures of 6–10 kbar.

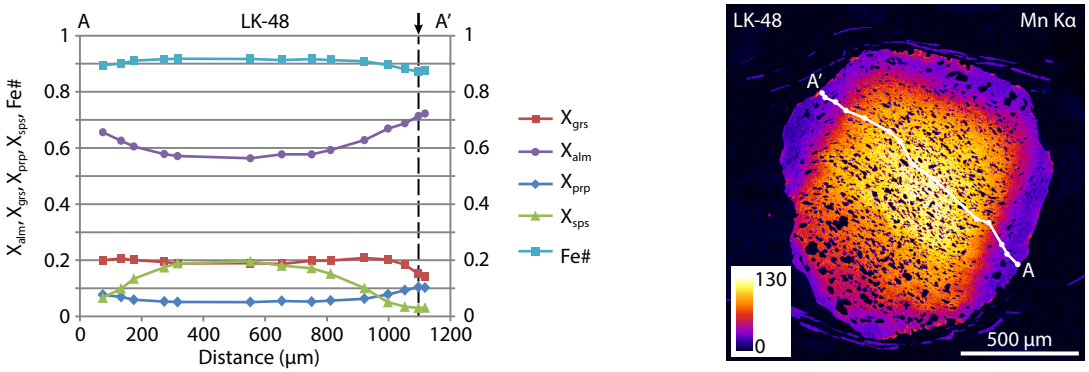
Sample LK11-42. The sample yields subtle garnet compositional (Mn and Fe#) variations indicative of growth zoning modified by diffusion (Fig. 2.6d). Garnet compositional end-members in a representative porphyroblast gradually reverse chemical trends over a distance of ~400 μm from the edge of the grain, indicating

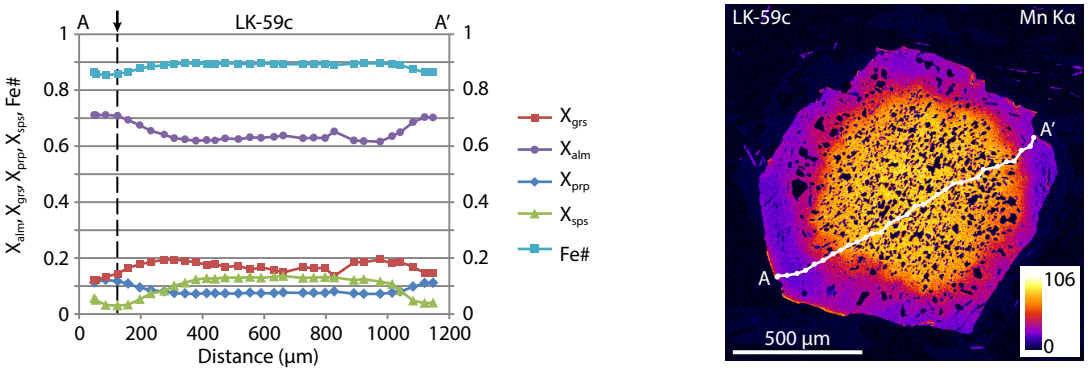
modification by post-growth reaction as well as self-diffusion. Plagioclase and biotite in the sample exhibit some compositional variation with no strong correlation to either microstructural setting or intracrystalline zonation, although matrix biotite grains have consistently lower Fe# than grains adjacent to or included in garnet. Similarly to sample LK11-59, the matrix biotite compositions in LK11-42 are less likely to have been modified by retrograde reactions with garnet, and thus better represent peak metamorphic conditions than those adjacent to garnet. Chlorite exhibits broad compositional variation, but it only occurs in randomly oriented clusters adjacent to garnet and as inclusions within garnet, so it is not considered part of the equilibrium assemblage. White mica is ubiquitous throughout the sample and exhibits a relatively uniform composition as both inclusions in garnet and as a matrix phase. Omitting chlorite from the assemblage yields THERMOCALC average P-T estimates of 634 ± 23 °C and 8.5 ± 1.1 kbar at X_{H2O} = 1.0, consistent with a GARB temperature of 655 °C at 8.5 kbar.

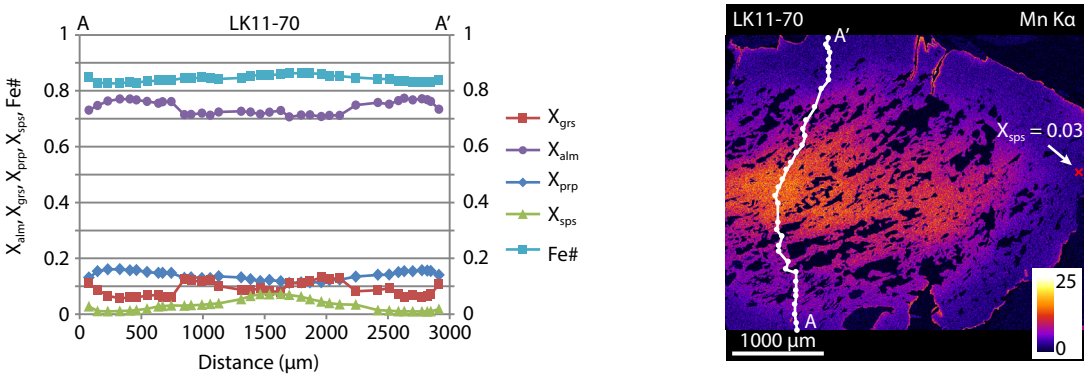
LK11-16c. As with the other representative gneissic samples, LK11-16c contains garnet with relatively homogenous chemical composition (Appendix 2.4). Despite the presence of a texturally distinct ~500 μm-thick reaction rim along one foliation-parallel face in a representative garnet porphyroblast, the chemical composition exhibits greater fluctuations with proximity to inclusions than to the grain edge. Both compositional X-ray imagery and a foliation-normal quantitative point analysis traverse demonstrate that the reaction rim (as well as the matrix foliation) truncates a growth zoning profile that preserved toward the grain boundary opposite the reaction rim. This profile includes a narrow (≤ 50 μm) near-rim reversal in Mn zoning. Biotite grains generally exhibit uniform composition with an average Fe# of 0.484 for matrix grains. Inclusions and near-garnet grains have slightly higher Fe# (0.500–0.520) than the matrix, but given that the large garnet grains exhibit diffusion-modified chemical profiles, it is assumed that biotite compositions are also affected. The near-garnet biotite grains also exhibit limited replacement by chlorite, which is not a texture associated with matrix biotite. White mica compositions throughout the sample are relatively homogeneous irrespective of microstructural setting. Plagioclase in the sample exhibits a range in composition ($An_{0.17–0.30}$), and grains included in garnet are generally more anorthitic than their matrix counterparts. Some matrix grains exhibit slight zonation, characterized by a decrease in An content from core to rim by ≤ 0.02. Some matrix plagioclase grains also exhibit patchy intergrowth with potassium feldspar. These intergrowths are most common at grain boundaries shared with biotite, and two single spot analyses from the intergrown plagioclase yield true albite compositions (~$An_{0.07}$). Because potassium feldspar is considered a higher temperature, lower pressure phase than expected of the kyanite-bearing peak assemblage, it is not considered for multi-equilibrium THERMOCALC calculations. All other matrix phases were averaged, and together with a garnet near-rim composition yield average conditions of 655 ± 26 °C and 10.4 ± 1.3 kbar at XH_2O = 0.3 for a GARB temperature of 651 °C at 10.4 kbar.

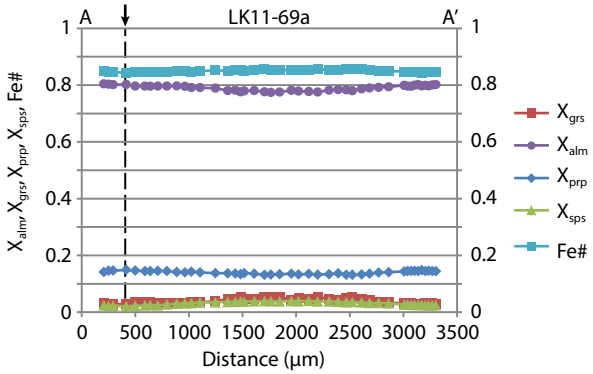
Appendix 2.4.
Additional Garnet Transects and X-ray Images

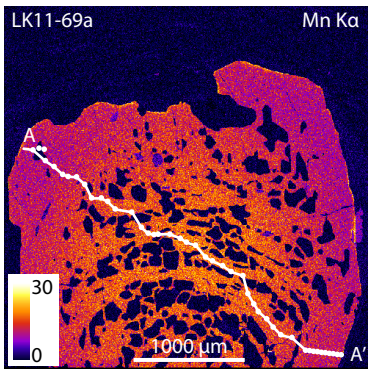


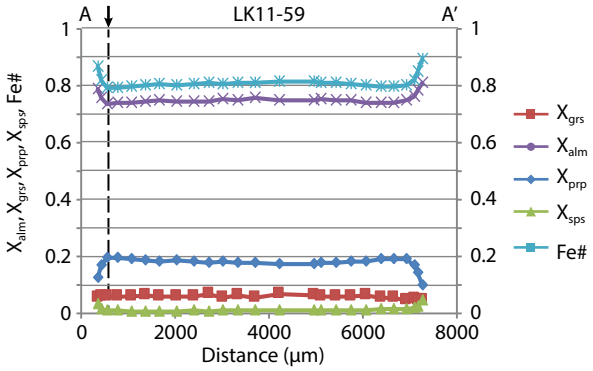


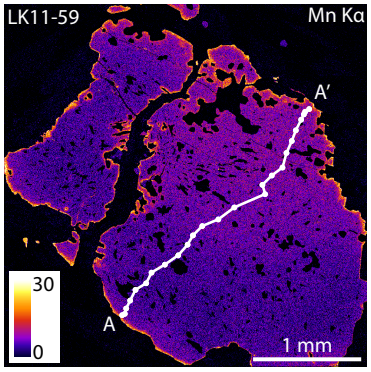


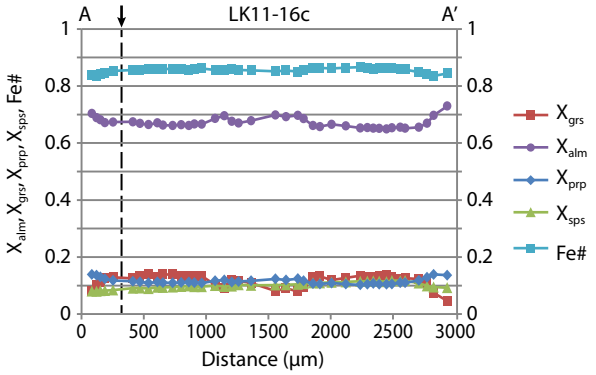


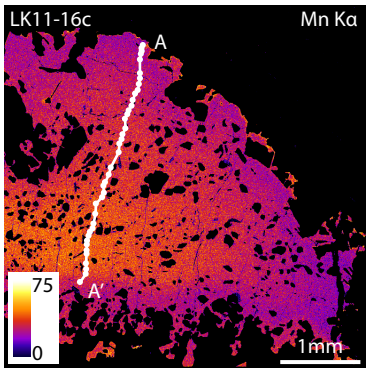

A
LK11-69a
A′
Distance (μm)
Fe#
X_{grs}
X_{alm}
X_{prp}
X_{sps}


LK11-69a
Mn Kα
A
A′
30
0
1000 μm


A
LK11-59
A′
Distance (μm)
Fe#
X_{grs}
X_{alm}
X_{prp}
X_{sps}


LK11-59
Mn Kα
A′
A
30
0
1 mm


A
LK11-16c
A′
Distance (μm)
Fe#
X_{grs}
X_{alm}
X_{prp}
X_{sps}


LK11-16c
Mn Kα
A
A′
75
0
1mm

Appendix 2.5.
Additional Pseudosection Modeling

Sample LK11-69a. Similarly to THERMOCALC average P-T results for LK11-69a, a P-T pseudosection model based on the estimated effective bulk composition is also poorly constrained (Appendix 2.7). The majority of the modeled phase diagram is occupied by large tetravariant and pentavariant phase fields with steeply sloped field boundaries. The center of the diagram, comprising moderate temperatures (550–650 °C) and low to moderate pressures (3–8 kbar), contains several trivariant and divariant fields with assemblages that include staurolite (± plagioclase). The model also predicts kyanite stability at T ≥ ~650 °C and P ≥ ~7.5 kbar. Given that sample LK11-69a was collected from the staurolite-kyanite zone (Fig. 2.1), it is assumed that one or both of these phases was present at peak metamorphic conditions and subsequently reacted out. One line of evidence to support this assumption is the presence of minor relict plagioclase in the matrix, which is composed predominantly of two interlayered white micas + biotite + quartz (Appendix 2.7). In previous sections the two white micas were identified as phengitic (Xcel = 0.04–0.05, Xms ≥ 0.65) and paragonitic (Xpg = 0.80–0.90), respectively, with textural evidence indicating that phengite predates paragonite. Detailed back-scattered electron (BSE) images of the matrix fabric show that phengite grains contain minute paragonite inclusions that indicate some paragonite formed either before or at the same time as the phengite (Appendix 2.7). Since no textural or compositional distinctions that would indicate multiple populations of phengite and/or paragonite, it is assumed that the two micas formed at or near equilibrium with one another, which is consistent with coexisting compositions along the muscovite-paragonite solvus (e.g. Guidotti et al., 1994). However, it should be re-emphasized that both bulk composition and expected P-T conditions are poorly constrained for sample LK11-69a. Nevertheless, a first order constraint on a portion of the P-T path for the sample is indicated by relict plagioclase in a two-white mica matrix, the compositions of which plot outside of the plagioclase stability field in modeled P-T space (Appendix 2.7). Emphasis thus far has been placed on the compositions and textural relationships of white mica phases in the sample, but garnet compositions (Xsps, Xprp, Fe#), biotite compositions (Fe#), and modeled biotite modal proportions also predict garnet-breakdown, biotite-forming reactions along a P-T path characterized by moderate cooling and decompression from plagioclase-bearing (± staurolite ± kyanite) fields to two-white mica-bearing fields.

Sample LK11-59. The P-T pseudosection for sample LK11-59 yields large trivariant and tetravariant fields, a few large pentavariant fields, and one hexavariant field at high temperature, low pressure (Appendix 2.7). This general topology is punctuated by several small divariant and trivariant fields. Garnet porphyroblasts in LK11-59 experienced post-growth diffusion as evidenced by the nearly homogenous chemical profiles, rendering interpretations of peak P-T conditions from garnet compositional isopleths questionable. However, garnet near-rim compositions coupled with average matrix plagioclase composition (An_{19}) constrain near-peak conditions at 610–660 °C and 9.6–11 kbar (Appendix 2.7). Composition isopleths from the core of a garnet porphyroblast (assuming it is a hemispheric section) are also shown in Appendix 2.7, but again, the effects of diffusion modification may render these values meaningless in terms of P-T constraints on garnet growth. In the model, plagioclase composition evolves toward higher An content with decreasing pressure, suggesting that measured matrix plagioclase compositions best represent pressure at near-peak temperature. As might be expected given the extent of post-growth garnet diffusion, measured biotite compositions are not predicted to be stable at the peak conditions. Unlike sample LK11-60 (previous section), biotite compositions in LK11-59 are not homogenized and the average compositions representing matrix (Fe# = 0.49) and near-garnet (Fe# = 0.55), further complicated by the fact that the range (Fe# = 0.49–0.55) is predicted to be stable during both garnet growth and post-peak garnet consumption.

As suggested previously and demonstrated by the pseudosection model, kyanite and cordierite are not in equilibrium in the sample. In the modeled system, cordierite compositions equivalent to those measured on kyanite rims require a decrease in pressure of at least 3 kbar to ~6.5 kbar. This value is constrained in P-T space by the absence of staurolite (Appendix 2.7) and melt textures in the sample, which collectively predicts a near-isothermal decompression path (Appendix 2.7) similar to that of sample LK11-60.

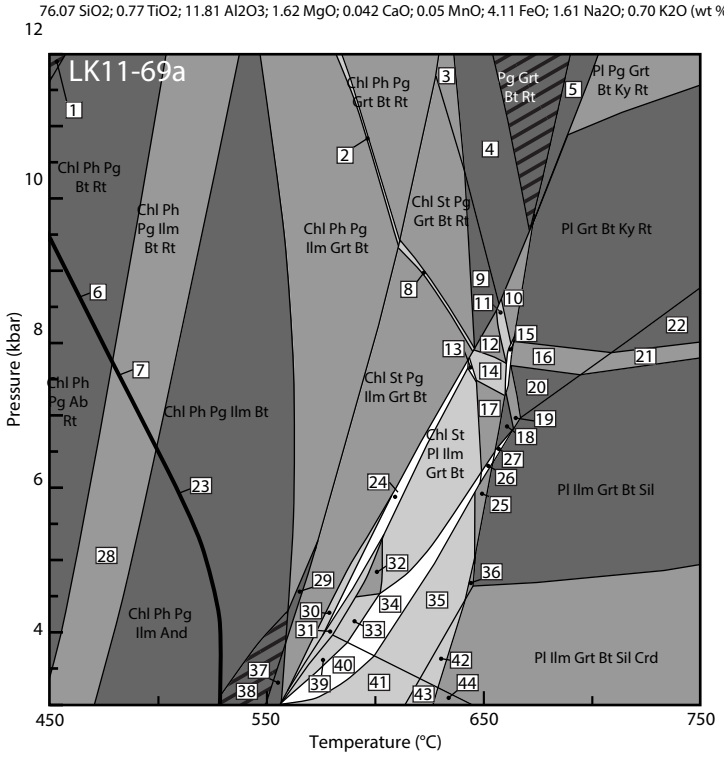
Sample LK11-16c. The P-T pseudeosection generated for LK11-16c is dominated by tetravariant fields with divariant and trivariant fields concentrated in the interior and three pentavariant fields along the perimeter (Appendix 2.7). The topology is distinct in that a much narrower stability field is predicted for staurolite than in

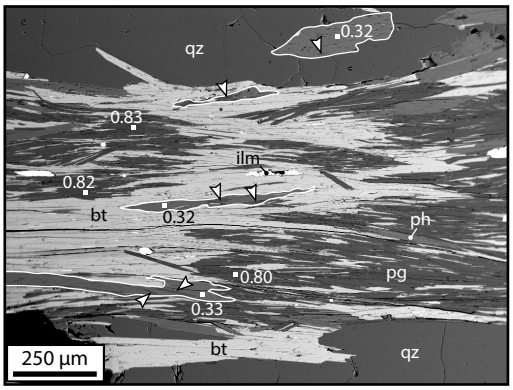
other samples. The mineral assemblage documented by petrographic analysis is represented by the pentavariant field: Bt + Ph + Pl + Grt + Rt. The small divariant fields below and to the left of this field (fields six and eight on Appendix 2.7) represent assemblages implied by garnet-hosted inclusions, notably staurolite and kyanite. Isopleths of garnet-hosted plagioclase inclusion compositions and a near-rim garnet composition (Appendix 2.7) provide further indication that the prograde P-T path passed at least through field six. Biotite Fe# isopleths representative of measured compositions are shown in Appendix 2.7, but they are too widely spaced to provide specific constraints. As with the two previously described sample pseudosections (LK11-60 and LK11-59), biotite Fe# compositions are higher with proximity to garnet, implying the effects of retrograde exchange ± net transfer reactions between garnet and biotite. In contrast to other samples though, averaged phase equilibria thermobarometry and GARB thermometry for LK11-16c yielded much more reasonable P-T estimates, and it is worth noting that the point defined by the average P-T (644 ± 21 °C and 9.9 ± 1.1 kbar) lies within the pentavariant field defined above. Using the same garnet, biotite, and plagioclase compositions as input parameters for compositional isopleths, forward modeling predicts near-peak conditions of 590–630 °C and 8.4–9.9 kbar with the large error in pressure estimates likely owing to the geometry of modeled compositional isopleths through this region of P-T space rather than any petrologic phenomenon experienced by the sample. In contrast to other samples described, petrologic data that constrain the retrograde portion of the P-T path (Appendix 2.7) for LK11-16c are indicated by the occurrence of potassium feldspar at the junctions between plagioclase and biotite as well as by minor cordierite growth on garnet porphyroblast tails. However, mineral compositions measured for sample LK11-16c are only consistent with near-peak conditions or post-peak departures from equilibrium via exchange and/or net transfer reactions.

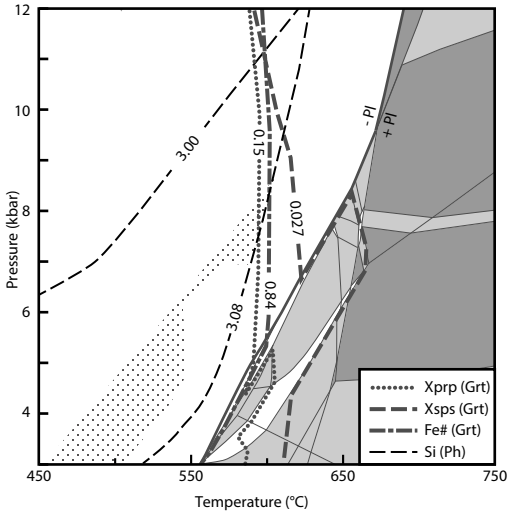
Appendix 2.6.
Additional P-T Pseudeosections

System: MnNCKFMASHT
All fields contain quartz, H_2O

76.07 SiO2; 0.77 TiO2; 11.81 Al2O3; 1.62 MgO; 0.042 CaO; 0.05 MnO; 4.11 FeO; 1.61 Na2O; 0.70 K2O (wt %)

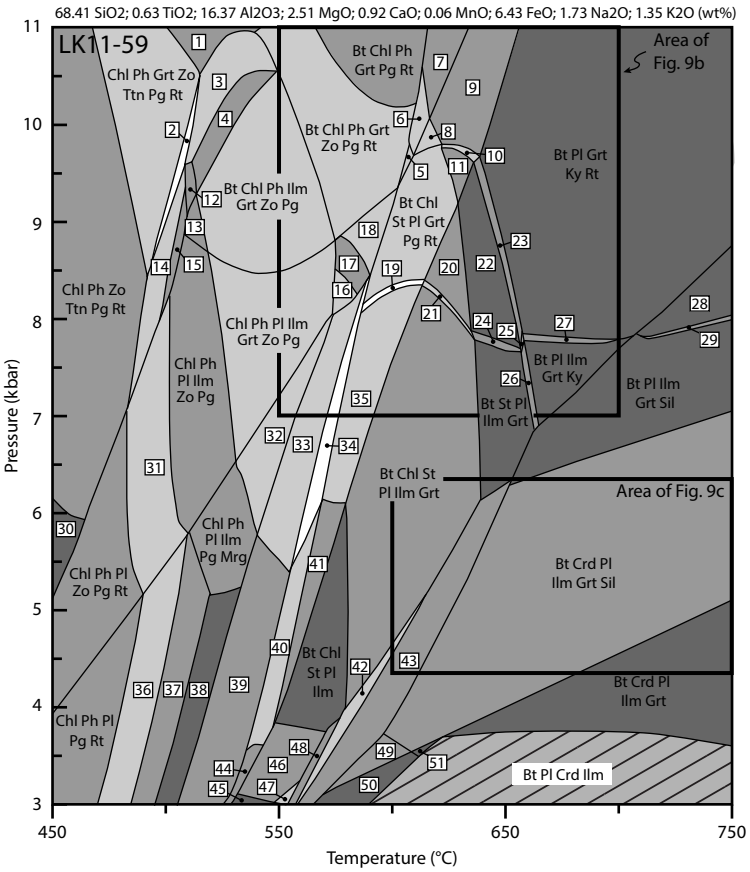


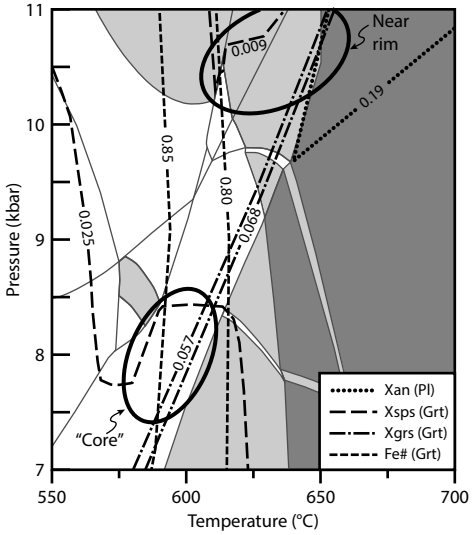


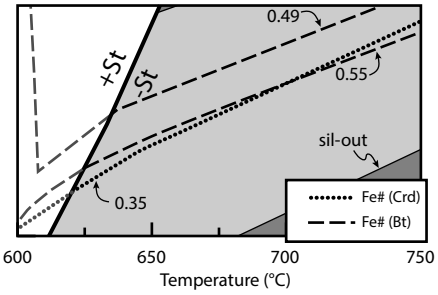


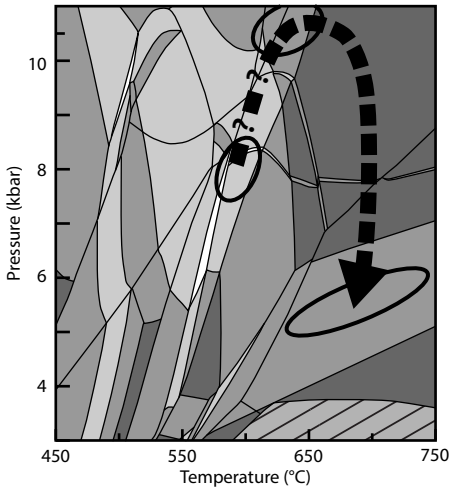
(1) Chl Ph Pg Rt
(2) Chl Ph Pg Ilm Grt Bt Rt
(3) Chl Pg Grt Bt Ky Rt
(4) Pg Grt Bt Ky Rt
(5) Pl Pg Grt Bt Rt
(6) Chl Ph Pg Bt Ab Rt
(7) Chl Ph Pg Ilm Bt Rt Ab
(8) Chl St Pg Ilm Grt Bt Rt
(9) St Pg Grt Bt Rt
(10) Pl Grt Bt Ky Rt
(11) St Pl Grt Bt Ky Rt
(12) St Pl Grt Bt Rt
(13) Chl St Pl Ilm Grt Bt Rt
(14) St Pl Ilm Grt Bt Rt
(15) St Pl Ilm Grt Bt Ky Rt
(16) Pl Ilm Grt Bt Ky Rt
(17) St Pl Ilm Grt Bt
(18) St Pl Ilm Grt Bt
(19) St Pl Ilm Grt Bt Ky
(20) Pl Ilm Grt Bt Ky
(21) Pl Ilm Grt Bt Sil Rt
(22) Pl Grt Bt Sil Rt
(23) Chl Ph Pg Ilm Bt Ab
(24) Chl St Pl Pg Ilm Grt Bt
(25) Pl Ilm Grt Bt Sil
(26) St Pl Ilm Grt Bt Sil
(27) St Pl Ilm Grt Bt Sil
(28) Chl Ph Pg Ilm Ab Rt
(29) Chl Pg Ilm Grt Bt
(30) Chl St Pg Ilm Grt Bt
(31) Chl St Pl Pg Ilm Bt
(32) Chl St Pl Ilm Bt
(33) Chl St Pl Ilm Bt Sil
(34) Chl St Pl Ilm Grt Bt Sil
(35) Chl Pl Ilm Grt Bt Sil
(36) Chl Pl Ilm Grt Bt Sil
(37) Chl St Pg Ilm Bt
(38) Chl Pg Ilm Bt
(39) Chl St Pl Ilm Bt And
(40) Chl St Pl Ilm Grt Bt And
(41) Chl Pl Ilm Grt Bt And
(42) Pl Ilm Grt Bt Sil Crd
(43) Pl Ilm Grt Bt And Crd
(44) Pl Ilm Grt Bt And Crd

System: MnNCKFMASHT
All fields contain Qz and H_2O





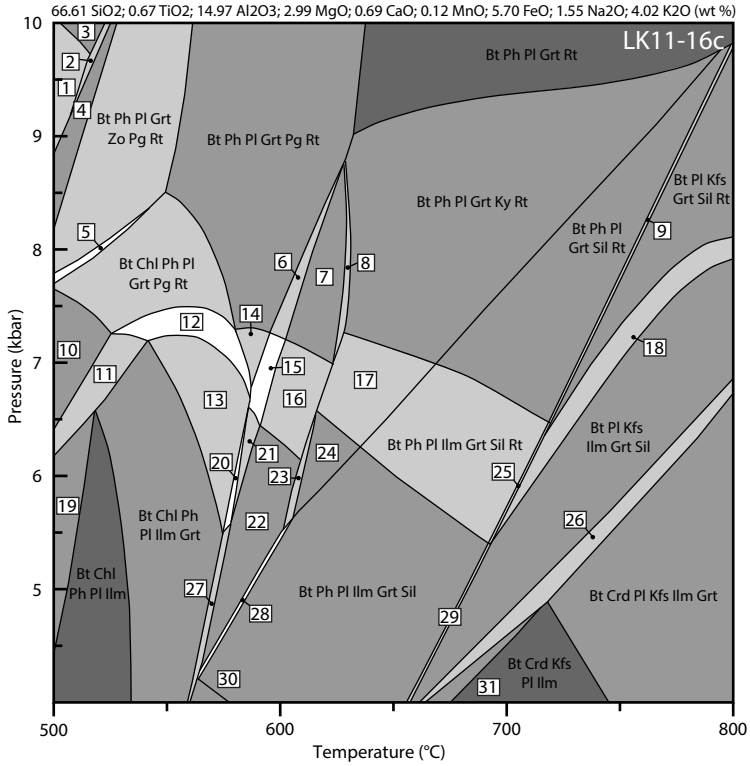


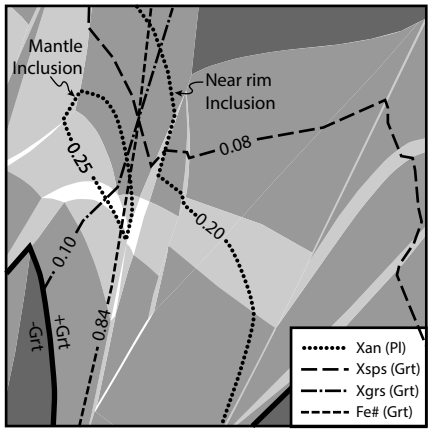


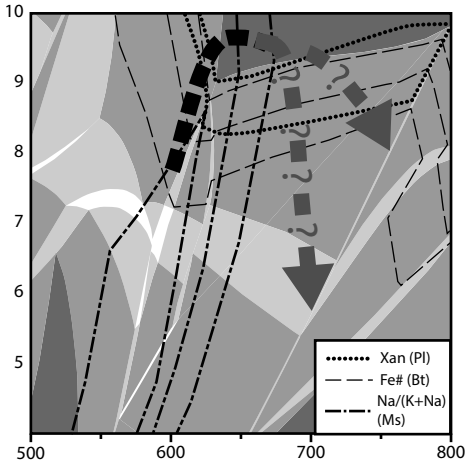
1) Chl Ph Grt Zo Pg Rt
2) Chl Ph Ilm Grt Zo Ttn Pg Rt
3) Chl Ph Ilm Grt Zo Pg Rt
4) Chl Ph Ilm Grt Zo Pg
5) Bt Chl St Grt Zo Pg Rt
6) Bt Chl Grt Ky Zo Pg Rt
7) Bt Ph Grt Ky Pg Rt
8) Bt Chl Pl Grt Ky Pg Rt
9) Bt Pl Grt Ky Pg Rt
10) Bt St Pl Grt Ky Pg Rt
11) Bt St Pl Grt Pg Rt
12) Chl Ph Ilm Zo Pg
13) Bt Chl Ph Ilm Zo Pg
14) Chl Ph Ilm Zo Ttn Pg Rt
15) Chl Ph Ilm Zo Ttn Pg
16) Chl Ph Pl Ilm Grt Pg Rt
17) Chl Ph Pl Grt Pg Rt
18) Bt Chl Ph Pl Grt Pg Rt
19) Bt Chl St Pl Ilm Grt Pg Rt
20) Bt Chl St Pl Grt Rt
21) Bt Chl St Pl Ilm Grt Rt
22) Bt St Pl Grt Rt
23) Bt St Pl Grt Ky Rt
24) Bt St Pl Ilm Grt Rt
25) Bt St Pl Ilm Grt Ky Rt
26) Bt St Pl Ilm Grt Ky
27) Bt Pl Ilm Grt Ky Rt
28) Bt Pl Grt Sil Rt
29) Bt Pl Ilm Grt Sil Rt
30) Chl Ph Zo Ttn Pg
31) Chl Ph Pl Ilm Zo Pg Rt
32) Chl Ph Pl Ilm Grt Pg Mrg
33) Chl Ph St Pl Ilm Grt Pg
34) Bt Chl Ph St Pl Ilm Grt Pg
35) Bt Chl St Pl Ilm Grt Pg
36) Chl Ph Ab An Ilm Pg Rt
37) Chl Ph Ab An Ilm Pg
38) Chl Ph Pl Ilm Pg
39) Chl Ph Pl Ilm Pg
40) Bt Chl Ph St Pl Ilm Pg
41) Bt Chl St Pl Ilm Pg
42) Bt Chl St Crd Pl Ilm Grt
43) Bt St Crd Pl Ilm Grt
44) Bt Chl Ph St Pl Ilm
45) Bt Chl Pl Ilm And
46) Bt Chl St Pl Ilm And
47) Bt Chl St Pl Ilm Grt And
48) Bt Chl St Crd Pl Ilm
49) Bt Crd Pl Ilm Grt And
50) Bt Crd Pl Ilm And
51) Bt Crd Pl Ilm Sil

System: MnNCKFMASHT
All fields contain Qz and H2O

66.61 SiO2; 0.67 TiO2; 14.97 Al2O3; 2.99 MgO; 0.69 CaO; 0.12 MnO; 5.70 FeO; 1.55 Na2O; 4.02 K2O (wt %)

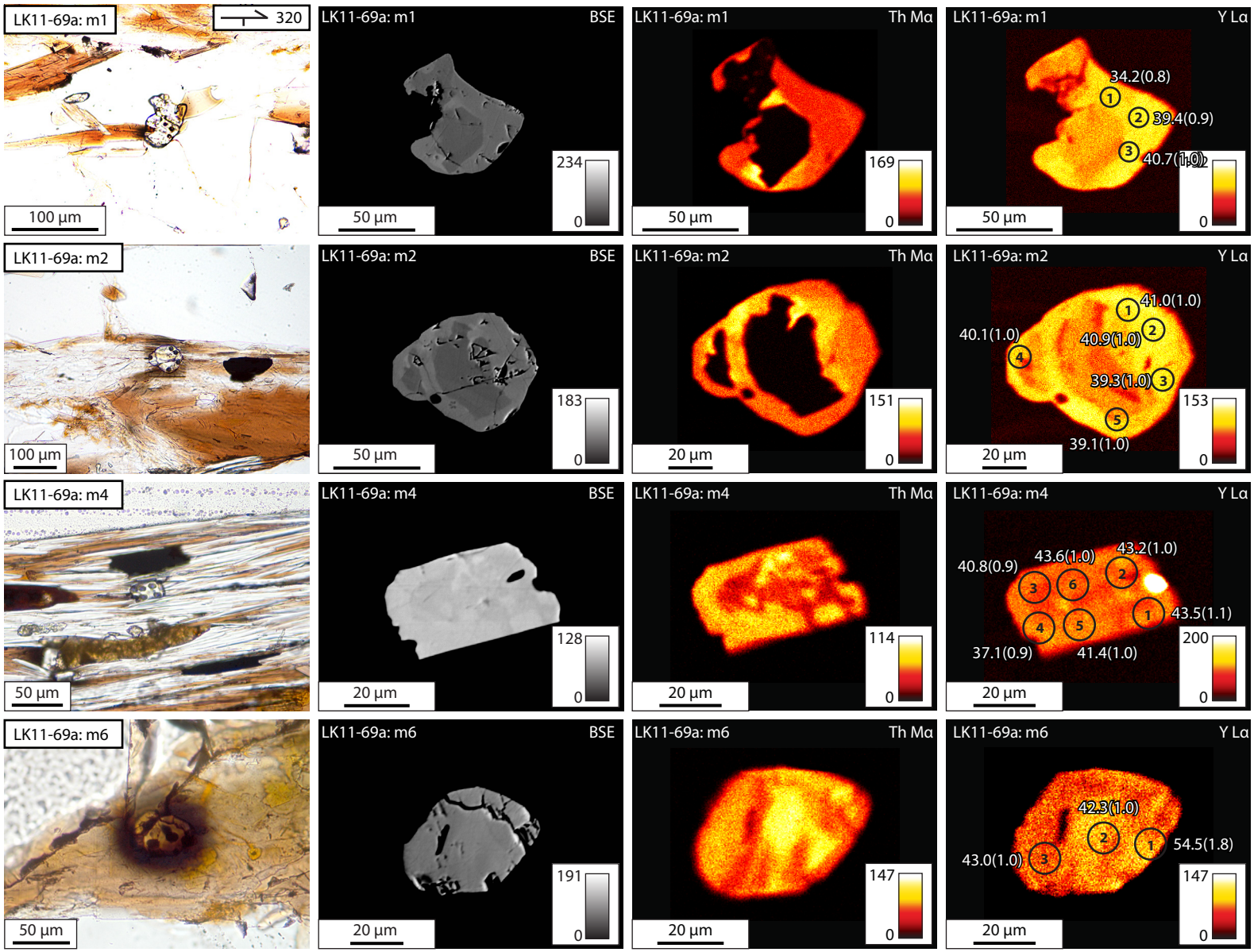


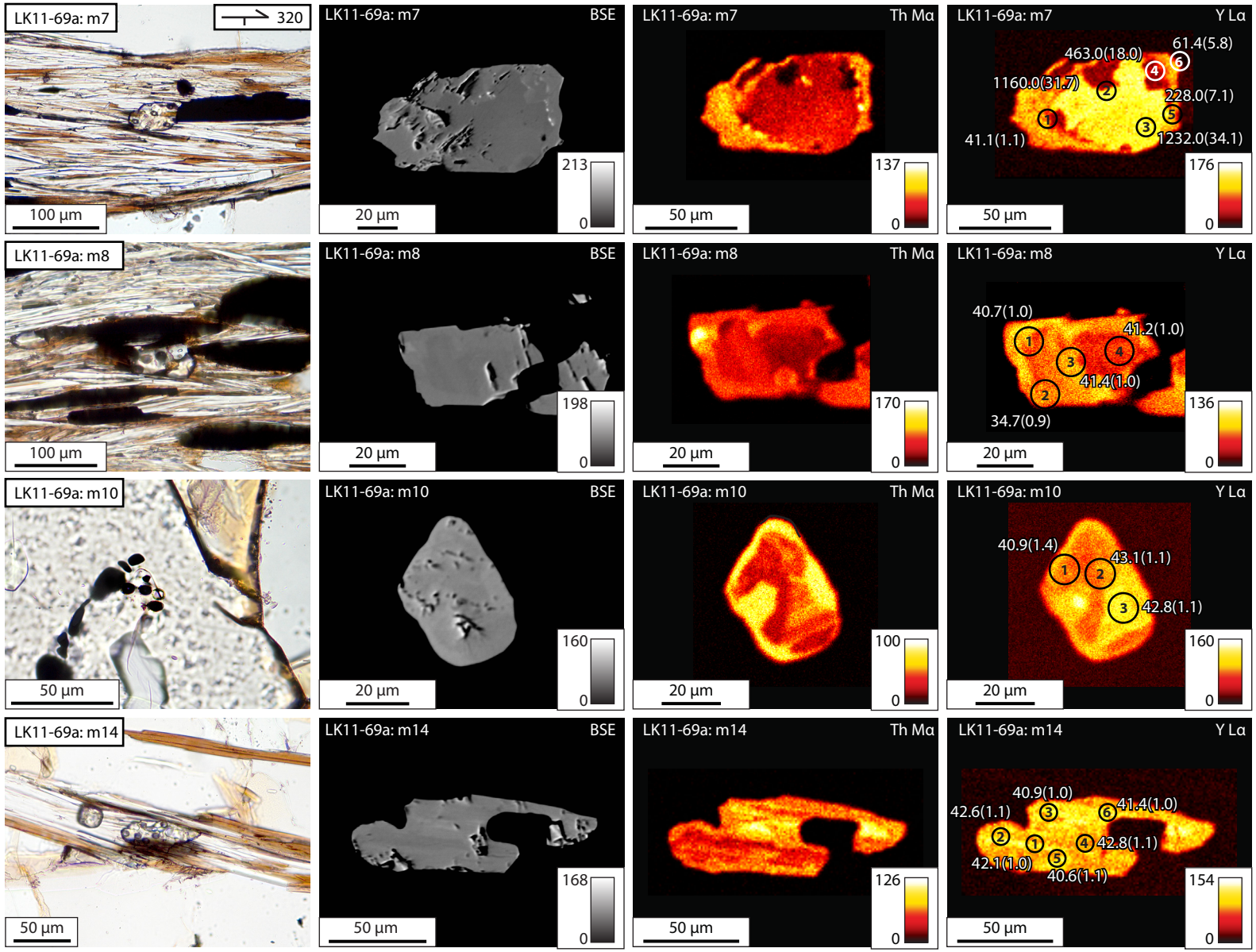


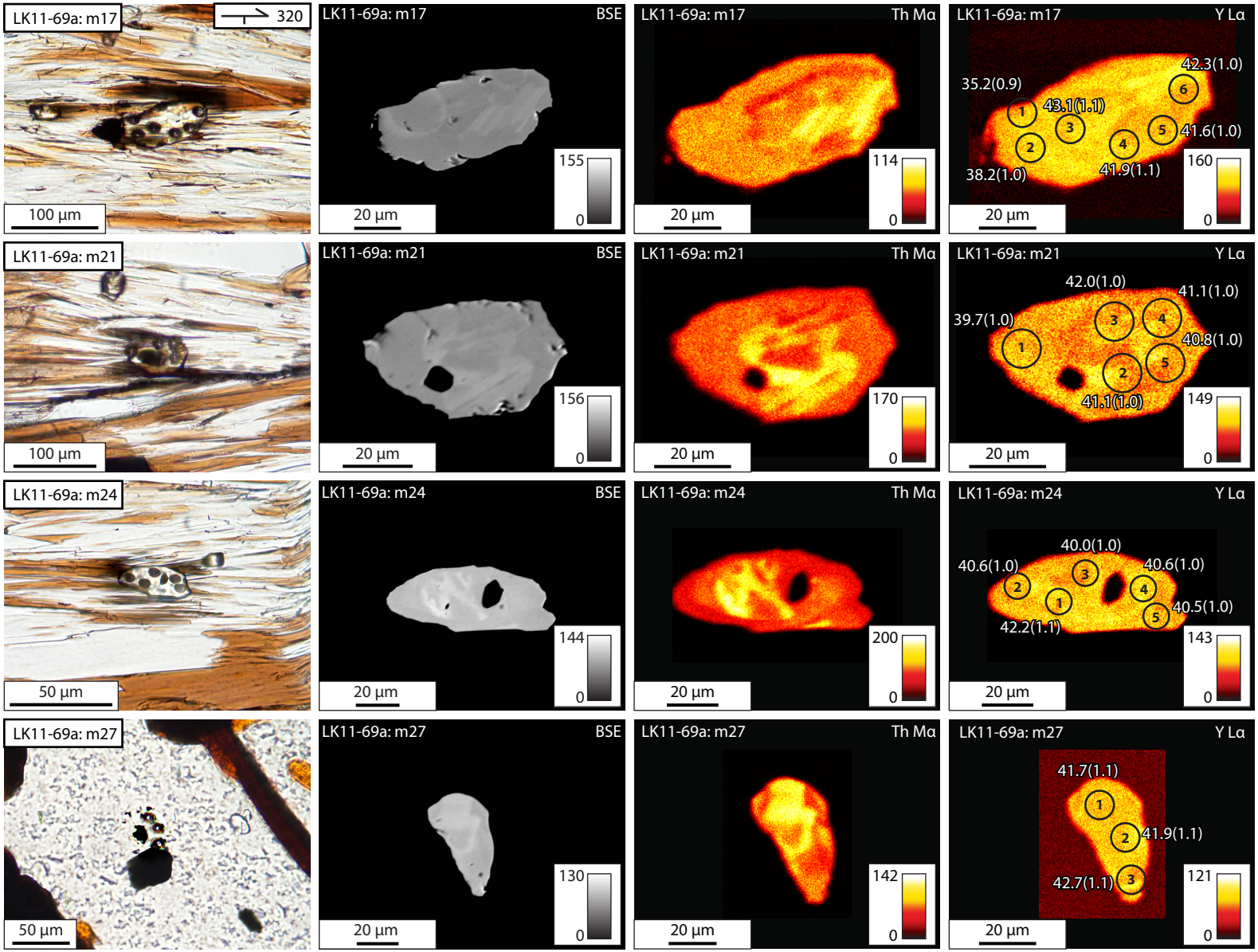


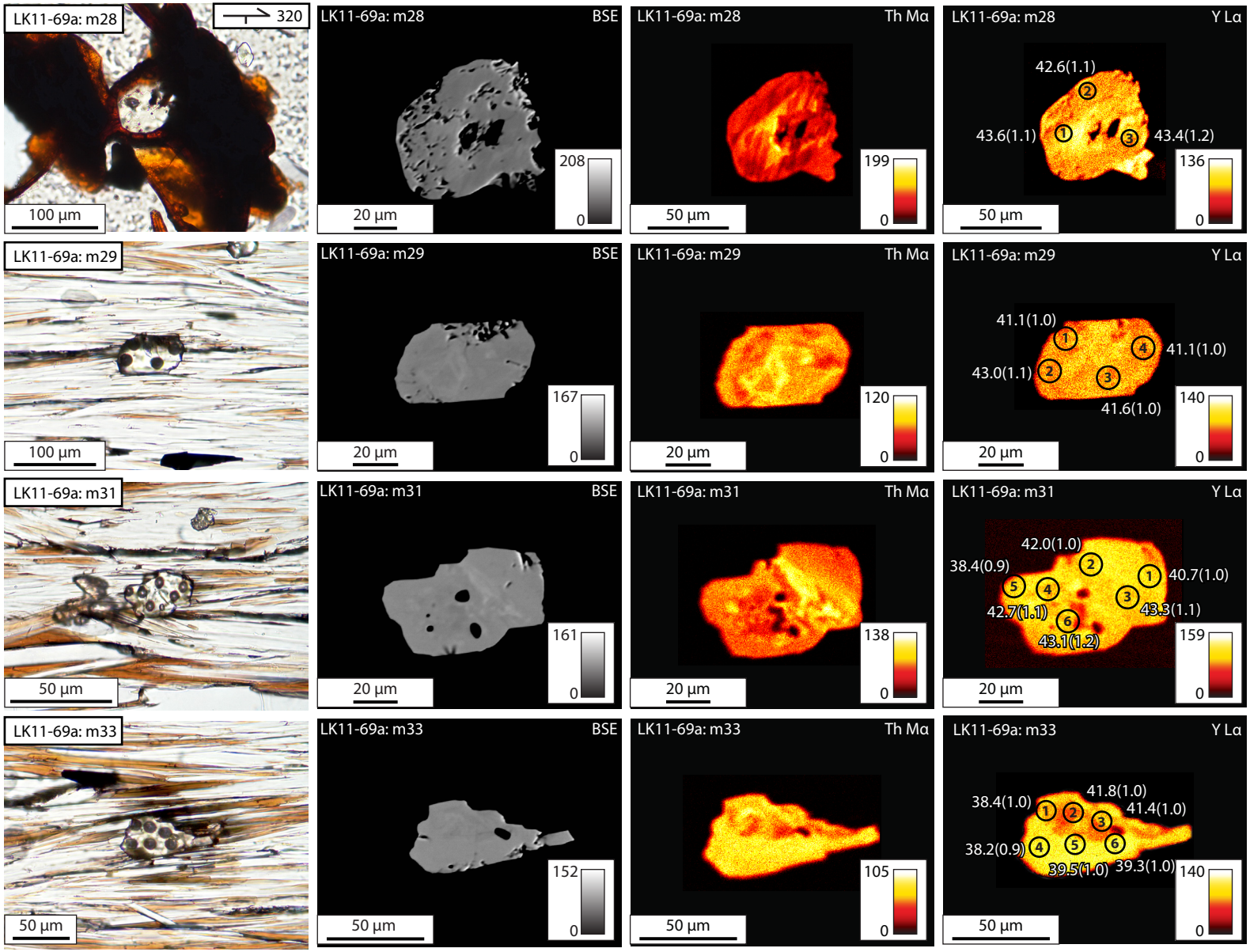
1) Bt Ph Grt Zo Ttn Pg Ab
2) Bt Ph Pl Grt Ttn Pg Ab
3) Bt Ph Grt Ttn Pg Ab
4) Bt Ph Pl Grt Ttn Pg
5) Bt Chl Ph Pl Grt Zo Pg Rt
6) Bt Ph St Pl Grt Pg Rt
7) Bt Ph St Pl Grt Rt
8) Bt Ph St Pl Grt Ky Rt
9) Bt Ph Pl Kfs Grt Sil Rt
10) Bt Chl Ph Pl Grt Rt
11) Bt Chl Ph Pl Ilm Grt Rt
12) Bt Chl Ph Pl Ilm Grt Pg Rt
13) Bt Chl Ph Pl Ilm Grt Pg
14) Bt Ph Pl Ilm Grt Pg Rt
15) Bt Ph St Pl Ilm Grt Pg Rt
16) Bt Ph St Pl Ilm Grt Rt
17) Bt Ph Pl Ilm Grt Ky Rt
18) Bt Pl Kfs Ilm Grt Sil Rt
19) Bt Chl Ph Pl Ilm Rt
20) Bt Chl Ph St Pl Ilm Grt Pg
21) Bt Ph St Pl Ilm Grt Pg
22) Bt Ph St Pl Ilm Grt
23) Bt Ph St Pl Ilm Grt Ky
24) Bt Ph Pl Ilm Grt Ky
25) Bt Ph Pl Kfs Grt Sil Rt Ilm
26) Bt Crd Pl Kfs Ilm Grt Sil
27) Bt Chl Ph St Pl Ilm Grt
28) Bt Ph St Pl Ilm Grt Sil
29) Bt Ph Pl Kfs Grt Sil Ilm
30) Ph Pl Ilm Grt And
31) Bt Crd Pl Kfs Ilm Sil

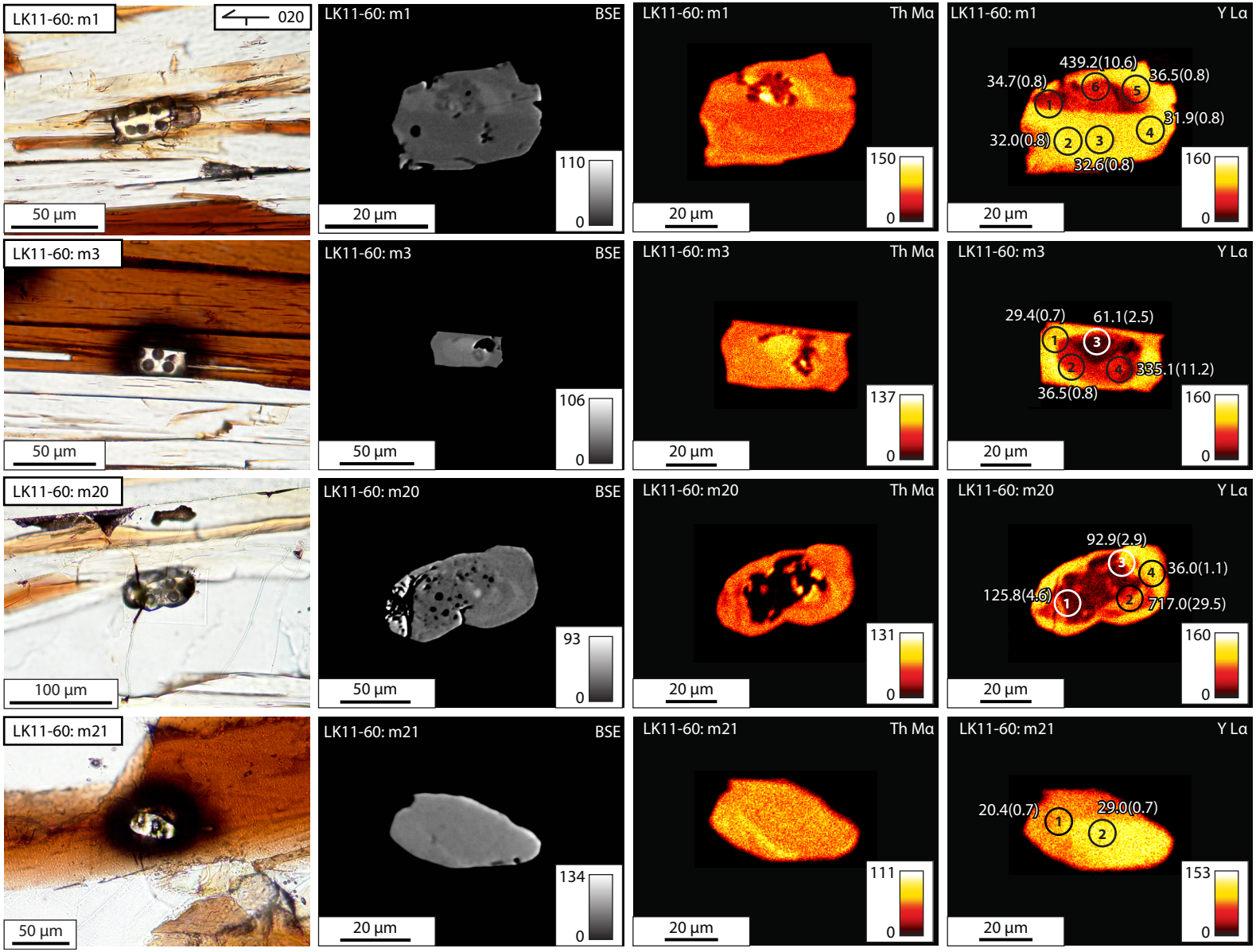
Appendix 2.7.
Monazite Photomicrographs, Chemical Zoning Maps, and Backscattered Electron Images

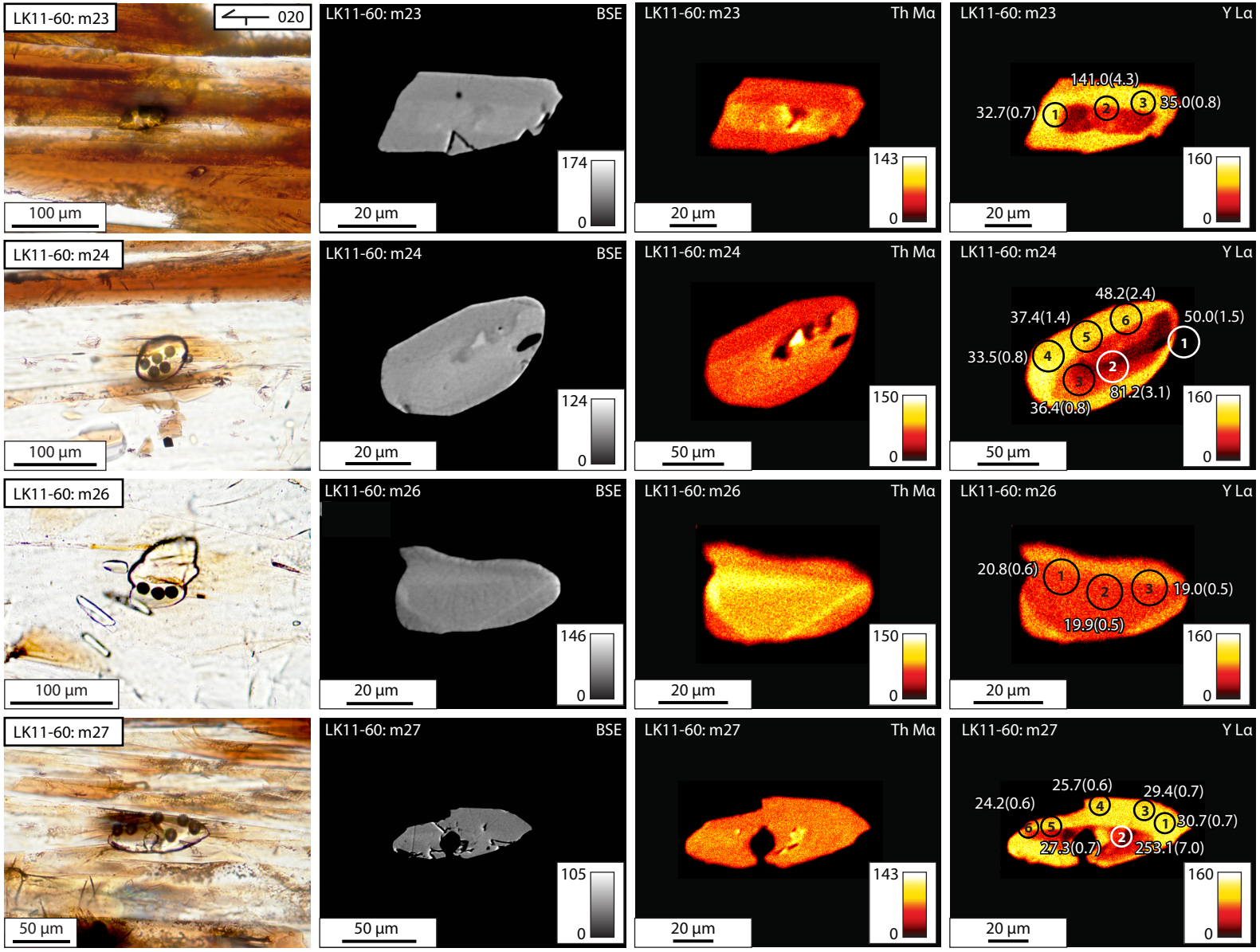

LK11-69a: m1
320
100 µm
LK11-69a: m1 BSE
234
0
50 µm
LK11-69a: m1 Th Mα
169
0
50 µm
LK11-69a: m1 Y Lα
34.2(0.8)
1
2
39.4(0.9)
3
40.7(1.0)
50 µm
LK11-69a: m2
100 µm
LK11-69a: m2 BSE
183
0
50 µm
LK11-69a: m2 Th Mα
151
0
20 µm
LK11-69a: m2 Y Lα
41.0(1.0)
1
2
40.1(1.0)
40.9(1.0)
4
39.3(1.0)
3
5
39.1(1.0)
153
0
20 µm
LK11-69a: m4
50 µm
LK11-69a: m4 BSE
128
0
20 µm
LK11-69a: m4 Th Mα
114
0
20 µm
LK11-69a: m4 Y Lα
43.2(1.0)
40.8(0.9)
43.6(1.0)
3
6
2
1
43.5(1.1)
4
5
37.1(0.9)
41.4(1.0)
200
0
20 µm
LK11-69a: m6
50 µm
LK11-69a: m6 BSE
191
0
20 µm
LK11-69a: m6 Th Mα
147
0
20 µm
LK11-69a: m6 Y Lα
42.3(1.0)
2
1
54.5(1.8)
43.0(1.0)
3
147
0
20 µm

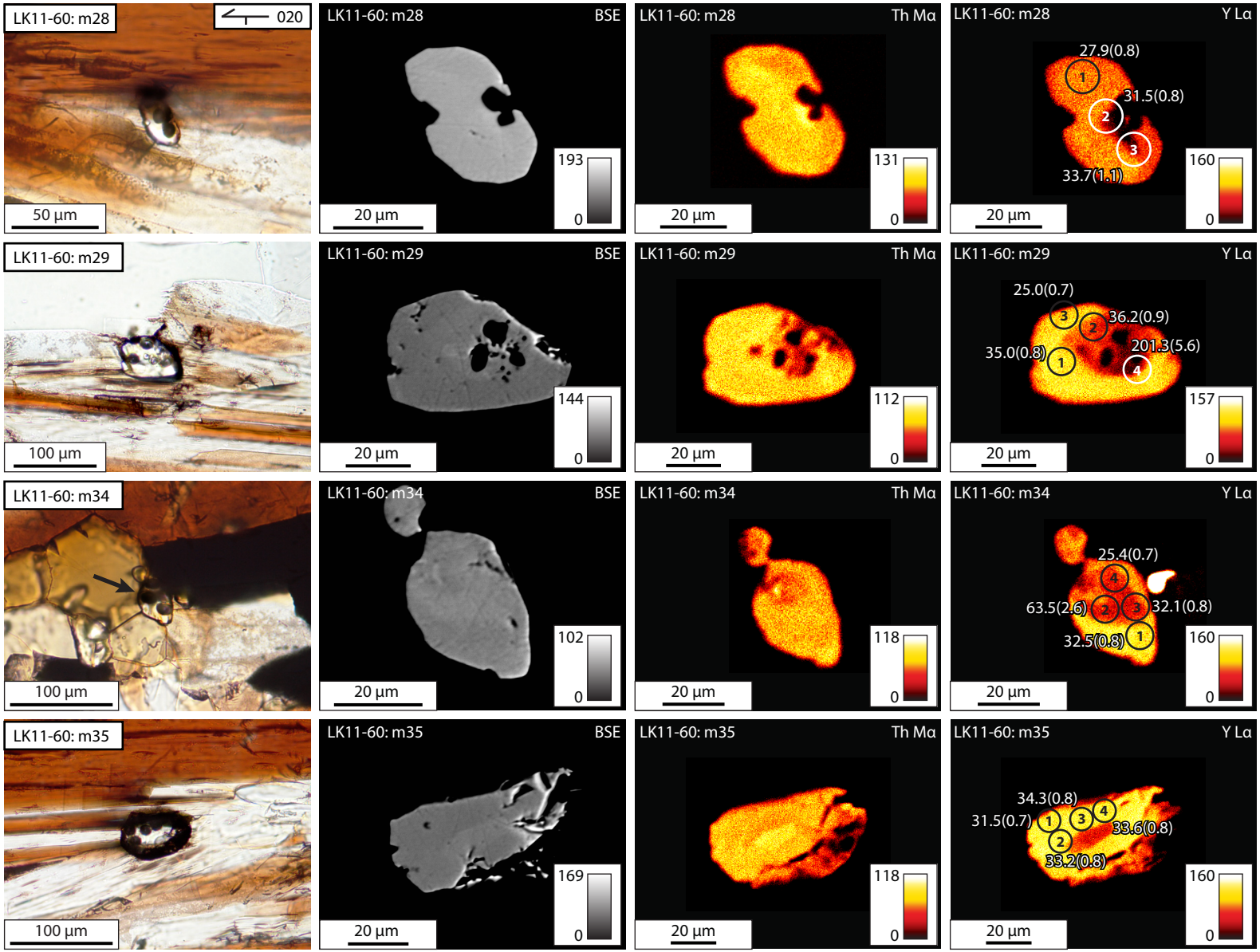

LK11-69a: m7
320
100 µm
LK11-69a: m7 BSE
213
0
20 µm
LK11-69a: m7 Th Mα
137
0
50 µm
LK11-69a: m7 Y Lα
463.0(18.0)
61.4(5.8)
1160.0(31.7)
228.0(7.1)
41.1(1.1)
1232.0(34.1)
176
0
50 µm
LK11-69a: m8
100 µm
LK11-69a: m8 BSE
198
0
20 µm
LK11-69a: m8 Th Mα
170
0
20 µm
LK11-69a: m8 Y Lα
40.7(1.0)
41.2(1.0)
41.4(1.0)
34.7(0.9)
136
0
20 µm
LK11-69a: m10
50 µm
LK11-69a: m10 BSE
160
0
20 µm
LK11-69a: m10 Th Mα
100
0
20 µm
LK11-69a: m10 Y Lα
40.9(1.4)
43.1(1.1)
42.8(1.1)
160
0
20 µm
LK11-69a: m14
50 µm
LK11-69a: m14 BSE
168
0
50 µm
LK11-69a: m14 Th Mα
126
0
50 µm
LK11-69a: m14 Y Lα
40.9(1.0)
42.6(1.1)
41.4(1.0)
42.8(1.1)
42.1(1.0)
40.6(1.1)
154
0
50 µm

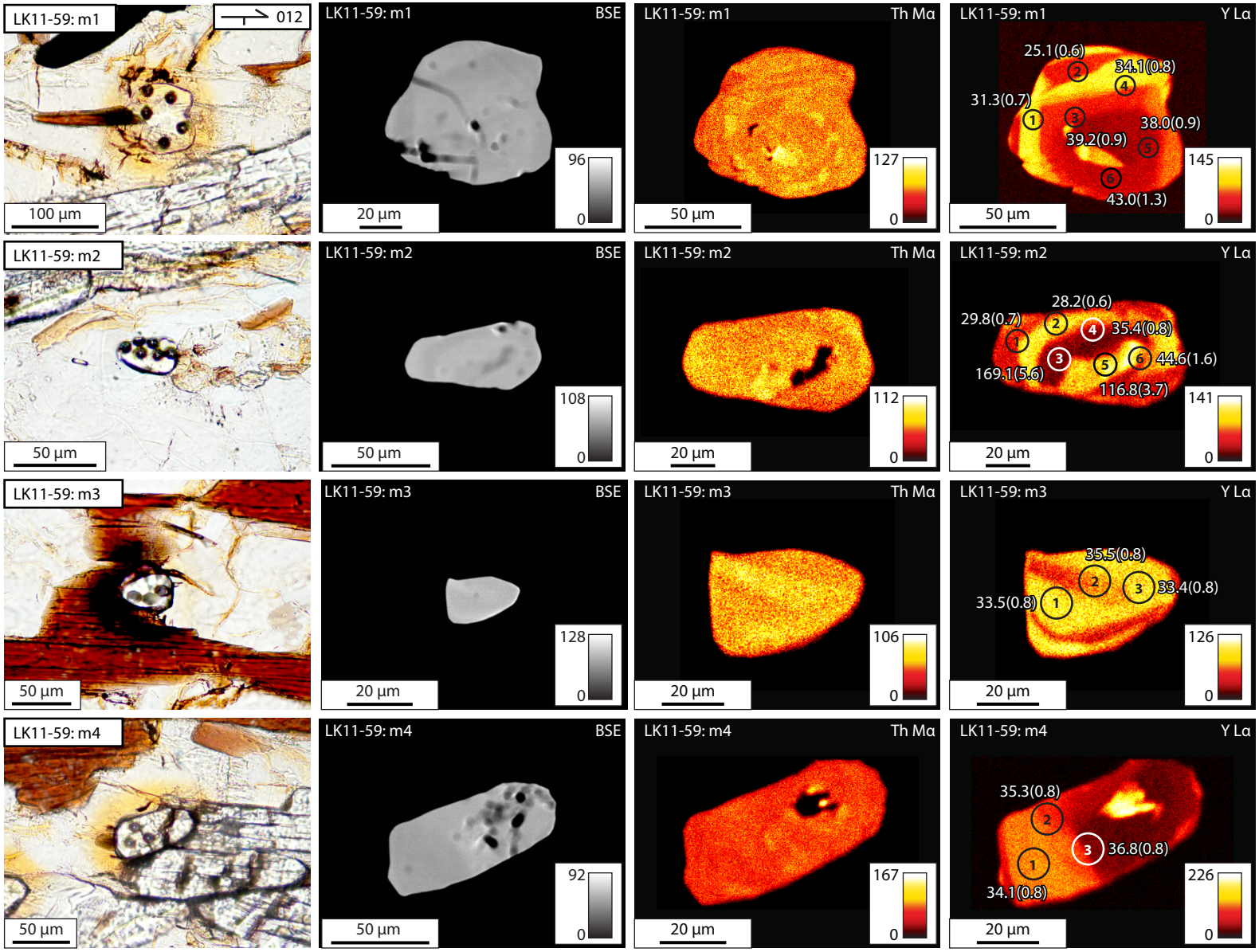

LK11-69a: m17
320
100 µm
LK11-69a: m17 BSE
155
0
20 µm
LK11-69a: m17 Th Mα
114
0
20 µm
LK11-69a: m17 Y Lα
35.2(0.9)
42.3(1.0)
43.1(1.1)
41.6(1.0)
38.2(1.0)
41.9(1.1)
160
0
20 µm
LK11-69a: m21
100 µm
LK11-69a: m21 BSE
156
0
20 µm
LK11-69a: m21 Th Mα
170
0
20 µm
LK11-69a: m21 Y Lα
42.0(1.0)
41.1(1.0)
39.7(1.0)
40.8(1.0)
41.1(1.0)
149
0
20 µm
LK11-69a: m24
50 µm
LK11-69a: m24 BSE
144
0
20 µm
LK11-69a: m24 Th Mα
200
0
20 µm
LK11-69a: m24 Y Lα
40.0(1.0)
40.6(1.0)
40.6(1.0)
40.5(1.0)
42.2(1.1)
143
0
20 µm
LK11-69a: m27
50 µm
LK11-69a: m27 BSE
130
0
20 µm
LK11-69a: m27 Th Mα
142
0
20 µm
LK11-69a: m27 Y Lα
41.7(1.1)
41.9(1.1)
42.7(1.1)
121
0
20 µm

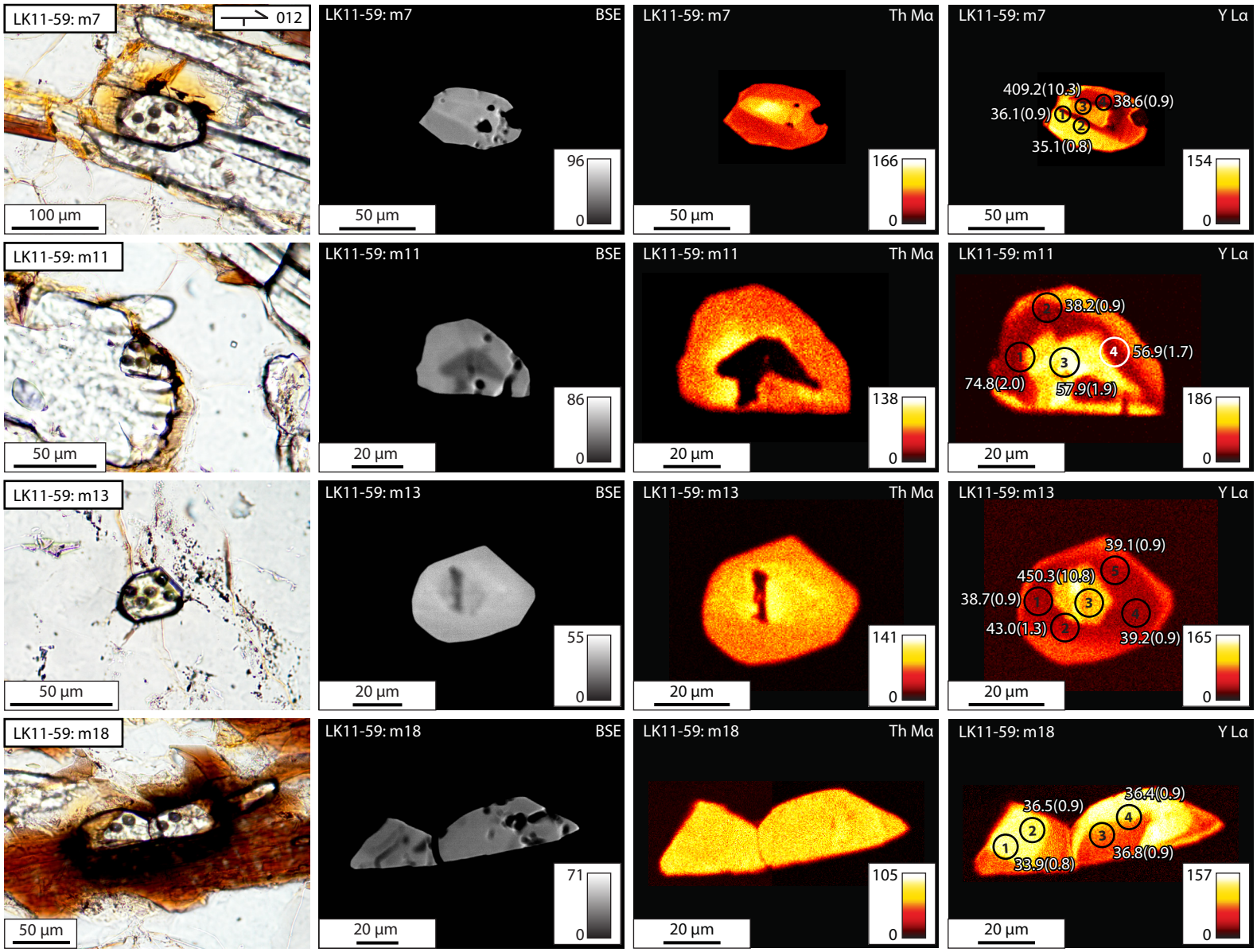

LK11-69a: m28
320
100 µm
LK11-69a: m28 BSE
208
0
20 µm
LK11-69a: m28 Th Mα
199
0
50 µm
LK11-69a: m28 Y Lα
42.6(1.1)
43.6(1.1)
43.4(1.2)
136
0
50 µm
LK11-69a: m29
100 µm
LK11-69a: m29 BSE
167
0
20 µm
LK11-69a: m29 Th Mα
120
0
20 µm
LK11-69a: m29 Y Lα
41.1(1.0)
41.1(1.0)
43.0(1.1)
41.6(1.0)
140
0
20 µm
LK11-69a: m31
50 µm
LK11-69a: m31 BSE
161
0
20 µm
LK11-69a: m31 Th Mα
138
0
20 µm
LK11-69a: m31 Y Lα
42.0(1.0)
38.4(0.9)
40.7(1.0)
42.7(1.1)
43.3(1.1)
43.1(1.2)
159
0
20 µm
LK11-69a: m33
50 µm
LK11-69a: m33 BSE
152
0
50 µm
LK11-69a: m33 Th Mα
105
0
50 µm
LK11-69a: m33 Y Lα
41.8(1.0)
38.4(1.0)
41.4(1.0)
38.2(0.9)
39.5(1.0)
39.3(1.0)
140
0
50 µm

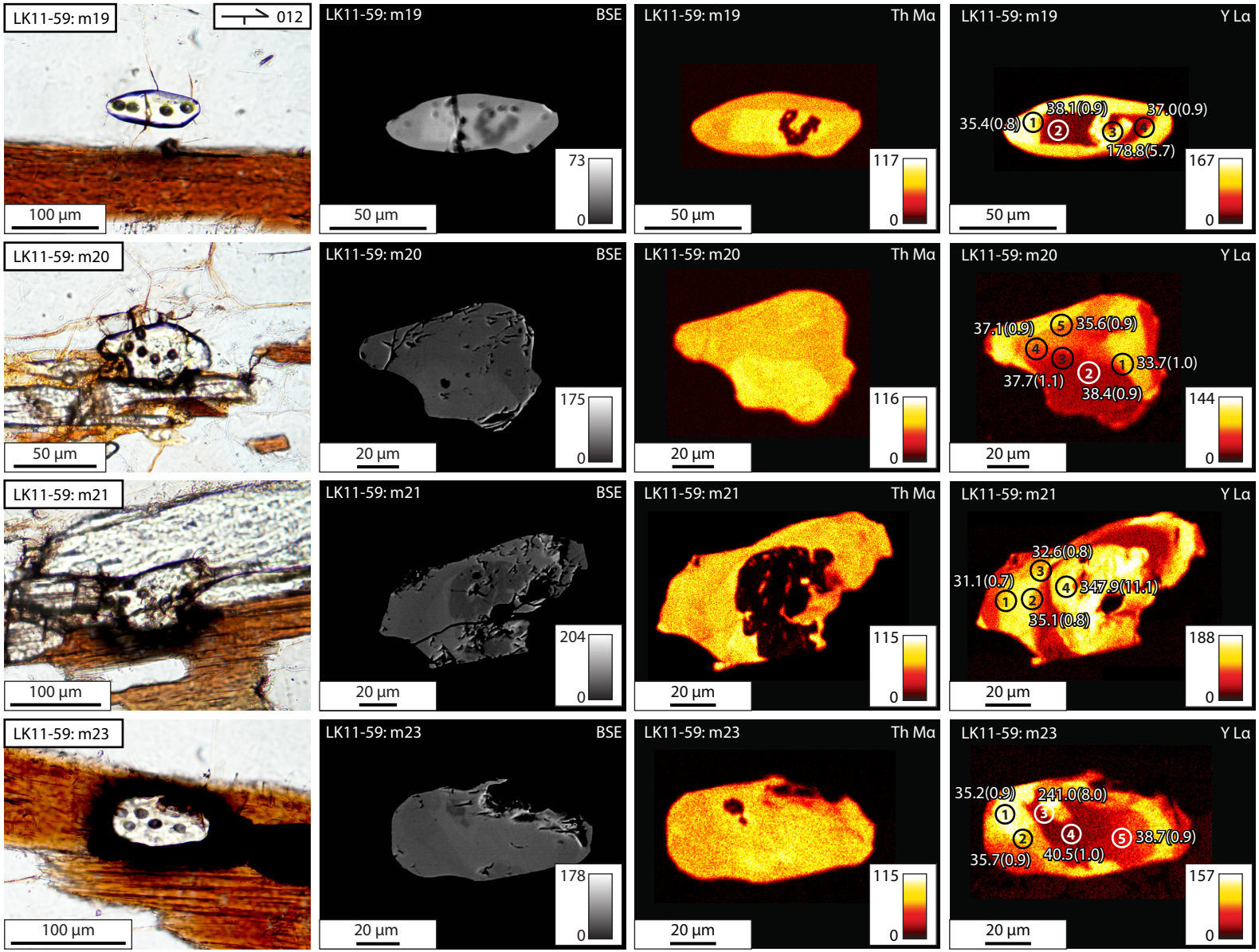

LK11-60: m1
020
50 µm
LK11-60: m1 BSE
20 µm
110
0
LK11-60: m1 Th Mα
20 µm
150
0
LK11-60: m1 Y Lα
439.2(10.6)
34.7(0.8)
36.5(0.8)
31.9(0.8)
32.0(0.8)
32.6(0.8)
20 µm
160
0
LK11-60: m3
50 µm
LK11-60: m3 BSE
50 µm
106
0
LK11-60: m3 Th Mα
20 µm
137
0
LK11-60: m3 Y Lα
29.4(0.7)
61.1(2.5)
335.1(11.2)
36.5(0.8)
20 µm
160
0
LK11-60: m20
100 µm
LK11-60: m20 BSE
50 µm
93
0
LK11-60: m20 Th Mα
20 µm
131
0
LK11-60: m20 Y Lα
92.9(2.9)
36.0(1.1)
125.8(4.6)
717.0(29.5)
20 µm
160
0
LK11-60: m21
50 µm
LK11-60: m21 BSE
20 µm
134
0
LK11-60: m21 Th Mα
20 µm
111
0
LK11-60: m21 Y Lα
20.4(0.7)
29.0(0.7)
20 µm
153
0

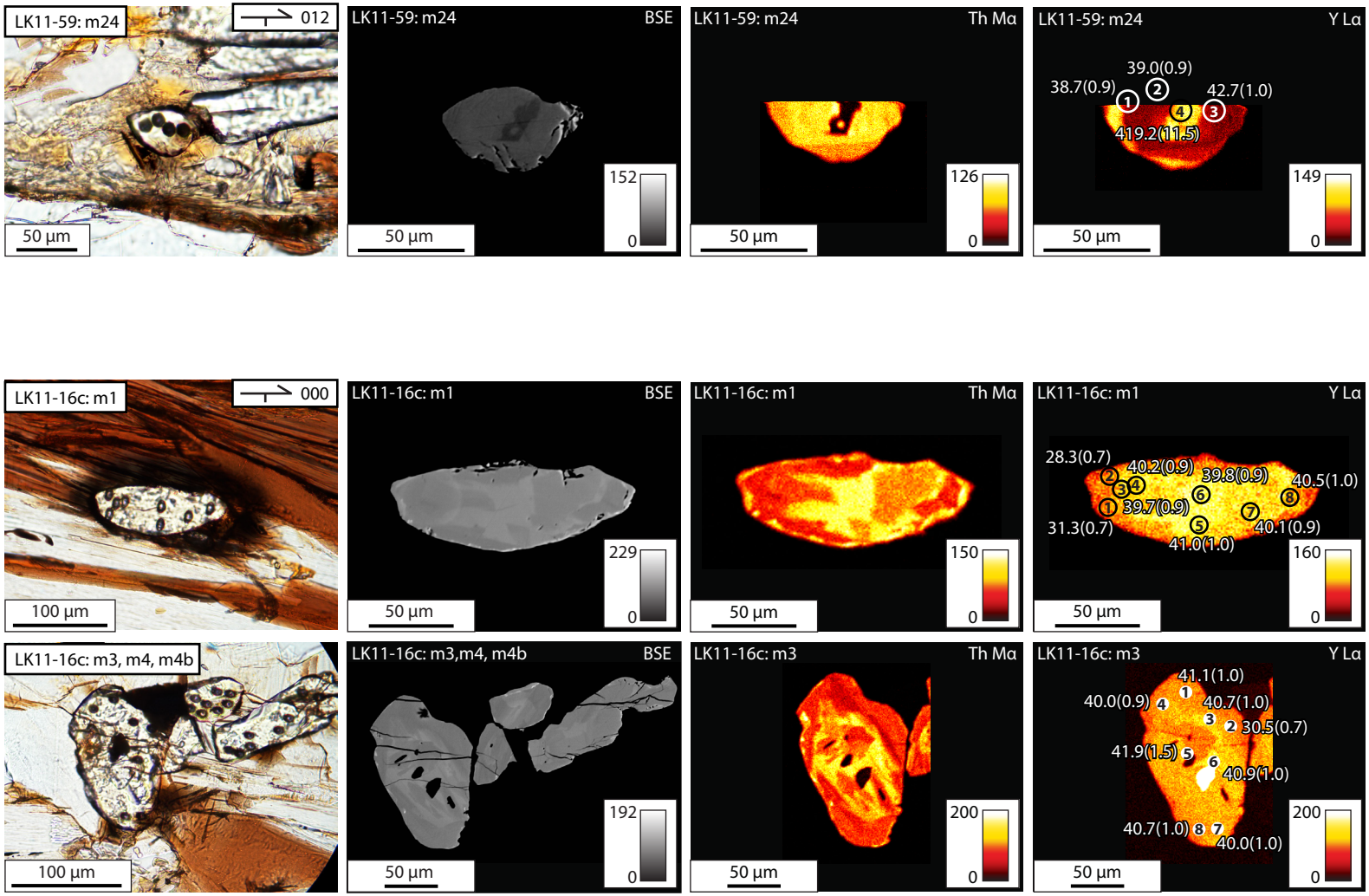

LK11-60: m23
020
100 µm
LK11-60: m23 BSE
174
0
20 µm
LK11-60: m23 Th Mα
143
0
20 µm
LK11-60: m23 Y Lα
141.0(4.3)
32.7(0.7)
35.0(0.8)
160
0
20 µm
LK11-60: m24
100 µm
LK11-60: m24 BSE
124
0
20 µm
LK11-60: m24 Th Mα
150
0
50 µm
LK11-60: m24 Y Lα
48.2(2.4)
37.4(1.4)
50.0(1.5)
33.5(0.8)
81.2(3.1)
36.4(0.8)
160
0
50 µm
LK11-60: m26
100 µm
LK11-60: m26 BSE
146
0
20 µm
LK11-60: m26 Th Mα
150
0
20 µm
LK11-60: m26 Y Lα
20.8(0.6)
19.0(0.5)
19.9(0.5)
160
0
20 µm
LK11-60: m27
50 µm
LK11-60: m27 BSE
105
0
50 µm
LK11-60: m27 Th Mα
143
0
20 µm
LK11-60: m27 Y Lα
25.7(0.6)
29.4(0.7)
24.2(0.6)
30.7(0.7)
27.3(0.7)
253.1(7.0)
160
0
20 µm

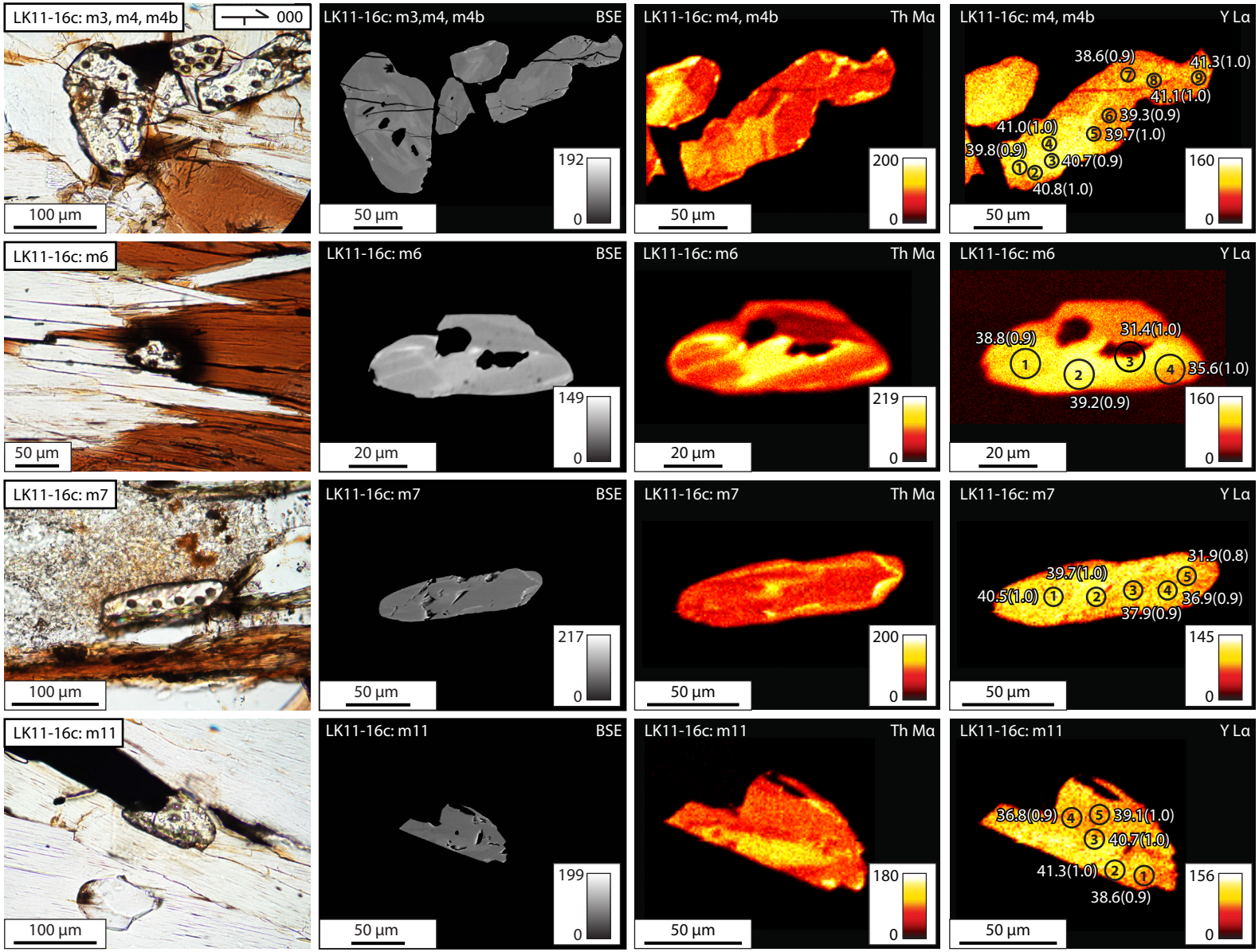

LK11-60: m28
020
50 µm
LK11-60: m28 BSE
193
0
20 µm
LK11-60: m28 Th Mα
131
0
20 µm
LK11-60: m28 Y Lα
27.9(0.8)
31.5(0.8)
33.7(1.1)
160
0
20 µm
LK11-60: m29
100 µm
LK11-60: m29 BSE
144
0
20 µm
LK11-60: m29 Th Mα
112
0
20 µm
LK11-60: m29 Y Lα
25.0(0.7)
36.2(0.9)
35.0(0.8)
201.3(5.6)
157
0
20 µm
LK11-60: m34
100 µm
LK11-60: m34 BSE
102
0
20 µm
LK11-60: m34 Th Mα
118
0
20 µm
LK11-60: m34 Y Lα
25.4(0.7)
63.5(2.6)
32.1(0.8)
32.5(0.8)
160
0
20 µm
LK11-60: m35
100 µm
LK11-60: m35 BSE
169
0
20 µm
LK11-60: m35 Th Mα
118
0
20 µm
LK11-60: m35 Y Lα
34.3(0.8)
31.5(0.7)
33.6(0.8)
33.2(0.8)
160
0
20 µm

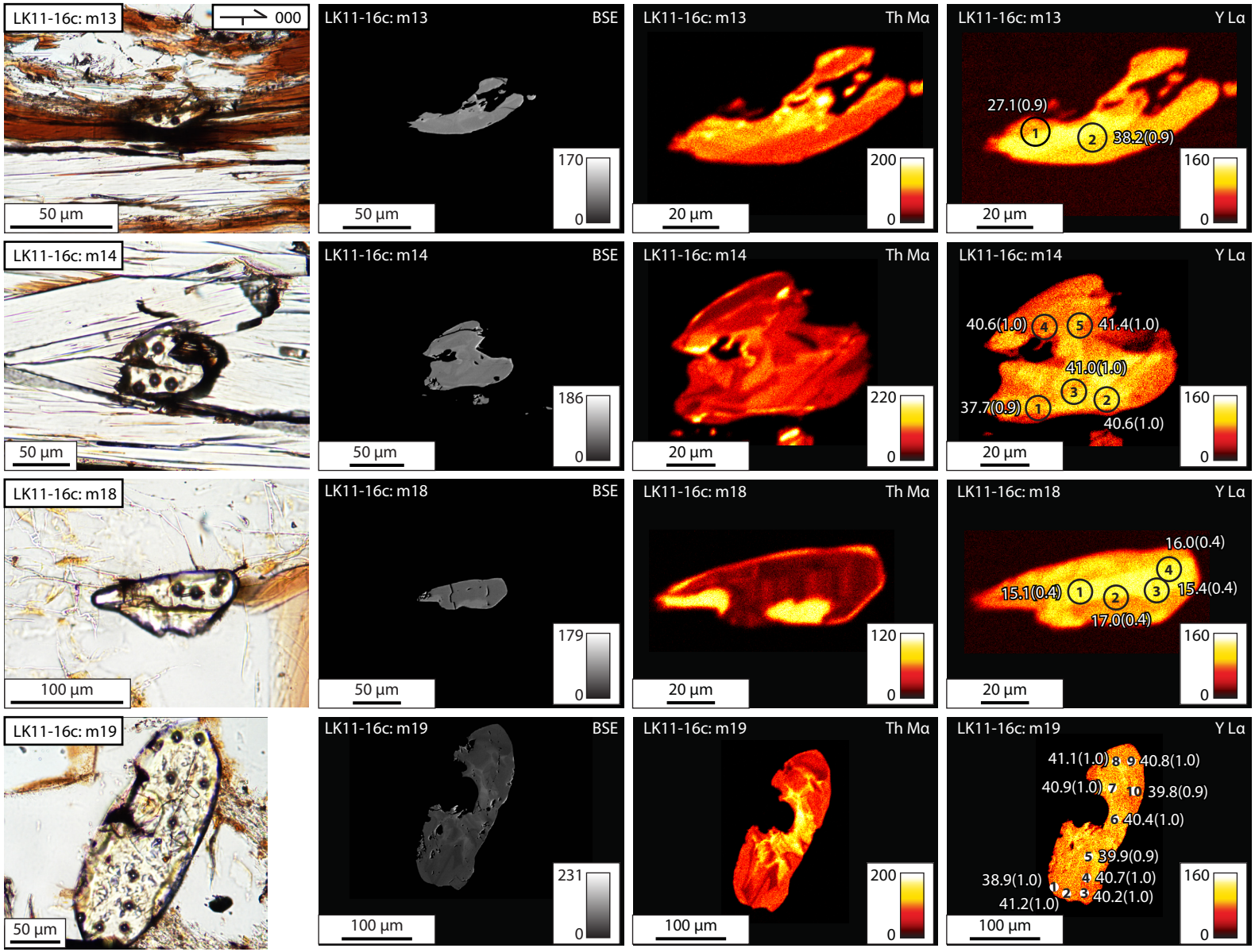

LK11-59: m1
012
100 µm
LK11-59: m1 BSE
20 µm
96
0
LK11-59: m1 Th Mα
50 µm
127
0
LK11-59: m1 Y Lα
25.1(0.6)
34.1(0.8)
31.3(0.7)
38.0(0.9)
39.2(0.9)
43.0(1.3)
50 µm
145
0
LK11-59: m2
50 µm
LK11-59: m2 BSE
50 µm
108
0
LK11-59: m2 Th Mα
20 µm
112
0
LK11-59: m2 Y Lα
28.2(0.6)
29.8(0.7)
35.4(0.8)
44.6(1.6)
169.1(5.6)
116.8(3.7)
20 µm
141
0
LK11-59: m3
50 µm
LK11-59: m3 BSE
20 µm
128
0
LK11-59: m3 Th Mα
20 µm
106
0
LK11-59: m3 Y Lα
35.5(0.8)
33.4(0.8)
33.5(0.8)
20 µm
126
0
LK11-59: m4
50 µm
LK11-59: m4 BSE
50 µm
92
0
LK11-59: m4 Th Mα
20 µm
167
0
LK11-59: m4 Y Lα
35.3(0.8)
36.8(0.8)
34.1(0.8)
20 µm
226
0


LK11-59: m7
012
100 µm
LK11-59: m7 BSE
96
0
50 µm
LK11-59: m7 Th Mα
166
0
50 µm
LK11-59: m7 Y Lα
409.2(10.3)
38.6(0.9)
36.1(0.9)
35.1(0.8)
154
0
50 µm
LK11-59: m11
50 µm
LK11-59: m11 BSE
86
0
20 µm
LK11-59: m11 Th Mα
138
0
20 µm
LK11-59: m11 Y Lα
38.2(0.9)
56.9(1.7)
74.8(2.0)
57.9(1.9)
186
0
20 µm
LK11-59: m13
50 µm
LK11-59: m13 BSE
55
0
20 µm
LK11-59: m13 Th Mα
141
0
20 µm
LK11-59: m13 Y Lα
39.1(0.9)
450.3(10.8)
38.7(0.9)
43.0(1.3)
39.2(0.9)
165
0
20 µm
LK11-59: m18
50 µm
LK11-59: m18 BSE
71
0
20 µm
LK11-59: m18 Th Mα
105
0
20 µm
LK11-59: m18 Y Lα
36.4(0.9)
36.5(0.9)
36.8(0.9)
33.9(0.8)
157
0
20 µm


LK11-59: m19
012
100 µm
LK11-59: m19 BSE
73
0
50 µm
LK11-59: m19 Th Ma
117
0
50 µm
LK11-59: m19 Y La
35.4(0.8)
38.1(0.9)
37.0(0.9)
178.8(5.7)
167
0
50 µm
LK11-59: m20
50 µm
LK11-59: m20 BSE
175
0
20 µm
LK11-59: m20 Th Ma
116
0
20 µm
LK11-59: m20 Y La
37.1(0.9)
35.6(0.9)
33.7(1.0)
37.7(1.1)
38.4(0.9)
144
0
20 µm
LK11-59: m21
100 µm
LK11-59: m21 BSE
204
0
20 µm
LK11-59: m21 Th Ma
115
0
20 µm
LK11-59: m21 Y La
32.6(0.8)
31.1(0.7)
347.9(11.1)
35.1(0.8)
188
0
20 µm
LK11-59: m23
100 µm
LK11-59: m23 BSE
178
0
20 µm
LK11-59: m23 Th Ma
115
0
20 µm
LK11-59: m23 Y La
35.2(0.9)
241.0(8.0)
38.7(0.9)
35.7(0.9)
40.5(1.0)
157
0
20 µm


LK11-59: m24
012
50 µm
LK11-59: m24
BSE
152
0
50 µm
LK11-59: m24
Th Mα
126
0
50 µm
LK11-59: m24
Y La
39.0(0.9)
38.7(0.9)
42.7(1.0)
419.2(11.5)
149
0
50 µm
LK11-16c: m1
000
100 µm
LK11-16c: m1
BSE
229
0
50 µm
LK11-16c: m1
Th Mα
150
0
50 µm
LK11-16c: m1
Y La
28.3(0.7)
40.2(0.9)
39.8(0.9)
40.5(1.0)
39.7(0.9)
31.3(0.7)
40.1(0.9)
41.0(1.0)
160
0
50 µm
LK11-16c: m3, m4, m4b
100 µm
LK11-16c: m3,m4, m4b
BSE
192
0
50 µm
LK11-16c: m3
Th Mα
200
0
50 µm
LK11-16c: m3
Y La
41.1(1.0)
40.0(0.9)
40.7(1.0)
30.5(0.7)
41.9(1.5)
40.9(1.0)
40.7(1.0)
40.0(1.0)
200
0
50 µm


LK11-16c: m3, m4, m4b
000
100 µm
LK11-16c: m3,m4, m4b
BSE
192
0
50 µm
LK11-16c: m4, m4b
Th Mα
200
0
50 µm
LK11-16c: m4, m4b
Y Lα
38.6(0.9)
41.3(1.0)
41.1(1.0)
39.3(0.9)
41.0(1.0)
39.7(1.0)
39.8(0.9)
40.7(0.9)
40.8(1.0)
160
0
50 µm
LK11-16c: m6
50 µm
LK11-16c: m6
BSE
149
0
20 µm
LK11-16c: m6
Th Mα
219
0
20 µm
LK11-16c: m6
Y Lα
38.8(0.9)
31.4(1.0)
35.6(1.0)
39.2(0.9)
160
0
20 µm
LK11-16c: m7
100 µm
LK11-16c: m7
BSE
217
0
50 µm
LK11-16c: m7
Th Mα
200
0
50 µm
LK11-16c: m7
Y Lα
31.9(0.8)
39.7(1.0)
40.5(1.0)
36.9(0.9)
37.9(0.9)
145
0
50 µm
LK11-16c: m11
100 µm
LK11-16c: m11
BSE
199
0
50 µm
LK11-16c: m11
Th Mα
180
0
50 µm
LK11-16c: m11
Y Lα
36.8(0.9)
39.1(1.0)
40.7(1.0)
41.3(1.0)
38.6(0.9)
156
0
50 µm


LK11-16c: m13
000
50 µm
LK11-16c: m13 BSE
170
0
50 µm
LK11-16c: m13 Th Mα
200
0
20 µm
LK11-16c: m13 Y Lα
27.1(0.9)
1
2
38.2(0.9)
160
0
20 µm
LK11-16c: m14
50 µm
LK11-16c: m14 BSE
186
0
50 µm
LK11-16c: m14 Th Mα
220
0
20 µm
LK11-16c: m14 Y Lα
40.6(1.0)
4
5
41.4(1.0)
41.0(1.0)
3
2
37.7(0.9)
1
40.6(1.0)
160
0
20 µm
LK11-16c: m18
100 µm
LK11-16c: m18 BSE
179
0
50 µm
LK11-16c: m18 Th Mα
120
0
20 µm
LK11-16c: m18 Y Lα
16.0(0.4)
4
15.1(0.4)
1
2
3
15.4(0.4)
17.0(0.4)
160
0
20 µm
LK11-16c: m19
50 µm
LK11-16c: m19 BSE
231
0
100 µm
LK11-16c: m19 Th Mα
200
0
100 µm
LK11-16c: m19 Y Lα
41.1(1.0)
8
9
40.8(1.0)
40.9(1.0)
7
10
39.8(0.9)
6
40.4(1.0)
5
39.9(0.9)
38.9(1.0)
4
40.7(1.0)
2
3
40.2(1.0)
41.2(1.0)
160
0
100 µm

Appendix 2.8.
Monazite Laser Ablation Split-stream U-Th/Pb Ages and Geochemical Analyses

This information has been uploaded as a supplemental file.

CHAPTER III
INFLUENCE OF METAMORPHISM AND DYNAMIC RECRYSTALLIZATION ON TITANIUM-IN-QUARTZ IN PELITIC ROCKS FROM THE LHAGOI KANGRI DOME, SOUTHERN TIBET

A version of this chapter will be submitted by Timothy Diedesch, Micah Jessup, John Cottle, and Lingsen Zeng:

Diedesch, T.F., Jessup, M.J., Cottle, J.M., Zeng, L., in prep, Influence of metamorphism and dynamic recrystallization on Titanium-in-quartz in pelitic rocks from the Lhagoi Kangri dome, southern Tibet: Journal of Metamorphic Geology.

My major contributions to this paper include: (1) conducting the cathodoluminescence and electron probe microanalyses, (2) calculating Titanium activities and modeling Ti-inquartz concentrations, (3) writing the manuscript, and (4) creating the illustrations.

Abstract

This study investigates the efficacy of titanium-in-quartz thermobarometry to reproduce pressure-temperature-deformation histories of high grade metasedimentary rocks. In this particular study samples from the Lhagoi Kangri dome, southern Tibet were selected because they record Barrovian metamorphism followed by near-isothermal decompression, both of which partially overlap in time with pervasive ductile deformation. The timing and conditions of these events are well documented in previous microstructural and petrologic investigations. Ti-in-quartz measurements and cathodoluminescent intensity from the selected samples indicate slight variations in [Ti] that are universally low (≤30 ppm), and when assuming $a\mathrm{TiO_2} = 1$, result in Ti-in-quartz temperatures that are much lower than expected from independent temperature estimates. Ti-in-quartz isopleths are calculated in P-T space for the sample compositions using $a\mathrm{TiO_2}$ values modeled by the software Perple_X. Modeled $a\mathrm{TiO_2}$ deviates substantially from ideal ($a\mathrm{TiO_2} = 1$) at or near the previously calculated peak metamorphic temperatures in three of four samples. However, even at these lower modeled $a\mathrm{TiO_2}$ values, temperature estimates from measured Ti-in-quartz abundances in most samples are still much lower than expected from independent temperature estimates on the same samples. The Ti-in-quartz values recorded in these samples are likely modified by the high-temperature deformation. From previous geochronologic constraints, minimum effective diffusion lengths for Ti-in-quartz in the samples were ~45 μm at 600 °C and ~325 μm at 700 °C, suggesting it is possible that at least near-rim compositions re-equilibrated during ductile deformation. If $a\mathrm{TiO_2}$ (real or apparent) is assumed to be significantly low ($a\mathrm{TiO_2} = 0.2$) during grain-boundary migration recrystallization because Ti-bearing phases do not typically recrystallize coevally, then measured Ti-in-quartz concentrations for Lhagoi Kangri dome samples result in isopleths

that correspond well with pressures and temperatures associated with the near-isothermal decompression portions of previously interpreted P-T paths.

Introduction

Experiments by Wark and Watson (2006) indicate that solubility of Ti in quartz is strongly temperature-dependent, and subsequent experimental calibrations of this solubility led to the development of the titanium-in-quartz (TitaniQ) thermobarometer (Thomas et al., 2010). TitaniQ has subsequently been used in a number of studies to estimate metamorphic temperatures (Ashley et al., 2013; Cherniak et al., 2007; Spear and Wark, 2009; Storm and Spear, 2009), deformation temperatures (Behr and Platt, 2011; Cross et al., 2015; Grujic et al., 2011; Kidder et al., 2013; Kohn and Northrup, 2009; Nachlas et al., 2014), and to constrain time scales of metamorphism via volume diffusion calculations (Cherniak et al., 2007; Spear et al, 2012). TitaniQ calculations require the assumption that $a\mathrm{TiO_2} = 1$ or that $a\mathrm{TiO_2}$ can be precisely calculated from phase equilibria involving Ti-bearing phases such as those of Ghent and Stout (1984). Studies employing TitaniQ typically rely on rutile-bearing rocks to justify the assumption that $a\mathrm{TiO_2} = 1$, or ~0.97 in the case of ilmenite-bearing rocks (e.g., Ashley et al., 2013). However, a recent study that models $a\mathrm{TiO_2}$ for an average metapelite bulk composition over moderate to high pressures and temperatures demonstrates that $a\mathrm{TiO_2}$ can deviate quite substantially from 1, particularly at high temperatures (Ashley and Law, 2015). Likewise, under conditions of dominant quartz grain-boundary migration (GBM) recrystallization, local $a\mathrm{TiO_2}$ is shown to be reduced, whether real or apparent, to ~0.2 (Grujic et al., 2011). Not only do these studies underscore the importance of accurately modeling $a\mathrm{TiO_2}$ for TitaniQ calculations, they also reinforce the need to thoroughly characterize microstructures and reaction textures to appropriately apply TitaniQ thermobarometry to rock samples.

In this study $a\mathrm{TiO_2}$ modeling and TitaniQ thermobarometry are applied to a suite of metasedimentary rocks that underwent upper amphibolite facies metamorphism and near peak-temperature ductile deformation, and for which the details of the metamorphic and deformation history have been previously characterized in the same samples (Diedesch et al., 2016, *in prep*). Using these previous constraints, the goal of this study is to evaluate the relative influences of metamorphic reactions and dynamic recrystallization on Ti-in-quartz distributions in high grade metasedimentary rocks. The

ability of modeled $a\mathrm{TiO_2}$ to predict Ti-in-quartz abundances is tested using one sample in which $a\mathrm{TiO_2}$ is expected to be low since rutile is not present and ilmenite is scarce, and thus resulting [Ti] isopleths should be markedly different from rutile-saturated ($a\mathrm{TiO_2} = 1$) conditions. Other samples selected contain abundant ilmenite or rutile implying $a\mathrm{TiO_2}$ is near 1, and modeled $a\mathrm{TiO_2}$ and calculated TitaniQ temperatures are used in conjunction with previous petrologic and deformation temperature constraints to evaluate whether or not $a\mathrm{TiO_2}$ was fixed during quartz-forming metamorphic reactions and quartz dynamic recrystallization.

Geologic Setting and Sample Description

Samples analyzed in this study were collected from two locations within the Lhagoi Kangri dome (LKD) in southern Tibet (Fig. 3.1), and they correspond to samples previously studied by Diedesch et al. (2016*, in prep*). All samples derive from structurally lower levels of a Paleozoic sequence of siliciclastic and minor carbonate metasedimentary rocks that underwent Barrovian metamorphism during crustal shortening (D1) followed closely by ductile deformation (D2) contemporaneous with nearly isothermal decompression during Eocene–Oligocene time (c. 40 to ≤ 24 Ma; Diedesch et al., *in prep*). D2 deformation in the LKD defines a distributed shear zone that is restricted to the lower structural levels of the metasedimentary rocks as well as an underlying orthogneiss unit (og, Fig. 3.1). Above the shear zone, the metasedimentary rocks also record Barrovian metamorphism, but the dominant rock fabric is a slaty cleavage associated with D1 (Diedesch et al., 2016). Previous work indicates that the rocks reached upper amphibolite facies conditions (600–700 °C, 7–10 kbar) during prograde metamorphism followed, at the lowest structural levels, by 5–6 kbar of decompression to cordierite-stable conditions (Diedesch et al., *in prep*; Rolfo et al., 2004). L-S fabric, porphyroblast strain shadows, and mica fish record D2 vertical thinning that began during the latest stages of Barrovian metamorphism and continued through nearly isothermal decompression. In quartz, D2 deformation was generally accommodated by high-temperature grain boundary migration and prism <a> ± prism [c] slip (Diedesch et al., *in prep*). Given the complex history of deformation and metamorphism in these rocks, quartz grains in the four selected samples were grouped into various microstructural domains as described in the following.

The sample selected from the northern LKD location (LK11-16c) is a garnet paragneiss with the

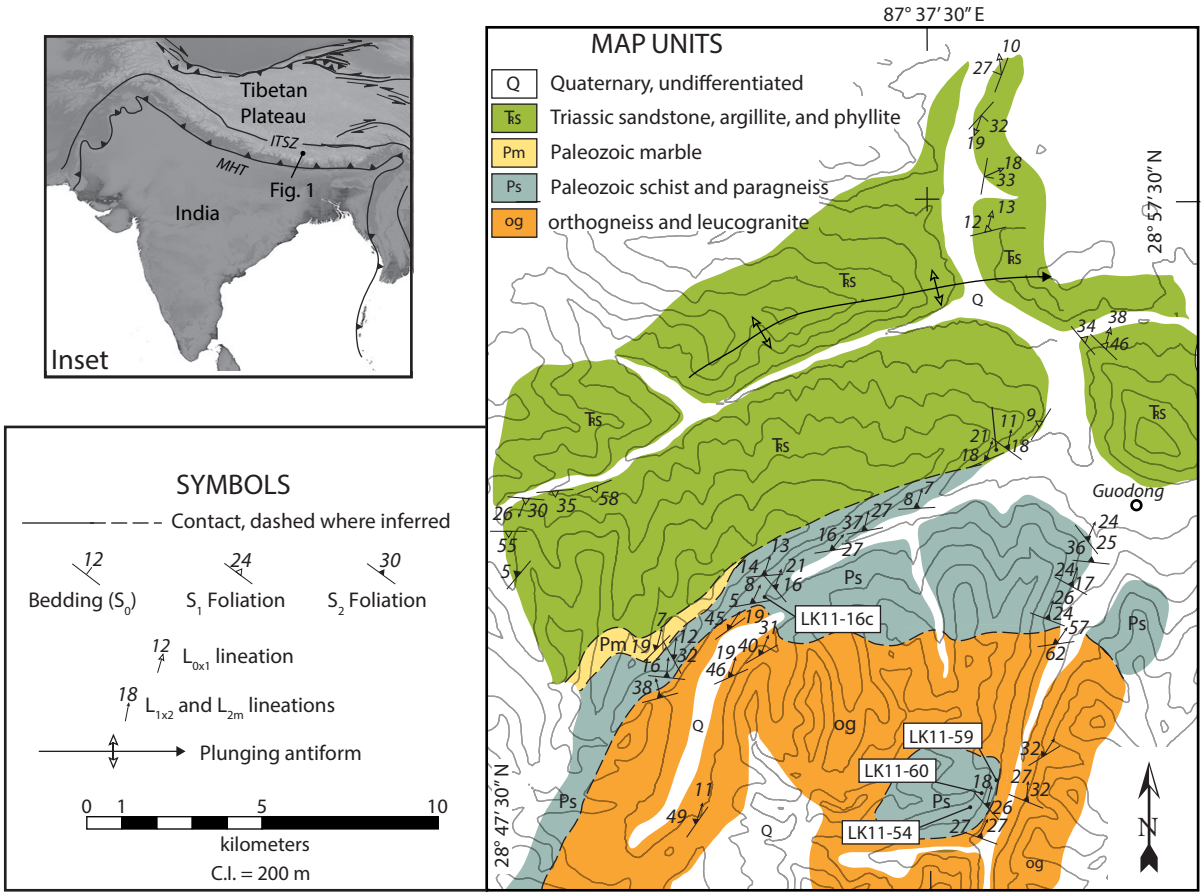


Figure 3.1. *Geologic map of a portion of the Lhagoi Kangri dome (LKD) showing the locations of samples discussed in this study. Inset shows the location of the LKD with respect to major modern structures bounding the Himalaya: MHT—Main Himalayan Thrust, ITSZ—Indus-Tsangpo Suture Zone. Modified from Diedesch et al. (*2016*).*

assemblage: garnet + biotite + white mica + plagioclase + K-feldspar + quartz + kyanite ± sillimanite + Fe-Ti oxides (Fig. 3.2). Phase equilibria calculations and pseudosection modeling indicate the sample reached peak Barrovian conditions of 644 ± 21 °C at 9.9 ± 1.1 kbar, but in the absence of low pressure, high temperature phases (e.g., cordierite) the post-peak P-T path is not defined (Diedesch et al., *in prep*). The sample contains a strong S-C fabric (Figs. 3.2a, 3.2b, 3.2d), and along with these two microstructural domains, quartz also occurs in garnet strain shadows and along garnet grain boundaries that are truncated by shear bands (Fig. 3.2c). In the S domains (Figs. 3.2b, 3.2d), quartz exhibits lobate grain boundaries, mica inclusions, and chessboard extinction microstructures that indicate fast grain-boundary migration (GBM; Stipp et al., 2002) recrystallization, previously interpreted to indicate deformation at ≥550 °C in LKD (Diedesch et al., 2016). Quartz in the shear bands appears finer grained and exhibits some subgrain rotation (SGR) recrystallization in addition to the lobate boundaries that indicate GBM (e.g., Figs 3.2a, 3.2d). In both garnet strain shadows and along garnet truncation surfaces, some quartz grains have lobate boundaries (i.e., GBM), but most exhibit well defined triple junctions that indicate static recrystallization.

The three samples selected from the central LKD location consist of two metapelites (LK11-59, LK11-60) and a biotite quartzite (LK11-54), the latter of which is included in this study to address possible differences in [Ti] in quartz results that can be attributed to compositional differences (Fig. 3.1). The metapelite samples were collected within 50 m structural thickness of one another and contain the assemblage: garnet + biotite + plagioclase + white mica + kyanite + fibrolite + cordierite + K-feldspar + quartz + Fe-Ti oxides ± staurolite. Phase equilibria calculations are complicated by the large number of phases and complex reaction textures, but are in general agreement with pseudosection models for the two samples that indicate Barrovian conditions of 650–700 °C at 9–10 kbar followed by nearly isothermal decompression to at least 5 kbar and possibly as low as 3 kbar (Diedesch et al., *in prep*). Both samples exhibit local microstructural domains like C' shear bands (Fig. 3.3a), porphyroblast (mostly garnet) strain shadows (Fig. 3.3d), and garnet inclusion trails (Fig. 3.3c) that all contain quartz, among other phases (Figs 3.3a–3.3d, 3.4a, 3.4b). Matrix fabric is complex, but in terms of quartz, can be subdivided into 'coarse' and 'fine' zones (e.g., Figs 3.3b, 3.4a–3.4b). These zones are not systematic throughout the samples, and are instead defined by the locally dominant quartz microstructure. The coarse zones contain relatively large quartz grains with mica inclusions and lobate boundaries indicating non-impurity hindered GBM (Fig. 3.3b) (Stipp et al., 2002), whereas the fine zones contain relatively

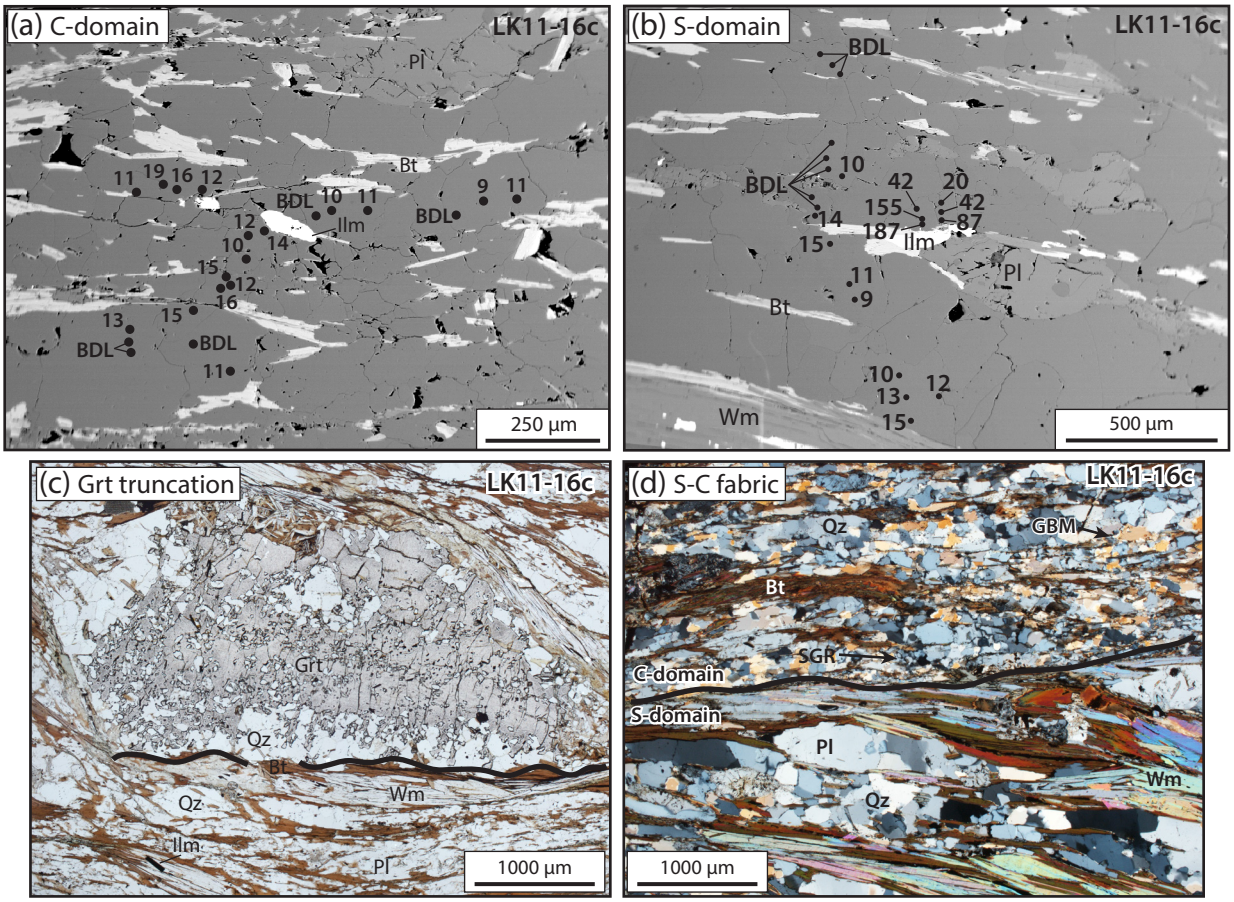


Figure 3.2. *Backscattered electron (BSE) images (a,b) and photomicrographs (c,d) of LK11-16c. Mineral abbreviations after Whitney and Evans (2010) with the exception of Wm—white mica. Dots are locations of Ti-in-quartz analyses labeled with the Ti concentration (ppm) measured at that location. BDL—below detection limit. Black line (c) marks the approximate location of the truncated garnet grain edge discussed in text. (d) C and S domains, as discussed in text, at top and bottom of photomicrograph. Horizontal black line denotes the approximate boundary between the two domains. Note that quartz grain sizes are generally smaller in the 'C' domain. GBM—grain-boundary migration recrystallization, SGR—subgrain rotation recrystallization.*

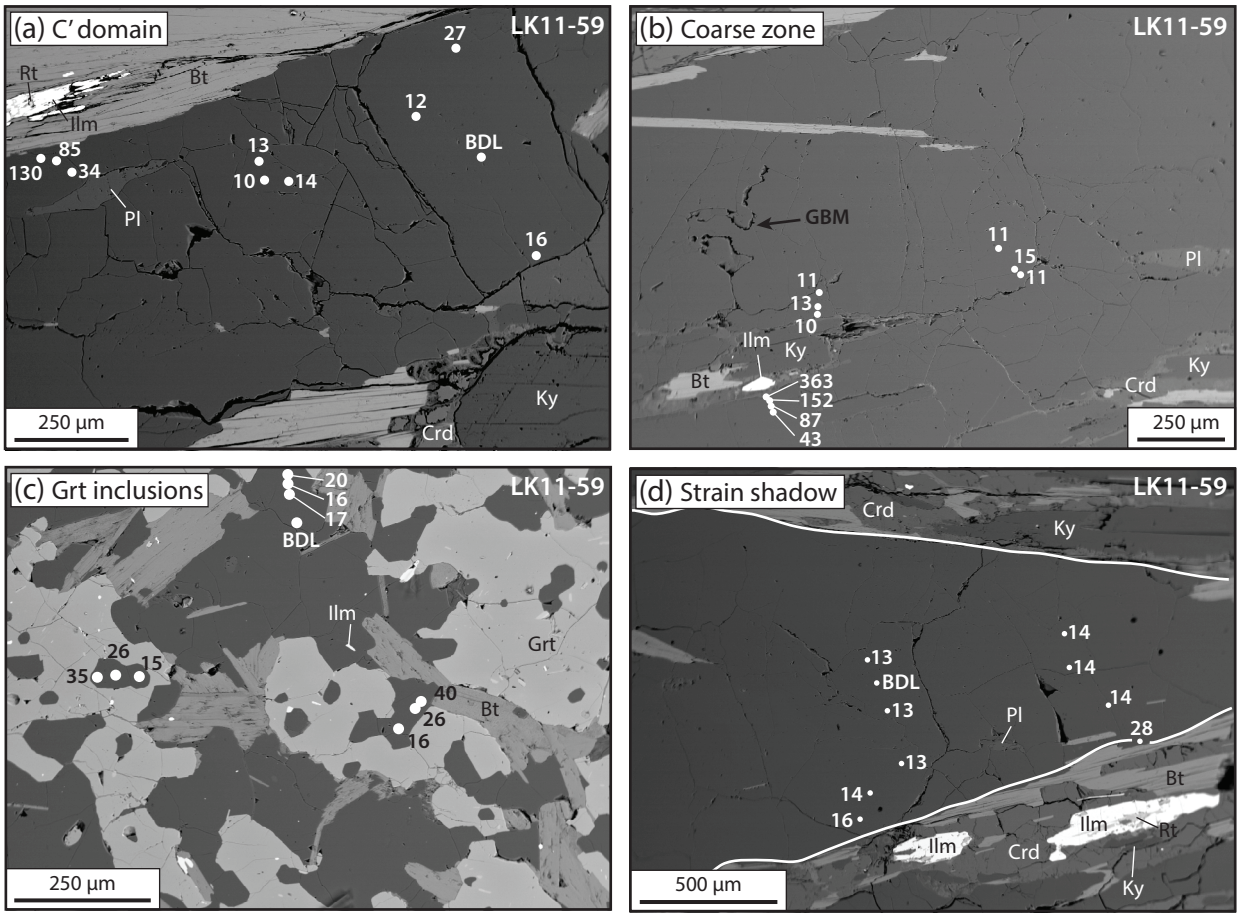


Figure 3.3. *BSE images of different microstructural domains in sample LK11-59. Dots are locations of Ti-in-quartz analyses labeled with measured concentrations (in ppm). Mineral abbreviations after Whitney and Evans (2010). BDL—below detection limit, GBM—grain boundary migration recrystallization.*

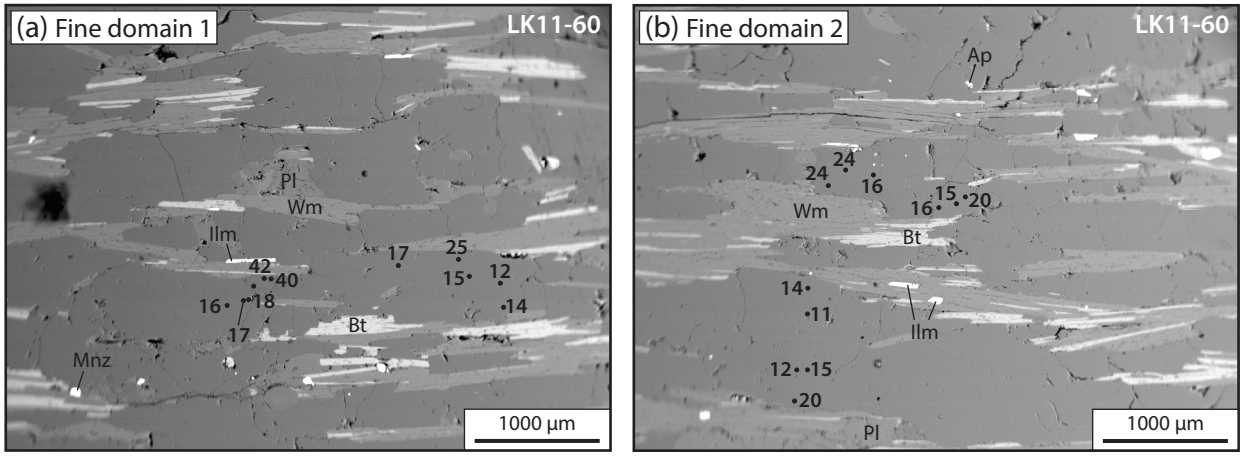


Figure 3.4. *BSE images of two fine matrix quartz domains from sample LK11-60. Dots are locations of Ti-in-quartz analyses labeled with measured concentrations (in ppm). Mineral abbreviations after Whitney and Evans (2010) with the exception of Wm—white mica.*

small quartz grains that commonly exhibit lobate boundaries but are often truncated by secondary phases, typically biotite, indicate impurity-hindered GBM (Stipp et al., 2002) (Fig. 3.4a). There is no clear distinction in quartz microstructure between the matrix versus those in C' shear bands. Quartz inclusions in garnet porphyroblasts and quartz grains in garnet strain shadows typically occur as polycrystalline aggregates with straight grain boundaries and triple junctions that indicate static recrystallization (Figs 3.3c, 3.3d).

Sample LK11-54 is a biotite quartzite, collected from ~120 m structurally below LK11-59 and ~170 m structurally below LK11-60, that contains minor white mica, plagioclase, Fe-Ti oxides, apatite, and tourmaline (Fig. 3.5). Non-impurity hindered GBM and chessboard extinction in quartz are ubiquitous throughout the sample (e.g., Fig. 3.5a) and are previously interpreted as indicators of deformation at ≥550 °C, consistent with quartz opening angle thermometry from the same sample that indicates ~595 ± 50 °C (Diedesch et al., 2016).

Methods

Cathodoluminescence (CL) imaging was conducted with a Premier American Technologies ELM-3R Luminoscope mounted on the stage of a Nikon Eclipse petrographic microscope equipped with an Olympus Magnafire CCD camera at the University of Tennessee. Although optical-CL imaging

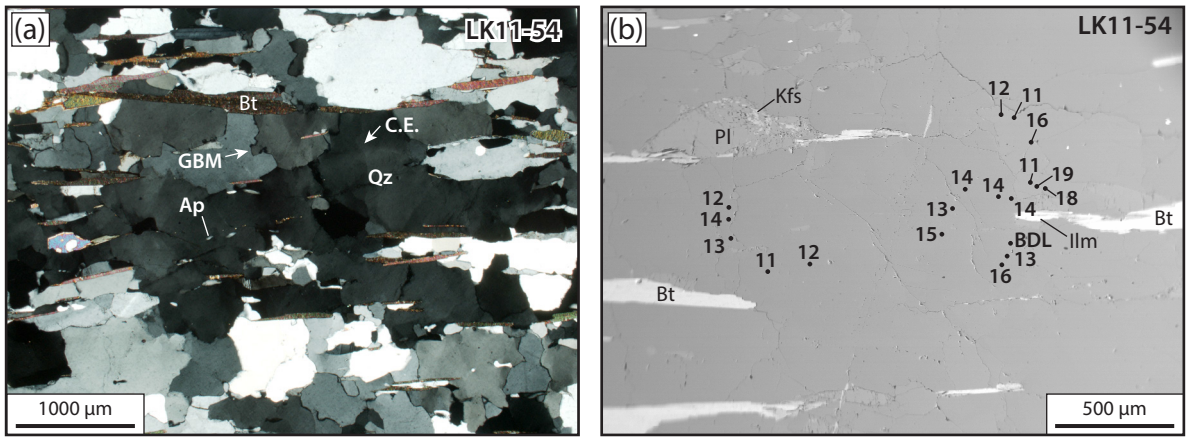


Figure 3.5. *BSE image and photomicrograph of LK11-54. (a) Cross-polarized transmitted light photomicrograph showing microstructures and mineral phases of sample LK11-54. GBM—grain boundary migration recrystallization, C.E.—chessboard extinction microstructure. (b) BSE image of sample LK11-54 showing examples of the variations in Ti-in-quartz analyses (black dots, labeled with concentrations in ppm) from this sample. Mineral abbreviations after Whitney and Evans (2010) with the exception of Wm—white mica.*

does not afford the high spatial resolution of scanning electron microscope (SEM) methods, the optical-CL method is acceptable for this study, given the large grain sizes and, more importantly, the analytical spot-sizes employed (see below). Furthermore, the CCD camera was the only readily available imaging system equipped with a filter wheel that allows isolation of blue wavelengths, the intensity of which is proportional to Ti concentration (e.g., Rusk et al., 2006; Spear and Wark, 2009). The CL was generated during imaging using an electron beam current of 1.5–2 mA with accelerating voltage of 20–25 kV. To minimize complications from time-dependent shifts in CL emission spectra (e.g., Götze et al., 2001), samples were not subjected to the electron beam for longer than ~10 minutes (typical blue exposure times ranged from 6–8 minutes) with the beam defocused by ~25% (corresponding to a beam current density of ~5 mA mm^{-2}).

Quantitative chemical analyses of quartz, ilmenite, and rutile were conducted on a Cameca SX100 Electron Probe Microanalyzer (EPMA) housed at the University of Tennessee. For Ti analyses three wavelength spectrometers were employed, two utilizing PET and one utilizing LiF analyzer crystals. Analyses were conducted using a 150–200 nA beam current and accelerating voltage of 20 keV. Spot sizes varied between 15 and 20 µm and peak count times were varied between 600 and 960 s

depending on the amount of visually estimated damage induced by the electron beam. To monitor and account for changes in X-ray intensity (Donovan et al., 2011), as well as beam damage, during such long analyses, counting was cycled between on-peak, low off-peak, and high off-peak over the course of the analysis (e.g., for a 960 s analysis: 160 s on-peak, 80 s low off-peak, 80 s high off-peak cycled six times). Peak and background counts were aggregated separately and combined after deadtime correction using the standard Cameca SX software package. This procedure was conducted to ensure detection limit statistics are propagated and reported accurately (Donovan et al., 2011). Two experimentally grown, Ti-doped quartz samples (10875 and 10925; Thomas et al., 2015), with independently measured Ti concentrations, were used as standards. Additionally, a Herkimer quartz grain was measured as a Ti-blank (<6 ppb; e.g., Kohn and Northrup). A three-sigma detection limit of ~9 ppm for all measurements was calculated with the SX software by the standard conversion of background counts to concentration using the ZAF correction factor (approximately = 1) and count-rate per weight percent of the titanium standard (I_{std}) using the following equation:

$$\text{d.l.} = 3(\text{ZAF})\left(\frac{1}{I_{std}}\right)\sqrt{I_b/t_b} \qquad (3\text{-}1)$$

where d.l. is detection limit, I_b is sample background count rate, and t_b is sample background count time in seconds. These calculated detection limits are similar to a 7 ppm value that was consistently attained from analyses on the Herkimer standard. Since titanium concentrations in the samples analyzed are much lower than those of the doped standards, uncertainties of 7–9 ppm reported here are the theoretical three-sigma values calculated using the square root of total counts after the deadtime correction procedure noted above.

For the metapelite samples discussed, thermodynamic models were previously constructed by Diedesch et al. (*in* prep) with Perple_X in the constrained minimization mode (Connolly, 2009) for the 10-component system: MnO–Na_2O–CaO–K_2O–FeO–MgO–Al_2O_3–SiO_2–TiO_2–H_2O (MnNCKFMASTH). This is the most realistic system to apply to metapelites (e.g. White et al., 2014). In this contribution TiO_2 activity and expected TiO_2 concentrations in the metapelites are calculated from the previously constructed models, which incorporated: (1) staurolite, chlorite, white mica, and hydrous cordierite solution models of Holland and Powell (1998); (2) the expanded garnet solution model of White et al.

(2000); (3) the ternary feldspar solution model of Fuhrman and Lindsley (1988); (4) an extended biotite solution model accounting for Ti and Fe^{3+} (Tajčmanová et al., 2009); and (5) an ideal mixing model for ilmenite–geikeilite–pyrophanite. Over the modeled P-T space, TiO_2 activity was calculated from the thermodynamic relationship:

$$\mu_{TiO_2} = \mu^{\circ}_{TiO_2} + RT\ln a_{TiO_2} \quad (3\text{-}2)$$

where μ_{TiO_2} is the chemical potential of TiO_2 in the modeled system, $\mu^{\circ}_{TiO_2}$ is the ideal standard state chemical potential (equivalent to the molar Gibbs free energy, G , of pure TiO_2), R is the ideal gas constant (8.31446 J K^{-1} mol^{-1}), T is temperature in Kelvins, and a_{TiO_2} is activity. The ideal chemical potential was derived from Perple_X by utilizing the equivalence between $\mu^{\circ}_{TiO_2}$ and G , and the resulting a_{TiO_2} was used to calculate expected TiO_2 concentrations in quartz with the Thomas et al. (2010) Ti-in-quartz solubility equation. The procedures for modelling a_{TiO_2} and Ti concentrations using Perple_X were originally developed and are described in greater detail by Ashley and Law (2015). The advantage of the Perple_X-modeled TiO_2 activities is that they do not require specific TiO_2-bearing phases such as rutile or ilmenite in the mineral assemblage, but as with any pseudosection model they are based on a variety of assumptions, most notably effective bulk composition, and will vary with the chosen solution models and thermodynamic dataset (Ashley and Law, 2015).

Results

Quartz CL Imaging

There are slight variations in the intensity of blue-filtered quartz CL in all three metapelite samples (Figs 3.6a–3.6d). The quartzite sample (LK11-54) is not included here because it was very faintly luminescent, resulting in underexposed images. It is likely that the quartz CL in LK11-54 was 'quenched' by electron beam damage (e.g., Stevens-Kalceff et al., 2000) during previous SEM analyses. In the remaining samples the variations in quartz CL intensity do not clearly delineate zoning with the possible exception of sample LK11-59. In this sample, matrix quartz grains (Fig. 3.6b) exhibit lower near-rim intensity than the grain interiors, whereas quartz inclusions in garnet (Fig. 3.6c) exhibit higher

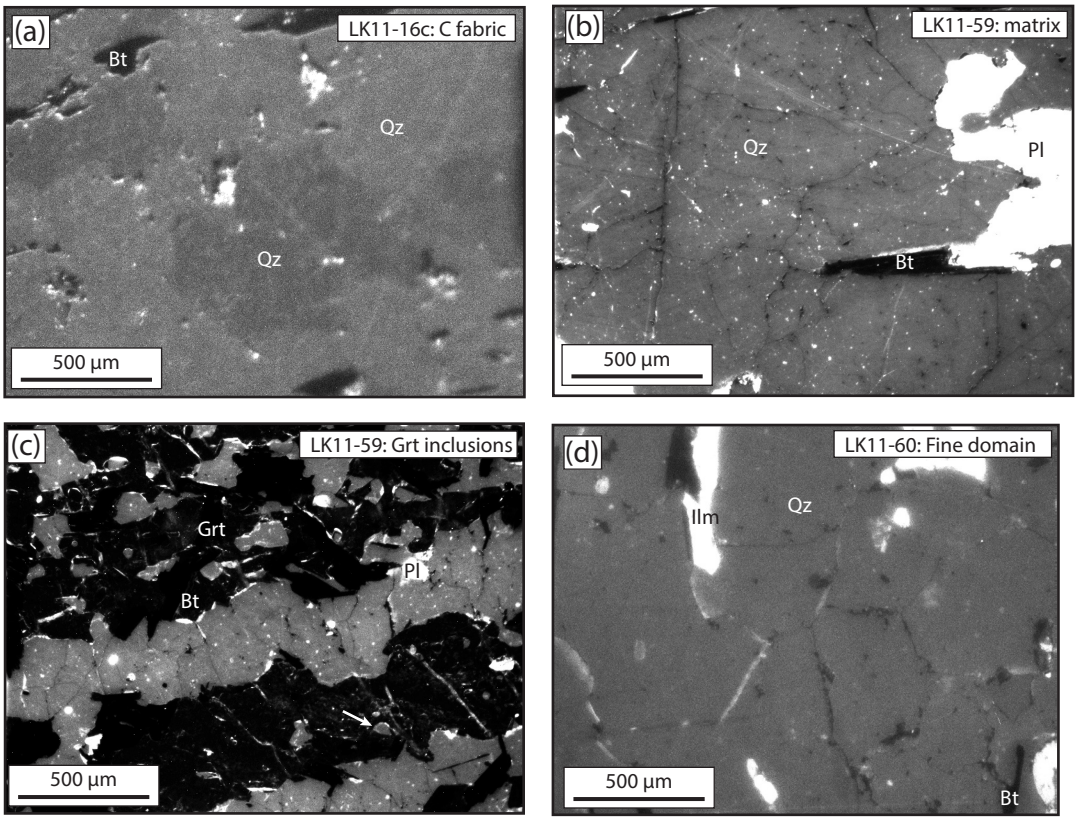


Figure 3.6. *Example blue-filtered cathodoluminescence (CL) images. (a) CL image taken on LK11-16c shows distinct intensity variations between grains, which is likely the result of differences in orientation as discussed in text. Within the brighter grains, there is a slight decrease in intensity from core to rim. (b) Representative CL image of matrix quartz in samples LK11-59. Similar to (a) there are intensity variations between grains as well as within individual grains, the latter characterized by slight decrease in intensity. (c) CL image of quartz inclusions in garnet. Blue-filtered CL contrast is brighter near the rims of the quartz grains than the cores (see white arrow near bottom of photomicrograph. (d) Example CL image of matrix quartz in LK11-60. The variations in CL are subtle, and some grains exhibit brighter rims than cores (lower right).*

near-rim intensity than the grain cores. In the other two metapelites, the most notable variations in intensity are between different grains rather than within individual grains, and in all three samples CL intensity appears to increase with proximity to inclusions or polishing artifacts (e.g., Figs 3.6a, 3.6b). Adjacent to Ti-bearing phases (i.e., biotite, ilmenite, rutile) quartz CL variation is not systematic in the LKD samples: in some instances, it remains relatively uniform, while in others, the intensity either increases or decreases. Other petrogenetic and kinetic considerations notwithstanding, this suggests that Ti concentrations are not the only significant influence on quartz CL in the LKD samples. One likely additional influence on the quartz CL in the LKD samples is crystallographic orientation (e.g., Spear and Wark, 2009) given the prevalence of intensity contrasts between grains (e.g. Fig. 3.6a).

Ti-in-Quartz Analyses

For this initial exploratory study, 5–10 grains were selected from each of the microstructural domains defined above for each sample. In the case of the quartzite sample (LK11-54) for which there are no discrete microstructural domains, grains were selected in regions where ilmenite ± rutile are present where a_{TiO_2} is more likely to be close to 1. For each grain, 3–5 spots were analyzed, with the number of spots depending on: (1) the amount of variation in measured Ti concentration from spot to spot, or (2) variation in CL intensity across the grain when present. The results are summarized in Table 3.1 and described briefly here. Because secondary fluorescence caused by mechanical excitation of the quartz lattice, particularly during long analyses, can produce Ti Kα X-rays that result in anomalously high measured Ti concentrations (e.g. Wark and Watson, 2006), analyses within 50–100 μm of rutile, ilmenite, or biotite grains are not considered in calculations involving Ti concentration. However, examples of these analyses described below for reference.

LK11-16c

In sample LK11-16c Ti concentrations are uniformly low—nearly half of the analyses yielded results below the 9 ppm detection limit—with the exception of analyses near ilmenite and biotite (Table 3.1). In both C and S domains, individual analyses vary from below detection limit (~9 ppm) to ~20 ppm (e.g., Figs 3.2a and 3.2b). Ti concentrations in quartz measured adjacent to Ti-bearing phases increase with proximity to the phase. The highest measured value is 187 ± 7 ppm at a distance of ~50 μm from

Table 3.1. Ti-in-quartz analyses and previous P-T constraints.

Sample	[a]Microstructure	[b]Domain	[c]n	[d,e][Ti] min. (ppm)	[e][Ti] max (ppm)	[e,f][Ti] near (ppm)	[g]Previous P-T	
							Pressure (kbar)	Temp. (°C)
LK11-16c	GBM, SGR	C	55 (19)	4	19	187, 155, 87, 42, 42	9.9 ± 1.1	644 ± 21
	GBM	S	32 (11)	2	20			
	Static	Grt truncation	7 (6)	5	17			
LK11-54	GBM	–	20 (1)	9	16	19, 18	–	–
LK11-59	GBM	Coarse	21 (3)	6	19	834, 363, 292, 152, 141, 87, 85, 43, 34	7.5–10.5	680–697
	GBM	C’	9 (1)	7	27			
	Static	Grt strain shadows	19 (2)	7	16			
	Static	Inclusions	10 (1)	9	35			
LK11-60	GBM	Coarse	2 (2)	6	9	111, 42, 40, 23, 20	8.8 ± 1.1	714 ± 27
	GBM, Static	Fine	31 (0)	11	25			

[a]GBM—grain boundary migration recrystallization, SGR—subgrain rotation recrystallization. After Stipp et al (2002).

[b]Microstructural domains defined in text. Inclusions are quartz inclusions in garnet.

[c]Number of analyses from each microstructural domain. Number of measurements below detection limit (9 ppm) are in parentheses.

[d]Note that most minimum [Ti] analyses are below the detection limit of 9 ppm.

[e]All [Ti] measurements have analytical uncertainty of ± 7 ppm.

[f][Ti] near—measurements within ~100 μm of rutile, ilmenite, or biotite and are likely influenced by secondary fluorescence as discussed in the text.

[g]Estimates from Diedesch et al. (in prep) based on average phase equilibria calculations (LK11-16c, LK11-60) and modeled mineral composition isopleths (LK11-59).

an ilmenite grain. Quartz along the truncated garnet grain boundary yielded only two concentration estimates (17 and 24 ppm) above the detection limit and both are within 100 μm of matrix biotite.

LK11-54

Despite the fact that this sample did not exhibit strong quartz luminescence, spot analyses from two different ~6.25 mm^2 -regions exhibit a range of Ti concentrations slightly above detection limit (11–16 ppm, Fig. 3.5b). Only two spots were measured within ~50 μm of an ilmenite grain and they exhibited slightly higher concentrations (18 and 19 ppm, respectively), but clearly a more subdued increase than that of sample LK11-16c.

LK11-59

Ti concentrations from sample LK11-59 were measured in four distinct domains: coarse, C' shear band, garnet strain shadow, and garnet inclusions (see Fig. 3.3 and 'Sample Descriptions' above). Measurements from the fine-grained domain are all below detection limit (9 ppm), whereas those in the coarse domain are slightly above, with one measurement as high as 19 ppm. In total, the coarse domain analyses vary from ≤9–19 ppm. There is no apparent correlation between spot location and Ti concentration in contrast to the CL imaging, which shows consistently higher intensities along quartz rims than cores (e.g., Fig. 3.6c). Quartz in a C' shear band in the sample is not markedly different from the coarse quartz values reported. Measured Ti concentrations in the C' shear band are 10–16 ppm with an average of 13 ppm. One spot at the margin of the shear band has a value of 27 ± 7 ppm, but the analysis is suspect because it is within 100 μm of a biotite grain and previously reported Ti-in-biotite concentrations for this sample are as high as 2.5–3.0 wt% (Diedesch et al., *in prep*). As with the C' shear band analyses, Ti-in-quartz in two garnet strain shadows is higher along the margins of the strain shadows (24–39 ppm) than in the interiors (11–16 ppm; e.g., Fig. 3.3d). Because adjacent domains contain large ilmenite grains with rutile inclusions, it is assumed that the higher values along the margins are spurious. Average Ti concentration is ~14 ppm, excluding the high values. In contrast to the microstructural domains described thus far, quartz inclusions in garnet exhibit more variability in Ti concentration and generally higher values (16–40 ppm; Table 3.1). Quartz inclusions in garnet are commonly mantled by biotite, and some contain Fe-Ti oxide inclusions (Fig. 3.3c), but CL intensity images (e.g., Fig.

3.6c) support the assumption that higher near-rim Ti concentrations are real results. Furthermore, the backscattered electron (BSE) images show that there are very few Fe-Ti oxides in the quartz inclusions selected for analysis, but possible presence of nanoscale Ti-bearing phases is not ruled out.

LK11-60

Measured Ti concentrations in quartz from the fine-grained matrix exhibit a range in Ti concentrations of 11–25 ppm. Grain rims consistently yield higher Ti concentrations than grain cores regardless of the adjacent mineral phase (Fig. 3.4). Abundances of Ti in coarse-zone and strain-shadow quartz grains were generally below detection limit (≤9 ppm), while C' shear bands in the representative thin section do not contain quartz layers.

Titanium Activity Modeling

The presence of ilmenite ± rutile in all three metapelite samples suggests that $a\mathrm{TiO_2}$ should be at or near 1 (e.g., Ashley, 2013; Chambers and Kohn, 2012; Ghent and Stout, 1984). The Ghent and Stout (1984) model, which is the original basis for inferring $a\mathrm{TiO_2}$ near 1, relies on phase equilibria involving rutile or ilmenite. However, it may be necessary to calculate $a\mathrm{TiO_2}$ in systems that do not contain these phases. More recent studies have shown that $a\mathrm{TiO_2}$ in higher temperature systems can deviate substantially from a value of 1 owing to Ti uptake by additional phases such as biotite (Ashley and Law, 2015); this also occurs, locally, by quartz dynamic recrystallization, particularly at temperatures where grain-boundary migration is the dominant mechanism (e.g., Ashley et al., 2014; Grujic et al., 2011; Kohn and Northrup, 2009). Quartz dynamic recrystallization is not generally accompanied by recrystallization of Ti-bearing phases, so effective activity at the time of quartz recrystallization is likely much lower than 1. A previous study on quartz mylonites from the Alps estimated effective $a\mathrm{TiO_2}$ as low as 0.2 during GBM recrystallization (Grujic et al., 2011). In that study, the authors noted that this relationship does not hold for the lower temperature SGR and bulging recrystallization (BLG) regimes, and they suggest that this is due to the slow rate of Ti volume diffusion coupled with short duration of deformation. It was also suggested that the physical migration of grain boundaries during GBM was responsible for Ti re-equilibration rather than volume diffusion (Ashley et al., 2014; Grujic et al., 2011). Previous pseudosection and phase equilibria modeling on the three LKD metapelites chosen for this study suggest

that they all reached peak temperatures of ≥600 °C (Fig. 3.7) and that deformation took place at or near peak conditions and involved predominantly GBM recrystallization (Diedesch et al., 2016*, in prep*). These observations justify modeling $a\mathrm{TiO_2}$ for each LKD sample, the results of which are shown in Figures 3.8a–3.8c.

All three models concur with the previous studies that suggest that $a\mathrm{TiO_2}$ in metapelites is generally 0.95–1 for moderate temperatures and pressures. However, two of the models (Figs 3.8b and 3.8c) also support a conclusion by Ashley and Law (2015) that $a\mathrm{TiO_2}$ for an average metapelite composition fluctuates dramatically over small P-T increments at higher grade metamorphic conditions. Recognition of this dynamic chemical activity pattern is particularly important for samples like LK11-16c (Fig. 3.8c) in which the calculated $a\mathrm{TiO_2}$ drops from ~1 to 0.5 over the P-T interval calculated from phase equilibria modeling (Fig. 3.7).

To understand the implications that $a\mathrm{TiO_2}$ deviations have for the P-T-d history of the LKD rocks, Ti isopleths were calculated over the same P-T interval as $a\mathrm{TiO_2}$ (3–10 kbar, 450–750 °C) using the modeled $a\mathrm{TiO_2}$ values in the Thomas et al. (2010) TitaniQ solubility equation:

$$\mathrm{RT ln X}_{\mathrm{TiO2}}^{\mathrm{quartz}} = -6095 + 1.520 \cdot \mathrm{T} - 1741 \cdot \mathrm{P} + \mathrm{RT ln} a_{\mathrm{TiO2}} \qquad (3\text{-}3)$$

Where R is the ideal gas constant, T is temperature in Kelvins, and P is pressure in kilobars (Figs 3.8d–3.8f). This particular form of the solubility equation was selected because it has been previously used on rocks of similar composition and metamorphic grade to calculate temperatures that are consistent with independently constrained petrologic temperatures (Ashley et al., 2013). Except at low pressure and high temperature, Ti isopleths modeled for LK11-59 closely match those resulting from ideal behavior ($a\mathrm{TiO_2}$ = 1 at all pressures and temperatures) (Fig. 3.8d). Sample LK11-60 represents an intermediate situation where, for most of the P-T window, calculated Ti isopleths remain linear and the magnitudes are similar to those calculated from ideal $a\mathrm{TiO_2}$, but there is a significant departure at the highest temperatures (Fig. 3.8e). This is not surprising since the Thomas et al. (2010) solubility equation predicts lower [Ti] for lower $a\mathrm{TiO_2}$ at fixed pressure and temperature. However, the result could be quite significant for the LKD because, at temperatures nearing 700 °C, the modeled drop in Ti activity results in the decrease of predicted [Ti] by ~5 ppm at 10 kbar and ~20–25 ppm at 8 kbar. These magnitudes are

Figure 3.7. *P-T pseudosections for Ps metapelites. (a) LK11-16c, (b) LK11-59, and (c) LK11-60 calculated in the 10-component system: MnO–Na2O–CaO–K2O–FeO–MgO–Al2O3–SiO2–H2O–TiO2 and modified from Diedesch et al. (in prep). Quartz and water are considered in excess in all models. Bold labeled fields represent the previously interpreted peak assemblages. Polygons labeled "Avg. P-T" are thermobarometric calculations from Diedesch et al. (in prep) and polygons labeled "Grt rims" and "Grt cores" are interpreted mineral composition isopleths from the same study. Dashed arrows represent interpreted P-T paths. Red lines indicate rutile-in and blue lines indicate ilmenite-out.*

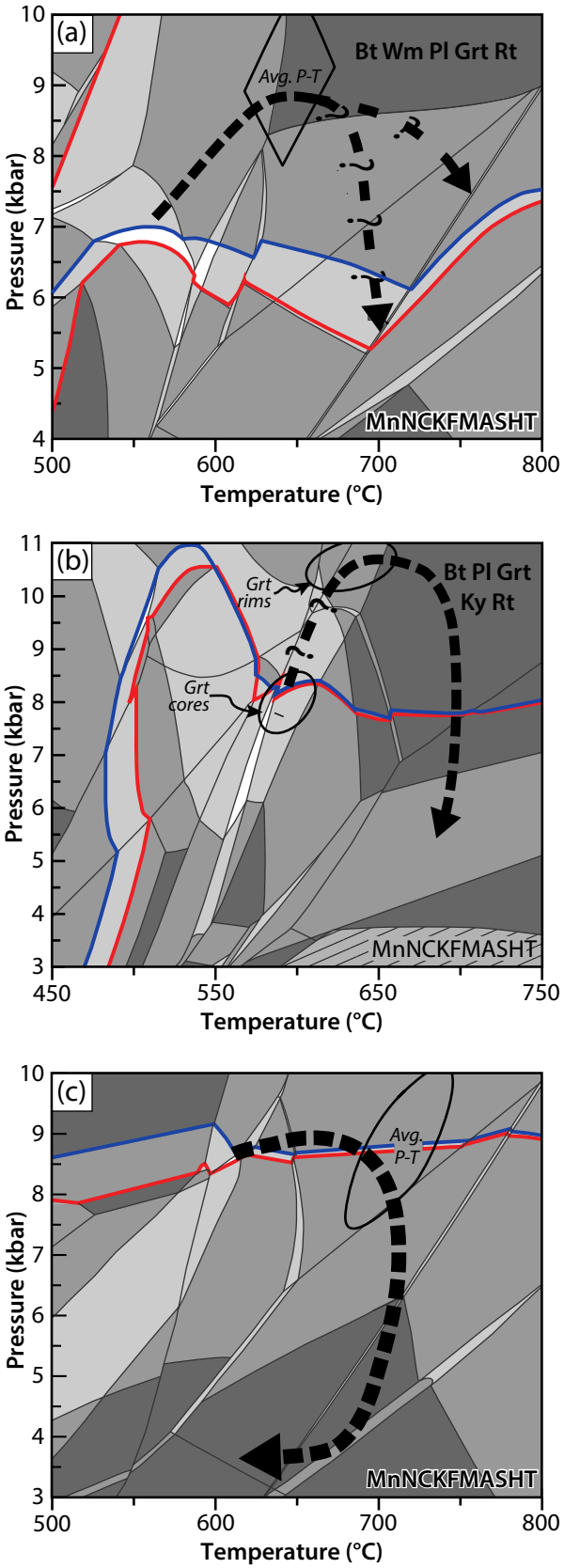


Figure 3.7. Continued.

Figure 3.8. *Modeled $aTiO_2$ for the LKD metapelites (a–c) and corresponding calculated Ti-in-quartz concentrations (d–f) using the calibration of Thomas et al. (2010). Gray dashed lines in (d) represent ideal isopleths ($aTiO_2$ = 1 at all pressures and temperatures). Gray-filled areas in (d–f) denote the maximum Ti-in-quartz measured in each sample. Polygons and bold dashed lines are as in Figure 3.7. Red dashed lines in (e) and (f) represent ideal Ti isopleths from (d) that correspond to pressures of 8 kbar and 10 kbar at 700 °C (intersections marked by red stars). Note that the modeled Ti concentrations in these samples are much lower than the ideal.*

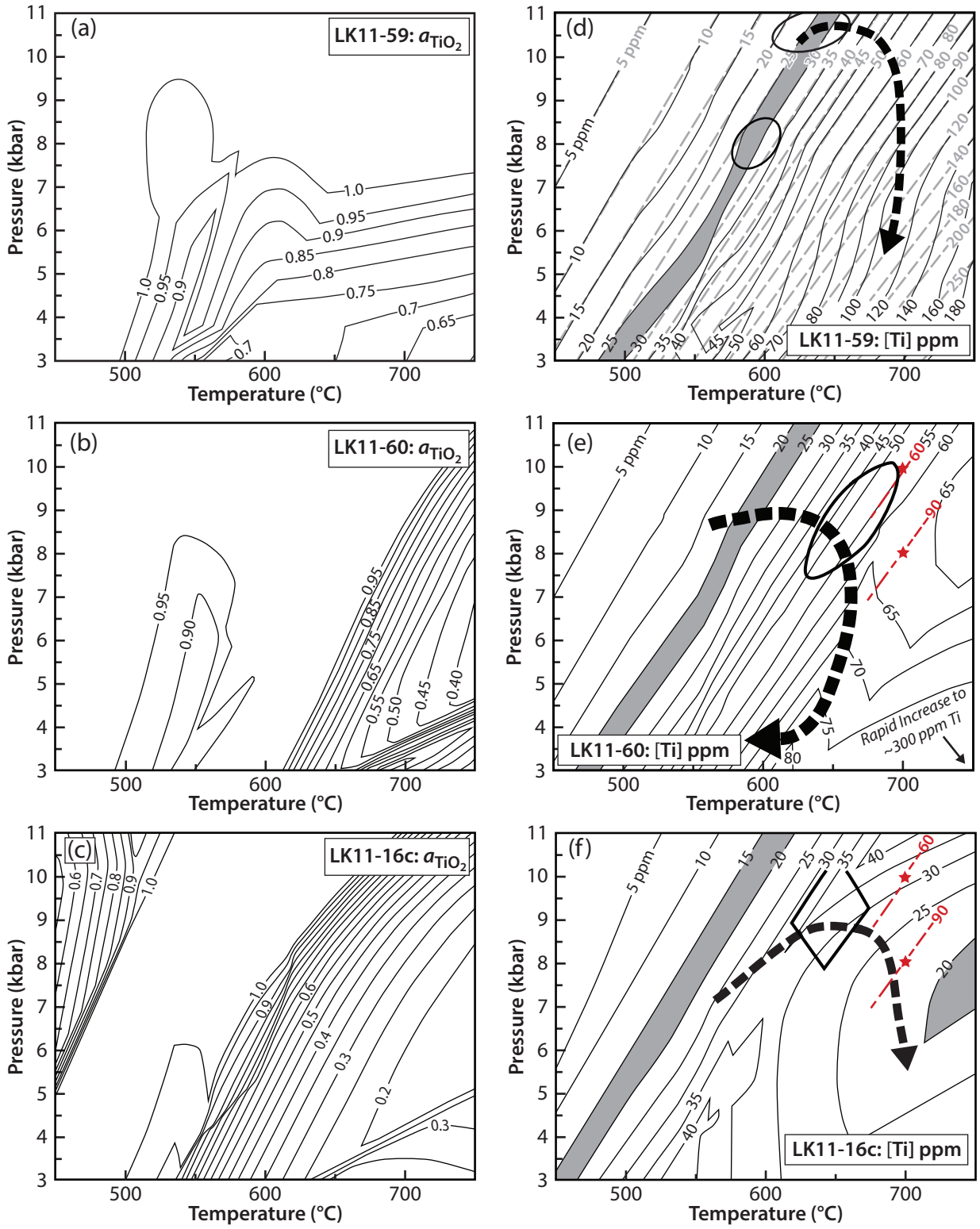


Figure 3.8. Continued.

even larger for LK11-16c, which exhibits the most substantial deviation from $a\mathrm{TiO_2} = 1$ (Fig. 3.8f). This model results in a decrease of [Ti] by 25–30 ppm at 10 kbar and 65–70 ppm at 8 kbar, in line with the original findings by for average metapelite composition Ashley and Law (2015).

Implications for Ti-in-Quartz Thermometry

Previous P-T results for the LKD samples from average phase equilibria calculations and pseudosection models are superposed on Figures 3.8d–3.8f along with the approximate upper limits of Ti-in-quartz measured in this study. Within analytical uncertainty of the EPMA, the measured Ti concentrations presented above do not vary significantly from one microstructural domain to another in individual samples (e.g., Figs 3.2–3.4), with the exception of inclusions in garnet from LK11-59 (Fig. 3.3c), which contain Ti concentrations >10 ppm higher than matrix grains in the same sample. Although the analytical uncertainty could be reduced by averaging the analyses from individual grains, CL imaging indicates that at least some of the measured variation can be attributed to real concentration differences as noted in the 'Results' section above. Regardless of the [Ti] measurements chosen (i.e., average of analyses, minimum and maximum concentration measured, etc.), when applied to the models that predict significantly reduced $a\mathrm{TiO_2}$ (LK11-60 and LK11-16c), the measured [Ti] concentrations still underestimate peak temperatures by 50–100 °C (Figs 3.8e and 3.8f). In contrast, the model for LK11-59 (Fig. 3.8d), which does not predict significant deviation from $a\mathrm{TiO_2} = 1$, yields TitaniQ temperatures that are consistent with previous petrologic temperature constraints. The observation that quartz grains in LK11-59 from matrix microstructural domains commonly exhibit straight grain edges and triple junctions (e.g., Fig. 3.3a) is consistent with static recrystallization and an interpretation that TitaniQ temperatures record prograde metamorphic conditions. This interpretation is also consistent with the fact that the maximum Ti-in-quartz measurements shown on Figure 3.8d derive from quartz inclusions in garnet (Fig. 3.3c) that grew during prograde metamorphism (Diedesch et al., *in prep*). However, the presence of: (1) crosscutting C' shear bands and (2) microstructural evidence indicating some dynamic quartz recrystallization in the sample (Fig. 3.3b), as well as the implications these two observations have for $a\mathrm{TiO_2}$ and TitaniQ calculations, cannot be ignored. Isopleths representing the range of Ti-in-quartz measured in the LKD metapelite samples were calculated for low to medium $a\mathrm{TiO_2}$ values (0.2,

0.4, 0.6) and plotted in Figure 3.9. This was done in order to evaluate the possible influence of dynamic recrystallization on measured Ti concentrations.

The notion that $a\mathrm{TiO_2}$ is significantly reduced during quartz dynamic recrystallization was first introduced by Grujic et al. (2011) in a study of mylonites from the Alps. The authors attributed reduced $a\mathrm{TiO_2}$ directly to the quartz recrystallization process or to (re)crystallization of a Ti-bearing phase concomitant with quartz deformation. The reduced $a\mathrm{TiO_2}$ calculations carried out by Grujic et al. (2011) for the quartz GBM recrystallization regime do not extrapolate to the SGR recrystallization regime, and it has been suggested that this incongruity could result from differences in deformation mechanisms (i.e., crystallographic slip systems) operative in the two recrystallization regimes (Ashley et al., 2014). Other factors besides locally reduced $a\mathrm{TiO_2}$ that influence [Ti] in recrystallized quartz are the duration of deformation, for which the low diffusivity of Ti may become a significant factor (e.g., Kidder et al., 2013), and the magnitude difference between fluid and lithostatic pressure (e.g., Ashley et al., 2014). These additional factors are not likely substantial influences on [Ti] in quartz for the LKD samples because these rocks reached upper amphibolite facies conditions, where the difference between fluid and lithostatic pressures are typically negligible, and previous monazite petrochronology indicates that ductile deformation in the LKD may have lasted ≥11 Myr (Diedesch et al., *in prep*). Using the Ti-in-quartz diffusion parameters established by Cherniak and Watson (2007) and the minimum duration of ductile deformation (11 Myr), Ti volume diffusion in quartz would be effective over a minimum of ~45 μm at 600 °C and ~325 μm at 700 °C. The calculated effective diffusion lengths suggest that re-equilibration of at least near-rim [Ti] during ductile deformation is very likely to have occurred in the LKD samples. The diffusion calculations assume that ductile deformation took place at or near the maximum metamorphic temperatures, and the following evidence suggests that this is a reasonable assumption: (1) synkinematic mineral assemblages that include staurolite + kyanite ± sillimanite, (2) quartz [c] fabric opening angles in quartzite that indicate deformation temperatures as high as 595 ± 50 °C, (3) pseudosection models that indicate nearly isothermal decompression at peak metamorphic temperatures, and (4) monazite petrochronology that suggests partially contemporaneous deformation and Barrovian metamorphism (Diedesch et al., 2016, *in prep*).

Based on the above discussion, it is suggested that dynamic recrystallization influenced [Ti] in quartz from the matrix of sample LK11-59. Given that this sample corresponds to the GBM

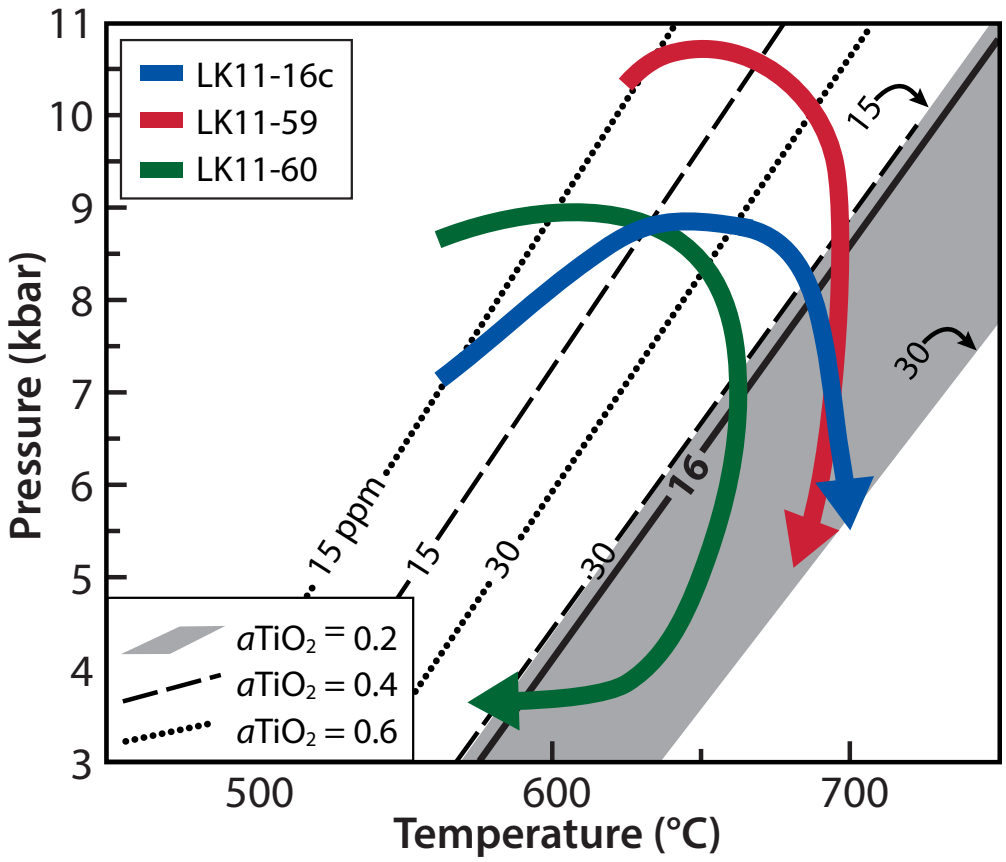


Figure 3.9. *Diagram showing effects of decreased $aTiO_2$ on location of Ti-in-quartz isopleths. Ti-in-quartz isopleths correspond to the highest measured concentrations plotted in P-T space for a range of low to medium aTiO2 values. Line labels are Ti concentration in ppm. Colored arrows are P-T paths derived from Figure 3.7. Note that at $aTiO_2$ = 0.2 the isopleths intersect the P-T paths at the near-isothermal decompression portion, which discussed further in the text. The bold 16-ppm isopleth represents the maximum Ti-in-quartz concentration measured (ignoring analytical uncertainty) in sample LK11-54 assuming $aTiO_2$ = 0.2.*

recrystallization regime, it is reasonable to assume similar local $a\mathrm{TiO_2}$ deviations during deformation to those calculated by Grujic et al. (2011). For the range in measured [Ti] and an $a\mathrm{TiO_2}$ of 0.2, calculated isopleths indicate pressures and temperatures that correspond to the decompression portion of the LK11-59 P-T path (Figs 3.7 and 3.9). However, it should be re-emphasized that modeled $a\mathrm{TiO_2}$ and [Ti] measurements from quartz inclusions produce isopleths that correspond well to pseudosection-modeled prograde metamorphism. Given that matrix quartz [Ti] measurements partially overlap with inclusion quartz [Ti] measurements it is possible that the matrix grains represent similar prograde metamorphic reactions, but this is unlikely assuming the temperature and duration of deformation as described above. Alternatively, quartz-forming reactions are possible during decompression and may explain why much of the matrix quartz exhibits textures indicative of static crystallization. In the other two metapelite samples (LK11-16c, LK11-60), dynamic recrystallization is much more prevalent and in LK11-16c the quartz microstructures are more clearly associated with development of S-C fabric in the rock (e.g., Fig. 3.2d). Unlike sample LK11-59, Ti isopleths calculated for LK11-16c and LK11-60 do not agree well with previously calculated petrologic pressures and temperatures for these samples (Table 3.1; Figs 3.7a, 3.7c). However, if locally reduced $a\mathrm{TiO_2}$ is assumed due to the influence of grain boundary migration recrystallization, then recalculated [Ti] isopleths correspond well with the decompression portions of the interpreted P-T paths of LK11-16c and LK11-60 (Fig. 3.9).

Thus far the Ti-in-quartz results from LK11-54 have been ignored, but here they are worth mentioning for the potential insight they offer into the discussion of the influence of dynamic recrystallization on [Ti] in quartz and local $a\mathrm{TiO_2}$. Sample LK11-54 was collected from ~120 m structurally below LK11-59 and ~175 m below LK11-60. Quartz microstructures and [c] fabric opening angles indicate deformation temperatures of ≥550 °C and 595 ± 50 °C, respectively (Diedesch et al., 2016). Therefore, it is reasonable to assume that this sample reached similar P-T conditions to those of LK11-59 and LK11-60. Rutile is absent in the sample and other Fe-Ti oxides are rare, suggesting $a\mathrm{TiO_2}$ in the sample is low irrespective of the potential influence of dynamic recrystallization. More importantly, it indicates that metamorphic reactions involving Ti likely played little or no role in the distribution of Ti-in-quartz in this sample. Despite these differences, quartz in LK11-54 yields a similar range in [Ti] values to that of the metapelites (Table 3.1; Fig. 3.5b). Since $a\mathrm{TiO_2}$ cannot be independently calculated for LK11-54, any value selected would be speculative, but it is worth noting that the isopleth representing

maximum measured [Ti] in LK11-54 (16 ± 7 ppm) crosses the decompression paths of all three metapelites when $a\mathrm{TiO_2}$ approaches the value calculated for quartz-GBM mylonites in the Alps (Grujic et al., 2011; Fig. 3.9). Given that deformation fabrics in the LKD samples formed during peak Barrovian metamorphism and subsequent decompression, it is suggested here that GBM recrystallization-induced perturbation of local $a\mathrm{TiO_2}$ was an important process that influenced (re)distribution of Ti in quartz in both metapelite and quartzite compositions during high temperature deformation. The modeled effective $a\mathrm{TiO_2}$ operative during deformation in the LKD (~0.2) was of similar magnitude in all four samples and is of similar magnitude to that estimated by Grujic et al. (2011). It must be emphasized that the latter similarity is likely only coincidence. On the other hand, interpretations presented here in conjunction with those of Grujic et al. (2011) indicate a similar magnitude $a\mathrm{TiO_2}$ perturbation (apparent or real) in three different rock types that underwent high-temperature deformation. This could be circumstantial evidence that the operative quartz deformation mechanism is an important influence on apparent $a\mathrm{TiO_2}$ and redistribution of Ti-in-quartz (e.g., Ashley et al., 2014). An alternate interpretation of the LKD TitaniQ results is that the similar matrix quartz [Ti] measured in all four samples reflects a characteristic closure temperature for Ti diffusion, as suggested by Storm and Spear (2009) for pelitic migmatites in the Adirondacks. However, this interpretation is derived from rutile-saturated samples where ideal $\mathrm{TiO_2}$ behavior is expected, whereas the LKD samples exhibit significant deviation from ideal $\mathrm{TiO_2}$.

Summary and Conclusions

Cathodoluminescence imaging and Ti-in-quartz analyses on high grade metasedimentary rocks from the LKD indicate small variations in [Ti] within individual quartz grains as well as between microstructural domains in deformed samples. These samples were selected because they afford the opportunity to evaluate the influence of both metamorphism and ductile deformation on the distribution of Ti-in-quartz. TitaniQ calculations using the maximum measured [Ti] in each sample and the Thomas et al. (2010) solubility equation generally yield lower temperatures than expected based on independent petrologic constraints. Activities of $\mathrm{TiO_2}$ modeled using Perple_X suggest that samples reached metamorphic equilibrium at $a\mathrm{TiO_2} = 0.6–1.0$. Recalculated Ti-in-quartz isopleths, using the reduced $a\mathrm{TiO_2}$ values and [Ti] measurements from garnet-hosted quartz grains, show good agreement

with previous P-T constraints for one sample. However, in the remaining samples $a\mathrm{TiO_2}$-corrected [Ti] isopleths still underestimate temperature conditions. In these samples, a substantially reduced $a\mathrm{TiO_2}$ (= 0.2) is assumed based on previous work, which suggested that grain-boundary migration recrystallization in quartz exerts significant influence on local, apparent $a\mathrm{TiO_2}$ (Grujic et al., 2011). Isopleths of [Ti], modeled for $a\mathrm{TiO_2} = 0.2$, intersect the high-temperature, near-isothermal decompression portion of P-T paths interpreted for three metapelite samples. Previous studies interpreted that high temperature deformation during this portion of the P-T history in the LKD lasted ≥10 Myr, providing ample time for Ti-in-quartz to re-equilibrate during GBM recrystallization. The results documented here reinforce the need to thoroughly characterize microstructures and P-T conditions of naturally deformed samples before ascribing geologic significance to TitaniQ calculations. This is especially necessary in settings like the LKD where both metamorphic reactions and ductile deformation are expected to have influenced $a\mathrm{TiO_2}$ and solubility titanium in quartz.

References

Ashley, K. T., Carlson, W. D., Law, R. D., and Tracy, R. J., 2014, Ti resetting in quartz during dynamic recrystallization: Mechanisms and significance: American Mineralogist, v. 99, no. 10, p. 2025-2030.

Ashley, K. T., and Law, R. D., 2015, Modeling prograde TiO2 activity and its significance for Ti-in-quartz thermobarometry of pelitic metamorphic rocks: Contributions to Mineralogy and Petrology, v. 169, no. 2, p. 1-7

Ashley, K. T., Webb, L. E., Spear, F. S., and Thomas, J. B., 2013, P-T-D histories from quartz: A case study of the application of the TitaniQ thermobarometer to progressive fabric development in metapelites: Geochemistry, Geophysics, Geosystems, v. 14, no. 9, p. 3821-3843.

Behr, W. M., and Platt, J. P., 2011, A naturally constrained stress profile through the middle crust in an extensional terrane: Earth and Planetary Science Letters, v. 303, no. 3–4, p. 181-192.

Chambers, J., Caddick, M., Argles, T., Horstwood, M., Sherlock, S., Harris, N., Parrish, R., and Ahmad, T., 2009, Empirical constraints on extrusion mechanisms from the upper margin of an exhumed high-grade orogenic core, Sutlej valley, NW India: Tectonophysics, v. 477, no. 1–2, p. 77-92.

Cherniak, D. J., Watson, E. B., and Wark, D. A., 2007, Ti diffusion in quartz: Chemical Geology, v. 236, no. 1–2, p. 65-74.

Connolly, J. A. D., 2009, The geodynamic equation of state: What and how: Geochemistry, Geophysics, Geosystems, v. 10, no. 10, p. Q10014.

Cross, A. J., Kidder, S., and Prior, D. J., 2015, Using microstructures and TitaniQ thermobarometry of quartz sheared around garnet porphyroclasts to evaluate microstructural evolution and constrain an Alpine Fault Zone geotherm: Journal of Structural Geology, v. 75, p. 17-31.

Diedesch, T., Jessup, M.J., Cottle, J.M., Zeng, L., 2016, Geologic evolution of Lhagoi Kangri dome, southern Tibet: Lithosphere, doi: 10.1130/L506.1.

Diedesch, T., Jessup, M.J., Cottle, J.M, Zeng, L., *in prep*, Barrovian metamorphism and ductile thinning in Lhagoi Kangri dome, southern Tibet: Journal of Metamorphic Geology.

Donovan, J. J., Lowers, H. A., and Rusk, B. G., 2011, Improved electron probe microanalysis of trace elements in quartz: American Mineralogist, v. 96, no. 2-3, p. 274-282.

Götze, J., Plötze, M., and Habermann, D., 2001, Origin, spectral characteristics and practical applications of the cathodoluminescence (CL) of quartz – a review: Mineralogy and Petrology, v. 71, no. 3, p. 225-250.

Ghent, E. D., and Stout, M. Z., 1984, TiO_2 activity in metamorphosed pelitic and basic rocks: principles and applications to metamorphism in southeastern Canadian Cordillera: Contributions to Mineralogy and Petrology, v. 86, no. 3, p. 248-255.

Grujic, D., Stipp, M., and Wooden, J. L., 2011, Thermometry of quartz mylonites: Importance of dynamic recrystallization on Ti-in-quartz reequilibration: Geochemistry, Geophysics, Geosystems, v. 12, no. 6, p. n/a-n/a.

Holland, T. J. B., and Powell, R., 1998, An internally consistent thermodynamic data set for phases of petrological interest: Journal of Metamorphic Geology, v. 16, no. 3, p. 309-343.

Kidder, S., Avouac, J. P., and Chan, Y. C., 2013, Application of titanium-in-quartz thermobarometry to greenschist facies veins and recrystallized quartzites in the Hsüehshan range, Taiwan: Solid Earth, v. 4, no. 1, p. 1-21.

Kohn, M. J., and Northrup, C. J., 2009, Taking mylonites' temperatures: Geology, v. 37, no. 1, p. 47-50.

Nachlas, W. O., Whitney, D. L., Teyssier, C., Bagley, B., and Mulch, A., 2014, Titanium concentration in quartz as a record of multiple deformation mechanisms in an extensional shear zone: Geochemistry, Geophysics, Geosystems, v. 15, no. 4, p. 1374-1397.

Rolfo, F., Lombardo, B., Musumeci, G., Pertusati, P., and Peruzzo, L., Geology and Metamorphism of the Lhako Kangri Metamorphic Dome, South Tibet, in Proceedings 32nd International Geological Congress, Florence, 2004, International Union of Geological Sciences.

Rusk, B. G., Reed, M. H., Dilles, J. H., and Kent, A. J. R., 2006, Intensity of quartz cathodoluminescence and trace-element content in quartz from the porphyry copper deposit at Butte, Montana: American Mineralogist, v. 91, no. 8-9, p. 1300-1312.

Spear, F. S., Ashley, K. T., Webb, L. E., and Thomas, J. B., 2012, Ti diffusion in quartz inclusions: implications for metamorphic time scales: Contributions to Mineralogy and Petrology, v. 164, no. 6, p. 977-986.

Spear, F. S., and Wark, D. A., 2009, Cathodoluminescence imaging and titanium thermometry in metamorphic quartz: Journal of Metamorphic Geology, v. 27, no. 3, p. 187-205.

Stevens-Kalceff, M. A., Phillips, M. R., Moon, A. R., and Kalceff, W., 2000, Cathodoluminescence Microcharacterisation of Silicon Dioxide Polymorphs, in Pagel, M., Barbin, V., Blanc, P., and Ohnenstetter, D., eds., Cathodoluminescence in Geosciences: Berlin, Heidelberg, Springer Berlin Heidelberg, p. 193-224.

Stipp, M., Stünitz, H., Heilbronner, R., and Schmid, S. M., 2002, The eastern Tonale fault zone: a 'natural laboratory' for crystal plastic deformation of quartz over a temperature range from 250 to 700°C: Journal of Structural Geology, v. 24, no. 12, p. 1861-1884.

Storm, L. C., and Spear, F. S., 2009, Application of the titanium-in-quartz thermometer to pelitic migmatites from the Adirondack Highlands, New York: Journal of Metamorphic Geology, v. 27, no. 7, p. 479-494.

Tajčmanová, L., Connolly, J. A. D., and Cesare, B., 2009, A thermodynamic model for titanium and ferric iron solution in biotite: Journal of Metamorphic Geology, v. 27, no. 2, p. 153-165.

Thomas, J. B., Bruce Watson, E., Spear, F. S., Shemella, P. T., Nayak, S. K., and Lanzirotti, A., 2010, TitaniQ under pressure: the effect of pressure and temperature on the solubility of Ti in quartz: Contributions to Mineralogy and Petrology, v. 160, no. 5, p. 743-759.

Thomas, J. B., Watson, E. B., Spear, F. S., and Wark, D. A., 2015, TitaniQ recrystallized: experimental confirmation of the original Ti-in-quartz calibrations: Contributions to Mineralogy and Petrology, v. 169, no. 3, p. 1-16.

Wark, D. A., and Watson, E. B., 2006, TitaniQ: a titanium-in-quartz geothermometer: Contributions to Mineralogy and Petrology, v. 152, no. 6, p. 743-754.

White, R.W., Powell, R., Holland, T.J.B., and Worley, B., 2000, The effect of TiO_2 and Fe_2O_3 on metapelitic assemblages at greenschist and amphibolite facies conditions: mineral equilibria calculations in the system K_2O–FeO–MgO–Al_2O_3–SiO_2–H_2O–TiO_2–Fe_2O_3: Journal of Metamorphic Geology, v. 18, no. 5, p. 497-511.

White, R. W., Powell, R., Holland, T. J. B., Johnson, T. E., and Green, E. C. R., 2014, New mineral activity–composition relations for thermodynamic calculations in metapelitic systems: Journal of Metamorphic Geology, v. 32, no. 3, p. 261-286.

CONCLUSION

Gneiss domes along the North Himalayan antiform, including the Lhagoi Kangri dome, provide exposures of middle crustal rocks that allow evaluation of the processes and structures that influenced early evolution of the Himalaya. Mapping and structural analysis in the Lhagoi Kangri dome provided the context for detailed microstructural, thermobarometric, and geochronologic analyses that collectively constrain magnitudes and rates of metamorphism, ductile deformation, and exhumation. Results indicate that the metasedimentary rocks that cap the dome reached maximum burial of 30–36 km by ~40 Ma, consistent with values for Barrovian metamorphism reported for other Himalayan middle crustal exposures. Following burial, rocks in the Lhagoi Kangri dome were subjected to high temperatures (550–700 °C) for a prolonged period (≥11 My) during which a distributed shear zone developed. The shear zone is characterized by heterogeneous general shear and attenuation across the zone that progressed from structurally low to structurally high (i.e., hotter isotherms to cooler isotherms) through time, resulting in an elevated thermal field gradient of at least 56 °C/km. Ductile deformation continued until at least 24 Ma and possibly even later. Nearly isothermal decompression occurred coevally with late stages of ductile deformation in the shear zone and indicates the rocks experienced at least 12 km of exhumation. This estimated magnitude is much larger than can be explained by vertical attenuation alone. Nearly isothermal decompression is consistent with models of doming and exhumation that involve local upper crustal extension, but the distributed shear zone documented in the Lhagoi Kangri dome is more consistent with doming by underthrusting. Neither model is ruled out for the Lhagoi Kangri dome, but it is clear that the shear zone does not account for the total exhumation calculated for the Lhagoi Kangri dome. These findings reinforce previous studies that suggest the Himalayan middle crust was subjected to high temperatures for a sufficient period of time to weaken the rocks and allow them to flow laterally. In the Lhagoi Kangri dome, lateral flow was accompanied by vertical attenuation that potentially reflects influence of local upper crustal extension.

VITA

Tim was born in Sacramento, CA to parents Barbara and Jon Diedesch. He is the middle of three children, whom include an older brother, Joshua, and a younger sister, Jessica. He attended Thomas W. Coleman Elemenatary School continuing to Andrew Carnegie Middle School follwed by Casa Roble Fundamental High School in Orangevale, CA. After graduating, Tim moved to San Luis Obispo, CA, to study Electrical Engineering at California Polytechnic Institute. After realizing that the program was not the right fit, he began taking Construction Management courses at which time he discovered his passion for geology and went on to earn a Bachelor of Science in Geology from Sacramento State University in December, 2008. He was an undergraduate teaching assistant for four upper division courses and was instrumental in organizing the department's Rock Auction, an annual fundraiser to help students offset field expenses. Tim took a half year off to finish recording an album with his former band Cuesta Drive before accepting an offer to attend graduate school at Idaho State University in Pocatello, ID. There, he completed a Master of Science in Geology in June, 2011, under the guidance of David W. Rodgers. Shortly thereafter, he completed his first summer of field work in the Himalaya with Micah Jessup, marking the beginning of his tenure as a graduate student pursuing a Doctor of Philosophy in Geology at The University of Tennessee.